Doctorate Dissertation

博士論文

Modeling the effect of helicity on the transport of the Reynolds stress in rotating inhomogeneous turbulence

（回転系非一様乱流におけるレイノルズ応力輸送に及ぼすヘリシティの効果のモデリング）

A Dissertation Submitted for Degree of Doctor of Philosophy
December 2018

平成 30 年 12 月博士（理学）申請

Department of Physics, Graduate School of Science,
The University of Tokyo

東京大学理学系研究科物理学専攻

Kazuhiro Inagaki

稲垣　和寛

Abstract

Effect of helicity on the transport for the Reynolds stress, which is the auto-correlation of velocity fluctuations, and its modeling in inhomogeneous turbulence are discussed. The numerical simulation of the previous study showed that the mean velocity is generated in rotating turbulence accompanied with helicity. This mean velocity generation phenomenon is consistent with the previously proposed algebraic model for the Reynolds stress accompanied with the turbulent helicity, which is the statistically averaged inner product of velocity and vorticity fluctuations. However, the mechanism that the turbulent helicity affects the Reynolds stress has not been clarified. In order to investigate the mechanism of the mean velocity generation phenomenon and its relation to the turbulent helicity, the numerical simulation of rotating turbulence in which the turbulent helicity is injected by using the external forcing is performed. It is shown that the pressure diffusion term, which is the spatial derivative of the correlation between velocity and pressure fluctuations, has a significant contribution to the Reynolds stress transport in the presence of both the system rotation and the turbulent helicity injection. It is revealed that the correlation between fluctuations of velocity and pressure associated with the rotation is closely related to the turbulent helicity. A new turbulence model for the pressure diffusion term accompanied with the turbulent helicity is proposed. It is also shown that the previously proposed algebraic model for the Reynolds stress accompanied with the turbulent helicity can be obtained by incorporating the effect of the pressure diffusion. It is shown that the model for the Reynolds stress accompanied with the turbulent helicity can account for the mean velocity generation phenomenon without contradiction to the simulation results. Since the pressure diffusion is conventionally neglected in the previous turbulence modeling, the present result points out the critical shortfall of the conventional turbulence model in rotating turbulence accompanied with the turbulent helicity.

In the previous studies, it was known that the turbulent energy is transferred faster in the direction of the rotation axis in rotating system than in non-rotating system. Such a fast energy transport in the direction of the rotation axis cannot be predicted by the conventional turbulence models using the gradient-diffusion approximation. In order to investigate the turbulence model predicting this phenomenon, the numerical simulation of decaying inhomogeneous turbulence in rotating system is performed. It is shown that the pressure diffusion term associated with the rotation significantly contributes to the fast energy transport in the rotating system. It is suggested that the energy flux due to the pressure associated with the rotation can be predicted by the newly proposed model accompanied with the turbulent helicity. It is shown that this energy flux due to the rotation is tightly connected to the group velocity of inertial waves described by the linearized momentum equation in a rotating system. Finally, the helical Rossby number is defined as an index for judging the significance of the energy flux due to the turbulent helicity in general turbulent flows.

Contents

Chapter 1

Introduction

1.1 Fluid turbulence

Fluids are ubiquitous in our daily life, e.g., the air in the atmosphere or the water from a tap. Many of these fluids flow in a complex form accompanied with vortices of various scales. Such complex flows of fluids are referred to as turbulence. The beginning of the research history on turbulence dates back to Reynolds (1883) of 130 years ago. Reynolds (1883) suggested that the transition from laminar or non-turbulent flow to turbulent flow in a straight pipe can be described by means of one parameter, the well-known Reynolds number Re. The Reynolds number is defined as $\mathrm{Re} = LU/\nu$ where U denotes the reference velocity, L the reference length, and ν the kinematic viscosity of a fluid, respectively. For example, in the case of a flow in a straight pipe schematically shown in Fig. 1.1, the bulk mean velocity U_m and the pipe diameter D are respectively chosen for U and L. Roughly speaking, the intensity of the inertia of fluid motion and the momentum diffusion due to the viscosity are respectively estimated as U^2/L and $\nu U/L^2$, so that the Reynolds number can be interpreted as the ratio of the former to the latter, $(U^2L^{-1})/(\nu UL^{-2}) = UL/\nu = \mathrm{Re}$. This fact indicates that the nonlinearity in fluid motion coming from the inertial term becomes significant as the Reynolds number increases. In fact, Reynolds (1883) showed that the flow becomes turbulent as the Reynolds number increases, $\mathrm{Re} \gg 1$ (Fig. 1.1). Note that the kinematic viscosity of the air is $\nu \sim 10^{-5}[\mathrm{m}^2/\mathrm{s}]$ and of the water is $\nu \sim 10^{-6}[\mathrm{m}^2/\mathrm{s}]$, so that the flows of the air or the water observed around us are almost turbulence. Nevertheless, many properties of turbulent flows are still open problem owing to its complexity. Researches for fluid turbulence are difficult but quite significant for understanding the physics of fluids around us.

1.2 Multi-scale property of turbulence

The structure of cumulus cloud is an example of visualization of turbulent flow (Fig. 1.2). As seen in Fig. 1.2, turbulent flow involves vortices of various scales. This suggests that turbulent flow is highly multi-scale phenomenon. It is known that the ratio of the largest length scale L to the smallest scale of turbulence η can be estimated as $L/\eta = O(\mathrm{Re}^{3/4})$ [Yoshizawa (1998); Pope (2000)] and turbulent eddies

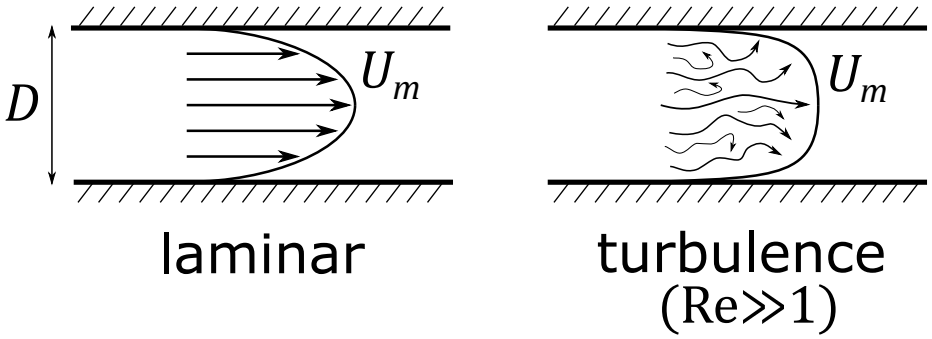

Figure 1.1: Schematic diagram for laminar and turbulent flow in a straight pipe.

are continuously distributed from L to η. The direct numerical simulation (DNS) of turbulence requires resolving eddies of the smallest scale η, so that the required grid number N increase as $N^3 \sim (L/\eta)^3 = O(\mathrm{Re}^{9/4})$ for three dimensional case. The Reynolds number is estimated as $\mathrm{Re} \sim 10^8$ for the flow around an aircraft and as $\mathrm{Re} \sim 10^{12}$ for a tropical cyclone. Hence, the DNS of such large-scale turbulent flows in real world is considered to be unfeasible even if we would use the high-performance computer of the near future.

Figure 1.2: Schematic image of turbulent flow in a cumulus cloud.

1.3 Closure problem

Despite complex and multi-scale feature of turbulence, statistical properties such as the mean velocity, turbulence intensity, and etc., are known to be reproducible. If we have a set of self-consistent equations

for the mean velocity, we can predict the mean velocity profile of high-Reynolds-number turbulent flows with much smaller numerical cost than using the DNS. However, governing equations for statistical values of turbulence are never closed due to the nonlinearity of the Navier–Stokes equation, the most basic momentum equation for fluids. Hence, the self-consistent equation for statistical values of turbulence cannot be derived without any assumptions for higher-order moments. This is referred to as the closure problem. Theoretical approach for the closure problem, which is referred to as the closure theory, has been developed mainly in simple homogeneous isotropic turbulence. A representative closure theory for turbulence is the direct-interaction approximation (DIA) developed by Kraichnan (1959). The remarkable point of the DIA is to introduce the response function for the nonlinear Navier–Stokes equation, describing the time history effect of turbulence. Although the DIA failed to predict the scale-similar energy spectrum suggested by Kolmogorov (1941) due to the breakage of the Galilean invariance, it was a remarkable success that the DIA derives the closed equation for statics of turbulence without empirical parameter. In the later time, the failure of the DIA was overcome by introducing the Lagrangian picture [Kraichnan (1965); Kaneda (1981)].

1.4 Turbulence modeling for inhomogeneous flow

In real world turbulent flows, flows are inhomogeneous, that is the statistical quantities vary in space. Theoretical approach for inhomogeneous turbulence is much more difficult than homogeneous turbulence where the sophisticated closure theories have been developed. For inhomogeneous turbulence, some turbulence correlations are modeled in terms of the statistical quantities such as the mean velocity gradient or the intensity of turbulence to close the governing equations. Such a modeling is referred to as the turbulence modeling. From the practical viewpoint, the prediction of the mean velocity is the first subject in real world flows since the mean velocity profile gives the flow rate for internal flows and the drag force for external flows. For example, the flow rate determines the ability of an engineering device and the drag force is required for development of an airplane or a building. In order to see the statistical behavior of the mean velocity, the ensemble average is taken for the Navier–Stokes equation. The ensemble averaged Navier–Stokes equation is referred to as the Reynolds-averaged Navier–Stokes (RANS) equation and related turbulence modeling is referred to as the RANS modeling. By using the RANS model, we can predict the mean velocity profile of high-Reynolds-number turbulent flows without numerically solving highly stochastic motion governed by the Navier–Stokes equation. The numerical cost is much decreased with the aid of the RANS modeling. It should be noted that the accuracy of the prediction obtained by using the RANS equation depends on the validity of the RANS modeling. Hence, the development of physically reliable RANS modeling is a significant subject.

In order to close the RANS equation, a model for the Reynolds stress, which is the auto-correlation of velocity fluctuations, is needed. The RANS modeling is roughly classified to two types; one is to give the algebraic model for the Reynolds stress and the other is to model the transport equation for the Reynolds stress. The former is referred to as the algebraic modeling or the eddy-viscosity type modeling, and the latter is referred to as the Reynolds stress equation modeling or the second-order modeling. A primitive model for the algebraic modeling is the eddy-viscosity model [Yoshizawa (1998); Pope (2000)]. The eddy-

viscosity model describes the effective viscosity due to turbulent eddies. The eddy-viscosity model is not just an empirical model but is algebraically related to the transport equation for the Reynolds stress [Pope (1975)]. Note that Pope (1975) proposed a more general model expression for the Reynolds stress, which is referred to as the nonlinear eddy-viscosity model, based on the Reynolds stress transport. This result suggests that the anisotropic property for the Reynolds stress can be deductively expressed from the Reynolds stress transport.

Yoshizawa (1984) developed a statistical theory for inhomogeneous turbulence modeling named the two-scale direct interaction approximation (TSDIA). The TSDIA is the combination of multiple-scale expansion method and the DIA developed by Kraichnan (1959). In the TSDIA, the effect of anisotropy and inhomogeneity is incorporated through the higher-order scale in a perturbational manner with the aid of the response function introduced in the DIA. The TSDIA succeeded in theoretically obtaining the nonlinear eddy-viscosity model. A remarkable point of the TSDIA is that the theory is based on the Navier–Stokes equation, so that it enables us to obtain the models for turbulence field affected by the system rotation, the buoyancy, or the magnetic field, starting from the basic equation [see, Yoshizawa (1998) for details].

1.5 Effects of helicity on turbulence

Helicity, strictly speaking the helicity density, denotes the inner product of velocity and vorticity (Fig. 1.3). Helicity characterizes the helical structure of the flow. The volume average of helicity is an inviscid invariant as the volume average of kinetic energy is, so that it is a basic quantity in fluid mechanics. Since helicity is a pseudo-scalar which changes its sign by the parity transformation, it is related to the breakage of the mirror or reflection symmetry. However, the effect of helicity on turbulence is not clearly understood and has been under discussion to date.

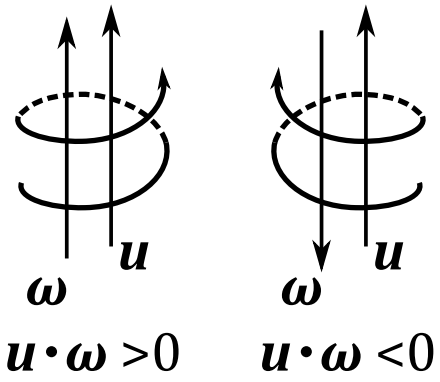

Figure 1.3: Schematic diagram for helicity. $\boldsymbol{u}$ denotes the velocity and $\boldsymbol{\omega}(= \boldsymbol{\nabla} \times \boldsymbol{u})$ denotes the vorticity.

For homogeneous turbulence, the effect of helicity was discussed in terms of the energy cascade or the inter-scale energy transfer [Brissaud *et al.* (1973)]; namely, the possibility of the inverse energy cascade was discussed on the analogy of the two-dimensional turbulence [Kraichnan (1967)]. André & Lesieur (1977)

examined the effect of helicity on homogeneous decaying turbulence by using the closure theory named the eddy-damped quasi-normal Markovian (EDQNM) approximation. They showed that in the presence of helicity, the decay rate of energy is reduced in the early stage. Morinishi *et al.* (2001*c*) performed a DNS of homogeneous decaying turbulence accompanied with helicity and observed the decrease of the decay of energy due to helicity shown by André & Lesieur (1977). They observed the inverse energy cascade only in the early stage with maximally helical initial condition. Biferale *et al.* (2012, 2013) performed the numerical simulation in which the projection operator which maps velocity field to homo-chiral component is introduced; that is, the turbulent flow which has either positive or negative helicity was investigated. They observed the inverse cascade in the homo-chiral homogeneous turbulence. Stepanov *et al.* (2015) suggested that the forward cascade is hindered when the turbulence is highly helical in the wide range of scales. This behavior was observed in the DNS of homogeneous turbulence [Kessar *et al.* (2015)]. However, such a highly helical condition is difficult to appear in real world turbulent flows since the mirror symmetry tends to be restored due to the nonlinear interaction [Kraichnan (1973); Chen *et al.* (2003)]. In the fully-developed stage of turbulence, the prediction of the EDQNM given by André & Lesieur (1977) suggested that the difference between the turbulent flows with and without helicity was not observed; namely, the energy spectrum in the fully-developed stage is not changed regardless of the presence of helicity. The same spectral behavior was observed in the DNS of forced homogeneous turbulence [Borue & Orszag (1997); Baerenzung *et al.* (2008)], the DNS of the Ekman boundary layer [Deusebio & Lindborg (2014)], and the experiment in the atmospheric boundary layer [Koprov *et al.* (2005)]. These results suggested that helicity has negligible effect on the dynamics of turbulence in the fully-developed stage and it looks like the same as a passive scalar [Moffatt (1978)]. However, the possibility of the effect of helicity on the inertial range of fully-developed turbulence was pointed out [Linkmann (2018)]. Hence, effect of helicity on fully-developed turbulence is not concluded but still under discussion. In another context, the relationship between the strong helicity and the small dissipation events has been argued. However, it was suggested that there is a tenuous relationship between helicity and the small dissipation rate event in several shear flows [Rogers & Moin (1987); Wallace *et al.* (1992)].

In the context of magnetohydrodynamics (MHD), the effect of helicity on the magnetic field has been discussed in relation to the dynamo action referred to as the α dynamo [Moffatt (1978); Krause & Rädler (1980); Brandenburg & Subramanian (2005)]; namely, large-scale magnetic field is generated by the α dynamo effect. Similar effect has been also discussed for neutral hydrodynamics from the viewpoint of the large-scale vortex generation, which is sometimes referred to as the vortex dynamo. For incompressible fluid, Frisch *et al.* (1987) suggested that the breakage of the parity-invariance is essential for the presence of the α-like effect for the vortex dynamo. They also suggested that the anisotropy invokes the α-like effect for the vortex dynamo, which is referred to as the anisotropic kinetic alpha (AKA) effect. In the context of the effect of helicity, Gvaramadze *et al.* (1989) suggested that not only the presence of helicity but also the inhomogeneity of the flow is required for the vortex dynamo effect. Yokoi & Yoshizawa (1993) proposed the model expression for the Reynolds stress accompanied with the turbulent helicity with the aid of the TSDIA [Yoshizawa (1984)]. Here, the turbulent helicity denotes the ensemble average of the inner product of velocity and vorticity fluctuations. In their model, the spatial derivative of the turbulent helicity is essential value rather than helicity itself. The spatially varying turbulent helicity was observed in several turbulent flows such as the flow in a straight pipe with wall rotation [Orlandi (1997)],

the swirling jet [Stepanov *et al.* (2018)], and the Ekman boundary layer [Deusebio & Lindborg (2014)]. The effect of helicity has been also argued in meteorological flows [Lilly (1986); Noda & Niino (2010)]. However, the contribution of the vortex dynamo effect due to the turbulent helicity to such turbulent flows is not clear.

An example of the flow which is related to the vortex dynamo effect is the turbulent swirling flow in a straight pipe [Kitoh (1991); Steenbergen (1995)]. In this flow, the radial distribution of the mean velocity in the direction of the pipe axis exhibits a dent in the center axis region of the pipe. This dent profile is sustained to the downstream over several tens of times of the pipe diameter. Moreover, it exhibits a reversal flow in the center axis region when the strong swirl is given [Kitoh (1991)]. This phenomenon is the local flow generation due to the swirling motion, so that it can be interpreted as an example of the vortex dynamo. In the context of turbulence modeling, the conventional models described by the eddy-viscosity model cannot predict the sustainment of the dent axial mean velocity profile in the turbulent swirling flow in a straight pipe [Kobayashi & Yoda (1987); Steenbergen (1995); Jakirlić *et al.* (2000)]. This fact suggests that a new model describing the effect of swirling motion of a fluid is required to predict the turbulent flows accompanied with swirling motion. The model proposed by Yokoi & Yoshizawa (1993) succeeded in predicting the sustainment the axial mean velocity in the swirling flow in a straight pipe without any empirical modification to the model constant in the eddy-viscosity model. However, the sustainment of the dent axial mean velocity profile was also predicted by the Reynolds stress equation model which does not involve the turbulent helicity [Jakirlić *et al.* (2000)] or by the history effect of the streamline on the eddy viscosity [Hamba (2017)]. In this sense, the physical origin of the mechanism of the sustainment the dent axial mean velocity profile in the turbulent swirling flow in a straight pipe is under discussion.

Another example of the vortex dynamo related phenomenon is the mean velocity generation phenomenon observed by Yokoi & Brandenburg (2016). They performed a numerical simulation of rotating turbulence starting from the zero-mean velocity condition in which the inhomogeneous distribution of the turbulent helicity is established by using the external forcing. In this simulation, the positive mean velocity in the direction of the rotation axis is generated at the region in which the turbulent helicity is positive, while the negative mean velocity is generated at the region in which the turbulent helicity is negative. Neither the conventional algebraic models in terms of the mean velocity gradients nor the Reynolds stress equation models can account for this mean velocity generation phenomenon since they give the trivial solution of the zero-mean velocity. The model given by Yokoi & Yoshizawa (1993) which is accompanied with the turbulent helicity can account for this phenomenon. In fact, Yokoi & Brandenburg (2016) confirmed that the Reynolds stress itself and the model expression given by Yokoi & Yoshizawa (1993) are well correlated at the early stage of the simulation.

However, physically unclear point lies in the model accompanied with the turbulent helicity proposed by Yokoi & Yoshizawa (1993). In the transport equation for the Reynolds stress, the turbulent helicity does not appear explicitly. Hence, the mechanism that the turbulent helicity affects the Reynolds stress is unclear. Owing to this fact, the model proposed by Yokoi & Yoshizawa (1993) cannot be derived in the systematic manner developed by Pope (1975) which is based on the Reynolds stress transport. This problem gives a question on the significance of helicity and the related vortex dynamo effect in real world turbulent flows. In order to assess when and how much the turbulent helicity affects the mean velocity

in turbulent flows, the effect of the turbulent helicity on the transport of the Reynolds stress and the turbulence energy must be examined in detail.

1.6 Effects of rotation on turbulence

Turbulent flows are sometimes affected by rotational motion. For example, in engineering flows, rotational turbulent flows are observed around a turbine or a propeller. Such a rotational motion of fluid is also observed at the wake of an aircraft [Spalart (1998)]. It is known that the wake vortices behind an aircraft persist over a long time. This phenomenon strongly affects the time interval of take-off or landing. For atmospheric turbulence, the effect of the Earth's rotation is significant for large-scale flows. The formation of the large vortex of a tropical cyclone is the result of the Coriolis force due to the Earth's rotation. Hence, it is worth researching the effects of rotation on turbulence.

In a rapidly rotating fluid, the Taylor–Proudman theorem suggests that the variation of a flow in the direction of the rotation axis is suppressed and the flow becomes two-dimensional [see, e.g., Davidson (2004)]. Such a two-dimensionalization of a fluid in a rotating system has been examined in homogeneous turbulence although the exactly two-dimensional state is not established [Cambon & Jacquin (1989); Cambon *et al.* (1997); Morinishi *et al.* (2001*a*); Yoshimatsu *et al.* (2011)]. The rotation not only leads to the anisotropy but also alters the inter-scale energy transfer; namely, the energy cascade rate from large to small scales is reduced due to the rotation for homogeneous decaying turbulence [Bardina *et al.* (1985); Cambon & Jacquin (1989); Morinishi *et al.* (2001*a*)]. In the RANS modeling, this phenomenon was indirectly treated by modeling the reduction of the energy dissipation rate instead of modeling the reduction of the energy cascade rate [Bardina *et al.* (1985)]. Okamoto (1995) proposed a model for expressing the reduction of the energy dissipation rate in rotating turbulence with the aid of the TSDIA. Using these models, the effect of rotation on homogeneous turbulence can be predicted by the RANS model.

For inhomogeneous turbulence, effects of rotation have been mainly discussed in terms of the Reynolds stress. For example, the nonlinear eddy-viscosity model incorporated with the rotation effect was proposed [Gatski & Speziale (1993); Craft *et al.* (1996); Wallin & Johanson (2000)] and the model accompanied with the turbulent helicity was also proposed [Yokoi & Yoshizawa (1993)]. However, the effect of rotation on the energy transport has not been so much discussed. Dickinson & Long (1983) performed an experiment of oscillating-grid turbulence in rotating system. In this experiment, the turbulent energy is injected by the oscillation of grid in a tank and the rotation axis is set in the direction perpendicular to the grid plane. They showed that the width of the turbulence region d grows as $d \sim t$ in the rotating case, while it is $d \sim t^{1/2}$ in the non-rotating case. Namely, the growth of the width of the turbulence region is faster in the rotating case than in the non-rotating case. The same result was shown by experiments [Davidson *et al.* (2006); Kolvin *et al.* (2009)] and the numerical simulation [Ranjan & Davidson (2014)]. This result suggests that the turbulent energy flux is enhanced by the rotation. In the RANS modeling, the energy flux is often modeled by the gradient-diffusion approximation [Yoshizawa (1998); Pope (2000)]. Since the gradient-diffusion approximation leads to the conventional diffusion equation for the turbulent energy, such an energy diffusion proportional to t observed in rotating system cannot be predicted. Therefore, a

new model for energy flux incorporated with the effect of rotation is required. Ranjan & Davidson (2014) suggested that this fast energy transport in rotating system is the result of the propagation of inertial wave which is described by the linearized momentum equation in a rotating system. Since the propagation direction of the group velocity of inertial waves is closely related to the sign of helicity [Moffatt (1970)], helicity is expected to play a significant role in the fast turbulent energy transport observed in rotating turbulence.

1.7 Overview of this dissertation

The objective of this dissertation is to clarify and model the effect of the turbulent helicity on the transport of the Reynolds stress. In this study, we focus on the two phenomena: one is the mean velocity generation observed by Yokoi & Brandenburg (2016) and the other is the fast energy transfer observed in rotating oscillating-grid turbulence [Dickinson & Long (1983); Davidson *et al.* (2006); Kolvin *et al.* (2009); Ranjan & Davidson (2014)]. In the former, we perform a numerical simulation of non-rotating and rotating turbulence in which the turbulent energy and helicity are locally injected by using the external forcing. Since the mean velocity is generated due to the Reynolds stress, we examine the transport for the Reynolds stress and survey the physical origin of this phenomenon and its relation to the turbulent helicity. In the latter, we perform freely decaying inhomogeneous turbulence in which the turbulent energy is diffused in one direction. This simulation is similar to that performed by Ranjan & Davidson (2014) which corresponds to the experiment of oscillating-grid turbulence with a single grid oscillation performed by Davidson *et al.* (2006). We examine the effect of rotation and the turbulent helicity on the transport for the turbulent energy which corresponds to the trace of the Reynolds stress.

The organization of this dissertation is as follows. In Chap. 2, summaries for the previous turbulence models are given. Shortfalls of the previous turbulence models are also given here. In Chap. 3, we show the results of the simulation of the mean flow generation. In this chapter, the effect of the turbulent helicity on the Reynolds stress transport is investigated. We propose a new model expression for the diffusion term associated with pressure in the Reynolds stress transport equation here. In Chap. 4, we show the results of the simulation of decaying inhomogeneous turbulence with and without system rotation. In this chapter, the effect of the rotation and the turbulent helicity on the turbulent energy transport is discussed. Here, the model newly proposed in Chap. 3 also plays a significant role. Discussion is given in Chap. 5. Summary and conclusions are given in Chap. 6. Part of the results given in Chap. 3 are published in Inagaki *et al.* (2017) and those given in Chap. 4 and Sec. 5.3 are published in Inagaki & Hamba (2018).

Chapter 2

Turbulence modeling and its shortfalls

2.1 Governing equations

2.1.1 Governing equations for incompressible fluid

Dynamics of fluid motion is known to be well described by the continuity equation and the Navier–Stokes equation:

$$\frac{\partial u_i}{\partial x_i} = 0, \tag{2.1}$$

$$\frac{\partial u_i}{\partial t} = -\frac{\partial}{\partial x_j}(u_i u_j) - \frac{\partial p}{\partial x_i} + \frac{\partial}{\partial x_j}(2\nu s_{ij}) + f_i. \tag{2.2}$$

Here and hereafter, incompressible fluid is considered, so that the mass density is constant. In Eqs. (2.1) and (2.2), $\boldsymbol{u}$ denotes the velocity, p the pressure (strictly speaking the pressure divided by the mass density), ν the kinematic viscosity, $s_{ij}[= (\partial u_i/\partial x_j + \partial u_j/\partial x_i)/2]$ the strain rate, and $\boldsymbol{f}$ the external forcing. In the first term on the right-hand side of Eq. (2.2), $u_i u_j$ represents the flux of u_i to the x_j direction due to u_j, so that u_i is spatially transferred when $u_i u_j$ varies in the x_j direction. Hence, the first term on the right-hand side of Eq. (2.2) represents the spatial momentum transport due to the velocity itself. Schematic diagram for the flux of u_x due to u_y through the nonlinear term is shown in Fig. 2.1(a). It should be noted that this nonlinearity is the source of turbulent motion of fluid. The second term on the right-hand side of Eq. (2.2) represents the forcing due to the pressure gradient. In the third term on the right-hand side of Eq. (2.2), $-2\nu s_{ij}$ represents the flux of u_i to the x_j direction due to the viscous stress. Schematic diagram for the flux of u_x due to the viscous stress is shown in Fig. 2.1(b) in the case that $\boldsymbol{u} = (u_x(y), 0, 0)$ and $\partial u_x/\partial y > 0$. As seen in Fig. 2.1(b), u_x is transferred from the large u_x region to the small u_x region. This indicates that the viscous term plays a role of flattening the velocity profile. Using the incompressibility condition (2.1), Eq. (2.2) is rewritten as

$$\frac{\partial u_i}{\partial t} = -\frac{\partial}{\partial x_j}(u_i u_j) - \frac{\partial p}{\partial x_i} + \nu\nabla^2 u_i + f_i, \tag{2.3}$$

where $\nabla^2 (= \partial^2/\partial x_i \partial x_i)$ denotes the Laplacian operator. Hence, the viscous term can be also interpreted as the momentum diffusion due to the viscous friction. In an incompressible fluid, the pressure is obtained through the Poisson equation derived by taking the divergence of Eqs. (2.2) or (2.3):

$$\nabla^2 p = -\frac{\partial^2}{\partial x_i \partial x_j}(u_i u_j) = -s_{ij} s_{ij} + \frac{1}{2}\omega_i \omega_i, \tag{2.4}$$

where $\boldsymbol{\omega} (= \boldsymbol{\nabla} \times \boldsymbol{u})$ denotes the vorticity and the forcing term is assumed to be solenoidal, $\boldsymbol{\nabla} \cdot \boldsymbol{f} = 0$. The nonlinear term in the Navier–Stokes equation can be rewritten as follows:

$$-\frac{\partial}{\partial x_j}(u_i u_j) = \epsilon_{ij\ell} u_j \omega_\ell - \frac{\partial}{\partial x_i}\left(\frac{1}{2} u_j u_j\right), \tag{2.5}$$

where $\epsilon_{ij\ell}$ is the alternating tensor. Then, Eq. (2.3) is rewritten as

$$\frac{\partial u_i}{\partial t} = \epsilon_{ij\ell} u_j \omega_\ell - \frac{\partial}{\partial x_i}\left(p + \frac{1}{2} u_j u_j\right) + \nu \nabla^2 u_i + f_i. \tag{2.6}$$

Taking the curl of Eq. (2.6), the equation for the vorticity $\boldsymbol{\omega}$ is written as

$$\begin{aligned} \frac{\partial \omega_i}{\partial t} &= \epsilon_{ij\ell} \frac{\partial}{\partial x_j}\left(\epsilon_{\ell ab} u_a \omega_b\right) + \nu \nabla^2 \omega_i + \epsilon_{ij\ell} \frac{\partial f_\ell}{\partial x_j} \\ &= -u_j \frac{\partial \omega_i}{\partial x_j} + \omega_j \frac{\partial u_i}{\partial x_j} + \nu \nabla^2 \omega_i + \epsilon_{ij\ell} \frac{\partial f_\ell}{\partial x_j}. \end{aligned} \tag{2.7}$$

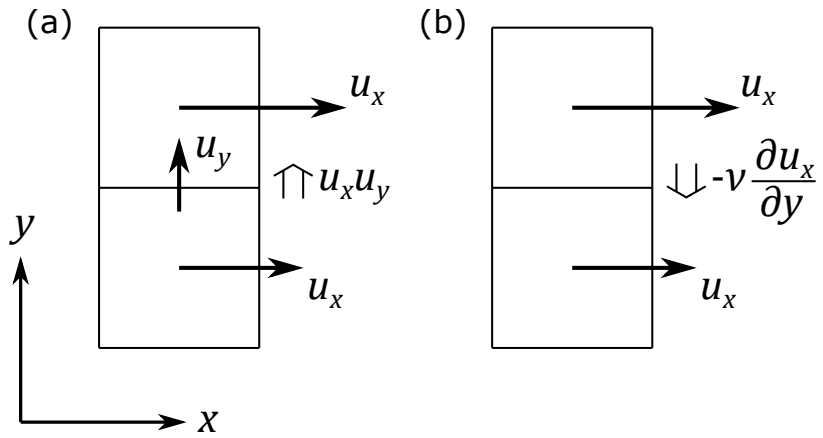

Figure 2.1: Schematic diagram for the flux of u_x due to (a) u_y through the nonlinear term and (b) viscous stress.

2.1.2 Inviscid invariant in fluid dynamics

Multiplying Eq. (2.3) by u_i, the equation for the kinetic energy $u_i u_i/2$ is derived:

$$\frac{\partial}{\partial t}\left(\frac{1}{2}u_i u_i\right) = -\nu\frac{\partial u_i}{\partial x_j}\frac{\partial u_i}{\partial x_j} - \frac{\partial}{\partial x_j}\left[u_j\frac{1}{2}u_i u_i + u_j p - \nu\frac{\partial}{\partial x_j}\left(\frac{1}{2}u_i u_i\right)\right] + u_i f_i. \tag{2.8}$$

The first term on the right-hand side of Eq. (2.8) represents the energy dissipation due to the viscosity. Since all terms on the right-hand side of Eq. (2.8) except for the viscous dissipation and forcing terms are written in the divergence form, the kinetic energy integrated in a whole volume is conserved in the case that $\nu = 0$, $\boldsymbol{f} = 0$, and the surface flux is zero. Such a conservative variable as the volume integrated kinetic energy is referred to as the inviscid invariant in fluid dynamics.

There is another inviscid invariant in fluid dynamics; namely, helicity defined as $u_i\omega_i$. The governing equation for helicity is derived from Eqs. (2.3) and (2.7) as

$$\frac{\partial}{\partial t}\left(u_i\omega_i\right) = -2\nu\frac{\partial u_i}{\partial x_j}\frac{\partial \omega_i}{\partial x_j} - \frac{\partial}{\partial x_j}\left[u_j u_i\omega_i + \omega_j p - \omega_j\frac{1}{2}u_i u_i - \nu\frac{\partial}{\partial x_j}\left(u_i\omega_i\right)\right] + u_i\epsilon_{ij\ell}\frac{\partial f_\ell}{\partial x_j} + \omega_i f_i. \tag{2.9}$$

Equation (2.9) has similar form to Eq. (2.8), and thus the volume integrated helicity is also the inviscid invariant. Note that helicity is a pseudo-scalar, so that it changes its sign under the reflection transformation. This property is proved as follows. Let us consider the transformation between the $\{\boldsymbol{x}\}$ system and the reflected system $\{\boldsymbol{x}^\dagger\} = \{-\boldsymbol{x}\}$. The velocity is transformed as [see, e.g., Ariki (2014, 2015)]

$$u_i^\dagger(\boldsymbol{x}^\dagger) = \frac{\partial x_i^\dagger}{\partial x_j}u_j(\boldsymbol{x}) = -u_i(\boldsymbol{x}), \tag{2.10}$$

where use is made of $\partial x_i^\dagger/\partial x_j = -\delta_{ij}$. On the other hand, the vorticity is transformed as

$$\omega_i^\dagger(\boldsymbol{x}^\dagger) = \epsilon_{ij\ell}\frac{\partial u_\ell^\dagger}{\partial x_j^\dagger}(\boldsymbol{x}^\dagger) = \epsilon_{ij\ell}\frac{\partial x_m}{\partial x_j^\dagger}\frac{\partial}{\partial x_m}\left[\frac{\partial x_\ell^\dagger}{\partial x_n}u_n(\boldsymbol{x})\right] = \epsilon_{ij\ell}\frac{\partial u_\ell}{\partial x_j}(\boldsymbol{x}) = \omega_i(\boldsymbol{x}). \tag{2.11}$$

Hence, the transformation for helicity reads

$$u_i^\dagger\omega_i^\dagger(\boldsymbol{x}^\dagger) = -u_i\omega_i(\boldsymbol{x}). \tag{2.12}$$

For the reflection or mirror symmetric case, any scalar quantities are unchanged by the reflection transformation:

$$q(\boldsymbol{x}^\dagger) = q(\boldsymbol{x}). \tag{2.13}$$

In such a case, helicity reads

$$\begin{aligned} &u_i^\dagger\omega_i^\dagger(\boldsymbol{x}^\dagger) = u_i\omega_i(\boldsymbol{x}) = -u_i\omega_i(\boldsymbol{x}) \\ &\Leftrightarrow u_i^\dagger\omega_i^\dagger(\boldsymbol{x}^\dagger) = u_i\omega_i(\boldsymbol{x}) = 0. \end{aligned} \tag{2.14}$$

Thus, helicity has a non-zero value only when the reflection symmetry is broken. The volume integrated helicity is considered as the linkage of the vortex filaments [Moffatt (1969)]. This fact means that the volume integrated helicity is also a topological invariant.

2.1.3 Governing equation in rotating system

In a rotating system, the Navier–Stokes equation (2.3) is affected by the system rotation. The derivation of the Navier-Stokes equation in a rotating system is given in Appendix A. It is written as

$$\frac{\partial u_i}{\partial t} = -\frac{\partial}{\partial x_j}(u_i u_j) - \frac{\partial p}{\partial x_i} + \nu \nabla^2 u_i + 2\epsilon_{ij\ell} u_j \Omega^{\mathrm{F}}_\ell + f_i, \tag{2.15}$$

where $\boldsymbol{\Omega}^{\mathrm{F}}$ denotes the angular velocity of the system rotation and p the pressure including the centrifugal force denoted as p^{tot} in Eq. (A14). The fourth term on the right-hand side of Eq. (2.15) denotes the Coriolis force and this term is the only difference from the equation in the non-rotating system given by Eq. (2.3). Note that the Poisson equation for the pressure given by Eq. (2.4) is modified due to the Coriolis force term as

$$\nabla^2 p = -s_{ij} s_{ij} + \frac{1}{2}\omega_i \omega_i + 2\omega_i \Omega^{\mathrm{F}}_i. \tag{2.16}$$

Since the Coriolis force term does not perform work, i.e. $u_i 2\epsilon_{ij\ell} u_j \Omega^{\mathrm{F}}_\ell = 0$, the equation for the kinetic energy given by Eq. (2.8) does not change its form. Using Eq. (2.5), Eq. (2.15) can be rewritten as

$$\frac{\partial u_i}{\partial t} = \epsilon_{ij\ell} u_j \left(\omega_\ell + 2\Omega^{\mathrm{F}}_\ell\right) - \frac{\partial}{\partial x_i}\left(p + \frac{1}{2} u_j u_j\right) + \nu \nabla^2 u_i + f_i. \tag{2.17}$$

Comparing Eqs. (2.6) and (2.17), we can interpret that the vorticity $\boldsymbol{\omega}$ is replaced by $\boldsymbol{\omega} + 2\boldsymbol{\Omega}^{\mathrm{F}}$ in the rotating system. Here, $\boldsymbol{\omega} + 2\boldsymbol{\Omega}^{\mathrm{F}}$ is referred to as the absolute vorticity.

2.2 Statistical viewpoint of fluid turbulence

2.2.1 Reynolds-averaged Navier–Stokes equation

The nonlinearity in the Navier–Stokes equation (2.2) causes the growth of small disturbance, leading to the turbulent motion of fluid. Although the instantaneous motion of turbulent fluid is stochastic and not reproducible, its statistical properties such as the mean velocity or the turbulent intensity are reproducible. In order to see the statistical properties of turbulent flow, we consider the statistically averaged equations. Here, the instantaneous physical quantities $q[= (\boldsymbol{u}, p, \boldsymbol{\omega}, \boldsymbol{f})]$ are decomposed into the mean or ensemble averaged values $Q[= \langle q \rangle = (\boldsymbol{U}, P, \boldsymbol{\Omega}, \boldsymbol{F})]$ and the fluctuation around the mean values $q'[= (\boldsymbol{u}', p', \boldsymbol{\omega}', \boldsymbol{f}')]$ as $q = Q + q'$. Taking the ensemble average (sometimes referred to as the Reynolds average) of the continuity equation (2.1) and the Navier–Stokes equation in a rotating system given by Eq. (2.15), the equations for the mean velocity are derived:

$$\frac{\partial U_i}{\partial x_i} = 0, \tag{2.18}$$

$$\frac{\partial U_i}{\partial t} = -\frac{\partial}{\partial x_j}\left(U_i U_j + R_{ij}\right) - \frac{\partial P}{\partial x_i} + \nu \nabla^2 U_i + 2\epsilon_{ij\ell} U_j \Omega^{\mathrm{F}}_\ell + F_i, \tag{2.19}$$

where $R_{ij}(=\langle u_i' u_j' \rangle)$ denotes the Reynolds stress. Equation (2.19) is referred to as the Reynolds-averaged Navier–Stokes (RANS) equation. Since the form of the RANS equation (2.19) is the same as the Navier–Stokes equation (2.15) except for R_{ij}, the Reynolds stress represents the effect of turbulent motion on the mean velocity. According to Reynolds (1883), the turbulence is observed at high-Reynolds-number flows where the Reynolds number is defined as $\mathrm{Re} = UL/\nu$ with the reference velocity U and length scale L. In such high-Reynolds-number flows, the viscous term is negligible in comparison with the nonlinear terms except for the vicinity of solid wall region. This suggests that the Reynolds stress is more significant in high-Reynolds-number turbulent flow.

2.2.2 Transport equation for the Reynolds stress and closure problem

Since the RANS equation (2.19) is not closed owing to the Reynolds stress, some closed relation for the Reynolds stress is required. Subtracting Eq. (2.19) from Eq. (2.15), the equation for the velocity fluctuation $\boldsymbol{u}'$ is derived:

$$\frac{\partial u_i'}{\partial t} + \frac{\partial}{\partial x_j}\left(U_j u_i'\right) = -u_j' \frac{\partial U_i}{\partial x_j} - \frac{\partial}{\partial x_j}\left(u_i' u_j' - R_{ij}\right) - \frac{\partial p'}{\partial x_i} + \nu \nabla^2 u_i' + 2\epsilon_{ij\ell} u_j' \Omega_\ell^{\mathrm{F}} + f_i'. \tag{2.20}$$

Note that the velocity fluctuation also satisfies the incompressibility condition, $\partial u_i'/\partial x_i = 0$. Hence, the transport equation for the Reynolds stress reads

$$\frac{DR_{ij}}{Dt} = P_{ij} - \varepsilon_{ij} + \Phi_{ij} + \Pi_{ij} + T_{ij} + D_{ij} + Co_{ij} + F_{ij}, \tag{2.21}$$

where $D/Dt(= \partial/\partial t + U_\ell \partial/\partial x_\ell)$ denotes the mean Lagrangian derivative which represents the time derivative along the mean streamline. On the right-hand side of Eq. (2.21), P_{ij} denotes the production rate, ε_{ij} the destruction rate, Φ_{ij} the pressure–strain correlation, Π_{ij} the pressure diffusion, T_{ij} the turbulent diffusion, D_{ij} the viscous diffusion, Co_{ij} the Coriolis effect, and F_{ij} the external work. They are defined as follows:

$$P_{ij} = -R_{i\ell}\frac{\partial U_j}{\partial x_\ell} - R_{j\ell}\frac{\partial U_i}{\partial x_\ell}, \tag{2.22a}$$

$$\varepsilon_{ij} = 2\nu \left\langle \frac{\partial u_i'}{\partial x_\ell}\frac{\partial u_j'}{\partial x_\ell} \right\rangle, \tag{2.22b}$$

$$\Phi_{ij} = 2\left\langle p' s_{ij}' \right\rangle, \tag{2.22c}$$

$$\Pi_{ij} = -\frac{\partial}{\partial x_j}\left\langle u_i' p' \right\rangle - \frac{\partial}{\partial x_i}\left\langle u_j' p' \right\rangle, \tag{2.22d}$$

$$T_{ij} = -\frac{\partial}{\partial x_\ell}\left\langle u_i' u_j' u_\ell' \right\rangle, \tag{2.22e}$$

$$D_{ij} = \nu \nabla^2 R_{ij}, \tag{2.22f}$$

$$Co_{ij} = 2\left(\epsilon_{i\ell m} R_{j\ell} + \epsilon_{j\ell m} R_{i\ell}\right)\Omega_m^{\mathrm{F}}, \tag{2.22g}$$

$$F_{ij} = \left\langle u_i' f_j' + u_j' f_i' \right\rangle. \tag{2.22h}$$

It is clearly seen that Eq. (2.21) is also not closed owing to additional unknown variables such as $\langle u_i' p' \rangle$ or $\langle u_i' u_j' u_\ell' \rangle$. In the same manner, the equation for $\langle u_i' u_j' u_\ell' \rangle$ involves the fourth-order moment of $\boldsymbol{u}'$. Hence, the statistically averaged equations for fluid are never closed without any assumptions or truncation. This is referred to as the closure problem. In order to close the RANS equation (2.19), some modeling for R_{ij} or its transport equation is required. We discuss the role of each term on the right-hand side of Eq. (2.21) in the next subsection in connection to the turbulent energy transport.

2.2.3 Transport equation for the turbulent energy

Taking the trace of Eq. (2.21) and dividing it by 2, the transport equation for the kinetic energy for the turbulent part $K(= \langle u_i' u_i' \rangle / 2)$ (hereafter simply referred to as the turbulent energy) is derived:

$$\frac{DK}{Dt} = P^K - \varepsilon + \Pi^K + T^K + D^K + F^K, \tag{2.23}$$

where P^K denotes the production rate, ε the dissipation rate, Π^K the pressure diffusion, T^K the turbulent diffusion, D^K the viscous diffusion, and F^K the external work. They are defined as follows:

$$P^K = -R_{ij} S_{ij}, \tag{2.24a}$$

$$\varepsilon = \nu \left\langle \frac{\partial u_i'}{\partial x_j} \frac{\partial u_i'}{\partial x_j} \right\rangle, \tag{2.24b}$$

$$\Pi^K = -\frac{\partial}{\partial x_j} \left\langle u_j' p' \right\rangle, \tag{2.24c}$$

$$T^K = -\frac{\partial}{\partial x_j} \left\langle u_j' \frac{1}{2} u_i' u_i' \right\rangle, \tag{2.24d}$$

$$D^K = \nu \nabla^2 K, \tag{2.24e}$$

$$F^K = \left\langle u_i' f_i' \right\rangle. \tag{2.24f}$$

Note that Φ_{ii} and Co_{ii} vanish since they are traceless tensor. In contrast to the instantaneous kinetic energy equation (2.8), there is another non-divergence term in the turbulent energy equation (2.23); namely, the production term P^K appears. Since the mean kinetic energy equation is written as

$$\frac{D}{Dt}\left(\frac{1}{2} U_i U_i\right) = -P^K - \nu \frac{\partial U_i}{\partial x_j} \frac{\partial U_i}{\partial x_j} - \frac{\partial}{\partial x_j} \left(U_j P + U_i R_{ij}\right) + \nu \nabla^2 \left(\frac{1}{2} U_i U_i\right) + U_i F_i, \tag{2.25}$$

and $-P^K$ appears on the right-hand side, P^K denotes the exchange of kinetic energy between the mean velocity and the velocity fluctuation. For simple turbulent shear flows, P^K is often positive, meaning that the energy is transferred from the mean velocity to the velocity fluctuation. This is the reason why P^K is referred to as the production term. On the other hand, ε is always positive, so that ε always decreases the turbulent energy. Π^K, T^K, and D^K represent the spatial transport or diffusion of the turbulent energy since they are written as the divergence form; namely, they must be zero when they are integrated in volume and the surface flux is zero. Consequently, Eq. (2.23) represents the transport of the turbulent

energy K involving its source, sink, and spatial transport. Here, we show the budget for the turbulent energy transport equation given by Eq. (2.23) in the turbulent flow in a straight pipe. Schematic flow configuration for the turbulent flow in a straight pipe is shown in Fig. 2.2(a). Figure 2.2(b) shows the spatial distribution of each term on the right-hand side of Eq. (2.23). Note that $F^K = 0$ in this flow. As seen in Fig. 2.2(b), the production and dissipation terms are dominant. Especially in the range at $0.5 < r/R < 0.85$, the production and dissipation terms are almost balanced each other, $P^K \simeq \varepsilon$. This balance suggests that the turbulent field is in the local equilibrium condition.

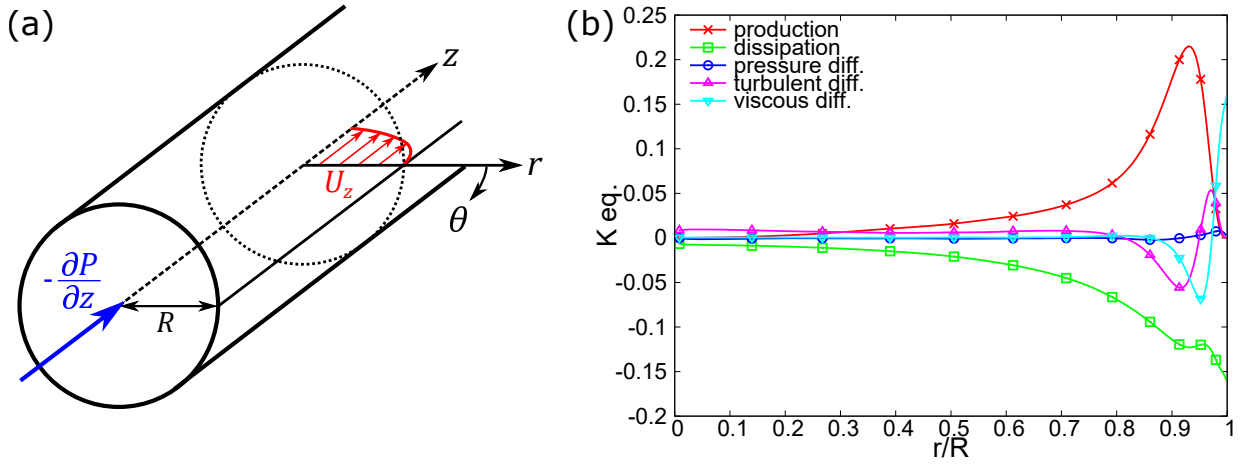

Figure 2.2: (a) Schematic flow configuration for the turbulent flow in a straight pipe and (b) the budget for the turbulent energy transport equation given by Eq. (2.23). Here, we use the turbulence data of the simulation performed by Fukagata & Kasagi (2002).

Similarly, Eq. (2.21) represents the transport of the Reynolds stress R_{ij} involving its source, sink, and spatial transport. P_{ij} represents the production of the Reynolds stress R_{ij}, while ε_{ij} represents the destruction of it due to the viscosity. Π_{ij}, T_{ij}, and D_{ij} represent the spatial transport or diffusion of the Reynolds stress. Φ_{ii} and Co_{ii} vanish as mentioned previously, so that Φ_{ij} and Co_{ij} do not affect the turbulent energy transport. However, they play a role redistributing the intensity among each component of the Reynolds stress.

2.2.4 Transport equation for the turbulent helicity

We can also derive the equation for the helicity for the turbulent part $H = \langle u_i' \omega_i' \rangle$ (hereafter referred to as the turbulent helicity). It is written as follows:

$$\frac{DH}{Dt} = P^H - \varepsilon^H + \Pi^H + T^H + D^H + Co^H + F^H, \tag{2.26}$$

where P^H denotes the production rate, ε^H the dissipation rate, Π^H the pressure diffusion, T^H the turbulent diffusion, D^H the viscous diffusion, Co^H the Coriolis effect, and F^H the external work. They are

defined as follows:

$$P^H = -R_{ij}\frac{\partial \Omega_i}{\partial x_j} + \Omega_i \frac{\partial R_{ij}}{\partial x_j}, \tag{2.27a}$$

$$\varepsilon^H = 2\nu \left\langle \frac{\partial u_i'}{\partial x_j}\frac{\partial \omega_i'}{\partial x_j} \right\rangle, \tag{2.27b}$$

$$\Pi^H = -\frac{\partial}{\partial x_j}\left\langle \omega_j' p' \right\rangle, \tag{2.27c}$$

$$T^H = -\frac{\partial}{\partial x_j}\left(\left\langle u_j' u_i' \omega_i' \right\rangle - \left\langle \omega_j \frac{1}{2} u_i' u_i' \right\rangle \right), \tag{2.27d}$$

$$D^H = \nu \nabla^2 H, \tag{2.27e}$$

$$Co^H = 2\Omega_i^{\mathrm{F}} \frac{\partial R_{ij}}{\partial x_j}, \tag{2.27f}$$

$$F^H = \left\langle \omega_i' f_i' \right\rangle + \left\langle u_i' \epsilon_{ij\ell} \frac{\partial f_\ell'}{\partial x_j} \right\rangle, \tag{2.27g}$$

The mathematical structure of the transport equation for the turbulent helicity given by Eq. (2.26) is similar to that of the turbulent energy given by Eq. (2.23) except for Co^H. In fact, the production term in the turbulent helicity transport P^H also appears in the equation for the mean helicity $U_i\Omega_i$ as follows:

$$\begin{aligned}\frac{D}{Dt}\left(U_i\Omega_i\right) = &-P^H - \nu \frac{\partial U_i}{\partial x_j}\frac{\partial \Omega_i}{\partial x_j} - \frac{\partial}{\partial x_j}\left(\Omega_j P - \Omega_j \frac{1}{2} U_i U_i - U_j U_i 2\Omega_i^{\mathrm{F}} + \Omega_j R_{ij} + U_i \epsilon_{ij\ell} \frac{\partial R_{\ell m}}{\partial x_m} \right) \\ &+ \nu \nabla^2 \left(U_i \Omega_i\right) + \Omega_i F_i + U_i \epsilon_{ij\ell} \frac{\partial F_\ell}{\partial x_j}.\end{aligned} \tag{2.28}$$

Hence, P^H denotes exchange of helicity between the mean field and the fluctuation field. This suggests that the turbulent helicity is expected to have non-zero value in the region where the mean helicity defined by $U_i\Omega_i$ is non-zero. For example, the positive turbulent helicity is possibly dominant in the region where the mean helicity is positive, while the turbulent helicity is zero far from that region, as schematically shown in Fig. 2.3. Note that the turbulent helicity is the Galilei invariant variable, while the mean helicity is not Galilei invariant; namely, the mean helicity changes its sign under the Galilei transformation. Owing to this fact, the sign of the mean helicity $U_i\Omega_i$ and the turbulent helicity H are not necessarily the same. However, it is expected that the turbulent helicity has non-zero value in the region in which the mean helicity is non-zero. In such a case, the turbulent helicity also characterizes the turbulent flow as the turbulent energy does. Since helicity is the inviscid invariant as is the case of the kinetic energy in fluid dynamics as mentioned in Sec. 2.1.2, the turbulent helicity is expected to be useful value characterizing the helical turbulent flows. However, the mechanism that the turbulent helicity affects the mean velocity or the Reynolds stress is not clear.

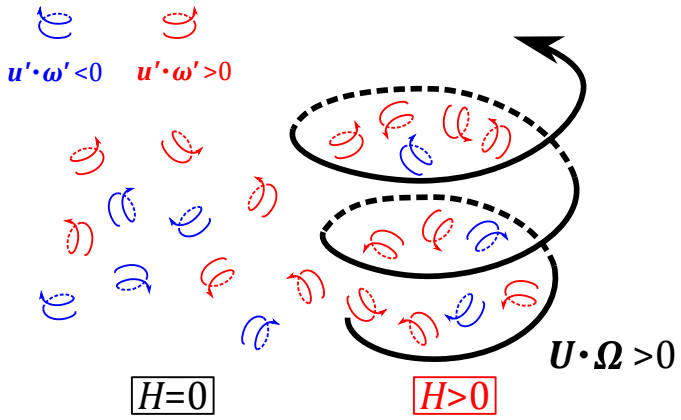

Figure 2.3: Schematic diagram for helical turbulent flow.

2.2.5 Statistical homogeneity

Let us consider the multiple point correlation of physical quantities q_n's:

$$\langle q_0(\boldsymbol{x})q_1(\boldsymbol{x}+\boldsymbol{r}_1)q_2(\boldsymbol{x}+\boldsymbol{r}_2)\cdots q_N(\boldsymbol{x}+\boldsymbol{r}_N)\rangle = Q_{0,1,2,\cdots,N}(\boldsymbol{x},\boldsymbol{r}_1,\boldsymbol{r}_2,\cdots,\boldsymbol{r}_N). \tag{2.29}$$

$Q_{0,1,2,\cdots,N}$ generally depends on both of the relative distance $\boldsymbol{r}_n$'s and its reference position $\boldsymbol{x}$. When $Q_{0,1,2,\cdots,N}$ only depends on $\boldsymbol{r}_n$'s and does not depend on $\boldsymbol{x}$, this turbulence field is referred to as homogeneous. Hence, in the homogeneous turbulence, we have

$$\langle q_0(\boldsymbol{x})q_1(\boldsymbol{x}+\boldsymbol{r}_1)q_2(\boldsymbol{x}+\boldsymbol{r}_2)\cdots q_N(\boldsymbol{x}+\boldsymbol{r}_N)\rangle = Q_{0,1,2,\cdots,N}(\boldsymbol{r}_1,\boldsymbol{r}_2,\cdots,\boldsymbol{r}_N). \tag{2.30}$$

Especially, one-point correlation does not depend on space, so that the spatial derivative of any one-point correlations should be zero:

$$\frac{\partial}{\partial x_i}\langle q_0(\boldsymbol{x})q_1(\boldsymbol{x})q_2(\boldsymbol{x})\cdots q_N(\boldsymbol{x})\rangle = \frac{\partial}{\partial x_i}Q_{0,1,2,\cdots,N}(\boldsymbol{0}) = 0. \tag{2.31}$$

Hence, the diffusion terms such as Π_{ij}, T_{ij}, and etc. in Eqs. (2.21), (2.23), and (2.26) vanish for homogeneous turbulence. We can use the spatial average in the homogeneous directions as the statistical average instead of the ensemble average. Similarly, we can use the time average as the statistical average when the statistical steadiness is guaranteed.

2.2.6 Fourier transformation

In the previous studies, statistical turbulence theories have been developed mainly in the Fourier space where the region far from the solid wall is concerned. We define the Fourier transformation as follows:

$$q(\boldsymbol{x}) = \int \mathrm{d}\boldsymbol{k}\ \tilde{q}(\boldsymbol{k})\mathrm{e}^{i\boldsymbol{k}\cdot\boldsymbol{x}}, \tag{2.32}$$

$$\tilde{q}(\boldsymbol{k}) = \frac{1}{(2\pi)^3}\int \mathrm{d}\boldsymbol{x}\ q(\boldsymbol{x})\mathrm{e}^{-i\boldsymbol{k}\cdot\boldsymbol{x}}. \tag{2.33}$$

Here and hereafter, the triple integral is simply denoted as $\int \mathrm{d}\boldsymbol{k} (= \int_{-\infty}^{\infty} \mathrm{d}k_x \int_{-\infty}^{\infty} \mathrm{d}k_y \int_{-\infty}^{\infty} \mathrm{d}k_z)$. The continuity equation (2.1) and the Navier–Stokes equation (2.15) are written in the Fourier space as

$$k_i \tilde{u}_i(\boldsymbol{k}) = 0, \tag{2.34}$$

$$\frac{\partial \tilde{u}_i}{\partial t}(\boldsymbol{k}) = -ik_j \int \mathrm{d}\boldsymbol{p} \int \mathrm{d}\boldsymbol{q}\ \delta(\boldsymbol{k}-\boldsymbol{p}-\boldsymbol{q}) \tilde{u}_i(\boldsymbol{p}) \tilde{u}_j(\boldsymbol{q}) - ik_i \tilde{p}(\boldsymbol{k}) - \nu k^2 \tilde{u}_i(\boldsymbol{k}) + 2\epsilon_{ij\ell} \tilde{u}_j(\boldsymbol{k}) \Omega_\ell^{\mathrm{F}} + \tilde{f}_i(\boldsymbol{k}), \tag{2.35}$$

where $\delta(\boldsymbol{k})$ denotes the Dirac's delta function and the forcing term is assumed to be solenoidal, $\boldsymbol{k} \cdot \tilde{\boldsymbol{f}} = 0$. The pressure is calculated as

$$\tilde{p}(\boldsymbol{k}) = -\frac{k_i k_j}{k^2} \int \mathrm{d}\boldsymbol{p} \int \mathrm{d}\boldsymbol{q}\ \delta(\boldsymbol{k}-\boldsymbol{p}-\boldsymbol{q}) \tilde{u}_i(\boldsymbol{p}) \tilde{u}_j(\boldsymbol{q}) - 2i\epsilon_{ij\ell} \frac{k_i}{k^2} \tilde{u}_j(\boldsymbol{k}) \Omega_\ell^{\mathrm{F}}. \tag{2.36}$$

Hence, the Navier–Stokes equation in the Fourier space given by Eq. (2.35) can be rewritten as

$$\frac{\partial \tilde{u}_i}{\partial t}(\boldsymbol{k}) = -iM_{ij\ell}(\boldsymbol{k}) \int \mathrm{d}\boldsymbol{p} \int \mathrm{d}\boldsymbol{q}\ \delta(\boldsymbol{k}-\boldsymbol{p}-\boldsymbol{q}) \tilde{u}_j(\boldsymbol{p}) \tilde{u}_\ell(\boldsymbol{q}) - \nu k^2 \tilde{u}_i(\boldsymbol{k}) + 2M_{im}(\boldsymbol{k}) \epsilon_{mj\ell} \tilde{u}_j(\boldsymbol{k}) \Omega_\ell^{\mathrm{F}} + \tilde{f}_i(\boldsymbol{k}), \tag{2.37}$$

where

$$M_{ij}(\boldsymbol{k}) = \delta_{ij} - \frac{k_i k_j}{k^2}, \quad M_{ij\ell}(\boldsymbol{k}) = \frac{1}{2} \left[k_j M_{i\ell}(\boldsymbol{k}) + k_\ell M_{ij}(\boldsymbol{k}) \right]. \tag{2.38}$$

Alternatively, the Navier–Stokes equation based on Eq. (2.17) can be written in the Fourier space as

$$\frac{\partial \tilde{u}_i}{\partial t}(\boldsymbol{k}) = M_{im}(\boldsymbol{k}) \epsilon_{mj\ell} \widetilde{u_j \omega_\ell}(\boldsymbol{k}) - \nu k^2 \tilde{u}_i(\boldsymbol{k}) + 2M_{im}(\boldsymbol{k}) \epsilon_{mj\ell} \tilde{u}_j(\boldsymbol{k}) \Omega_\ell^{\mathrm{F}} + \tilde{f}_i(\boldsymbol{k}). \tag{2.39}$$

2.2.7 Velocity correlation in homogeneous isotropic turbulence

In homogeneous turbulence, the correlation of the velocity fluctuations in the Fourier space is calculated as follows:

$$\begin{aligned}
\left\langle \tilde{u}_i'(\boldsymbol{k}) \tilde{u}_j'(\boldsymbol{k}') \right\rangle &= \frac{1}{(2\pi)^6} \int \mathrm{d}\boldsymbol{x} \int \mathrm{d}\boldsymbol{x}' \left\langle u_i'(\boldsymbol{x}) u_j'(\boldsymbol{x}') \right\rangle \mathrm{e}^{-i(\boldsymbol{x}\cdot\boldsymbol{k} + \boldsymbol{x}'\cdot\boldsymbol{k}')} \\
&= \frac{1}{(2\pi)^6} \int \mathrm{d}\boldsymbol{r} \int \mathrm{d}\boldsymbol{x}' \left\langle u_i'(\boldsymbol{x}'+\boldsymbol{r}) u_j'(\boldsymbol{x}') \right\rangle \mathrm{e}^{-i\boldsymbol{x}'\cdot(\boldsymbol{k}+\boldsymbol{k}') - i\boldsymbol{r}\cdot\boldsymbol{k}} \\
&= \frac{1}{(2\pi)^3} \int \mathrm{d}\boldsymbol{r}\ Q_{ij}(\boldsymbol{r}) \mathrm{e}^{-i\boldsymbol{r}\cdot\boldsymbol{k}} \delta(\boldsymbol{k}+\boldsymbol{k}') \\
&= \tilde{Q}_{ij}(\boldsymbol{k}) \delta(\boldsymbol{k}+\boldsymbol{k}'),
\end{aligned} \tag{2.40}$$

where $Q_{ij}(\boldsymbol{r}) = \left\langle u_i'(\boldsymbol{x}+\boldsymbol{r}) u_j'(\boldsymbol{x}) \right\rangle$ and $\tilde{Q}_{ij}(\boldsymbol{k})$ is its Fourier coefficient. For homogeneous isotropic but non-mirror symmetric case, the second-order correlation tensor for the velocity fluctuations in the Fourier space $\tilde{Q}_{ij}(\boldsymbol{k})$ is uniquely written as follows [Yoshizawa (1998); Kida & Yanase (1999)]:

$$\tilde{Q}_{ij}(\boldsymbol{k}) = M_{ij}(\boldsymbol{k}) \frac{E(k)}{4\pi k^2} - \frac{i}{2} \epsilon_{ij\ell} \frac{k_\ell}{k^2} \frac{E^H(k)}{4\pi k^2}, \tag{2.41}$$

where $E(k)$ and $E^H(k)$ are the energy and helicity spectra. They are respectively defined as

$$K = \int_0^\infty \mathrm{d}k\ E(k), \tag{2.42}$$

$$H = \int_0^\infty \mathrm{d}k\ E^H(k). \tag{2.43}$$

2.3 Turbulence modeling

In order to close the RANS equation (2.19), some modeling for the Reynolds stress or its transport equation is required. Such a modeling is referred to as the turbulence modeling. Especially, the turbulence modeling for the RANS equation is referred to as the RANS modeling. The RANS modeling is roughly classified to two types, as mentioned in Sec. 1.4. One is the algebraic modeling which expresses the Reynolds stress in terms of K, ε, S_{ij}, and etc. as $R_{ij} = R_{ij}\{K, \varepsilon, S_{ij}, \cdots\}$. The other is the Reynolds stress equation modeling which expresses the unclosed terms in the Reynolds stress transport equation given by Eq. (2.23), such as ε_{ij} or Φ_{ij}, in terms of R_{ij}, ε, S_{ij}, and etc. as $\varepsilon_{ij} = \varepsilon_{ij}\{R_{ij}, \varepsilon, S_{ij}, \cdots\}$, $\Phi_{ij} = \Phi_{ij}\{R_{ij}, \varepsilon, S_{ij}, \cdots\}$, and etc. In this section, a brief review of the algebraic modeling and its relation to the Reynolds stress transport are given.

2.3.1 Eddy-viscosity model

The most primitive model for the algebraic model for the Reynolds stress is the eddy-viscosity model:

$$R_{ij} = \frac{2}{3}K\delta_{ij} - 2\nu^{\mathrm{T}}S_{ij}, \tag{2.44}$$

where ν^{T} denotes the eddy viscosity and $S_{ij}[= (\partial U_i/\partial x_j + \partial U_j/\partial x_i)/2]$ denotes the mean strain rate. The eddy viscosity is often modeled as [Yoshizawa (1998); Pope (2000)]

$$\nu^{\mathrm{T}} = C_\nu \frac{K^2}{\varepsilon}. \tag{2.45}$$

In the typical RANS model, K and ε are obtained by solving their transport equations. Such a model is referred to as the K–ε model. Substituting Eqs. (2.44) and (2.45) into the RANS equation (2.19), we have

$$\frac{\partial U_i}{\partial t} = -\frac{\partial}{\partial x_j}\left(U_i U_j\right) - \frac{\partial P}{\partial x_i} + \frac{\partial}{\partial x_j}\left[2\left(\nu + \nu^{\mathrm{T}}\right)S_{ij}\right] + 2\epsilon_{ij\ell}U_j\Omega^{\mathrm{F}}_\ell + F_i, \tag{2.46}$$

where the viscous term is rewritten in the same form as Eq. (2.2). For turbulent flows, it can be evaluated as $\nu^{\mathrm{T}} \gg \nu$ except for the vicinity of the solid wall. Therefore, Eq. (2.46) suggests that the viscous friction is enhanced due to the turbulent motion through the effective viscosity $\nu + \nu^{\mathrm{T}}$. Moreover, ν^{T} varies in space and time. In the case of the turbulent flow in a straight pipe which is schematically shown in Fig. 2.2(a), ν^{T} is large at the center axis region, while it is small in the vicinity of the solid wall. As a

result, the mean velocity profile is much flattened at the center axis region, while it is not affected by turbulence in the vicinity of the solid wall. Owing to this spatial dependence of ν^{T}, the eddy-viscosity model can account for not only the reduction of the flow rate due to the enhancement of the friction force but also the flat profile of the streamwise mean velocity in the turbulent flow in a straight pipe as shown in Fig. 2.4.

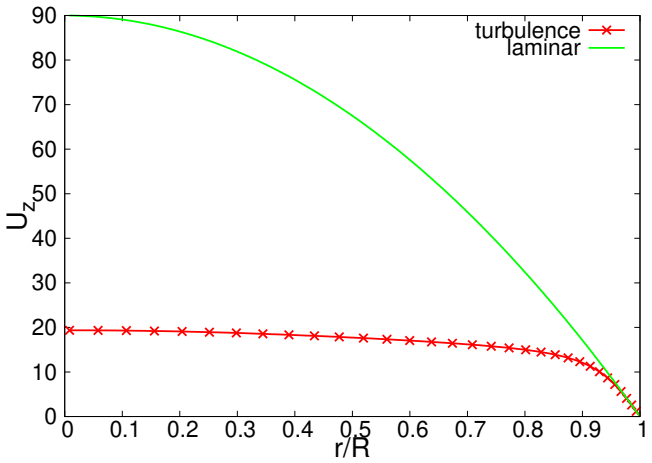

Figure 2.4: Comparison of the mean velocity profile between the laminar and turbulence for the flow in a straight pipe in the same pressure gradient condition. Here, we use the turbulence data of the simulation performed by Fukagata & Kasagi (2002).

2.3.2 Modeling the transport equation for K and ε

In the transport equation for K given by Eq. (2.23), $\langle u_j' p' \rangle$ in Π^K [Eq. (2.24c)] and $\langle u_j' u_i' u_i'/2 \rangle$ in T^K [Eq. (2.24d)] are required to be modeled. Here, modeling the external work is not concerned. The conventional modeling for such flux terms in the turbulent energy transport is the gradient-diffusion approximation [Pope (2000)]; that is, the sum of $\langle u_j' p' \rangle$ and $\langle u_j' u_i' u_i'/2 \rangle$ is modeled as

$$\left\langle u_j' p' \right\rangle + \left\langle u_j' \frac{1}{2} u_i' u_i' \right\rangle = -\frac{\nu^{\mathrm{T}}}{\sigma_K} \frac{\partial K}{\partial x_j}, \tag{2.47}$$

where σ_K is a model constant. Hence, the transport equation for the turbulent energy reads

$$\frac{DK}{Dt} = P^K - \varepsilon + \frac{\partial}{\partial x_j} \left[\left(\nu + \frac{\nu^{\mathrm{T}}}{\sigma_K} \right) \frac{\partial K}{\partial x_j} \right] + F^K. \tag{2.48}$$

Namely, the gradient-diffusion approximation suggests the enhancement of the energy flux due to turbulence. This effect is similar to that of the momentum transport expressed by the eddy-viscosity model given by Eq. (2.44).

On the other hand, the model for the transport equation for ε is not straightforwardly derived from the Navier–Stokes equation. The standard model of the transport equation for ε is empirically written as [Yoshizawa (1998); Pope (2000)]

$$\frac{D\varepsilon}{Dt} = C_{\varepsilon 1}\frac{\varepsilon}{K}P^K - C_{\varepsilon 2}\frac{\varepsilon^2}{K} + \frac{\partial}{\partial x_j}\left[\left(\nu + \frac{\nu^{\mathrm{T}}}{\sigma_\varepsilon}\right)\frac{\partial \varepsilon}{\partial x_j}\right], \tag{2.49}$$

where $C_{\varepsilon 1}$, $C_{\varepsilon 2}$, and σ_ε are model constants and the contributions from the forcing and the Coriolis terms are neglected. Since the velocity gradient is involved in the definition of the dissipation rate ε in contrast to the turbulent energy K, ε is related to small scale motion of turbulence, while K is related to large scale motion. Nevertheless, Eq. (2.49) is mathematically similar to the model for the transport equation for K given by Eq. (2.48). In this background, the local similarity hypothesis proposed by Kolmogorov (1941) is considered; namely, ε can be interpreted as the energy cascade rate from large to small scale motions in addition to the dissipation rate at the smallest scale of turbulence. Thus, the transport equation for ε given by Eq. (2.49) is interpreted as the energy cascade rate related to the large scale which balances with the dissipation rate related to the small scale [Yoshizawa (1998)]. Here, the K–ε model composed of Eqs. (2.44), (2.45), (2.48), (2.49) is referred to as the standard K–ε model.

The standard K–ε model describes the primitive property of turbulence owing to the eddy viscosity. However, it is known that the eddy-viscosity model given by Eq. (2.44) does not include the effect of anisotropy of turbulence or the rotation [Speziale (1987); Yoshizawa (1998); Speziale *et al.* (2000)]. In order to overcome these shortfalls, other models for the Reynolds stress shown in the subsequent sections have been proposed and their physical property and validity have been discussed.

2.3.3 Reynolds stress equation modeling

Another approach of closing the RANS equation (2.19) is to model the transport equation for the Reynolds stress given by Eq. (2.21). In Eq. (2.21), there are four unclosed terms except for the forcing term, the destruction rate ε_{ij} [Eq. (2.22b)], the pressure–strain correlation Φ_{ij} [Eq. (2.22c)], the pressure diffusion Π_{ij} [Eq. (2.22d)], and the turbulent diffusion T_{ij} [Eq. (2.22e)]. The basic modeling for these terms were given by Launder *et al.* (1975) as follows. The destruction rate is assumed to be isotropic and modeled as

$$\varepsilon_{ij} = \frac{2}{3}\varepsilon\delta_{ij}. \tag{2.50}$$

This isotropic assumption is justified from the viewpoint of the local isotropy hypothesis proposed by Kolmogorov (1941). Here, ε is obtained by solving its transport equation model such as Eq. (2.49). The pressure–strain correlation is modeled as

$$\Phi_{ij} = -C_{S1}\frac{\varepsilon}{K}B_{ij} + C_{R1}KS_{ij} + C_{R2}\left[S_{i\ell}B_{\ell j} + S_{j\ell}B_{\ell i}\right]_{\mathrm{D}} + C_{R3}\left(W_{i\ell}B_{\ell j} + W_{j\ell}B_{\ell i}\right), \tag{2.51}$$

where $[A_{ij}]_{\mathrm{D}} = A_{ij} - A_{\ell\ell}\delta_{ij}/3$, $B_{ij}(= R_{ij} - 2K\delta_{ij}/3)$ denotes the deviatoric part of the Reynolds stress, and $W_{ij}[= (\partial U_i/\partial x_j - \partial U_j/\partial x_i)/2 - \epsilon_{ij\ell}\Omega^{\mathrm{F}}_\ell]$ denotes the absolute vorticity tensor. Note that the model given by Eq. (2.51) is extended to the rotating system by using the absolute vorticity tensor from the viewpoint

of the covariance principle [see, e.g., Speziale *et al.* (1991); Ariki (2014, 2015)]. The first term on the right-hand side of Eq. (2.51) represents the relaxation of anisotropy with the time scale K/ε and is referred to as the return to isotropy term. The second to fourth terms on the right-hand side of Eq. (2.51) reduce the effect of the production rate P_{ij} and the Coriolis effect C_{ij}, so that these terms are referred to as the isotropization of production term. For diffusion terms, the pressure diffusion is conventionally neglected by assuming that it has small contribution compared with the turbulent diffusion. This assumption is reasonable for the turbulent energy transport in the turbulent flow in a straight pipe as shown in Fig. 2.2(b). The triple correlation of the velocity fluctuation $\langle u_i' u_j' u_\ell' \rangle$ in Eq. (2.22e) is modeled as

$$\left\langle u_i' u_j' u_\ell' \right\rangle = -C_D \frac{K}{\varepsilon} \left(R_{im} \frac{\partial R_{j\ell}}{\partial x_m} + R_{jm} \frac{\partial R_{i\ell}}{\partial x_m} + R_{\ell m} \frac{\partial R_{ij}}{\partial x_m} \right). \tag{2.52}$$

Hence, Eq. (2.21) is modeled as

$$\begin{aligned} \frac{DR_{ij}}{Dt} = & -\frac{2}{3}\varepsilon\delta_{ij} - C_{S1}\frac{\varepsilon}{K}B_{ij} \\ & + \left(\frac{4}{3} - C_{R1}\right) K S_{ij} + (1 - C_{R2}) \left[S_{i\ell} B_{\ell j} + S_{j\ell} B_{\ell i} \right]_{\mathrm{D}} - \frac{2}{3} S_{\ell m} B_{\ell m} \delta_{ij} \\ & + (1 - C_{R3}) \left(W_{i\ell} B_{\ell j} + W_{j\ell} B_{\ell i} \right) + \left(\epsilon_{im\ell} B_{jm} + \epsilon_{jm\ell} B_{im} \right) \Omega_\ell^{\mathrm{F}} \\ & + \frac{\partial}{\partial x_\ell} \left[C_D \frac{K}{\varepsilon} \left(R_{im} \frac{\partial R_{j\ell}}{\partial x_m} + R_{jm} \frac{\partial R_{i\ell}}{\partial x_m} + R_{\ell m} \frac{\partial R_{ij}}{\partial x_m} \right) \right] + \nu \nabla^2 R_{ij} + F_{ij}. \end{aligned} \tag{2.53}$$

In Eq. (2.53), the first line denotes the destruction, the second line denotes the production due to the mean strain, the third line denotes the production due to the mean vorticity or rotation, and the last line denotes the diffusion and the external forcing of the Reynolds stress, respectively. Since the Reynolds stress equation model treats the production and destruction of the Reynolds stress explicitly, it gives more accurate prediction than the eddy-viscosity model for several turbulent flows. However, the Reynolds stress equation model should calculate six individual transport equations for each component of the Reynolds stress, so that numerical cost is large. Moreover, it sometimes gives the unphysical result such as the negative solution of R_{xx} which must be positive by definition [see, e.g., Schumann (1977); Hanjalić & Launder (2011)]. Owing to such an unphysical property, the Reynolds stress equation model is sometimes numerically unstable. From the practical viewpoint, the nonlinear eddy-viscosity model for the Reynolds stress shown in the next subsection is more convenient.

2.3.4 Relationship between the algebraic modeling and the Reynolds stress transport

The eddy-viscosity model given by Eq. (2.44) seems to be empirical model but it is closely related to the transport for the Reynolds stress. Since ν^{T} related part in Eq. (2.44) corresponds to the deviatoric part of the Reynolds stress, we consider the transport equation for B_{ij}. The modeled transport equation for

the Reynolds stress given by Eq. (2.53) is rewritten as follows:

$$\begin{aligned}\frac{DB_{ij}}{Dt} = &-C_{S1}\frac{\varepsilon}{K}B_{ij} - \left(\frac{4}{3} - C_{R1}\right)KS_{ij} - (1-C_{R2})\left[S_{i\ell}B_{\ell j} + S_{j\ell}B_{\ell i}\right]_{\mathrm{D}} \\ &- (1-C_{R3})\left(W_{i\ell}B_{\ell j} + W_{j\ell}B_{\ell i}\right) + \left(\epsilon_{im\ell}B_{jm} + \epsilon_{jm\ell}B_{im}\right)\Omega_{\ell}^{\mathrm{F}} \\ &+ \frac{\partial}{\partial x_\ell}\left[C_D\frac{K}{\varepsilon}\left(R_{im}\frac{\partial R_{j\ell}}{\partial x_m} + R_{jm}\frac{\partial R_{i\ell}}{\partial x_m} + R_{\ell m}\frac{\partial R_{ij}}{\partial x_m}\right)\right]_{\mathrm{D}} + \nu\nabla^2 B_{ij} + \left[F_{ij}\right]_{\mathrm{D}}. \end{aligned} \tag{2.54}$$

In the turbulent flow in a straight pipe, the budget for the turbulent energy transport can be approximately evaluated as $P^K \simeq \varepsilon$, as shown in Fig. 2.2(b). Here, the similar condition is considered in the transport for the deviatoric part of the Reynolds stress; namely, we consider the balance between the source and sink terms. For the sink term, the relaxation term given by the first term on the right-hand side of Eq. (2.54) is considered. For the source term, the primitive part of the production term, that is the second term on the right-hand side of Eq. (2.54) is considered. Then, we have

$$\begin{aligned} &-C_{S1}\frac{\varepsilon}{K}B_{ij} - \left(\frac{4}{3} - C_{R1}\right)KS_{ij} = 0 \\ &\Leftrightarrow B_{ij} = 2\frac{4-3C_{R1}}{6C_{S1}}\frac{K^2}{\varepsilon}S_{ij}. \end{aligned} \tag{2.55}$$

This is nothing but the eddy-viscosity model given by Eqs. (2.44) and (2.45) where $C_\nu = (4-3C_{R1})/(6C_{S1})$.

Pope (1975) proposed the systematic modeling for the algebraic expression for the Reynolds stress based on the modeled transport equation given by Eq. (2.54) in a non-rotating system. Here, the system rotation is neglected, $\boldsymbol{\Omega}^{\mathrm{F}} = 0$. Its modeling procedure is as follows. First, quasi-homogeneity condition is assumed, so that the diffusion terms are neglected. Second, the weak-equilibrium assumption is adopted; namely, we assume

$$\begin{aligned} &\frac{D}{Dt}\left(\frac{R_{ij}}{K}\right) = 0 \\ \Leftrightarrow\ &\frac{DR_{ij}}{Dt} = \frac{R_{ij}}{K}\frac{DK}{Dt} = \frac{R_{ij}}{K}\left(P^K - \varepsilon\right). \end{aligned} \tag{2.56}$$

Using above two assumptions, Eq. (2.54) is reduced to

$$\begin{aligned}\frac{B_{ij}}{K}\left(P^K - \varepsilon\right) = &-C_{S1}\frac{\varepsilon}{K}B_{ij} + \left(\frac{4}{3} - C_{R1}\right)KS_{ij} + (1-C_{R2})\left[S_{i\ell}B_{\ell j} + S_{j\ell}B_{\ell i}\right]_{\mathrm{D}} \\ &+ (1-C_{R3})\left(W_{i\ell}^{\mathrm{N}}B_{\ell j} + W_{j\ell}^{\mathrm{N}}B_{\ell i}\right), \end{aligned} \tag{2.57}$$

where $W_{ij}^{\mathrm{N}}[= (\partial U_i/\partial x_j - \partial U_j/\partial x_i)/2]$ denotes the vorticity tensor in a non-rotating system and the forcing term is neglected. Equation (2.57) gives the algebraic relation for the deviatoric part of the Reynolds stress. Pope (1975) expanded the Reynolds stress in the velocity gradient and obtained the algebraic

expression for the Reynolds stress The resulting expression for the Reynolds stress can be written as

$$R_{ij} = \frac{2}{3}K\delta_{ij} - 2\nu^{\mathrm{T}}S_{ij} + \zeta_{SS}\left[S_{i\ell}S_{\ell j}\right]_{\mathrm{D}} - \zeta_{SW}\left(S_{i\ell}W^{\mathrm{N}}_{\ell j} + S_{j\ell}W^{\mathrm{N}}_{\ell i}\right) + \zeta_{SSW}\left(S_{i\ell}S_{\ell m}W^{\mathrm{N}}_{mj} + S_{j\ell}S_{\ell m}W^{\mathrm{N}}_{mi}\right) + \cdots, \tag{2.58}$$

Note that ν^{T} is not the same as Eq. (2.45) but is written in the functional form as $\nu^{\mathrm{T}} = F\{P^K/\varepsilon, K^2S_{ij}S_{ij}/\varepsilon^2, K^2W^{\mathrm{N}}_{ij}W^{\mathrm{N}}_{ij}/\varepsilon^2, \cdots\}K^2/\varepsilon$ and ζ_n's are also functional of P^K/ε, $K^2S_{ij}S_{ij}/\varepsilon^2$, and etc. Such a form of the Reynolds stress given by Eq. (2.58) is referred to as the nonlinear eddy-viscosity model. Several types of the nonlinear eddy-viscosity models were proposed and their performance was discussed [Speziale (1987); Taulbee (1992); Shih *et al.* (1993, 1995); Craft *et al.* (1996)]. These papers showed that the higher-order nonlinear terms on the velocity gradient shown on the right-hand side of Eq. (2.58) are essential in predicting the anisotropy of turbulence intensity or the effect of curvature of the streamline on the Reynolds stress. Namely, the nonlinear eddy-viscosity model succeeded in accounting for some essences of turbulent flows without solving its transport. The extension of this modeling to the general coordinate system including the rotating system is discussed in Appendix B.

2.4 Statistical theory for turbulence modeling: TSDIA

The modeling proposed by Pope (1975) revealed the relationship between the transport equation for the Reynolds stress and the nonlinear eddy-viscosity model. However, its theoretical basis is still empirical model given by Eq. (2.53). In the turbulence closure theory for homogeneous turbulence, the direct-interaction approximation (DIA) developed by Kraichnan (1959) was a representative one which includes no empirical parameter. Yoshizawa (1984) developed a statistical theory for inhomogeneous turbulence by combining the DIA and the multiple-scale analysis, which is referred to as the two-scale direct-interaction approximation (TSDIA). Using the TSDIA, we can deductively obtain not only the eddy-viscosity model given by Eq. (2.44) but also the higher-order nonlinear eddy-viscosity model given by Eq. (2.58) from the Navier–Stokes equation [c.f., Okamoto (1994)]. Since the TSDIA is based on the Navier–Stokes equation, it enables us to obtain the models for turbulence field affected by the system rotation, the buoyancy, or the magnetic field, starting from the basic equation [see, Yoshizawa (1998) for details]. Details for the TSDIA is given in Appendix C. In this section, we review a brief introduction of the TSDIA and two representative examples of the results for rotating turbulence.

2.4.1 Two-scale direct interaction approximation

In the TSDIA, a small scale parameter δ and two space and time variables are introduced:

$$\boldsymbol{\xi} = \boldsymbol{x}, \quad \boldsymbol{X} = \delta\boldsymbol{x}, \quad \tau = t, \quad T = \delta t, \tag{2.59}$$

where $\boldsymbol{\xi}$ and τ are referred to as fast variables, while $\boldsymbol{X}$ and T are slow variables. We assume that the mean values are slowly varying, so that they only depend on slow variables, while the fluctuation values

depend on both fast and slow variables. This is expressed as

$$q = Q(\boldsymbol{X}; T) + q'(\boldsymbol{\xi}, \boldsymbol{X}; \tau, T), \tag{2.60}$$

where we note again that $q = (\boldsymbol{u}, p, \boldsymbol{\omega}, f)$. Schematic diagram of this two-scale representation for spatial variable is shown in Fig. 2.5. Under Eq. (2.59), the spatial and time derivatives are expressed as

$$\frac{\partial}{\partial x_i} = \frac{\partial}{\partial \xi_i} + \delta \frac{\partial}{\partial X_i}, \quad \frac{\partial}{\partial t} = \frac{\partial}{\partial \tau} + \delta \frac{\partial}{\partial T}. \tag{2.61}$$

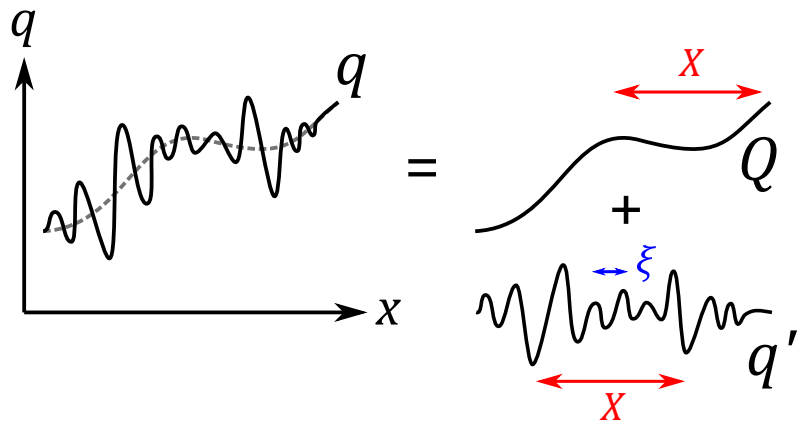

Figure 2.5: Schematic diagram of two-scale representation for spatial variable for a physical quantity q.

In order to make full use of the closure theory for homogeneous turbulence, we assume the statistical homogeneity for $\boldsymbol{\xi}$ space. In addition, we expand the velocity and pressure fluctuations in powers of δ and the rotation parameter $|\Omega^{\mathrm{F}}|$ as [Shimomura & Yoshizawa (1986); Yokoi & Yoshizawa (1993)]

$$u'(\boldsymbol{\xi}, \boldsymbol{X}; \tau, T) = \sum_{n,m=0}^{\infty} \delta^n |\Omega^{\mathrm{F}}|^m u^{(nm)}(\boldsymbol{\xi}, \boldsymbol{X}; \tau, T), \quad p'(\boldsymbol{\xi}, \boldsymbol{X}; \tau, T) = \sum_{n,m=0}^{\infty} \delta^n |\Omega^{\mathrm{F}}|^m p^{(nm)}(\boldsymbol{\xi}, \boldsymbol{X}; \tau, T). \tag{2.62}$$

Under this parameter expansion, the basic $O(\delta^0 |\Omega^{\mathrm{F}}|^0)$ field corresponds to the homogeneous isotropic and non-rotating turbulence, except for the dependence on the slow variables $(\boldsymbol{X}; T)$. The effects of inhomogeneity and anisotropy are incorporated in $O(\delta^n)$ fields with $n \geq 1$ and these of rotation are in $O(|\Omega^{\mathrm{F}}|^m)$ fields with $m \geq 1$, in a perturbational manner. We apply the Fourier transformation to $\boldsymbol{\xi}$ field in the frame moving with the mean velocity $\boldsymbol{U}(\boldsymbol{X}; T)$; namely, we define the Fourier transformation as

$$q(\boldsymbol{\xi}, \boldsymbol{X}; \tau, T) = \int \mathrm{d}\boldsymbol{k}\ \tilde{q}(\boldsymbol{k}, \boldsymbol{X}; \tau, T) \mathrm{e}^{i\boldsymbol{k}\cdot(\boldsymbol{\xi} - \boldsymbol{U}\tau)}, \tag{2.63}$$

$$\tilde{q}(\boldsymbol{k}, \boldsymbol{X}; \tau, T) = \frac{1}{(2\pi)^3} \int \mathrm{d}\boldsymbol{\xi}\ q(\boldsymbol{\xi}, \boldsymbol{X}; \tau, T) \mathrm{e}^{-i\boldsymbol{k}\cdot(\boldsymbol{\xi} - \boldsymbol{U}\tau)}. \tag{2.64}$$

The higher-order fields are formally solved with the aid of the response function for the basic field, which was introduced in the DIA [Kraichnan (1959)]. As a result, higher-order velocities are expressed as a function of the basic field velocity $\tilde{\boldsymbol{u}}^{(00)}(\boldsymbol{k};\tau)$, the mean velocity $\boldsymbol{U}(\boldsymbol{X};T)$, and the angular velocity of the rotation $\boldsymbol{\Omega}^{\mathrm{F}}$. Since the basic field corresponds to the homogeneous isotropic turbulence, the second-order correlation for the basic field velocities is given similar to Eqs. (2.40) and (2.41) as

$$\begin{aligned}\left\langle \tilde{u}_i^{(00)}(\boldsymbol{k},\boldsymbol{X};\tau,T)\tilde{u}_j^{(00)}(\boldsymbol{k}',\boldsymbol{X};\tau',T)\right\rangle &= \tilde{Q}_{ij}^{(00)}(\boldsymbol{k},\boldsymbol{X};\tau,\tau',T)\delta(\boldsymbol{k}+\boldsymbol{k}') \\ &= \left[M_{ij}(\boldsymbol{k})\frac{E^{\mathrm{B}}(k,\boldsymbol{X};\tau,\tau',T)}{4\pi k^2} - \frac{i}{2}\epsilon_{ij\ell}\frac{k_\ell}{k^2}\frac{E^{H\mathrm{B}}(k,\boldsymbol{X};\tau,\tau',T)}{4\pi k^2}\right]\delta(\boldsymbol{k}+\boldsymbol{k}'). \end{aligned} \tag{2.65}$$

Here, $E^{\mathrm{B}}(k,\boldsymbol{X};\tau,\tau',T)$ and $E_{\mathrm{B}}^{H}(k,\boldsymbol{X};\tau,\tau',T)$ respectively satisfy

$$K^{\mathrm{B}} = \frac{1}{2}\left\langle u_i^{(00)}u_i^{(00)}\right\rangle = \int_0^\infty \mathrm{d}k\ E^{\mathrm{B}}(k,\boldsymbol{X};\tau,\tau,T), \tag{2.66}$$

$$H^{\mathrm{B}} = \left\langle u_i^{(00)}\omega_i^{(00)}\right\rangle = \int_0^\infty \mathrm{d}k\ E^{H\mathrm{B}}(k,\boldsymbol{X};\tau,\tau,T). \tag{2.67}$$

Third-order correlation of the basic field velocities is calculated with the aid of the DIA and expressed in terms of the second-order correlations and the response function. Therefore, any turbulence correlations are systematically calculated.

2.4.2 Effect of rotation on homogeneous turbulence

For homogeneous turbulence, it was suggested the system rotation affects the energy cascade or the inter-scale energy transfer [Cambon & Jacquin (1989); Cambon *et al.* (1997); Morinishi *et al.* (2001*a*); Yoshimatsu *et al.* (2011)]. In a freely decaying homogeneous turbulence under rotation, it was shown that the energy cascade rate from large to small scales is reduced due to the system rotation [Bardina *et al.* (1985); Cambon & Jacquin (1989); Morinishi *et al.* (2001*a*)]. This leads to the reduction of the decaying rate of the turbulent energy. Since the turbulent energy transport equation in the decaying homogeneous turbulence under rotation is written as

$$\frac{\partial K}{\partial t} = -\varepsilon, \tag{2.68}$$

the reduction of the decaying rate of the turbulent energy indicates the reduction of the energy dissipation rate ε. In the RANS model, this reduction of the energy dissipation rate is modeled by modifying the transport equation for ε [Bardina *et al.* (1985)]. Okamoto (1995) proposed the following model for the transport equation for ε with the aid of the TSDIA:

$$\frac{\partial \varepsilon}{\partial t} = -C_{\varepsilon 2}\frac{\varepsilon^2}{K} - F\{\Omega^{\mathrm{F}}K/\varepsilon\}K(\Omega^{\mathrm{F}})^2, \tag{2.69}$$

where $F\{\Omega^{\mathrm{F}}K/\varepsilon\}(>0)$ denotes some functional of $\Omega^{\mathrm{F}}K/\varepsilon$. Here, $F\{\Omega^{\mathrm{F}}K/\varepsilon\} = \text{const.}$ is the simplest expression. With the aid of the second term on the right-hand side of Eq. (2.69), the reduction of the energy dissipation rate due to the rotation can be predicted, so that the model succeeded in predicting the reduction of the decaying rate of the turbulent energy.

2.4.3 Vortex dynamo effect

In the magnetohydrodynamics (MHD), large scale or mean magnetic field generation phenomenon due to turbulent motion has been discussed in terms of the dynamo effect. In the MHD, the mean magnetic field equation is written as [Moffatt (1978); Krause & Rädler (1980)]

$$\frac{\partial \boldsymbol{B}}{\partial t} = \boldsymbol{\nabla} \times \left(\boldsymbol{U} \times \boldsymbol{B} + \boldsymbol{E}^{\mathrm{M}} - \lambda \boldsymbol{\nabla} \times \boldsymbol{B} \right), \tag{2.70}$$

where $\boldsymbol{E}^{\mathrm{M}} (= \langle \boldsymbol{u}' \times \boldsymbol{b}' \rangle)$ denotes the electromotive force, $\boldsymbol{B}$ and $\boldsymbol{b}'$ respectively denote the mean magnetic field and the magnetic field fluctuation, and λ denotes the magnetic diffusivity. A conventional model for the electromotive force is given by [Moffatt (1978); Krause & Rädler (1980)]

$$\boldsymbol{E}^{\mathrm{M}} = \alpha \boldsymbol{B} - \beta \boldsymbol{\nabla} \times \boldsymbol{B}. \tag{2.71}$$

Here, β expresses the diffusivity due to turbulence, while α expresses the dynamo effect. Note that α must be a pseudo-scaler considering the invariance of the electromotive force by the reflection transformation and it is often modeled to be proportional to the turbulent helicity as $\alpha \simeq -\tau H$ with some timescale τ, while β is modeled as $\beta \simeq \tau K$ [Moffatt (1978); Krause & Rädler (1980); Brandenburg & Subramanian (2005)]. In the case that the magnetic Reynolds number $\mathrm{Re}_{\mathrm{M}} (\propto \beta/\lambda)$ is high, and $\boldsymbol{U}$ and $\boldsymbol{B}$ are parallel to each other, the statistically steady state reads

$$\begin{aligned} \boldsymbol{E}^{\mathrm{M}} = \alpha \boldsymbol{B} - \beta \boldsymbol{\nabla} \times \boldsymbol{B} = 0 \\ \Leftrightarrow \boldsymbol{J} = \frac{\alpha}{\beta} \boldsymbol{B}, \end{aligned} \tag{2.72}$$

where $\boldsymbol{J} (= \boldsymbol{\nabla} \times \boldsymbol{B})$ denotes the mean current. Hence, the mean current aligned with the mean magnetic field is established due to the presence of α term. This effect is referred to as the α dynamo.

Similar effect has been also discussed for neutral hydrodynamics from the viewpoint of the large-scale vortex generation, which is sometimes referred to as the vortex dynamo. For incompressible fluid, Frisch *et al.* (1987) suggested that the breakage of the parity-invariance is essential for the presence of the vortex dynamo effect similar to the α effect in the MHD. They also suggested that the anisotropy invokes the vortex dynamo effect similar to the α effect, which is referred to as the anisotropic kinetic alpha (AKA) effect. Gvaramadze *et al.* (1989) examined the effect of helicity on the vortex dynamo effect. They suggested that not only the presence of helicity but also the inhomogeneity of the flow is required for the vortex dynamo effect. For incompressible fluid, the mean vorticity equation can be written as

$$\frac{\partial \boldsymbol{\Omega}}{\partial t} = \boldsymbol{\nabla} \times \left(\boldsymbol{U} \times \boldsymbol{\Omega}^{\mathrm{A}} + \boldsymbol{V}^{\mathrm{M}} - \nu \boldsymbol{\nabla} \times \boldsymbol{\Omega} \right), \tag{2.73}$$

where $\boldsymbol{V}^{\mathrm{M}} (= \langle \boldsymbol{u}' \times \boldsymbol{\omega}' \rangle)$ is referred to as the vortex-motive force and $\boldsymbol{\Omega}^{\mathrm{A}} (= \boldsymbol{\Omega} + 2\boldsymbol{\Omega}^{\mathrm{F}})$ denotes the mean absolute vorticity vector. We assume that the vortex-motive force can be modeled as the similar form to the electromotive force given by Eq. (2.71):

$$\boldsymbol{V}^{\mathrm{M}} = \alpha^{V} \boldsymbol{\Omega}^{\mathrm{A}} - \nu^{\mathrm{T}} \boldsymbol{\nabla} \times \boldsymbol{\Omega}. \tag{2.74}$$

Here, $\nu^{\rm T}$ is the eddy viscosity which corresponds to that on the second term on the right-hand side of Eq. (2.44), while α^V related term represents the vortex dynamo effect. The mathematical structure of Eqs. (2.73) and (2.74) is quite similar to that of the mean magnetic field equations given by Eqs. (2.70) and (2.71). In the case that the Reynolds number Re is high, and $\boldsymbol{U}$ and $\boldsymbol{\Omega}^{\rm A}$ are parallel to each other, the statistically steady state reads

$$\begin{aligned} \boldsymbol{V}^{\rm M} &= \alpha^V \boldsymbol{\Omega}^{\rm A} - \nu^{\rm T} \boldsymbol{\nabla} \times \boldsymbol{\Omega} = 0 \\ &\Leftrightarrow \ \nabla^2 \boldsymbol{U} = -\frac{\alpha^V}{\nu^{\rm T}} \boldsymbol{\Omega}^{\rm A}. \end{aligned} \tag{2.75}$$

Hence, the Laplacian of the mean velocity aligned with the mean absolute vorticity is established, which is similar to the establishment of the mean current due to the α effect as seen in Eq. (2.72). The Laplacian of the mean velocity expresses the presence of the spatially local increase or decrease of the mean velocity, so that the vortex dynamo effect can be interpreted as the generation phenomenon of the spatially local mean velocity in the direction of the rotation axis.

Yokoi & Yoshizawa (1993) proposed the following model with the aid of the TSDIA up to the calculation of $O(\delta|\Omega^{\rm F}|)$:

$$R_{ij} = \frac{2}{3} K \delta_{ij} - 2\nu^{\rm T} S_{ij} + \eta^{\rm T} \left[\frac{\partial H}{\partial x_j} \Omega_i^{\rm A} + \frac{\partial H}{\partial x_i} \Omega_j^{\rm A} \right]_{\rm D}, \tag{2.76}$$

where $\eta^{\rm T} = C_\eta K^4/\varepsilon^3$, C_η is a constant. In Eq. (2.76), the second term is the eddy-viscosity model given by Eq. (2.44) and the third term denotes the effect of the turbulent helicity on the Reynolds stress. Hereafter, we refer to the model given by Eq. (2.76) as the helicity model. Using Eq. (2.5), the vortex-motive force is connected to the Reynolds stress as

$$V_i^{\rm M} = -\frac{\partial R_{ij}}{\partial x_j} + \frac{\partial K}{\partial x_i}. \tag{2.77}$$

Substituting the helicity model given by Eq. (2.76) into this, we have

$$\boldsymbol{V}^{\rm M} = -\left[\boldsymbol{\nabla} \cdot \left(\eta^{\rm T} \boldsymbol{\nabla} H \right) \right] \boldsymbol{\Omega}^{\rm A} - \nu^{\rm T} \boldsymbol{\nabla} \times \boldsymbol{\Omega} + \cdots, \tag{2.78}$$

where the leading terms are only written. Namely, the helicity model predicts that α^V is written in terms of the spatial gradient of the turbulent helicity, while α in Eq. (2.71) is often modeled to be proportional to the turbulent helicity itself.

In comparison with the nonlinear eddy-viscosity model given by Eqs. (2.58) or (B5), the helicity model has quite different form. In the nonlinear eddy-viscosity models, the effect of the mean vorticity or rotation is coupled with the mean strain rate. On the other hand, in the helicity model, the effect of rotation is coupled with the spatial gradient of the turbulent helicity H. Considering the derivation of the nonlinear-eddy viscosity model, the effect of rotation comes from the anisotropy of the Reynolds stress B_{ij} as seen in the fourth term on the right-hand side of Eq. (B3). In this sense, the effect of rotation in the nonlinear eddy-viscosity model is related to the anisotropy of turbulence. In the helicity model,

the effect of rotation rather comes from the inhomogeneity of the basic field helicity expressed by $E^{H\mathrm{B}}$ in Eq. (2.65). In the usage of the helicity model, an additional transport equation for H is solved, so that it is referred to as the K–ε–H model or the three-equation model [Yokoi & Yoshizawa (1993)]. By using the K–ε–H model, it is expected to be able to predict the turbulent phenomena accompanied with swirling motion, e.g., the sustainment of a strong vortex such as wake vortices behind an aircraft [Spalart (1998)] or supercell in meteorological flow [Lilly (1986); Noda & Niino (2010)], with much smaller numerical cost than using the DNS.

2.5 Vortex dynamo related phenomena

2.5.1 Turbulent swirling flow in a straight pipe

An example of the flow which is related to the vortex dynamo is the turbulent swirling flow in a straight pipe [Kitoh (1991); Steenbergen (1995)]. The flow configuration is schematically shown in Fig. 2.6. In this flow, the strong swirl is generated in the center axis of the pipe at the inlet, which is referred to as the concentrated vortex type [Steenbergen (1995)]. Experimental studies showed that the radial profile of the mean velocity in the direction of the pipe axis exhibit a dent at the center axis in contrast to the flat profile observed in the non-rotating case [see, Fig. 2.4]. This dent profile of the axial mean velocity is sustained to the downstream over several tens of times of the pipe diameter. Moreover, it exhibits a reversal flow in the center axis region when the strong swirl is given [Kitoh (1991)]. The generation of the dent axial velocity at the center axis can be primitively explained as follows. The axial vorticity is so strong in the center axis region at the upstream that the pressure is roughly estimated as $\nabla^2 p \simeq \omega_z^2/2$ according to the Poisson equation for the pressure given by Eq. (2.4). Therefore, it is considered that the pressure in the center axis region at the upstream decreases compared with the non-swirling case. At the downstream, the strong axial vorticity is disappeared so that the pressure in the center axis region is larger than the upstream. Hence, the axial pressure gradient in the center axis region is positive, $\partial p/\partial z > 0$. This pressure gradient gives the negative force on the axial velocity, leading to the dent profile of the axial velocity. Note that the consistency of this primitive analysis in the strongly turbulent flow is not so clear. For example, it is expected that the concentrated vortex is not sustained but smeared out by the strong mixing due to turbulence expressed by the eddy viscosity. However, the dent axial mean velocity profile is persistent in turbulent flow as shown in the experiment [Kitoh (1991); Steenbergen (1995)]. This phenomenon can be understood as the generation of the negative axial mean velocity due to the rotational motion, so that it is an example of the vortex dynamo. In the context of the turbulence modeling, it was known that the standard K–ε model using the eddy-viscosity model given by Eqs. (2.44) and (2.45) cannot predict the sustainment of the dent profile of the axial mean velocity [Kobayashi & Yoda (1987); Steenbergen (1995); Jakirlić *et al.* (2000)]. This shortfall is difficult to be rectified even when the nonlinear eddy-viscosity models are applied [Jakirlić *et al.* (2000)]. Kobayashi & Yoda (1987) showed that the dent profile is sustained further downstream when the model constant for the eddy viscosity C_ν is artificially modified to the smaller value. This result suggests that some effect related to the swirling motion effectively reduces the large momentum diffusion due to the eddy viscosity.

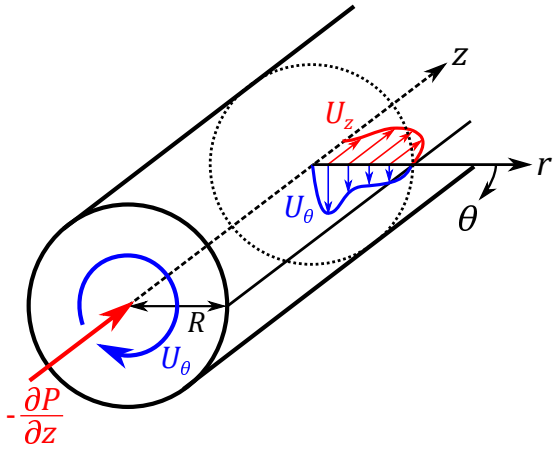

Figure 2.6: Schematic flow configuration for the turbulent swirling flow in a straight pipe.

Yokoi & Yoshizawa (1993) applied the helicity model given by Eq. (2.76) to the turbulent swirling flow in a straight pipe. Figure (a)2.7 shows the comparison between the experimental result and the prediction of the turbulence models. The standard K–ε model predicts the rapid decrease of the dent profile of the axial mean velocity. However, the helicity model succeeded in predicting the sustainment of the dent axial mean velocity. Note that the model constant for the eddy-viscosity model C_ν is not artificially modified in the helicity model, so that the difference between the standard K–ε model and the helicity model is the presence of the third term on the right-hand side of Eq. (2.76). Namely, the helicity effect described by the third term on the right-hand side of Eq. (2.76) counterbalances the eddy-viscosity term in the second term. In the model calculation performed by Yokoi & Yoshizawa (1993), the negative turbulent helicity appears in the center axis region as shown in Fig. 2.7(b) and the deviation of the axial mean velocity from the non-swirling flow is written as $\delta U_z < 0$. Namely, it can be understood that the negative axial mean velocity δU_z is generated at the region in which the turbulent helicity is negative. However, the experimental value of the turbulent helicity is not obtained, so that the validity of the model calculation cannot be discussed. Moreover, the sustainment of the dent axial mean velocity profile was also predicted by the Reynolds stress equation model which does not involve the turbulent helicity [Jakirlić *et al.* (2000)] or by the history effect of the streamline on the eddy viscosity [Hamba (2017)]. In this sense, the physical origin of the mechanism for the sustainment of the dent axial mean velocity in the turbulent swirling flow in a straight pipe is under discussion.

2.5.2 Mean velocity generation in rotating turbulence

The vortex dynamo effect given by Eq. (2.75) suggests the possibility that the local mean velocity is generated due to the α^V and the system rotation $\boldsymbol{\Omega}^{\mathrm{F}}$. Yokoi & Brandenburg (2016) performed the DNS of rotating turbulence stating from the zero-mean velocity condition. In their simulation, the rotation axis is set in the y direction and the turbulent helicity is inhomogeneously injected by using the external

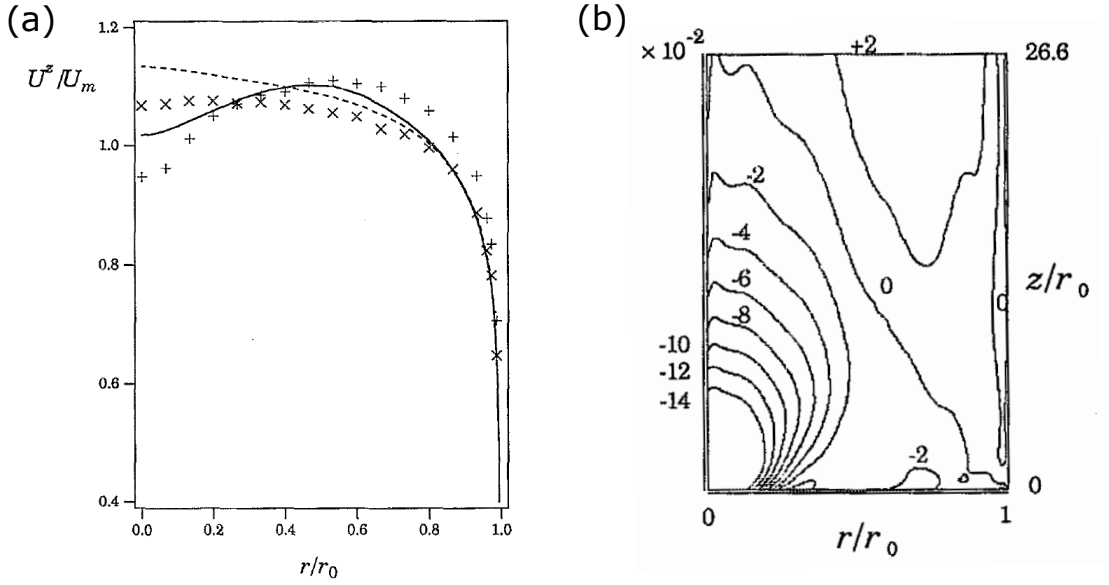

Figure 2.7: (a) Axial mean velocity in the turbulent swirling flow in a straight pipe [cited from Fig. 3 in Yokoi & Yoshizawa (1993) p.473]. Here, U^z denotes the mean velocity in the direction of the pipe axis (z), U_m the axial bulk mean velocity, and r_0 the pipe radius. + and $\times$ symbols respectively denote the experimental results at the inlet and $z/r_0 = 26.6$ given by Kitoh (1991). The dotted line denotes the prediction of the standard K–ε model, while the solid line denotes the prediction of the helicity model. (b) Contour of the turbulent helicity H obtained from the model calculation [cited from Fig. 5 in Yokoi & Yoshizawa (1993) p.474].

forcing. With the aid of this external forcing, the spatial distribution of the turbulent helicity given by $H(z) \propto \sin(z)$ is established as shown in the top figure of Fig. 2.8(a) in which the vertical axis denotes the z direction. They showed that the mean velocity aligned with the rotation axis is generated and sustained. As shown in Fig. 2.8(a), the positive mean velocity in the direction of the rotation axis is generated at the region in which the turbulent helicity is positive, while the negative mean velocity is generated at the region in which the turbulent helicity is negative.

This mean velocity generation phenomenon can be predicted by neither the nonlinear eddy-viscosity model given by Eqs. (2.58) or (B5) nor the conventional Reynolds stress model given by Eq. (2.53) since both of them give the trivial solution $R_{ij} = 0$, so that they predict $\boldsymbol{U} = 0$. However, the helicity model given by Eq. (2.76) can account for this phenomenon. When the mean velocity is zero but the angular velocity of the system is non-zero, the helicity model reads

$$R_{yz} = 2\eta^{\mathrm{T}} \frac{\partial H}{\partial z} \Omega_y^{\mathrm{F}}. \tag{2.79}$$

Namely, the helicity model predicts that $R_{yz} \neq 0$ when both the z derivative of the turbulent helicity and Ω_y^{F} are non-zero. Yokoi & Brandenburg (2016) numerically confirmed that the exact value of R_{yz}

and the right-hand side of Eq. (2.79) are well correlated in the early stage of the simulation in which the mean velocity is not established [Fig. 2.8(b)]. Substituting Eq. (2.79) into the RANS equation (2.19), the equation for the axial mean velocity U_y is written as

$$\frac{\partial U_y}{\partial t} = -2\eta^{\mathrm{T}} \frac{\partial^2 H}{\partial z^2} \Omega_y^{\mathrm{F}}, \tag{2.80}$$

where the spatial derivative of η^{T} is neglected for simplicity. Here, the high-Reynolds-number condition is concerned, so that the kinematic viscosity term is neglected. Since the spatial distribution of the turbulent helicity is given by $H(z) \propto \sin(z)$, Eq. (2.80) is evaluated as

$$\frac{\partial U_y}{\partial t} \propto \sin(z) \Omega_y^{\mathrm{F}}. \tag{2.81}$$

Therefore, the positive axial mean velocity U_y is generated at $0 < z < \pi$ where the turbulent helicity is positive, while the negative axial mean velocity is generated at $-\pi < z < 0$ where the turbulent helicity is negative. This prediction of the mean velocity by means of the helicity model is consistent with the result shown in Fig. 2.8(a). This correspondence of the sign between the mean velocity and the turbulent helicity can be also explained by using Eqs. (2.75) and (2.78). Here, the following approximation is given for simplicity: $\nabla^2 \boldsymbol{U} \simeq -(\ell^u)^{-2} \boldsymbol{U}$ and $\alpha^V = -\boldsymbol{\nabla} \cdot (\eta^{\mathrm{T}} \boldsymbol{\nabla} H) \simeq -\eta^{\mathrm{T}} \nabla^2 H \simeq \eta^{\mathrm{T}} (\ell^h)^{-2} H$. Under these approximations, Eq. (2.75) is reduced to

$$\boldsymbol{U} = \frac{(\ell^u)^2 \eta^{\mathrm{T}} H}{(\ell^h)^2 \nu^{\mathrm{T}}} \boldsymbol{\Omega}^{\mathrm{A}}. \tag{2.82}$$

Hence, the positive mean velocity aligned with the mean absolute vorticity is established at the region in which the turbulent helicity is positive, while the negative mean velocity is established at the region in which the turbulent helicity is negative. Consequently, the helicity model proposed by Yokoi & Yoshizawa (1993) can account for the mean velocity generation phenomenon observed by Yokoi & Brandenburg (2016). It should be noted, however, the mechanism that the turbulent helicity affects the Reynolds stress was not shown there.

2.6 Problems in the modeling of rotating turbulence

We briefly reviewed the previous studies for turbulence modeling so far. There are some problems which are not clarified, especially in rotating turbulence. Since the system rotation is closely related to the breakage of the mirror symmetry, pseudo-scalar quantities, such as helicity, are expected to play a significant role. However, the mechanism that helicity affects inhomogeneous turbulent flows is not so much clarified. In order to clarify how and when helicity affects turbulent flows, its mechanism should be investigated in detail. In this dissertation, we focus on the two points described in the following subsections.

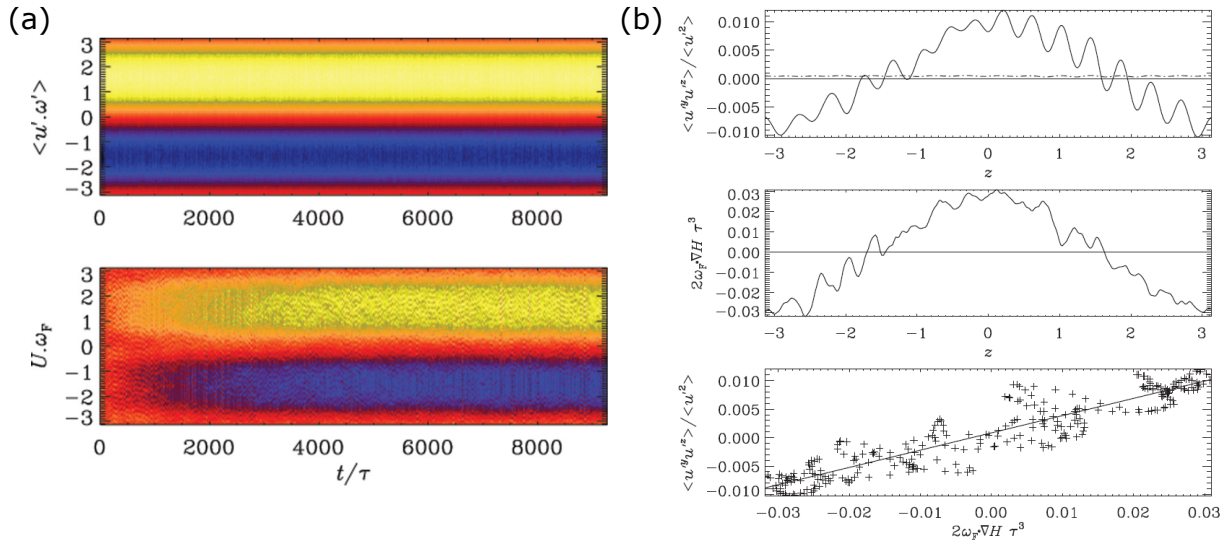

Figure 2.8: Figures from Yokoi & Brandenburg (2016). (a) Time evolution of the turbulent helicity (top) and the mean velocity in the direction of the rotation axis (y) (bottom) [cited from Fig. 3 in Yokoi & Brandenburg (2016) p.7]. Here, the color denotes the value of H or $\boldsymbol{U} \cdot \boldsymbol{\Omega}^{\mathrm{F}}$ and the vertical axis denotes the z direction. (b) The spatial distribution of $R_{yz}/(2K)$ (top), the helicity model term $2\Omega_y^{\mathrm{F}} \partial H/\partial z \tau^3$ (middle), and the correlation between them (bottom) where τ denotes the turbulence time scale [cited from Fig. 4 in Yokoi & Brandenburg (2016) p.7].

2.6.1 Physical origin of the helicity model

The helicity model analytically proposed by Yokoi & Yoshizawa (1993) with the aid of the TSDIA exhibited some significant features in rotating turbulent flows. It should be emphasized, however, the helicity model cannot be obtained by the systematic modeling based on the Reynolds stress transport developed by Pope (1975), which was discussed in Sec. 2.3.4 and Appendix B. This inconsistency comes from the lack of the mechanism that the turbulent helicity affects the Reynolds stress transport. Since the algebraic model for the Reynolds stress is tightly connected to the production mechanism of the Reynolds stress, the helicity model should be also connected to some effects in the Reynolds stress transport. Although Yokoi & Brandenburg (2016) suggested that the helicity model is sufficient to account for the mean velocity generation phenomenon which is observed in their simulation, the physical origin of the helicity model itself was not shown. In this sense, the physical origin of the mean velocity generation is not completely clarified. In order to clarify when and how much the turbulent helicity affects the Reynolds stress or the mean velocity, the mechanism that the turbulent helicity affects the Reynolds stress transport should be investigated. By revealing the relationship between the turbulent helicity and the Reynolds stress transport, it can be examined whether the turbulence model using the turbulent helicity as a representative variable is physically reliable or not in predicting the turbulent flows accompanied with

swirling motion.

2.6.2 Effects of rotation on energy transport

As seen in Sec. 2.3.2, the energy flux terms for the turbulent energy transport are conventionally modeled by using the gradient-diffusion approximation given by Eq. (2.47). A simple example of the diffusion problem of turbulence is oscillating-grid turbulence [Hopfinger & Toly (1976); Dickinson & Long (1978)]. Its schematic flow configuration is shown in Fig. 2.9 in which $\mathbf{\Omega}^{\mathrm{F}} = 0$. In this experiment, velocity fluctuation is generated by the oscillation of the grid and the turbulent energy falls off away from the grid. When the direction perpendicular to the grid plane is set in the z direction, the transport equation for the turbulence energy given by Eqs. (2.23) and (2.24a)–(2.24f) is written as

$$\frac{\partial K}{\partial t} = -\varepsilon - \frac{\partial}{\partial z}\left(\left\langle u_z' p' \right\rangle + \frac{1}{2}\left\langle u_z' \frac{1}{2} u_i' u_i' \right\rangle\right) + \nu \frac{\partial^2 K}{\partial z^2} + F^K. \tag{2.83}$$

Here, we assume that the turbulence field is homogeneous in the x and y directions and the mean velocity can be assumed to be zero in such a case. In this turbulent flow, F^K represents the energy injection due to the grid oscillation. Dickinson & Long (1978) suggested that the width of the turbulence region d grows as $d \simeq (\kappa t)^{1/2}$ where κ corresponds to the eddy viscosity. They also suggested that κ is proportional to the integral length scale L and the turbulent intensity $K^{1/2}$ as $\kappa \sim LK^{1/2}$. Substituting the Taylor's dissipation law $\varepsilon \sim K^{3/2}/L$ [Taylor (1935)], this κ is nothing but the eddy viscosity given by Eq. (2.45). In fact, Matsunaga *et al.* (1999) showed that the spatial distribution of the turbulent energy in oscillating-grid turbulence can be predicted by using the standard K–ε model described by Eqs. (2.48) and (2.49). Here, the transport equation for the turbulent energy reads

$$\frac{\partial K}{\partial t} = -\varepsilon - \frac{\partial}{\partial z}\left(\frac{C_\nu}{\sigma_K}\frac{K^2}{\varepsilon}\frac{\partial K}{\partial z}\right) + F^K. \tag{2.84}$$

Note that the kinematic viscosity is neglected since the high-Reynolds-number condition, $\nu^{\mathrm{T}}/\nu \gg 1$, is concerned. These facts suggest that the model for the energy flux given by the gradient-diffusion approximation with the eddy viscosity is appropriate for simple inhomogeneous turbulent flows.

However, this is not the case for rotating turbulence. Dickinson & Long (1983) performed the experiment of rotating oscillating-grid turbulence in which the rotation axis is perpendicular to the grid plane (Fig. 2.9). They suggested that the width of the turbulence region d grows as $d \sim t$ for rotating case, while $d \sim t^{1/2}$ for non-rotating case. The same result was shown by the experiments [Davidson *et al.* (2006); Kolvin *et al.* (2009)] and the numerical simulation [Ranjan & Davidson (2014)]. Hence, in the rotating case, the turbulent energy is transferred faster in the direction of the rotation axis than in the non-rotating case. Since the conventional model given by Eq. (2.84) does not explicitly depend on the rotation rate, this model seems to be unable to predict the fast energy transfer observed in the rotating oscillating-gird turbulence. Moreover, this fast energy transport cannot be predicted by the gradient-diffusion approximation since the diffusion time scale is not $t^{1/2}$ but t. Hence, the modification of the transport equation for ε due to the rotation given by Eq. (2.69) which was proposed for homogeneous turbulence is insufficient to account for the fast energy transfer observed in rotating oscillating-grid

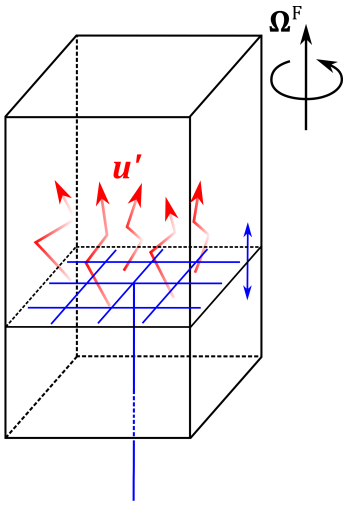

Figure 2.9: Schematic diagram for oscillating-grid turbulence. In the experiment of rotating oscillating-grid turbulence, the rotation axis is set in the direction perpendicular to the grid plane.

turbulence as long as the energy diffusion is modeled by the gradient-diffusion approximation. Namely, a new model for the energy flux associated with the rotation is required. In the exact equation for the turbulent energy transport given by Eq. (2.83), the rotation rate does not explicitly appear. However, the effect of rotation is possibly incorporated through the pressure. Yoshizawa (2002) proposed the following model for the correlation between the velocity and pressure fluctuations with the aid of the TSDIA:

$$\left\langle u_i' p' \right\rangle = C_{KPS} \frac{K^3}{\varepsilon^2} S_{ij} \frac{\partial K}{\partial x_j} + C_{KPW} \frac{K^3}{\varepsilon^2} W_{ij} \frac{\partial K}{\partial x_j}. \tag{2.85}$$

When the mean velocity is zero, this model is written as

$$\left\langle u_i' p' \right\rangle = -C_{KPW} \frac{K^3}{\varepsilon^2} \epsilon_{ij\ell} \Omega_\ell^{\mathrm{F}} \frac{\partial K}{\partial x_j}. \tag{2.86}$$

Although this model includes the effect of rotation on the energy flux, this model gives the energy flux in the direction perpendicular to the rotation axis since $\langle u_i' p' \rangle \Omega_i^{\mathrm{F}} = 0$. Thus, the model proposed by Yoshizawa (2002) cannot account for the fast energy transfer in rotating oscillating-grid turbulence.

Ranjan & Davidson (2014) suggested that the fast energy transfer observed in rotating oscillating-grid turbulence can be explained by the propagation of inertial wave. Inertial wave is governed by the linearized Navier–Stokes equation in a rotating system. Its property is given in Appendix D in detail. An interesting feature of the inertial wave is that the direction of the group velocity is related to the sign of helicity as seen in Eqs. (D6) and (D8) [Moffatt (1970); Davidson (2004)]; namely, the wave packets with negative helicity propagate upward in the direction of the rotation axis, while the wave packets with positive helicity propagate downward. In fact, it was observed in the numerical simulation similar to the

rotating oscillating-grid turbulence that the negative turbulent helicity is dominant at the upper side of the grid, while the positive turbulent helicity is dominant at the lower side [Godeferd & Lollini (1999); Ranjan & Davidson (2014)], which suggests that the direction of the group velocity is outward from the grid. These results suggest that the fast energy transfer in rotating oscillating-grid turbulence can be modeled in terms of the turbulent helicity.

2.6.3 Approach to the problems

As mentioned above, there are two problems in the modeling for rotating turbulence. One is the lack of the knowledge on the mechanism that the turbulent helicity affects the Reynolds stress transport. The other is the lack of the model for the energy flux which accounts for the fast energy transfer in the direction of the rotation axis. In order to solve these problems, we perform two types of numerical simulations in Chaps. 3 and 4. In Chap. 3, the simulation of the mean velocity generation phenomenon similar to Yokoi & Brandenburg (2016) is performed. In contrast to Yokoi & Brandenburg (2016), we examine the transport equation for the Reynolds stress to explore the physical origin of the mean velocity generation and its relation to the turbulent helicity. In this chapter, we proposed a new model for the pressure diffusion term [Eq. (2.22d)] in terms of the turbulent helicity. In Chap. 4, we perform the simulation of decaying inhomogeneous turbulence under system rotation in which the turbulent energy is diffused in the direction of the rotation axis. In this simulation, we examine the transport equation for the turbulent energy which corresponds to the trace of the Reynolds stress. Here, we discuss the relationship between the fast energy transfer in the direction of the rotation axis and the turbulent helicity through the newly proposed model in Chap. 3.

Chapter 3

Effect of helicity on the Reynolds stress transport

3.1 Simulation of the mean velocity generation phenomenon

In order to clarify the physical origin of the mean velocity generation phenomenon and its relation to the turbulent helicity, we perform the numerical simulation similar to that performed by Yokoi & Brandenburg (2016). The helicity model is a candidate predicting this phenomenon. We investigate the relationship between the mean velocity generation phenomenon and the helicity model by means of the Reynolds stress transport.

3.1.1 Numerical setup

The computational domain is a rectangular parallelepiped region as shown in Fig. 3.1. In contrast to the simulation performed by Yokoi & Brandenburg (2016), the localized forcing is adopted in order to restrict the effect of the forcing in the local region around the $y = 0$ plane. The periodic boundary condition is adopted to all directions. The turbulent field is homogeneous in the x and z directions. The rotation axis is set in the x direction. In order to achieve the high-Reynolds-number turbulent flow, we perform the large eddy simulation (LES) instead of the direct numerical simulation (DNS). The concept of the LES is given in Appendix E. Governing equations for the LES are given by

$$\frac{\partial \overline{u}_i}{\partial x_i} = 0, \tag{3.1}$$

$$\frac{\partial \overline{u}_i}{\partial t} = -\frac{\partial}{\partial x_j}(\overline{u}_i \overline{u}_j) - \frac{\partial \overline{p}}{\partial x_i} + \frac{\partial}{\partial x_j}(\nu^{\rm sgs} \overline{s}_{ij}) + 2\epsilon_{ij1}\overline{u}_j \Omega^{\rm F} + C^{\rm ex}\overline{f}_i, \tag{3.2}$$

where $\overline{q}$ denotes the grid scale (GS) or filtered quantity of q, $\overline{p}$ denotes the GS pressure including the subgrid scale (SGS) energy $k^{\rm sgs}[(\overline{u_i u_i} - \overline{u}_i \overline{u}_i)/2]$ and the centrifugal force, $\overline{s}_{ij}[= (\partial \overline{u}_i/\partial x_j + \partial \overline{u}_j/\partial x_i)/2]$ denotes the GS strain rate, $\nu^{\rm sgs}$ denotes the SGS viscosity, and $C^{\rm ex}$ denotes the coefficient adjusting the

intensity of the external forcing. For the high-Reynolds-number case, it can be assumed that $\nu^{\rm sgs} \gg \nu$, so that the kinematic viscosity is neglected in the present simulation. With respect to the model for $\nu^{\rm sgs}$, the Smagorinsky model [Smagorinsky (1963)] is adopted:

$$\nu^{\rm sgs} = (C_S\overline{\Delta})^2\sqrt{2\overline{s}_{ij}\overline{s}_{ij}}. \tag{3.3}$$

Here, we use $\overline{\Delta} = (\Delta x \Delta y \Delta z)^{1/3}$ in which Δx, Δy, and Δz denote the grid size for each direction. For the Smagorinsky constant C_S, we adopt $C_S = 0.19$ which corresponds to the value optimized for homogeneous isotropic turbulence [Yoshizawa (1998); Kida & Yanase (1999); Piomelli (1999)]. The derivation of the Smagorinsky model is given in Appendix E.

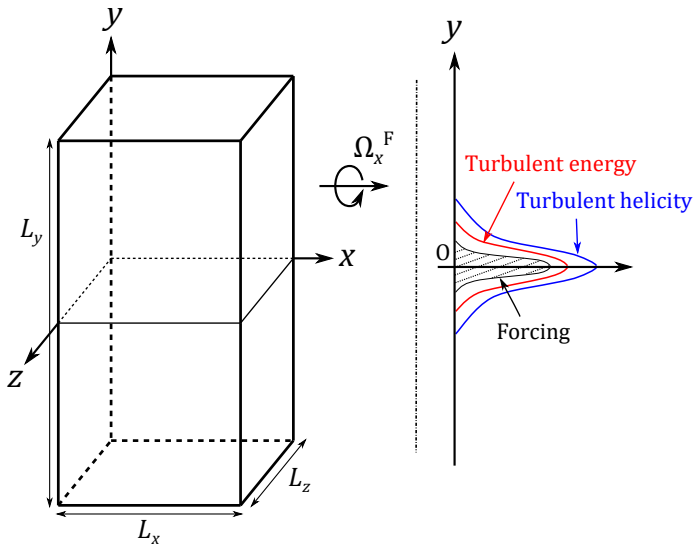

Figure 3.1: Computational domain for the simulation of the mean velocity generation phenomenon.

3.1.2 Effect of plane averaged pressure and centrifugal force

Since the turbulence field is homogeneous in the x and z directions, any statistical quantities do not depend on x and z but depend on y and t. In such a case, $\langle\overline{u}_x\rangle_{\rm S}$ and $\langle\overline{u}_z\rangle_{\rm S}$ are not affected by $\langle\overline{p}\rangle_{\rm S}$ since $\partial\langle\overline{p}\rangle_{\rm S}/\partial x = \partial\langle\overline{p}\rangle_{\rm S}/\partial z = 0$. Here, $\langle\rangle_{\rm S}$ denotes the x–z plane average. Since the centrifugal force $(\boldsymbol{\Omega}^{\rm F}\times\boldsymbol{x})^2/2$ is involved in $\langle\overline{p}\rangle_{\rm S}$, it does not affect $\langle\overline{u}_x\rangle_{\rm S}$ and $\langle\overline{u}_z\rangle_{\rm S}$. For the plane averaged velocity of the y component, the continuity equation reads

$$\frac{\partial\langle\overline{u}_y\rangle_{\rm S}}{\partial y}(y,t) = 0 \quad\Leftrightarrow\quad \langle\overline{u}_y\rangle_{\rm S}(y,t) = \langle\overline{u}_y\rangle_{\rm S}(t). \tag{3.4}$$

Moreover, we have

$$\frac{\partial^2}{\partial t^2}\left[\int_{-L_y/2}^{L_y/2}\mathrm{d}y\,\langle\overline{u}_y\rangle_{\mathrm{S}}(y,t)\right]=\frac{\partial^2}{\partial t^2}\left[L_y\,\langle\overline{u}_y\rangle_{\mathrm{S}}(t)\right]=-\left(2\Omega^{\mathrm{F}}\right)L_y\,\langle\overline{u}_y\rangle_{\mathrm{S}}(t)$$
$$\Leftrightarrow\ \langle\overline{u}_y\rangle_{\mathrm{S}}(t)=\langle\overline{u}_y\rangle_{\mathrm{S}}(t=0)\cos(2\Omega^{\mathrm{F}}t) \tag{3.5}$$

Therefore, $\langle\overline{u}_y\rangle_{\mathrm{S}}(y,t)=0$ for the initial condition $\langle\overline{u}_y\rangle_{\mathrm{S}}(t=0)=0$ regardless of the value of $\langle\overline{p}\rangle_{\mathrm{S}}$. Hence, $\langle\overline{p}\rangle_{\mathrm{S}}$ and the centrifugal force do not affect the mean velocities. Obviously, $\langle\overline{p}\rangle_{\mathrm{S}}$ does not affect the velocity fluctuations. Consequently, $\langle\overline{p}\rangle_{\mathrm{S}}$ and the centrifugal force do not affect the turbulent flow in the present simulation.

3.1.3 External forcing

We obtain the confined helical forcing using the following procedure. Let us define homogeneous, isotropic, and solenoidal vector $\boldsymbol{w}$. In the wavenumber space, any solenoidal vector can be expressed as follows [Herring (1974); Cambon & Jacquin (1989)]:

$$\tilde{\boldsymbol{w}}=\xi_+\boldsymbol{N}^+ +\xi_-\boldsymbol{N}^-,\quad \boldsymbol{N}^\pm=\boldsymbol{e}^{(2)}\mp i\boldsymbol{e}^{(1)},\quad \boldsymbol{e}^{(1)}=\frac{\boldsymbol{k}\times\boldsymbol{n}}{|\boldsymbol{k}\times\boldsymbol{n}|},\quad \boldsymbol{e}^{(2)}=\frac{\boldsymbol{k}\times\boldsymbol{e}^{(1)}}{|\boldsymbol{k}\times\boldsymbol{e}^{(1)}|}, \tag{3.6}$$

where $\tilde{\boldsymbol{w}}$ denotes the Fourier coefficient of $\boldsymbol{w}$ and $\boldsymbol{n}$ denotes arbitrary vector. Here, we adopt $n_i=M_{ij}(\boldsymbol{k})\delta_{j3}$ so as to satisfy $\boldsymbol{k}\cdot\boldsymbol{n}=0$ in which $M_{ij}(\boldsymbol{k})$ is defined in Eq. (2.38). The energy and helicity spectra for $\boldsymbol{w}$, $E^w(k)$ and $E^{wH}(k)$, are respectively written as

$$\frac{E^w(k)}{4\pi k^2}=\left\langle|\xi_+|^2+|\xi_-|^2\right\rangle,\quad \frac{E^{wH}(k)}{4\pi k^2}=2k\left\langle|\xi_+|^2-|\xi_-|^2\right\rangle. \tag{3.7}$$

where

$$\frac{1}{2}\langle w_i w_i\rangle=\int_0^\infty \mathrm{d}k\ E^w(k),\quad \left\langle w_i\epsilon_{ij\ell}\frac{\partial w_\ell}{\partial x_j}\right\rangle=\int_0^\infty \mathrm{d}k\ E^{wH}(k). \tag{3.8}$$

Here, the homogeneity and isotropy for $\boldsymbol{w}$ are used. Note that there is the following inequality condition between $E^w(k)$ and $E^{wH}(k)$ referred to as the realizability condition [Moffatt (1970); Brissaud *et al.* (1973)]:

$$|E^{wH}(k)|\le 2kE^w(k). \tag{3.9}$$

We introduce the following functions [Morinishi *et al.* (2001*c*)]:

$$\zeta_\pm=\frac{1}{8\pi k^2}\left(E^w\pm\frac{E^{wH}}{2k}\right). \tag{3.10}$$

When we assume

$$\xi_+=\zeta_+^{1/2}\mathrm{e}^{2\pi i\theta},\quad \xi_-=\zeta_-^{1/2}\mathrm{e}^{2\pi i(\theta+\phi)}, \tag{3.11}$$

with the uniform random variable $\theta, \phi (\in [0,1])$, we can obtain the random vector field $\boldsymbol{w}$ which satisfies the given spectra $E^w(k)$ and $E^{wH}(k)$. Here, the spectra are determined as

$$E^w(k) \propto \begin{cases} k^{-5/3} & \text{for } 10 \leq k \leq 14, \\ 0 & \text{otherwise}, \end{cases} \tag{3.12}$$

$$E^{wH}(k) = \alpha 2 k E^w(k). \tag{3.13}$$

Here, $E^{wH}(k) \propto k^{-5/3}$ is selected corresponding to the energy spectrum of the inertial range [Kolmogorov (1941)] and α denotes the parameter for determining the intensity of helicity for the forcing. According to the realizability condition given by Eq. (3.9), $\alpha = 1(-1)$ corresponds to the maximally positive (negative) helical forcing and $\alpha = 0$ corresponds to the non-helical forcing. The random vector $\boldsymbol{r}$ confined around the $y = 0$ plane is obtained by using the stream function $\boldsymbol{\psi}$ which satisfies $\boldsymbol{w} = \boldsymbol{\nabla} \times \boldsymbol{\psi}$ and $\boldsymbol{\nabla} \cdot \boldsymbol{\psi} = 0$ as follows:

$$r_i = \epsilon_{ij\ell} \frac{\partial}{\partial x_j} [g(y) \psi_\ell], \tag{3.14}$$

where $g(y)$ is the weighting function. We adopt $g(y) = \exp[-(y/\sigma)^2]$ where $\sigma = L_y/32$. The external forcing is determined by the similar form to the Ornstein–Uhlenbeck process [Eswaran & Pope (1988); Gillespie (1996)]:

$$\overline{f}_i(t + \Delta t) = \left(1 - \frac{\Delta t}{\tau}\right) \overline{f}_i(t) + \frac{\Delta t}{\tau} r_i, \tag{3.15}$$

where Δt denotes the time step and τ is a parameter for the relaxation time of the forcing. In the simulation, $\tau = 50\Delta t$ is adopted and $\boldsymbol{r}$ is normalized as $\langle r_i r_i \rangle_{\mathrm{S}}(y = 0)/2 = 1$. Note that the x–z plane average of the external forcing is removed, $\langle \overline{\boldsymbol{f}} \rangle_{\mathrm{S}} = 0$, such that the external force does not directly excite the mean velocity. The coefficient C^{ex} is determined to satisfy $\langle \overline{u}_i' \overline{u}_i' \rangle_{\mathrm{S}}(y = 0)/2 = 1$ at each time step.

3.1.4 Simulation parameters

The box size is $L_x \times L_y \times L_z = 2\pi \times 4\pi \times 2\pi$ and the number of the grid point is $N_x \times N_y \times N_z = 128 \times 256 \times 128$. For the space discretization, the second-order finite difference scheme is adopted. For time integration, the second-order Adams–Bashforth method is adopted for all terms. The time step is set to $\Delta t = 10^{-3}$. The pressure is directly solved in the wavenumber space by using a fast Fourier transformation (FFT). Simulation parameters are shown in Table 3.1. Here, in the name of run 'rxhyy', 'x' indicates the rotation rate Ω^{F} and 'yy' indicates the parameter for the helicity injection rate α. For example, run r5h05 indicates the run in which $\Omega^{\mathrm{F}} = 5$ and $\alpha = 0.5$. Hence, run r0h0 is non-rotating and non-helical case, run r0h05 is non-rotating but helical case, run r0h05 is rotating but non-helical case, and other runs are rotating and helical cases. For rotating and helical cases, it is expected that the axial mean velocity is generated according to Yokoi & Brandenburg (2016). We can examine the effect of the helicity injection rate on the mean velocity generation by comparing runs r5h01, r5h02, and r5h05. We

Table 3.1: Parameters for the simulation of the mean velocity generation phenomenon.

Run	$\Omega^{\rm F}$	α	$L^{\rm GS}/\overline{\Delta}$	${\rm Ro}^{\rm GS}$
r0h0	0	0	10.3	∞
r0h05	0	0.5	11.1	∞
r5h0	5	0	11.0	0.185
r5h01	5	0.1	11.2	0.182
r5h02	5	0.2	11.2	0.182
r1h05	1	0.5	11.1	0.917
r2h05	2	0.5	11.1	0.459
r5h05	5	0.5	12.3	0.166

can examine the effect of the rotation rate by comparing runs r1h05, r2h05, and r5h05. The GS length scale $L^{\rm GS}$ and the GS Rossby number ${\rm Ro}^{\rm GS}$ are respectively defined as

$$L^{\rm GS} = \frac{(K_0^{\rm GS})^{3/2}}{\varepsilon_0^{\rm SGS}}, \quad {\rm Ro}^{\rm GS} = \frac{\varepsilon_0^{\rm SGS}}{K_0^{\rm GS} 2\Omega^{\rm F}}, \tag{3.16}$$

where $K^{\rm GS} = \langle \overline{u}_i' \overline{u}_i' \rangle/2$, $K_0^{\rm GS} = K^{\rm GS}(y=0)$, $\varepsilon^{\rm SGS} = 2\langle \nu^{\rm sgs} \overline{s}_{ij} \overline{s}_{ij}' \rangle$, $\varepsilon_0^{\rm SGS} = \varepsilon^{\rm SGS}(y=0)$, and $\langle\rangle$ denotes the average over the x–z plane and time. The time average is taken over $20 \le t \le 30$ as mentioned later. According to the Taylor's dissipation law [Taylor (1935)], $L^{\rm GS}$ represents the integral length scale, so that the present simulation resolves the integral scale eddies by about 10 grids. The size of the integral scale eddy is estimated as $L^{\rm GS} = 0.5$–0.6, while the width of the forcing region is $2\sigma = 0.785$ and the width of the turbulence region is $2\ell^\nabla = 0.8$ where ℓ^∇ is defined such that $K^{\rm GS}(y=\ell^\nabla) = K_0^{\rm GS}/{\rm e}$. Hence, the width of the turbulence region is 1.5 times as wide as the integral scale eddy. Since $K^{\rm GS}/\varepsilon^{\rm SGS}$ represents the time scale of the energetic GS turbulent eddies, the GS Rossby number given by Eq. (3.16) represents the ratio of the rotation time scale $(2\Omega^{\rm F})^{-1}$ to the GS turbulence time scale $K^{\rm GS}/\varepsilon^{\rm SGS}$ at $y=0$. Namely, the effect of rotation is large for low-Rossby-number flows. For the cases in which the turbulent helicity is injected, $\alpha = 0.1$, 0.2, or 0.5 is adopted. The reason why we do not use the maximally helical forcing is to avoid the hindering effect on the energy cascade suggested by Stepanov *et al.* (2015) and Kessar *et al.* (2015). It should be noted that the mean velocity is set to zero at the initial condition and the plane average of the external forcing is also zero as mentioned previously.

3.2 Results of the simulation of the mean velocity generation

3.2.1 Time evolution of statistical quantities

Figure 3.2 shows the time evolution of the GS turbulent energy $\langle \overline{u}_i' \overline{u}_i' \rangle_{\rm S}/2$ for runs r0h0, r0h05, r5h0, and r5h05. Here, $\overline{q}'$ denotes the GS fluctuation value around $\langle \overline{q} \rangle_{\rm S}$. Owing to the spatially confined forcing, the spatially confined distribution of the turbulent energy is established at $|y| < 0.4 (\simeq \sigma)$. For all runs, the turbulent energy reaches almost statistically steady state at the later stage. Figure 3.3 shows the time

evolution of the GS turbulent helicity $\langle \overline{u}_i' \overline{\omega}_i' \rangle_S$ for runs r0h0, r0h05, r5h0, and r5h05. The statistically clear distribution of the turbulent helicity is not observed for run r0h0 and r5h0 since the turbulent helicity is not injected by the external forcing, that is $\alpha = 0$. On the other hand, for runs r0h05 and r0h05, the positive turbulent helicity is clearly established and sustained at $|y| < 0.4$ as is the case of the turbulent energy shown in Fig. 3.2.

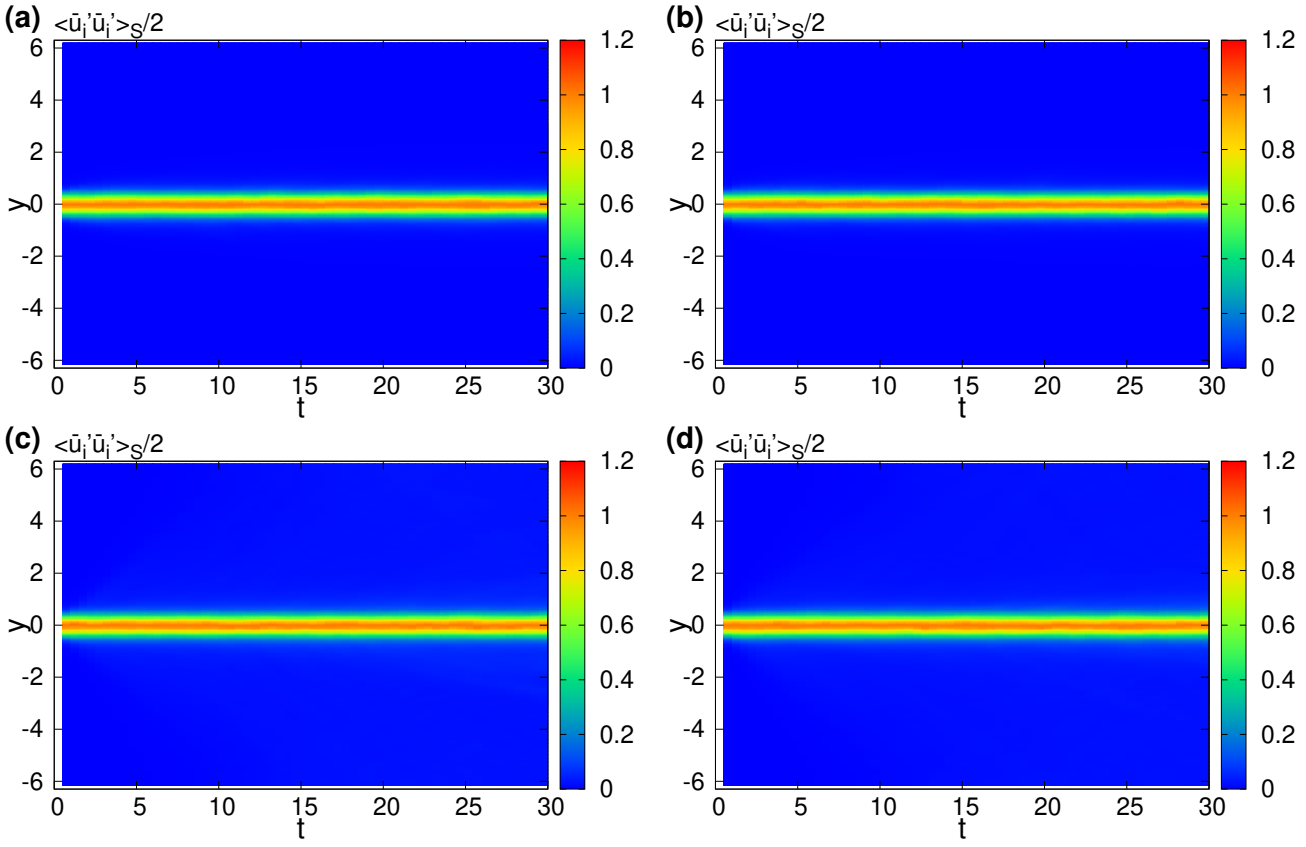

Figure 3.2: Time evolution of the GS turbulent energy for runs (a) r0h0, (b) r0h05, (c) r5h0, and (d) r5h05.

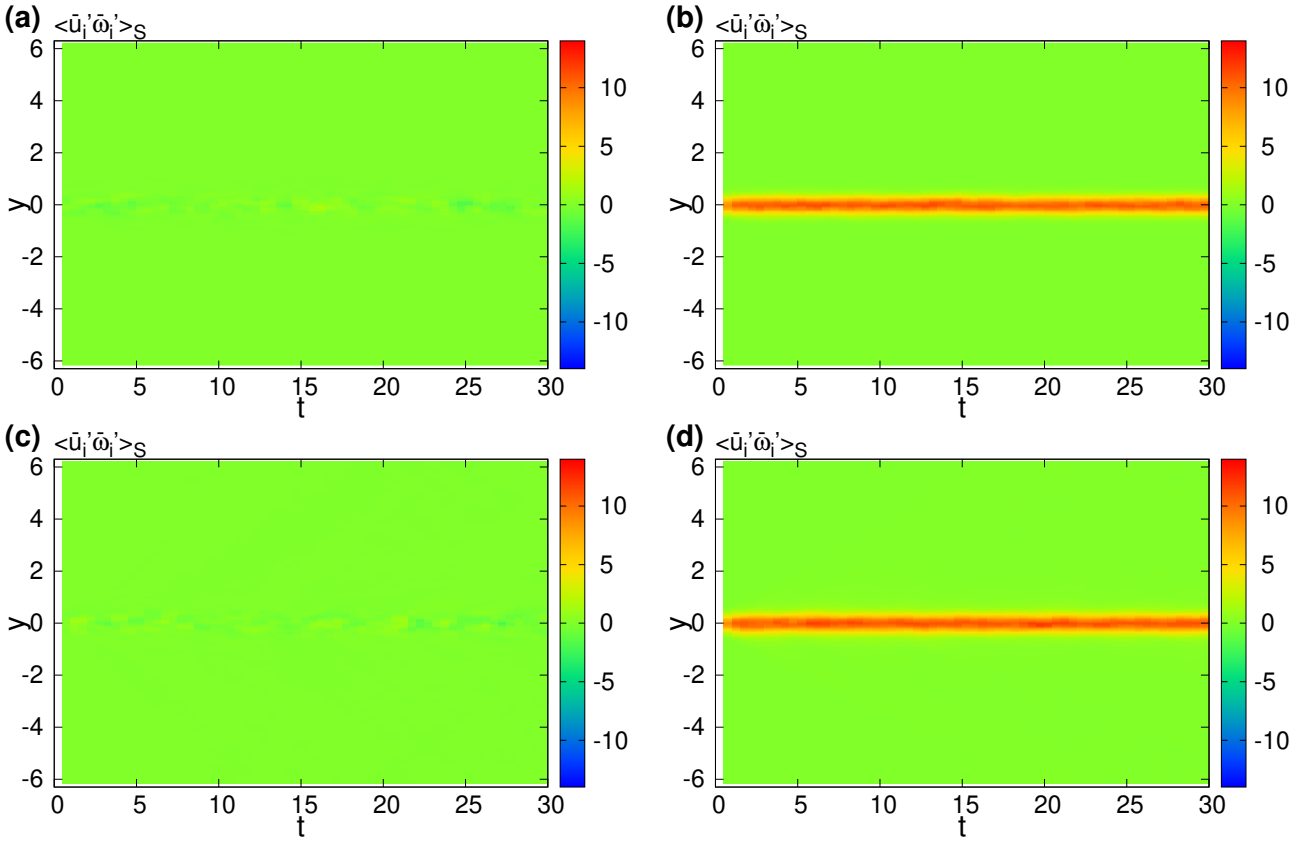

Figure 3.3: Time evolution of the GS turbulent helicity for runs (a) r0h0, (b) r0h05, (c) r5h0, and (d) r5h05.

3.2.2 Time averaged turbulence statics

As seen in Figs. 3.2 and 3.3, the x–z plane averaged quantities are almost statistically steady at the later stage. Hereafter, we take the average over $20 \leq t \leq 30$ as well as the x–z plane, and this average is denoted as $\langle\rangle$.

Figure 3.4 shows the spatial distribution of the GS turbulent energy $K^{\rm GS}(= \langle \overline{u}_i' \overline{u}_i' \rangle/2)$. Comparing the results between runs r0h0 and r0h05 or between other rotating runs in Fig. 3.4(a), the distribution of $K^{\rm GS}$ is not so changed by the helicity injection rates. The spatial distribution of $K^{\rm GS}$ is slightly broader for rotating cases (runs r5h0, r5h01, r5h02, and r5h05) than the non-rotating cases (runs r0h0 and r0h05). Figure 3.4(b) shows the comparison of the GS turbulent energy between the rotation rates with the same helicity injection rate. Although the spatial distribution of the GS turbulent energy becomes broad as the rotation rate increases, the difference is not so large. Figure 3.5 shows the spatial distribution of the GS turbulent helicity $H^{\rm GS}(= \langle \overline{u}_i' \overline{\omega}_i' \rangle)$. As seen in the results for runs r0h0 and r5h05 in Fig 3.5(a), the GS turbulent helicity is not generated solely by the rotation in this simulation, so that $H^{\rm GS} = 0$ for runs

r0h0 and r5h0. Comparing the results between runs r5h01, r5h02, r5h05 in Fig. 3.5(a), it is seen that the intensity of $H^{\rm GS}$ at $y = 0$ is almost linear to the parameter for the helicity injection rate α. As seen in Fig. 3.5(b), the spatial distribution and the intensity of the turbulent helicity are not so changed by the rotation rates although the spatial distribution is slightly broad for the strongly rotating case as is seen for the turbulent energy $K^{\rm GS}$ (Fig. 3.4).

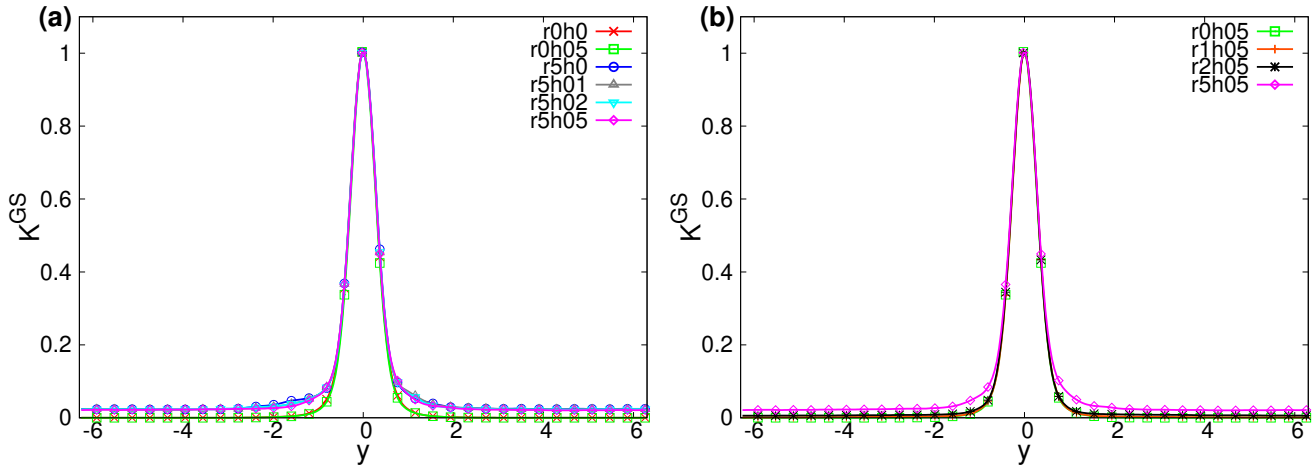

Figure 3.4: Spatial distribution of the GS turbulent energy $K^{\rm GS}$. (a) Comparison between the helicity injection rates and (b) between the rotation rates with the same helicity injection rate.

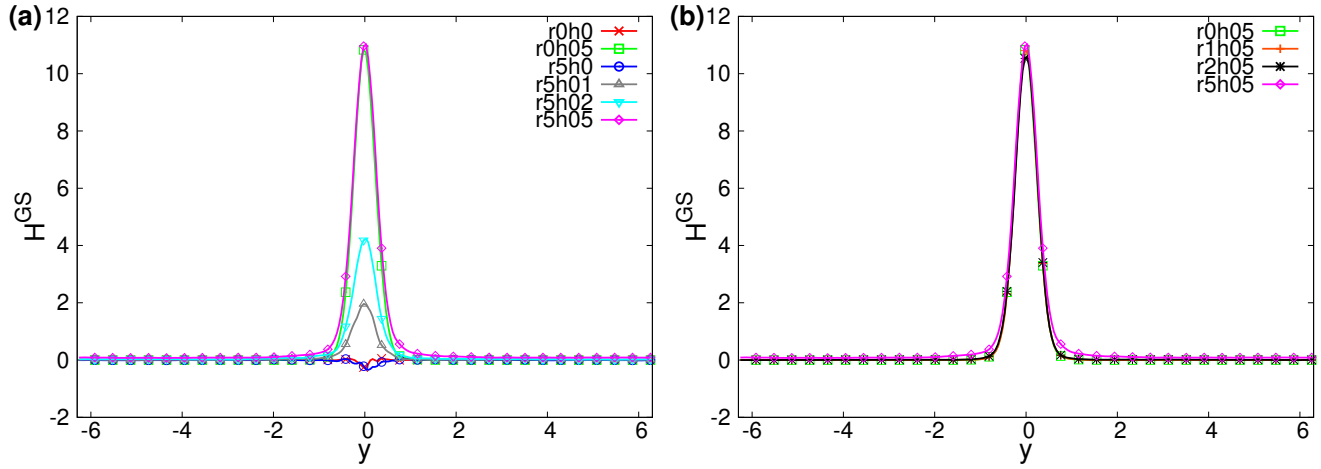

Figure 3.5: Spatial distribution of the GS turbulent helicity $H^{\rm GS}$. (a) Comparison between the helicity injection rates and (b) between the rotation rates with the same helicity injection rate.

In order to see the anisotropy of turbulence in this simulation, we investigate the GS anisotropy tensor which is defined as

$$b_{ij}^{\mathrm{GS}} = \frac{R_{ij}^{\mathrm{GS}}}{K^{\mathrm{GS}}} - \frac{2}{3}\delta_{ij}. \tag{3.17}$$

The anisotropy tensor satisfies the following inequality condition [Schumann (1977); Hanjalić & Launder (2011)]

$$-\frac{2}{3} \le b_{\alpha\alpha}^{\mathrm{GS}} \le \frac{4}{3}, \quad -1 \le b_{\alpha\beta}^{\mathrm{GS}} \le 1, \tag{3.18}$$

where summation is not taken for the Greek indices. Figures 3.6(a) and (b) respectively show the spatial distribution of the GS anisotropy tensor for runs r0h0 and r5h05. Note that the range of the y is limited to $-2 \le y \le 2$ since we concern the anisotropy around the region in which the turbulent energy is intense. It is seen that b_{yy}^{GS} becomes large as it leaves away from $y = 0$ for run r0h0, while such anisotropy is decreased for run r5h05. Hence, the turbulence field is nearly isotropic for run r5h05.

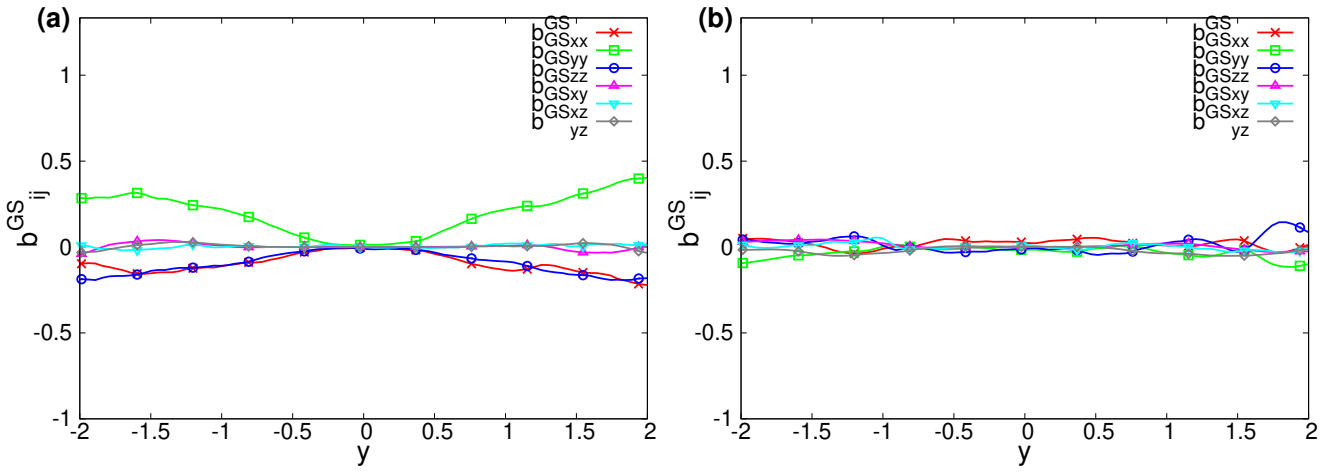

Figure 3.6: Spatial distribution of the GS anisotropy tensor b_{ij}^{GS} for runs (a) r0h0 and (b) r5h05.

Here, we investigate the budget for the GS turbulent energy transport. The transport equation for the GS turbulent energy is written as follows:

$$\frac{\partial K^{\mathrm{GS}}}{\partial t} = P^{K,\mathrm{GS}} - \varepsilon^{\mathrm{SGS}} + \Pi^{K,\mathrm{GS}} + T^{K,\mathrm{GS}} + D^{K,\mathrm{SGS}} + F^{K,\mathrm{GS}}, \tag{3.19}$$

where $P^{K,\mathrm{GS}}$ denotes the GS production rate, $\varepsilon^{\mathrm{SGS}}$ the SGS viscous dissipation rate, $\Pi^{K,\mathrm{GS}}$ the GS pressure diffusion, $T^{K,\mathrm{GS}}$ the GS turbulent diffusion, $D^{K,\mathrm{SGS}}$ the SGS viscous diffusion, and $F^{K,\mathrm{GS}}$ the

GS external work. In the present simulation, they are respectively written as

$$P^{K,\mathrm{GS}} = -R^{\mathrm{GS}}_{xy}\frac{\partial U_x}{\partial y} - R^{\mathrm{GS}}_{yz}\frac{\partial U_z}{\partial y}, \tag{3.20a}$$

$$\varepsilon^{\mathrm{SGS}} = 2\left\langle \nu^{\mathrm{sgs}}\overline{s}_{ij}\overline{s}'_{ij}\right\rangle, \tag{3.20b}$$

$$\Pi^{K,\mathrm{GS}} = -\frac{\partial}{\partial y}\left\langle \overline{u}'_y\overline{p}'\right\rangle, \tag{3.20c}$$

$$T^{K,\mathrm{GS}} = -\frac{\partial}{\partial y}\left\langle \overline{u}'_y\frac{1}{2}\overline{u}'_i\overline{u}'_i\right\rangle, \tag{3.20d}$$

$$D^{K,\mathrm{SGS}} = \frac{\partial}{\partial y}\left\langle 2\nu^{\mathrm{sgs}}\overline{s}_{iy}\overline{u}'_i\right\rangle, \tag{3.20e}$$

$$F^{K,\mathrm{GS}} = \left\langle \overline{u}'_i\overline{f}'_i\right\rangle, \tag{3.20f}$$

where $R^{\mathrm{GS}}_{ij}(=\langle\overline{u}'_i\overline{u}'_j\rangle)$ denotes the GS Reynolds stress and $\boldsymbol{U}=\langle\overline{\boldsymbol{u}}\rangle$. Budgets for the GS turbulent energy for runs r0h0 and r5h05 are respectively shown in Figs. 3.7(a) and (b). Here, the range of the y is limited to $-2\le y\le 2$ since the GS turbulent energy is dominant at this region as shown in Fig. 3.4. Overall profiles for the right-hand side of Eq. (3.19) are not changed between runs r0h0 and r5h05 although the value of $\varepsilon^{\mathrm{SGS}}$ is smaller for run r5h05 than run r0h0. The turbulent energy is injected by the external work term. About 80% of the injected energy is lost by the SGS viscous dissipation at $y=0$ and the resultant is transferred to $|y|>0.3$ mainly by the GS turbulent diffusion. The decrease of $\varepsilon^{\mathrm{SGS}}_0$ is observed in the presence of either the helicity injection or the system rotation as seen in $L^{\mathrm{GS}}/\overline{\Delta}[\propto(\varepsilon^{\mathrm{SGS}}_0)^{-1}]$ in Table 3.1; namely, the value of L^{GS} for runs r0h05 or r5h0 is larger than that for run r0h0. Note that $K^{\mathrm{GS}}(y=0)=1$ as shown in Fig. 3.4 since the intensity of the external forcing is determined so as to satisfy $K^{\mathrm{GS}}(y=0)=1$. The decrease of the SGS viscous dissipation rate is considered to be related to the reduction of energy cascade due to helicity [André & Lesieur (1977); Morinishi *et al.* (2001*c*); Linkmann (2018); Stepanov *et al.* (2015); Kessar *et al.* (2015)] or the rotation [Bardina *et al.* (1985); Cambon & Jacquin (1989); Morinishi *et al.* (2001*a*)]. The details for these mechanisms in the present simulation are beyond the scope of the present study since we focus on the effect of the turbulent helicity on the mean velocity generation phenomenon or the Reynolds stress transport. As seen in Fig. 3.4, the spatial distribution of the turbulent energy K^{GS} in the rotating cases is broader than that in the non-rotating cases. Figure 3.8(a) shows the budget for the GS turbulent energy focusing on the outer region at $|y|>2$ for run r5h05. Here, the dominant terms are only plotted. As seen in Fig. 3.8(a), the GS pressure diffusion is positive at $|y|>2$ and it almost balances with the SGS viscous dissipation rate $\varepsilon^{\mathrm{SGS}}$ there. However, the GS turbulent diffusion $T^{K,\mathrm{GS}}$ is negligible at $|y|>2$. Note that $\int_{-L_y/2}^{L_y/2}\mathrm{d}y\Pi^{K,\mathrm{GS}}=0$ by definition. Hence, it is seen that the GS turbulent energy is transferred to the outer region at $|y|>2$ by the GS pressure diffusion $\Pi^{K,\mathrm{GS}}$. Figure 3.8(b) shows the spatial distribution of the GS pressure diffusion for each run. This figure suggests that this energy transfer due to $\Pi^{K,\mathrm{GS}}$ does not depend on the helicity injection rate but depend on the rotation rate.

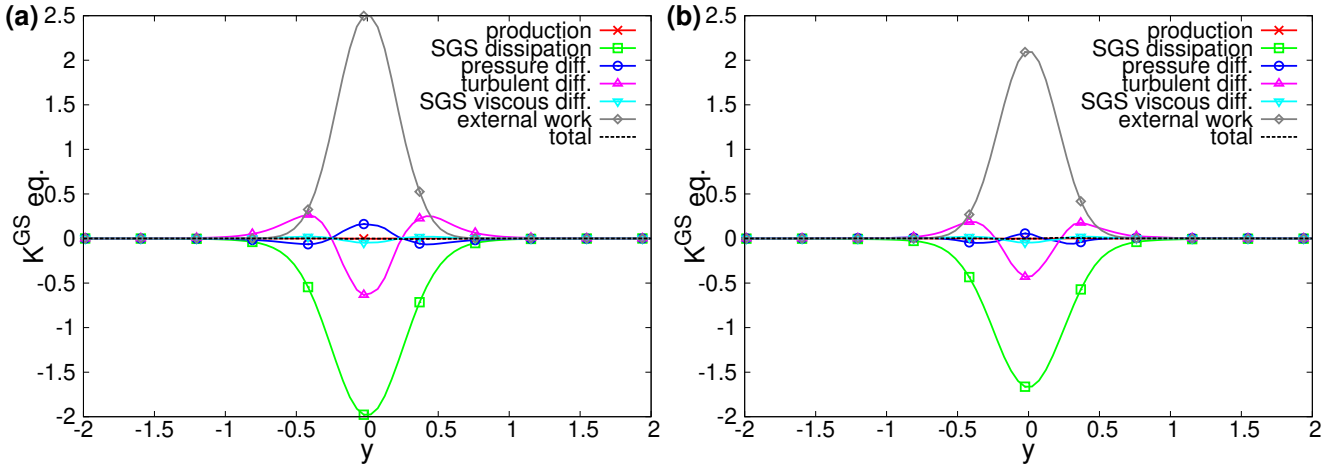

Figure 3.7: Budget for the GS turbulent energy given by Eq. (3.17) for runs (a) r0h0 and (b) r5h05.

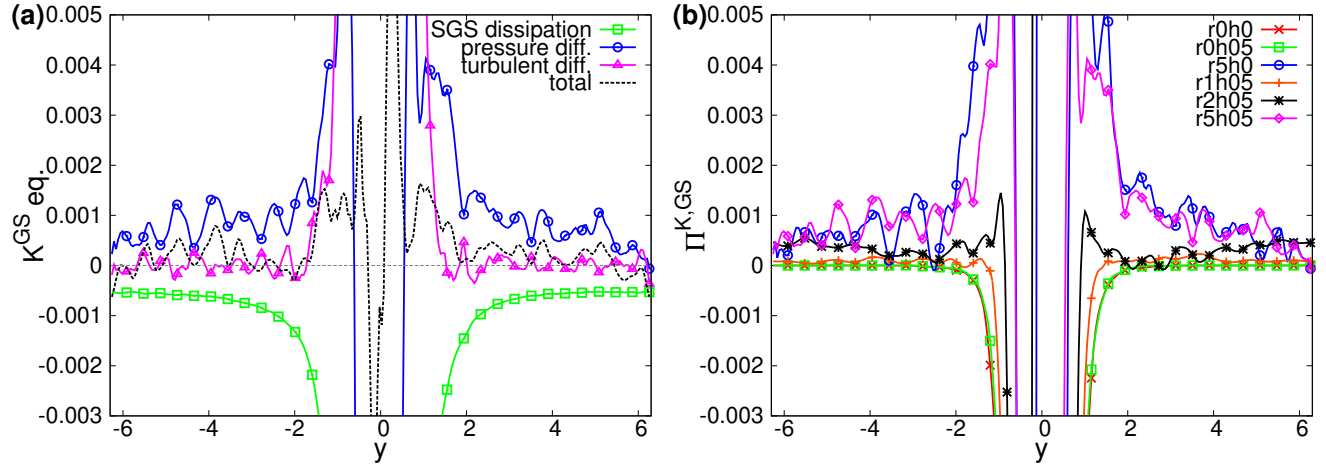

Figure 3.8: (a) Budget for the GS turbulent energy focusing on the outer region at $|y| > 2$ for run r5h05. Here, the dominant terms are only plotted. (b) Spatial distribution of the GS pressure diffusion $\Pi^{K,\mathrm{GS}}$ for each run.

3.2.3 Mean velocity in the direction of the rotation axis

Now we investigate the mean velocity generation phenomenon. Figure 3.9 shows the time evolution of the mean velocity in the direction of the rotation axis $\langle \overline{u}_x \rangle_{\rm S}$ for runs r0h0, r0h05, r5h0, and r5h05. It is clearly seen that the positive axial mean velocity is generated and sustained for run r5h05, while such a mean velocity profile is not observed for runs r0h0, r0h05, and r5h0. It should be noted again that the x–z plane average of the external forcing is removed, $\langle \overline{\boldsymbol{f}} \rangle_{\rm S} = 0$. Since the kinematic viscosity is neglected in this simulation, the equation for the plane averaged axial velocity reads

$$\frac{\partial \langle \overline{u}_x \rangle_{\rm S}}{\partial t} = -\frac{\partial R^{\rm S}_{xy}}{\partial y} \tag{3.21}$$

where $R^{\rm S}_{xy} = \langle \overline{u}'_x \overline{u}'_y \rangle_{\rm S} - 2\langle \nu^{\rm sgs} \overline{s}_{xy} \rangle_{\rm S}$. Therefore, this axial mean velocity is generated by the effect of the Reynolds stress $R^{\rm S}_{xy}$. Note again that the axial mean velocity is generated and sustained for run r5h05 in which the system is rotating and the turbulent helicity is injected, while such a phenomenon is not observed for runs r0h0, r0h05, and r5h0. This result suggests that neither the helicity injection nor the system rotation by themselves are sufficient to generate the Reynolds stress $R^{\rm S}_{xy}$ which generates the positive axial mean velocity. Here, the sign of the generated mean velocity for run r5h05 is consistent with the result of Yokoi & Brandenburg (2016); namely, the positive mean velocity is generated at positively helical region.

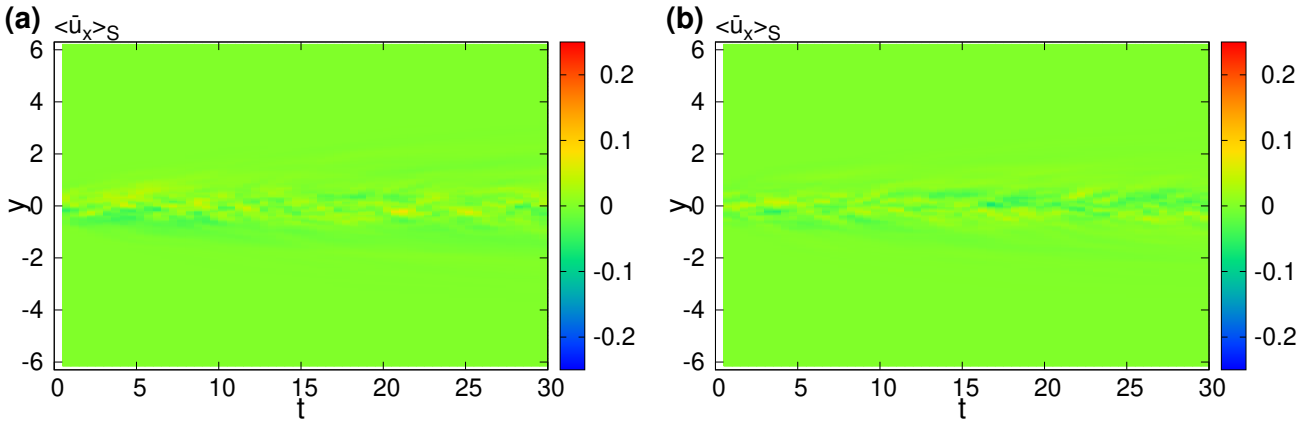

Figure 3.9: Time evolution of the axial mean velocity for runs (a) r0h0 and (b) r0h05.

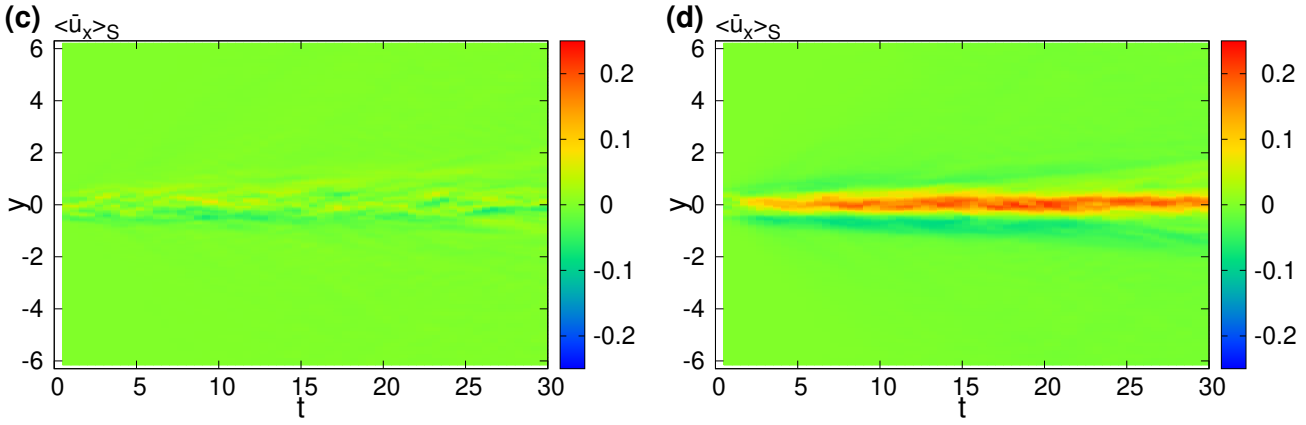

Figure 3.9: (continued) Time evolution of the axial mean velocity for runs (c) r5h0 and (d) r5h05.

Figure 3.10 shows the spatial distribution of the axial mean velocity $U_x(=\langle\overline{u}_x\rangle)$ for each run. In Fig. 3.10(a), the positive axial mean velocity is observed at $y = 0$ for run r5h05 in which the system is rotating and the turbulent helicity is injected, while the axial mean velocity is negligible for runs r0h0, r0h05, and r5h0 as already seen in Fig. 3.9. Note that the volume averaged momentum should be conserved; namely, $\int_{-L_y/2}^{L_y/2} \mathrm{d}y\ U_x = 0$ in this simulation in which the initial condition of the volume averaged momentum and the volume averaged external forcing are zero. Hence, the generation of the positive U_x around $y = 0$ suggests the generation of the negative U_x in its surroundings. In fact, the sign of U_x at $|y| > 0.5$ is negative for run r5h05 in which the positive U_x is generated at $|y| < 0.5$ as shown in Fig. 3.10. For run r5h05, the profile of the axial mean velocity is slightly asymmetric about $y = 0$ although it is expected to be symmetric about $y = 0$ when the statistical averaging is sufficient. This asymmetric profile is considered to be caused by the limitation of time or statistical average. However, this small asymmetry does not affect the essence of the following discussion. As seen in Fig. 3.10(b), the peak value of the generated mean velocity at $y = 0$ is almost linear to the helicity injection rate and the rotation rate; namely, when we denote the peak value of U_x at $y = 0$ for run rxhyy as U_0^{rxhyy}, it is roughly evaluated as $U_0^{\mathrm{r1h05}} : U_0^{\mathrm{r5h01}} : U_0^{\mathrm{r2h05}} : U_0^{\mathrm{r5h02}} : U_0^{\mathrm{r5h05}} = 1 : 1 : 2 : 2 : 5$. Since the peak value of the turbulent helicity at $y = 0$ is linear to the helicity injection rate and does not depend on the rotation rate as seen in Fig. 3.5, it is understood that the peak value of the generated axial mean velocity at $y = 0$ is linear to the turbulent helicity and the rotation rate. This result suggests that the estimation for the mean velocity given by Eq. (2.82), which is the simplified solution of the helicity model, is qualitatively good.

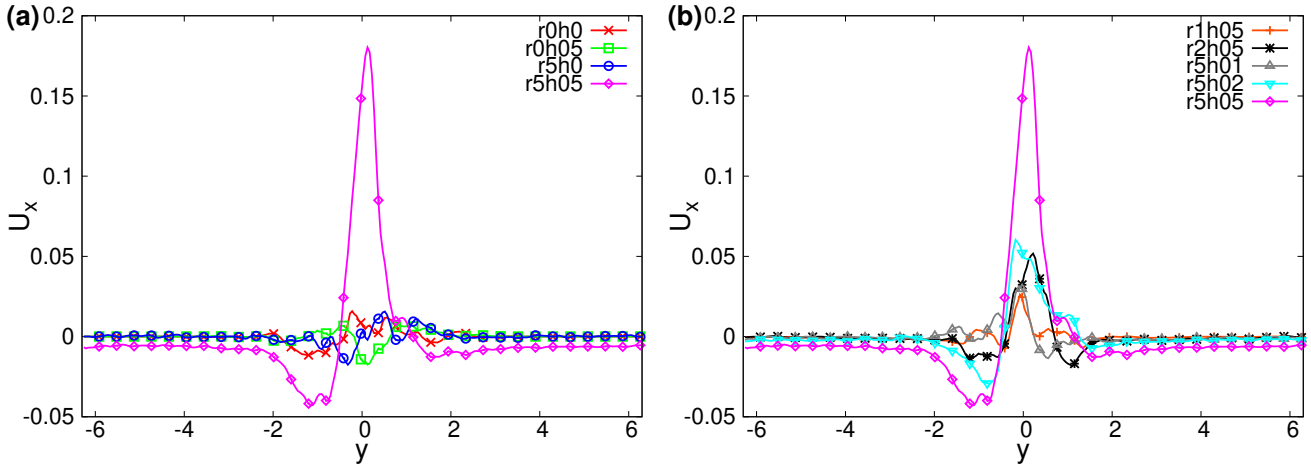

Figure 3.10: Spatial distribution of the axial mean velocity U_x. (a) Comparison between the presence or absence of the helicity injection and the rotation and (b) between the helicity injection rates and the rotation rates.

3.2.4 Shortfall of the eddy-viscosity model

Here, we evaluate the validity of the eddy-viscosity model given by Eq. (2.44). In the present simulation configuration, the axial mean velocity equation in the statistically steady state reads

$$\frac{\partial U_x}{\partial t} = -\frac{\partial R_{xy}}{\partial y} = 0, \tag{3.22}$$

where $R_{xy}(= R_{xy}^{\rm GS} - 2\langle \nu^{\rm sgs}\overline{s}_{xy}\rangle)$ denotes the exact Reynolds stress. Since the Reynolds stress vanishes at the edge of the boundary, $y = \pm L_y/2$, the solution of Eq. (3.22) is $R_{xy} = 0$. The green line with squares in Fig. 3.11 shows the spatial distribution of R_{xy} for run r5h05. It is confirmed that R_{xy} is nearly equal to zero although it is not exactly equal to zero at $y = 0$ due to the insufficiency of the time averaging for achieving the statistically steady state. The eddy-viscosity model given by Eq. (2.44) is written as

$$R_{xy} = -\nu^{\rm T}\frac{\partial U_x}{\partial y}, \tag{3.23}$$

where $\nu^{\rm T}$ is given by Eq. (2.45). The red line with crosses in Fig. 3.11 shows the prediction of R_{xy} by the eddy-viscosity model. Here, $\nu^{\rm T}$ is evaluated as $\nu^{\rm T} = C_\nu (K^{\rm GS})^2/\varepsilon^{\rm SGS}$ with $C_\nu = 0.09$. It is clearly seen that the eddy-viscosity model predicts excessively high non-zero value around $y = 0$. Namely, the eddy-viscosity model is inconsistent with the analytical solution $R_{xy} = 0$ or the numerical result shown in the green line with squares in Fig. 3.11. In other words, if we try to predict this sustainment of the mean velocity profile by using the eddy-viscosity model, the velocity gradient must vanish in order to satisfy the analytical solution $R_{xy} = 0$ since $\nu^{\rm T} \neq 0$ in Eq. (3.23) around $y = 0$, leading to the trivial solution $U_x = 0$. Therefore, the eddy-viscosity model cannot predict the sustainment of the axial mean velocity

generated at $y = 0$. This inadequacy of the eddy-viscosity model can be overcome by adding another term N_{xy} to the eddy-viscosity model as

$$R_{xy} = -\nu^{\mathrm{T}} \frac{\partial U_x}{\partial y} + N_{xy}, \tag{3.24}$$

in which N_{xy} should have negative gradient at $y = 0$ so as to counterbalance the eddy-viscosity term. If N_{xy} has the negative gradient at $y = 0$ regardless of the presence of the mean velocity gradient, the Reynolds stress can be estimated as $R_{xy} = N_{xy}$ at the initial stage of the present simulation in which the mean velocity gradient is zero so that the first term on the right-hand side of Eq. (3.24) vanishes. In such a case, R_{xy} has negative gradient at $y = 0$ and it has positive contribution to the mean velocity equation there; namely, the positive axial mean velocity at $y = 0$ is increased. In this sense, the term which has negative gradient at $y = 0$ such as N_{xy} not only counterbalances the eddy-viscosity term but also generates the positive axial mean velocity at $y = 0$ when the mean velocity is zero in which the eddy-viscosity term is zero. Namely, N_{xy} is also the source of the mean velocity generation. As discussed previously in connection to Fig. 3.10(b), the peak value of the generated axial mean velocity at $y = 0$ is almost linear to the turbulent helicity and the rotation rate. This fact suggests that N_{xy} should be also linear to the turbulent helicity and the rotation rate. In this sense, the helicity model given by Eq. (2.76) is a good candidate. However, the mechanism that the turbulent helicity affects the Reynolds stress is unclear. In the following section, we discuss the appropriate expression of N_{xy} for the mean velocity generation observed in the present simulation in terms of the Reynolds stress transport.

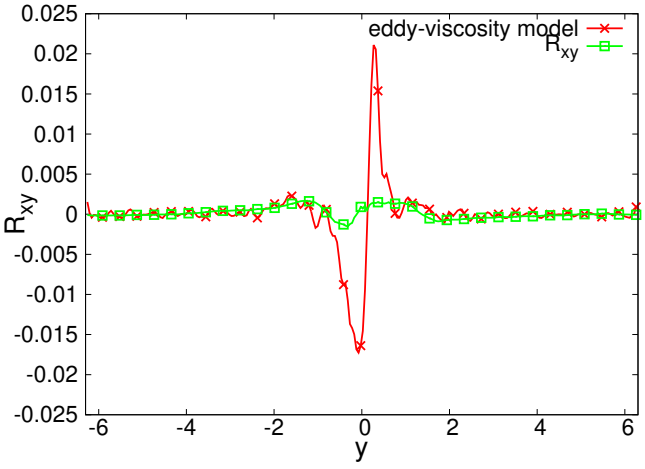

Figure 3.11: Evaluation of the eddy-viscosity model for run r5h05.

3.3 Investigation of the Reynolds stress transport

3.3.1 Budget for the Reynolds stress transport

In order to investigate the effect different from the eddy viscosity on the Reynolds stress, we examine the budget for the GS Reynolds stress transport. R_{ij}^{GS} does not exactly correspond to the Reynolds stress $R_{ij}(= R_{ij}^{\mathrm{GS}} - \langle \nu^{\mathrm{sgs}} \overline{s}_{ij} \rangle)$ owing to the SGS viscosity term $\langle \nu^{\mathrm{sgs}} \overline{s}_{ij} \rangle$. Since the SGS viscosity term is expected to decrease the generated axial mean velocity due to the SGS viscosity, we focus on R_{xy}^{GS}. The transport equation for R_{xy}^{GS} in the present simulation is written as follows:

$$\frac{\partial R_{xy}^{\mathrm{GS}}}{\partial t} = P_{xy}^{\mathrm{GS}} - \varepsilon_{xy}^{\mathrm{SGS}} + \Phi_{xy}^{\mathrm{GS}} + \Pi_{xy}^{\mathrm{GS}} + T_{xy}^{\mathrm{GS}} + D_{xy}^{\mathrm{SGS}} + Co_{xy}^{\mathrm{GS}} + F_{xy}^{\mathrm{GS}}, \tag{3.25}$$

where P_{xy}^{GS} denotes the GS production rate, $\varepsilon_{xy}^{\mathrm{SGS}}$ the SGS viscous destruction rate, Φ_{xy}^{GS} the GS pressure–strain correlation, Π_{xy}^{GS} the GS pressure diffusion, T_{xy}^{GS} the GS turbulent diffusion, D_{xy}^{SGS} the SGS viscous diffusion, Co_{xy}^{GS} the GS Coriolis effect, and F_{xy}^{GS} the GS external work. They are defined as follows:

$$P_{xy}^{\mathrm{GS}} = -\frac{2}{3} K^{\mathrm{GS}} \frac{\partial U_x}{\partial y} - B_{yy}^{\mathrm{GS}} \frac{\partial U_x}{\partial y}, \tag{3.26a}$$

$$\varepsilon_{xy}^{\mathrm{SGS}} = 2 \left\langle \nu^{\mathrm{sgs}} \left(\overline{s}_{x\ell} \frac{\partial \overline{u}'_y}{\partial x_\ell} + \overline{s}_{y\ell} \frac{\partial \overline{u}'_x}{\partial x_\ell} \right) \right\rangle, \tag{3.26b}$$

$$\Phi_{xy}^{\mathrm{GS}} = 2 \left\langle \overline{p}' \overline{s}'_{xy} \right\rangle, \tag{3.26c}$$

$$\Pi_{xy}^{\mathrm{GS}} = -\frac{\partial}{\partial y} \left\langle \overline{u}'_x \overline{p}' \right\rangle, \tag{3.26d}$$

$$T_{xy}^{\mathrm{GS}} = -\frac{\partial}{\partial y} \left\langle (\overline{u}'_y)^2 \overline{u}'_x \right\rangle, \tag{3.26e}$$

$$D_{xy}^{\mathrm{SGS}} = \frac{\partial}{\partial y} \left\langle 2\nu^{\mathrm{sgs}} \left(\overline{s}_{xy} \overline{u}'_y + \overline{s}_{yy} \overline{u}'_x \right) \right\rangle, \tag{3.26f}$$

$$Co_{xy}^{\mathrm{GS}} = 2 R_{xz}^{\mathrm{GS}} \Omega^{\mathrm{F}}, \tag{3.26g}$$

$$F_{xy}^{\mathrm{GS}} = \left\langle \overline{u}'_x \overline{f}'_y + \overline{u}'_y \overline{f}'_x \right\rangle, \tag{3.26h}$$

where $B_{ij}^{\mathrm{GS}} = R_{ij}^{\mathrm{GS}} - 2K^{\mathrm{GS}} \delta_{ij}/3$. Figure 3.12 shows the budget for R_{xy}^{GS} for run r5h05. It is clearly seen that the GS pressure–strain correlation Φ_{xy}^{GS} and the GS pressure diffusion Π_{xy}^{GS} have significant contribution. The GS production and the GS pressure–strain correlation terms have positive gradient around $y = 0$, while the GS pressure diffusion and the GS Coriolis effect terms have negative gradient there. When R_{xy} has positive gradient around $y = 0$, it has negative contribution to the mean velocity equation there according to Eq. (3.22); namely, the positive axial mean velocity around $y = 0$ is decreased. On the other hand, when R_{xy} has negative gradient around $y = 0$, it has positive contribution to the mean velocity equation there; namely, the positive axial mean velocity around $y = 0$ is increased. In this sense, on the right-hand side of Eq. (3.25), the terms which have positive gradient around $y = 0$ intend to decrease the

generated mean velocity, while the terms which have negative gradient around $y = 0$ intend to sustain the generated mean velocity. In fact, the GS production term has positive gradient around $y = 0$ and this term corresponds to the eddy-viscosity model as discussed in Sec. 2.3.4. Hence, the pressure diffusion and the Coriolis effect terms are the candidate for N_{xy} in Eq. (3.24) which is balanced with the eddy-viscosity term. Note that the sum of $\Phi_{xy}^{\rm GS}$ and $\Pi_{xy}^{\rm GS}$ does not vanish but still has negative gradient around $y = 0$ like $\Pi_{xy}^{\rm GS}$ as shown in Fig. 3.12(b). Figures 3.13(a) and (b) respectively show the spatial distribution of the GS pressure diffusion and the GS Coriolis effect terms for each run. As seen in Fig. 3.13(a), the pressure diffusion $\Pi_{xy}^{\rm GS}$ depends almost linearly on the helicity injection rate and the rotation rate; namely, the peak value of $\Pi_{xy}^{\rm GS}$ at $|y| = 0.3$ changes linearly in the value of $\Omega^{\rm F}$ and α. This fact suggests that $\Pi_{xy}^{\rm GS}$ can be described linearly in the turbulent helicity and the rotation rate. In Fig. 3.13(b), however, the Coriolis effect $Co_{xy}^{\rm GS}$ does not exhibit such a clear dependence on the rotation rate or the helicity injection rate. Since N_{xy} is expected to be linear to the turbulent helicity and the rotation rate as discussed in Sec. 3.2.4, the pressure diffusion term $\Pi_{xy}^{\rm GS}$ is an appropriate candidate for the origin of N_{xy}.

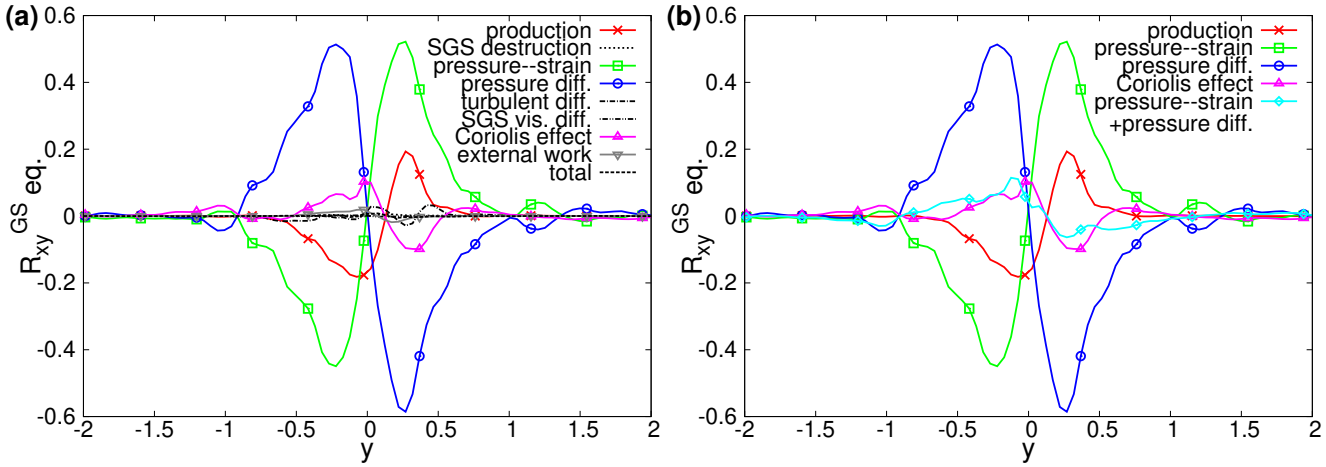

Figure 3.12: Budget for the transport equation for $R_{xy}^{\rm GS}$ for run r5h05. All terms are plotted in (a), while leading terms and the sum of $\Phi_{xy}^{\rm GS}$ and $\Pi_{xy}^{\rm GS}$ are plotted in (b).

3.3.2 Analysis on the pressure diffusion term

The Poisson equation for the GS pressure fluctuation is written as

$$\nabla^2\overline{p}' = -2\overline{s}'_{ij}S_{ij} + \overline{\omega}'_i\Omega_i + \overline{\omega}'_x 2\Omega^{\rm F} - \overline{s}'_{ij}\overline{s}'_{ij} + \frac{1}{2}\overline{\omega}'_i\overline{\omega}'_i + \frac{\partial^2}{\partial x_i \partial x_j}\left[2\left(\nu^{\rm sgs}\overline{s}_{ij} - \langle\nu^{\rm sgs}\overline{s}_{ij}\rangle\right)\right]. \tag{3.27}$$

In order to investigate the pressure diffusion term, we approximate the Laplacian of the pressure as

$$\nabla^2\overline{p}' \simeq -(\ell^p)^{-2}\overline{p}', \tag{3.28}$$

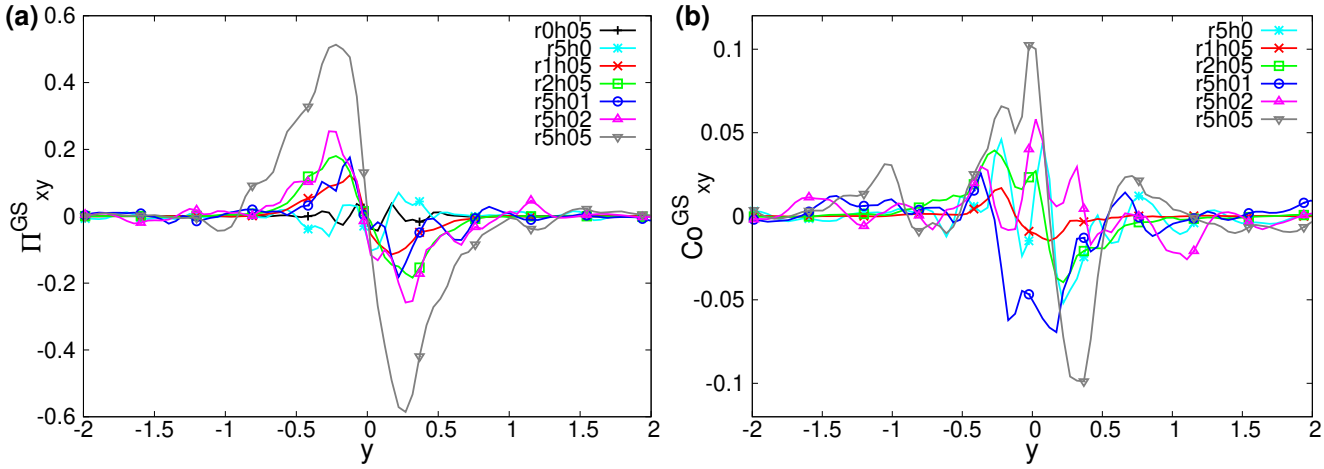

Figure 3.13: Spatial distribution of (a) the GS pressure diffusion Π_{xy}^{GS} and (b) the GS Coriolis effect Co_{xy}^{GS} for each run.

where ℓ^p is the length scale associated with the pressure fluctuation. Then, the GS pressure diffusion term is evaluated as

$$\Pi_{xy}^{\mathrm{GS}}/(\ell^p)^2 \simeq \frac{\partial}{\partial y}\Bigg[-2\left\langle \overline{u}'_x\overline{s}'_{ij}\right\rangle S_{ij} + \left\langle \overline{u}'_x\overline{\omega}'_i\right\rangle \Omega_i + \left\langle \overline{u}'_x\overline{\omega}'_x\right\rangle 2\Omega^{\mathrm{F}} - \left\langle \overline{u}'_x\overline{s}'_{ij}\overline{s}'_{ij}\right\rangle + \frac{1}{2}\left\langle \overline{u}'_x\overline{\omega}'_i\overline{\omega}'_i\right\rangle + \left\langle \overline{u}'_x\frac{\partial^2}{\partial x_i\partial x_j}\left(2\nu^{\mathrm{sgs}}\overline{s}_{ij}\right)\right\rangle\Bigg], \tag{3.29}$$

where ℓ^p is approximated to be constant in space for simplicity. Figure 3.14 shows the spatial distribution of each term on the right-hand side of Eq. (3.29) for run r5h05. It is clearly seen that the third term which is related to the rotation rate is dominant. Hence, the pressure diffusion term can be approximated as

$$\Pi_{xy}^{\mathrm{GS}} \simeq \frac{\partial}{\partial y}\left[(\ell^p)^2\left\langle \overline{u}'_x\overline{\omega}'_x\right\rangle 2\Omega^{\mathrm{F}}\right] = \frac{\partial}{\partial y}\left[\frac{1}{3}(\ell^p)^2 H^{\mathrm{GS}} 2\Omega^{\mathrm{F}}\right], \tag{3.30}$$

where we assume the isotropy for the GS turbulent helicity, $\left\langle \overline{u}'_x\overline{\omega}'_x\right\rangle = \left\langle \overline{u}'_y\overline{\omega}'_y\right\rangle = \left\langle \overline{u}'_z\overline{\omega}'_z\right\rangle = H^{\mathrm{GS}}/3$. Hence, the pressure diffusion Π_{xy}^{GS} is evaluated that it is linear to the turbulent helicity and the rotation rate, as expected form the result shown in Fig. 3.13(a).

In order to propose the general model expression for the pressure diffusion associated with the turbulent helicity, we analytically calculate Π_{ij} [Eq. (2.22d)] with the aid of the TSDIA. Details for the calculation are given in Appendix F. In the K–ε model, the pressure diffusion associated with the turbulent helicity is modeled as

$$\Pi_{ij} = C_{PDH}\left[\frac{\partial}{\partial x_j}\left(\frac{K^3}{\varepsilon^2}H\Omega_i^{\mathrm{A}}\right) + \frac{\partial}{\partial x_i}\left(\frac{K^3}{\varepsilon^2}H\Omega_j^{\mathrm{A}}\right)\right], \tag{3.31}$$

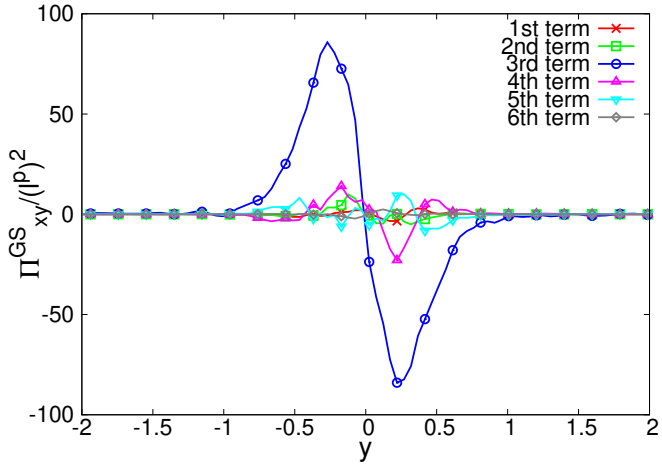

Figure 3.14: Evaluation of the GS pressure diffusion term $\Pi^{\rm GS}_{xy}$ for run r5h05.

where C_{PDH} is a model constant. Note that the TSDIA gives not only the model for the pressure diffusion but also the model for the pressure–strain correlation Φ_{ij} [Eq. (2.22c)] (see, Appendix F). It is given by

$$\Phi_{ij} = -C_{PSH}\left[\frac{\partial}{\partial x_j}\left(\frac{K^3}{\varepsilon^2}H\Omega^{\rm A}_i\right) + \frac{\partial}{\partial x_i}\left(\frac{K^3}{\varepsilon^2}H\Omega^{\rm A}_j\right)\right]_{\rm D}, \tag{3.32}$$

where C_{PSH} is a model constant and the term related to the turbulent helicity is only written. An interesting point is that the TSDIA predicts that C_{PDH} is slightly larger than C_{PSH}, $C_{PDH} > C_{PSH}$. This result is consistent with the result that sum of $\Phi^{\rm GS}_{xy}$ and $\Pi^{\rm GS}_{xy}$ also has negative gradient at $y = 0$ like the pressure diffusion $\Pi^{\rm GS}_{xy}$ for run r5h05 as shown in Fig. 3.12(b). It can be interpreted that the model given by Eq. (3.32) plays a role of reducing the effect of the pressure diffusion given by Eq. (3.31) as the second to fourth terms on the right-hand side of Eq. (2.51) reduce the effect of the production rate and the Coriolis effect (Sec. 2.3.3).

3.3.3 Derivation of the helicity model based on Reynolds stress transport

Here, we examine again the relationship between the Reynolds stress transport and the algebraic model for the Reynolds stress by incorporating the effect of the turbulent helicity given by Eqs. (3.31) and (3.32). In order to satisfy the covariance of the model [Ariki (2015)], we start from Eq. (B3) instead of Eq. (2.54). Here, the model proposed by Launder *et al.* (1975) is extended by adding the model given by Eqs. (3.31) and (3.32). Hence, the modeled transport equation for B_{ij} reads

$$\begin{aligned}\left[\frac{\mathfrak{D}B_{ij}}{\mathfrak{D}t}\right]_{\rm D} &= -C_{S1}\frac{\varepsilon}{K}B_{ij} - \left(\frac{4}{3} - C_{R1}\right)KS_{ij} \\ &\quad - (2 - C_{R2})\left[S_{i\ell}B_{\ell j} + S_{j\ell}B_{\ell i}\right]_{\rm D} - (2 - C_{R3})\left(W_{i\ell}B_{\ell j} + W_{j\ell}B_{\ell i}\right)\end{aligned}$$

$$+ C_{PH}\left[\frac{\partial}{\partial x_j}\left(\frac{K^3}{\varepsilon^2}H\Omega_i^{\mathrm{A}}\right)+\frac{\partial}{\partial x_i}\left(\frac{K^3}{\varepsilon^2}H\Omega_j^{\mathrm{A}}\right)\right]_{\mathrm{D}}$$
$$+ \frac{\partial}{\partial x_\ell}\left[C_D\frac{K}{\varepsilon}\left(R_{im}\frac{\partial R_{j\ell}}{\partial x_m}+R_{jm}\frac{\partial R_{i\ell}}{\partial x_m}+R_{\ell m}\frac{\partial R_{ij}}{\partial x_m}\right)\right]_{\mathrm{D}}+\nu\nabla^2 B_{ij}+[F_{ij}]_{\mathrm{D}}\,, \tag{3.33}$$

where $C_{PH}=C_{PDH}-C_{PSH}(>0)$. Here, we retain the turbulent helicity related term coming from the pressure diffusion and pressure–strain correlation, while other diffusion terms are assumed to be neglected. The external work term is also assumed to be neglected. These approximations are consistent with the result of the present simulation for the budget for R_{xy}^{GS} shown in Fig. 3.12(a). Then, Eq. (3.33) is reduced to

$$B_{ij}=-\frac{4-3C_{R1}}{3C_{S1}}\frac{K^2}{\varepsilon}S_{ij}+\frac{C_{PH}}{C_{S1}}\frac{K}{\varepsilon}\left[\frac{\partial}{\partial x_j}\left(\frac{K^3}{\varepsilon^2}H\Omega_i^{\mathrm{A}}\right)+\frac{\partial}{\partial x_i}\left(\frac{K^3}{\varepsilon^2}H\Omega_j^{\mathrm{A}}\right)\right]_{\mathrm{D}}$$
$$-\frac{2-C_{R2}}{C_{S1}}\frac{K}{\varepsilon}\left[S_{i\ell}B_{\ell j}+S_{j\ell}B_{\ell i}\right]_{\mathrm{D}}-\frac{2-C_{R3}}{C_{S1}}\frac{K}{\varepsilon}\left(W_{i\ell}B_{\ell j}+W_{j\ell}B_{\ell i}\right)-\frac{1}{C_{S1}}\frac{K}{\varepsilon}\left[\frac{\mathfrak{D}B_{ij}}{\mathfrak{D}t}\right]_{\mathrm{D}}. \tag{3.34}$$

In the case that the anisotropy of turbulence is weak, $B_{ij}/K\ll 1$, as is the case of the present simulation shown in Fig. 3.6, the first and second term on the right-hand side of Eq. (3.34) remain:

$$B_{ij}=-2\nu^{\mathrm{T}}S_{ij}+\tau^V\left[\frac{\partial}{\partial x_j}\left(\frac{K^3}{\varepsilon^2}H\Omega_i^{\mathrm{A}}\right)+\frac{\partial}{\partial x_i}\left(\frac{K^3}{\varepsilon^2}H\Omega_j^{\mathrm{A}}\right)\right]_{\mathrm{D}}, \tag{3.35}$$

where $\nu^{\mathrm{T}}=[(4-3C_{R1})/(6C_{S1})]K^2/\varepsilon$ and $\tau^V=(C_{PH}/C_{S1})K/\varepsilon$. This equation corresponds to the helicity model given by Eq. (2.76). Therefore, the term associated with the turbulent helicity in the helicity model given by Eq. (2.76) has its origin to the pressure diffusion term in the Reynolds stress transport equation. In contrast to the model given by Eq. (2.76), the model given by Eq. (3.35) includes the spatial derivative of K^3/ε^2 and $\boldsymbol{\Omega}^{\mathrm{A}}$.

In the present flow configuration, the model given by Eq. (3.35) with the zero-mean velocity condition leads to R_{xy} as follows:

$$R_{xy}=2\tau^V\frac{\partial}{\partial y}\left(\frac{K^3}{\varepsilon^2}H\Omega_x^{\mathrm{F}}\right)\neq 0. \tag{3.36}$$

Considering the spatial distributions of the turbulent energy, its dissipation rate, and the turbulent helicity shown in Figs. 3.4, 3.5, and 3.7, the right-hand side of Eq. (3.36) has negative gradient at $y=0$. Therefore, the positive mean velocity U_x is generated according to Eq. (3.22). For the fully-developed stage, the model given by Eq. (3.35) is written as

$$R_{xy}=-\nu^{\mathrm{T}}\frac{\partial U_x}{\partial y}+2\tau^V\frac{\partial}{\partial y}\left(\frac{K^3}{\varepsilon^2}H\Omega_x^{\mathrm{F}}\right). \tag{3.37}$$

The first term on the right-hand side of Eq. (3.37) has positive gradient at $y=0$, while the second term has negative gradient at $y=0$. Therefore, they are balanced with each other and the statistically steady

solution $R_{xy} = 0$ can be predicted. The same discussion is valid for the helicity model given by Eq. (2.76). Consequently, the algebraic model for the Reynolds stress accompanied with the turbulent helicity given by Eqs. (2.76) or (3.35) accounts for the mean velocity generation phenomenon without contradiction to the simulation results. In other words, the second term on the right-hand side of Eq. (3.35) which originates from the pressure diffusion term is appropriate to N_{xy} in Eq. (3.24). It should be noted that the pressure diffusion term is often is neglected in the conventional turbulence modeling as mentioned in Sec. 2.3.3. However, the pressure diffusion term plays an essential role in the mean velocity generation phenomenon in rotating turbulence accompanied with the turbulent helicity.

3.4 Summary

In this chapter, we performed the numerical simulation of rotating turbulence in which the turbulent energy and helicity are injected locally in space. In the present simulation, the mean velocity in the direction of the rotation axis was generated only when the system is rotating and the turbulent helicity is injected as shown in Figs. 3.9 and 3.10. This mean velocity generation phenomenon is caused by the effect of the Reynolds stress. It was discussed that this mean velocity generation phenomenon cannot be predicted by the eddy-viscosity model. In order to clarify the source of the mean velocity, the transport equation for the Reynolds stress was investigated. As a result, it was shown that the pressure diffusion term significantly contributes to the Reynolds stress transport in which it intends to sustain the generated mean velocity as shown in Fig. 3.12. It was revealed that the pressure diffusion can be expressed in terms of the turbulent helicity. The new model for the pressure diffusion accompanied with the turbulent helicity given by Eq. (3.31) was proposed with the aid of the TSDIA. By incorporating the effect of the pressure diffusion modeled by Eq. (3.31), we can derive the algebraic model for the Reynolds stress accompanied with the turbulent helicity given by Eq. (3.35), which corresponds to the helicity model given by Eq. (2.76) which is proposed in the previous study [Yokoi & Yoshizawa (1993)]. These models for the Reynolds stress accompanied with the turbulent helicity account for the mean velocity generation phenomenon without contradiction ton the simulation results.

In the present study, the LES was used instead of the DNS to achieve the high-Reynolds-number turbulence. Due to the usage of the SGS model given by Eq. (3.3), the quantitative validity such as the value of the turbulent helicity dissipation rate is still room for consideration [Li *et al.* (2006)]. In order to discuss the quantitative assessment of the model for the Reynolds stress accompanied with the turbulent helicity, the DNS of the present turbulent flow should be performed. Using the DNS, we can examine the value of the model constant C_{PHD} or the difference between the models given by Eqs. (2.76) and (3.35) in detail. Moreover, the present simulation configuration is somewhat artificial. In this sense, the validity of the model for the Reynolds stress accompanied with the turbulent helicity should be discussed in more realistic turbulent flows such as the turbulent swirling flow in a straight pipe [Kitoh (1991); Steenbergen (1995)] or the turbulent flow in a straight pipe with wall rotation [Orlandi (1997)]. These points should be examined in the future work.

Chapter 4

Effect of helicity on the turbulent energy transport

4.1 Model for the turbulent energy flux expressed by the turbulent helicity

In Sec. 3.3.2, Chap. 3, a new turbulence model for the pressure diffusion Π_{ij} was proposed. This model suggests the effect of the turbulent helicity not only on the Reynolds stress transport but also on the turbulent energy transport. The pressure diffusion term for the turbulent energy transport equation given by Eq. (2.24c) is expressed by means of the newly proposed model given by Eq. (3.31) as

$$\Pi^K = \frac{1}{2}\Pi_{jj} = C_{PDH}\frac{\partial}{\partial x_j}\left(\frac{K^3}{\varepsilon^2}H\Omega_j^{\mathrm{A}}\right). \tag{4.1}$$

This model can be interpreted that the energy flux due to the pressure fluctuation given by $\langle u_i' p' \rangle$ is expressed as

$$\langle u_i' p' \rangle = -C_{PDH}\frac{K^3}{\varepsilon^2}H\Omega_i^{\mathrm{A}}. \tag{4.2}$$

Hence, this model suggests that the negative turbulent helicity invokes the energy flux in the positive direction of the rotation axis, while the positive turbulent helicity invokes the energy flux in the negative direction. This property is closely similar to that of the group velocity of inertial waves given in Appendix D; namely, the wave packets with negative helicity propagate upward in the direction of the rotation axis, while the wave packets with positive helicity propagate downward. Since Ranjan & Davidson (2014) suggested that the fast energy transfer observed in rotating oscillating-grid turbulence is explained in terms of inertial wave as mentioned in Sec. 2.6.2, the model given by Eqs. (4.1) or (4.2) is expected to account for this phenomenon in terms of the turbulence model.

4.2 Simulation of decaying inhomogeneous turbulence

In order to explore the appropriate model which predicts the fast energy transport observed in rotating oscillating-grid turbulence, we perform the numerical simulation similar to its experiment. The flow configuration of rotating oscillating-grid turbulence is previously shown in Fig. 2.9; namely, the turbulent energy is generated locally in space by the oscillation of the grid and it falls off away from the grid. The rotation axis is set in the direction perpendicular to the grid plane. In the present study, we perform the simulation similar to that performed by Ranjan & Davidson (2014), which corresponds to the experiment of oscillating-grid turbulence with a single grid oscillation performed by Davidson *et al.* (2006). Hence, the external forcing is not used in the present simulation.

4.2.1 Numerical setup

The computational domain is a cubic box. The box size is $(2\pi)^3$ as mentioned later. The initial velocity field is shown in Fig. 4.1; namely, the velocity field is spatially confined around $z = 0$. The turbulence field is homogeneous in the x and y directions and inhomogeneous in the z direction. The rotation axis is set in the z direction. The periodic boundary condition is adopted to all directions. Namely, the turbulent energy is diffused in the z direction. In the present simulation, the direct numerical simulation (DNS) based on the Navier–Stokes equation in the Fourier space given by Eq. (2.39) is performed.

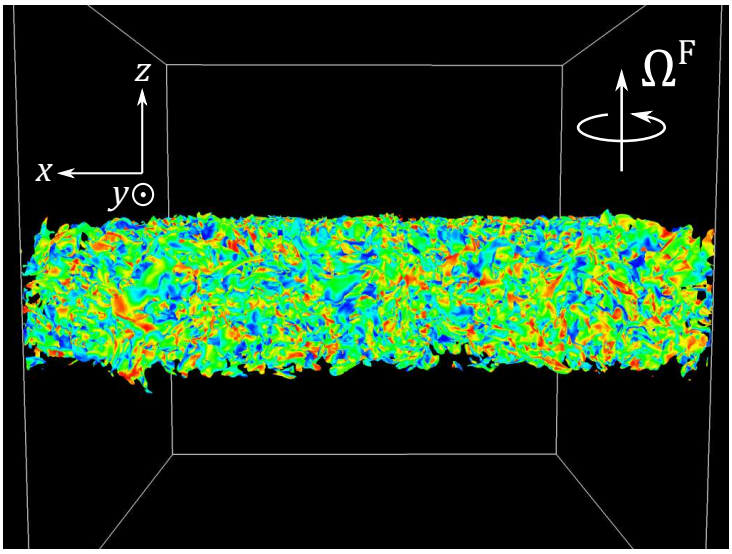

Figure 4.1: Iso-surfaces of the kinetic energy $u_i u_i/2$ for the initial velocity field for the present simulation. Color denotes the relative helicity defined as $u_i\omega_i/\sqrt{u_j u_j \omega_\ell \omega_\ell}$ in which the red color denotes the positive value while the blue color denotes the negative value.

The initial velocity field is generated by using the velocity field of fully-developed homogeneous isotropic turbulence. Details for the fully-developed homogeneous isotropic turbulence for the initial

velocity is given in Appendix G. Let us define the stream function $\boldsymbol{\psi}^{\rm hit}$ for homogeneous isotropic turbulence which satisfies $\boldsymbol{u}^{\rm hit} = \boldsymbol{\nabla}\times\boldsymbol{\psi}^{\rm hit}$ and $\boldsymbol{\nabla}\cdot\boldsymbol{\psi}^{\rm hit} = 0$ where $\boldsymbol{u}^{\rm hit}$ denotes the velocity for the fully-developed homogeneous isotropic turbulence. The initial velocity for the present simulation $\boldsymbol{u}^{\rm ini}$ is obtained by

$$u_i^{\rm ini} = \epsilon_{ij\ell}\frac{\partial}{\partial x_j}\left[g(z)\psi_\ell^{\rm hit}\right], \tag{4.3}$$

where $g(z)$ denotes the weighting function which confines the velocity field around $z = 0$. Here, we adopt $g(z) = \exp[-(z/\sigma)^4]$ where $\sigma = L_z/8$.

4.2.2 Simulation parameters

The box size is $L_x \times L_y \times L_z = 2\pi \times 2\pi \times 2\pi$ and the number of the grid point is $N_x \times N_y \times N_z = 512 \times 512 \times 512$. For the space discretization, the pseudo-spectral method is used and the aliasing error is eliminated by using the phase shift method [Orszag (1969); Kida & Yanase (1999)]. The governing equation in the Fourier space given by Eq. (2.39) is numerically solved. For time integration, the third-order Runge–Kutta scheme is adopted for nonlinear term, while the viscous and the Coriolis terms are solved exactly by using the integral factor technique [Morinishi *et al.* (2001*b*)]. The time step is set to $\Delta t = 2 \times 10^{-3}$. Simulation parameters are shown in Table 4.1. Here, the name of run corresponds to the parameter for the rotation rate $\Omega^{\rm F}$. Namely, we perform five cases with different rotation rates including non-rotating case. The Reynolds number Re and the Rossby number Ro are respectively defined as

$$\mathrm{Re} = \frac{K_0^2}{\nu\varepsilon_0}, \quad \mathrm{Ro} = \frac{\varepsilon_0^2}{K_0 2\Omega^{\rm F}}, \tag{4.4}$$

where $K_0 = K(z = 0, t = 0)(= 0.704)$ and $\varepsilon_0 = \varepsilon(z = 0, t = 0)(= 1.24)$. Here and hereafter, the x–y plane average is used for statistical average denoted as $\langle\rangle$. Similar to the GS Rossby number defined in Eq. (3.16), the Rossby number given by Eq. (4.4) represents the ratio of the rotation time scale $(2\Omega^{\rm F})^{-1}$ to the turbulence time scale K/ε at $z = 0$ and $t = 0$. Hence, the time scale of the rotation is almost comparable to that of turbulence for runs r08 and r1, while it is shorter than that of turbulence for runs r2 and r5. Namely, runs r2 and r5 are the cases in which the rotation is strong. The width of the confined turbulence region is $2\sigma = 1.57$, while the integral scale obtained from $\boldsymbol{u}^{\rm hit}$ field is $L^{\rm int} = 0.516$ as mentioned in Appendix G. Hence, the width of the confined turbulence region at the initial condition is three times as wide as the integral length scale $L^{\rm int}$.

Table 4.1: Parameters for the simulation of decaying inhomogeneous turbulence with and without system rotation. In all runs, the kinematic viscosity is set to $\nu = 10^{-3}$ and the Reynolds number is Re = 400.

Run	Ω^{F}	Ro
r0	0	∞
r08	0.8	1.10
r1	1	0.880
r2	2	0.440
r5	5	0.176

4.3 Results of the simulation of decaying inhomogeneous turbulence

4.3.1 Time evolution of the turbulent energy

Figures 4.2(a) and (b) respectively show the spatial distribution of the turbulent energy K at each time for runs r0 and r1. For both runs, the turbulent energy at $|z| < 1$ decreases as the time goes by, while that at $|z| > 1$ increases. Comparing the results between runs r0 and r1 in Fig. 4.2, it is clearly seen that the increase of energy at $|z| > 1$ for run r1 is faster than that for run r0. This result suggests that the turbulent energy is transferred faster in the rotating case than in the non-rotating case, which is the same result as the previous studies [Dickinson & Long (1983); Davidson *et al.* (2006); Kolvin *et al.* (2009); Ranjan & Davidson (2014)]. Figure 4.3(a) shows the spatial distribution of the turbulent energy for each run at $t = 1$. As the rotation rate increases, the spatial distribution of the turbulent energy becomes broad. This suggests that the transfer rate of the turbulent energy from $|z| < 1$ to $|z| > 1$ increases as the rotation rate increases. Figure 4.3(b) shows the spatial distribution of the turbulent energy for each run at the time $2\Omega^{\mathrm{F}}t = 2$; namely, we compare the results for each run at the same time normalized by the rotation rate Ω^{F}. When the time is normalized by the rotation rate, the spatial distribution of the turbulent energy for each run collapses to a single curve at $|z| > 1$, while it is different from each other at $|z| < 1$. At $|z| > 1$, all curves collapse to the result of the linear inviscid solution (linear inv.) and that of the linear viscous solution for run r1 (r1 linear vis.). Here, the linear inviscid solution denotes the solution of Eq. (D1) stating from the same initial condition, while the linear viscous solution for run r1 denotes the solution for run r1 in which the first term on the right-hand side of Eq (2.39) is neglected. This result suggests that the fast energy transfer in the rotating system is closely related to the linear inviscid motion of fluid. On the other hand, at $|z| < 1$, the result of the linear viscous solution for run r1 (r1 linear vis.) does not collapse to that of run 1. This result suggests that the nonlinearity is essential at $|z| < 1$ region. Hence, this flow cannot be described simply by the linearized equation given by Eq. (D1) or Eq (2.39) in which the first term on the right-hand side is neglected considering the nonlinear turbulence region at $|z| < 1$.

Here, we define the width of the turbulence region d as $d = |z(K = 0.02K_0)|$; namely, d denotes the location of the turbulence edge where the value of the turbulent energy takes $K = 0.02K_0$. Figure 4.4 shows the time evolution of the width of the turbulence region. The result for run r0 does not exactly satisfy $d \sim t^{1/2}$ which is experimentally suggested one [Dickinson & Long (1978)]. This is because

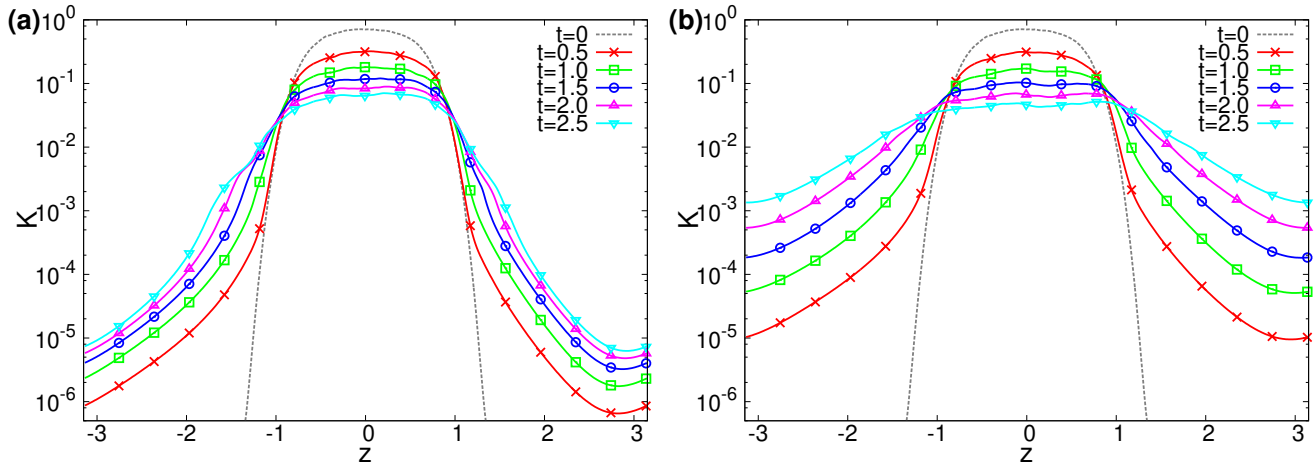

Figure 4.2: Spatial distribution of the turbulent energy at each time for runs (a) r0 and (b) r1.

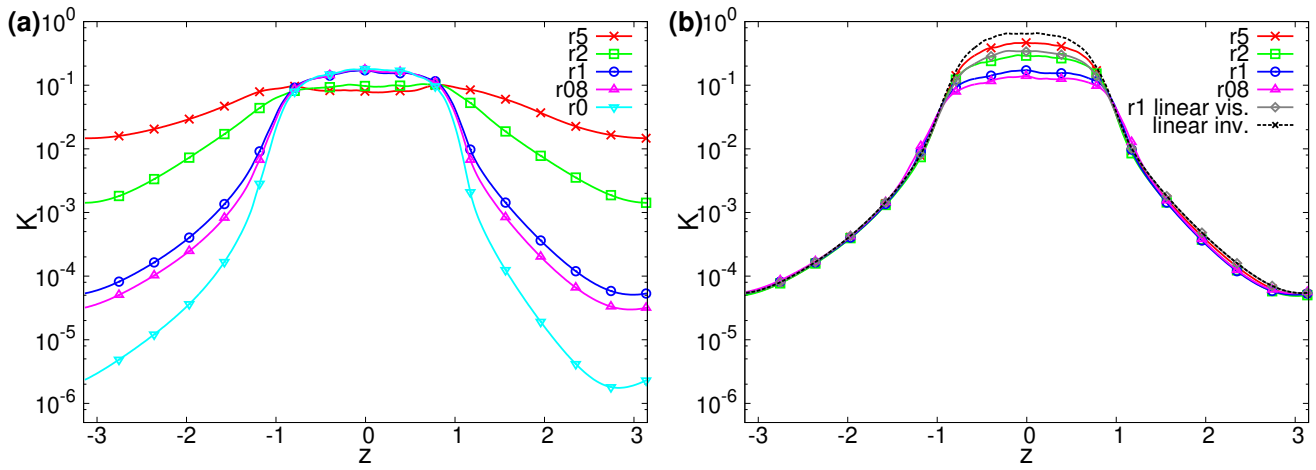

Figure 4.3: Spatial distribution of the turbulent energy at the time (a) $t = 1$ and (b) $2\Omega^{\mathrm{F}}t = 2$ for each run. In (b), 'r1 linear vis.' denotes the result of run r1 without the nonlinear term and 'linear inv.' denotes the result of linear inviscid solution.

the energy injection is absent, so that the energy rather decays due to the viscous dissipation than is transferred by the diffusion terms. In Fig. 4.4(a), the result for run r0 is saturated at $t = 1.5$, while it still grows linearly for other runs with system rotation. Figure 4.4(b) shows the time evolution of the width of the turbulence region against the time normalized by the rotation rate. In Fig. 4.4(b), the time evolution of the width of the turbulence region also collapses to the linear inviscid solution like the spatial distribution of the turbulent energy shown in Fig. 4.3(b) except for run r08. The same result was shown by the previous studies [Dickinson & Long (1983); Davidson *et al.* (2006); Kolvin *et al.* (2009); Ranjan &

Davidson (2014)]. It is seen, however, the deviation from the linear inviscid solution becomes large as the rotation rate decreases or the Rossby number increases. Moreover, the result for run r08 does not agree with other runs including the linear inviscid solution in Fig. 4.4(b). These results suggest the possibility that not only the effect of the rotation but also the nonlinear motion of turbulent flow is essential for the cases in which the Rossby number is comparable to unity.

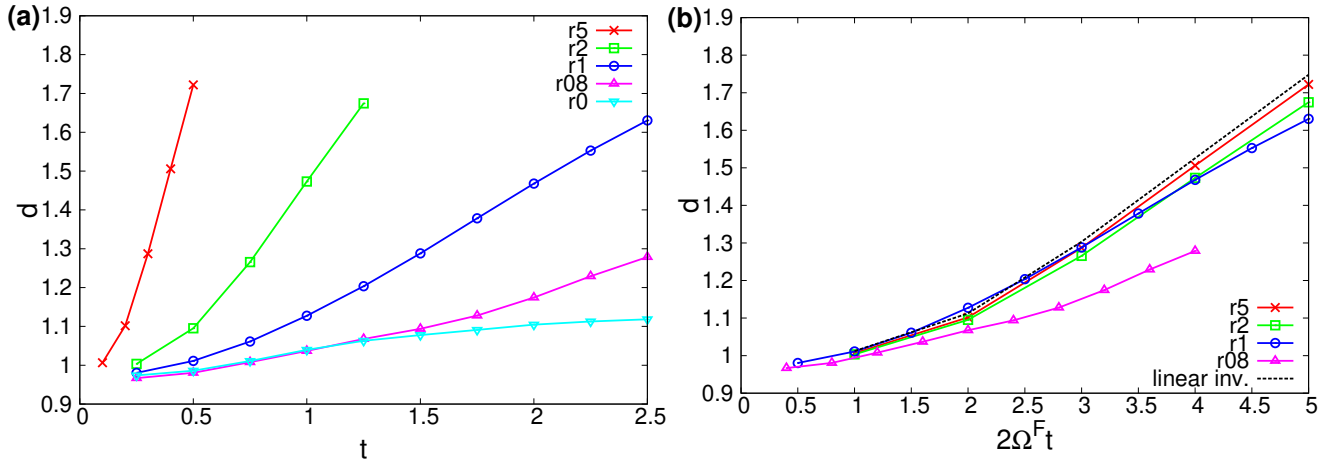

Figure 4.4: Time evolution of the width of the turbulence region d (a) against the time t and (b) against the time normalized by the rotation rate $2\Omega^{\mathrm{F}}t$.

4.3.2 Budget for the turbulent energy transport

We investigate the budget for the turbulent energy transport. In order to directly see the effect of rotation, we decompose the pressure as $p = p^{\mathrm{N}} + p^{\Omega}$ where p^{N} and p^{Ω} respectively satisfy

$$\nabla^2 p^{\mathrm{N}} = -s_{ij}s_{ij} + \frac{1}{2}\omega_i\omega_i, \tag{4.5}$$

$$\nabla^2 p^{\Omega} = 2\omega_i\Omega_i^{\mathrm{F}}. \tag{4.6}$$

Namely, p^{Ω} represents a part of the pressure induced by the effect of the system rotation, while p^{N} represents a part of the pressure induced by the nonlinearity of fluid motion. Here, p^{N} and p^{Ω} are respectively referred to as the nonlinear pressure and the rotational pressure. Similarly, we decompose the pressure diffusion term given in Eq. (2.24c) as $\Pi^K = \Pi^{\mathrm{N}} + \Pi^{\Omega}$ where Π^{N} and Π^{Ω} are respectively defined as

$$\Pi^{\mathrm{N}} = -\frac{\partial}{\partial x_j}\left\langle u_j' p^{\mathrm{N}\prime}\right\rangle, \tag{4.7}$$

$$\Pi^{\Omega} = -\frac{\partial}{\partial x_j}\left\langle u_j' p^{\Omega\prime}\right\rangle. \tag{4.8}$$

Note that $\langle u_i' p^{\Omega\prime} \rangle$ does not includes the effect of the centrifugal force since the centrifugal force expressed by $(\boldsymbol{\Omega}^{\mathrm{F}} \times \boldsymbol{x})^2/2$ is not fluctuating value. Hence, the transport equation for the turbulent energy in this flow is written as

$$\frac{\partial K}{\partial t} = -\varepsilon - \frac{\partial}{\partial z} \langle u_z' p^{\mathrm{N}\prime} \rangle - \frac{\partial}{\partial z} \langle u_z' p^{\Omega\prime} \rangle - \frac{\partial}{\partial z} \left(\frac{1}{2} \left\langle u_z' \frac{1}{2} u_i' u_i' \right\rangle \right) + \nu \frac{\partial^2 K}{\partial z^2}. \tag{4.9}$$

Here, the terms on the right-hand side of Eq. (4.9) are respectively referred to as the dissipation, nonlinear pressure diffusion, rotational pressure diffusion, turbulent diffusion, and viscous diffusion.

Figure 4.5 shows the budget for the turbulent energy transport equation given by Eq. (4.9) for runs r0, r1, and r5. Here, p^{N} and p^{Ω} in the second and third terms on the right-hand side of Eq. (4.9) are obtained by solving Eqs. (4.5) and (4.6), respectively. In the present simulation, $\tilde{p}(k_x = k_y = k_z = 0) = 0$ owing to the periodic boundary condition, so that the Poisson equation is directly solved in the Fourier space, e.g., $\tilde{p}^{\Omega}(\boldsymbol{k}) = -2\tilde{\omega}_i(\boldsymbol{k})\Omega_i^{\mathrm{F}}/k^2$. As seen in Fig. 4.5(a), the turbulent energy is lost by the dissipation term at $|z| < 1$ and transferred from $|z| < 0.6$ to $|z| > 0.6$ due to the turbulent diffusion term for run r0 at $t = 1$. At the same time for run r1 [Fig. 4.5(b)], the rotational pressure diffusion term appears in the budget. The intensity of the rotational pressure diffusion for run r1 at $t = 1$ is comparable to that of the turbulent diffusion as seen in Fig. 4.5(b). It should be noted that the turbulent energy is transferred solely by the rotational pressure diffusion in the outer region at $1 < |z| < 2$. Namely, the rotational pressure diffusion has the tendency to have broader spatial distribution than the nonlinear pressure diffusion or the turbulent diffusion. This tendency is more clear for run r1 at $t = 2$ as shown in Fig. 4.5(c) or for run r5 at $2\Omega^{\mathrm{F}}t = 2$ as shown in Fig. 4.5(d).

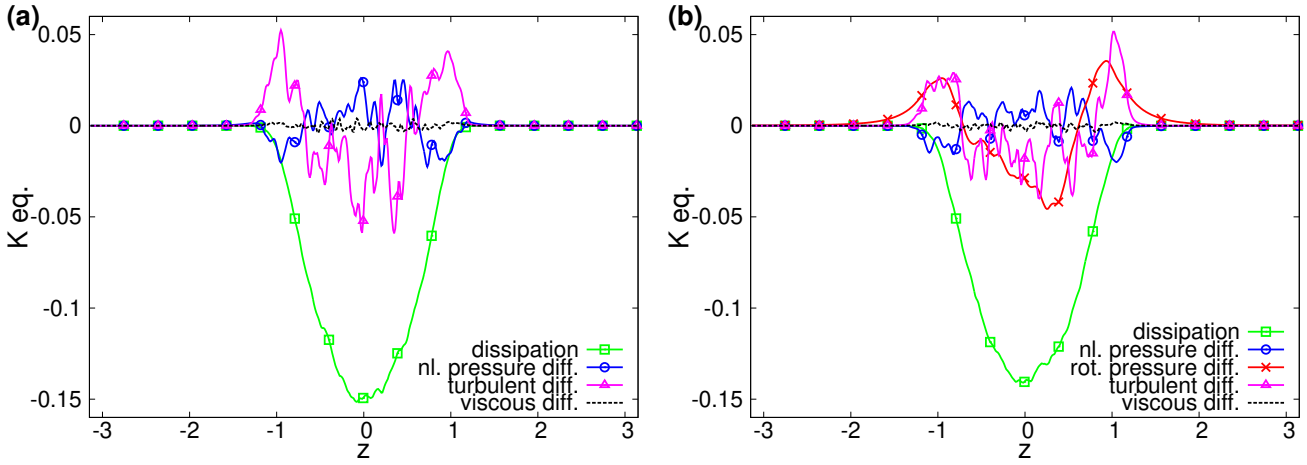

Figure 4.5: Budget for the turbulent energy transport equation for (a) run r0 at the time $t = 1$ and (b) run r1 at the time $t = 1$ ($2\Omega^{\mathrm{F}}t = 2$). Here, 'nl. pressure diff.' denotes the nonlinear pressure diffusion and 'rot. pressure diff.' denotes the rotational pressure diffusion.

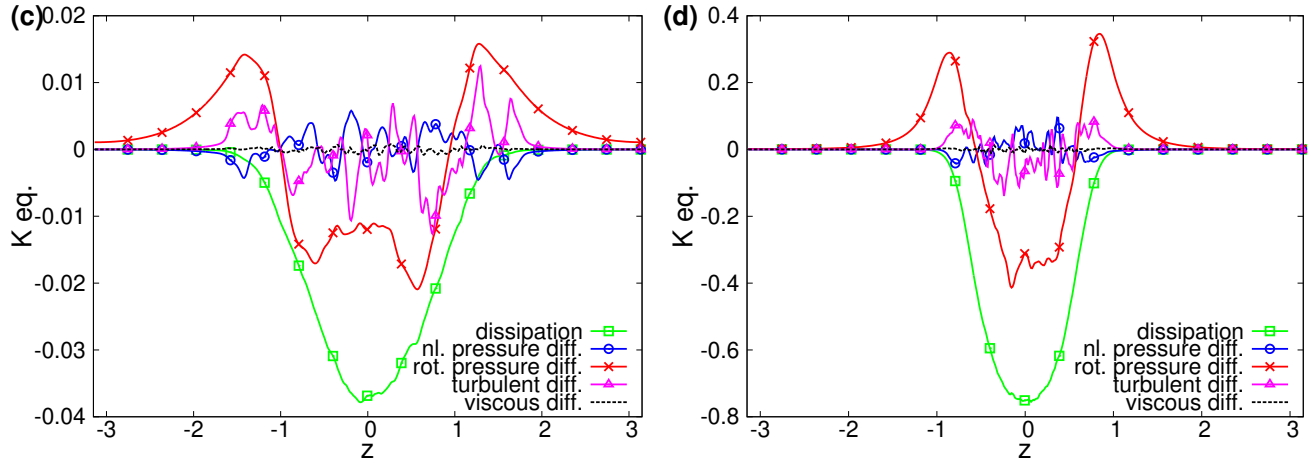

Figure 4.5: (continued) Budget for the turbulent energy transport equation for (c) run r1 at the time $t = 2$ ($2\Omega^{\mathrm{F}}t = 4$) and (d) run r5 at the time $t = 0.2$ ($2\Omega^{\mathrm{F}}t = 2$).

4.3.3 Assessment of the gradient-diffusion approximation

The gradient-diffusion approximation of the energy flux due to turbulence given by $\langle u_z' p' \rangle + \langle u_z' u_i' u_i'/2 \rangle$ can be written as

$$\langle u_z' p' \rangle + \left\langle u_z' \frac{1}{2} u_i' u_i' \right\rangle = -\frac{C_\nu}{\sigma_K} \frac{K^2}{\varepsilon} \frac{\partial K}{\partial z}. \tag{4.10}$$

Figures 4.6(a) and (b) respectively show the comparison between exact value of $\langle u_z' p' \rangle + \langle u_z' u_i' u_i'/2 \rangle$ and the prediction by the gradient-diffusion approximation given by Eq. (4.10) for runs r0 and r1. Here, $C_\nu/\sigma_K = 0.22$ is adopted so that the model agrees with the exact value for run r0. This value is twice as large as the conventional value $C_\nu/\sigma_K = 0.09$ [Yoshizawa (1998); Pope (2000)]. The gradient-diffusion approximation gives a good prediction for the spatial distribution of the energy flux for run r0 at each time [Fig. 4.6(a)], while it underestimates the exact value for run r1 [Fig. 4.6(b)]. In particular, the spatially broad distribution of the exact value is not predicted by the gradient-diffusion approximation in Fig. 4.6(b). Figures 4.7(a) and (b) respectively show the comparison between the energy flux due to the nonlinearity of turbulence given by $\langle u_z' p^{\mathrm{N}\prime} \rangle + \langle u_z' u_i' u_i'/2 \rangle$ and the prediction by the gradient-diffusion approximation given by Eq. (4.10) for runs r08 and r1. Note that $C_\nu/\sigma_K = 0.22$ is also used for the model constant. In contrast to the result shown in Fig. 4.6(b), the gradient-diffusion approximation gives a good prediction for both runs at each time in Fig. 4.7. This result suggests that the energy flux due to the nonlinearity of turbulence can be predicted by the gradient-diffusion approximation. Namely, the following modeling is appropriate:

$$\langle u_z' p^{\mathrm{N}\prime} \rangle + \left\langle u_z' \frac{1}{2} u_i' u_i' \right\rangle = -\frac{C_\nu}{\sigma_K} \frac{K^2}{\varepsilon} \frac{\partial K}{\partial z}. \tag{4.11}$$

In order to predict the large value of the total energy flux for rotating cases, modeling the energy flux due to the rotational pressure, $\langle u_i' p^{\Omega\prime} \rangle$, is required.

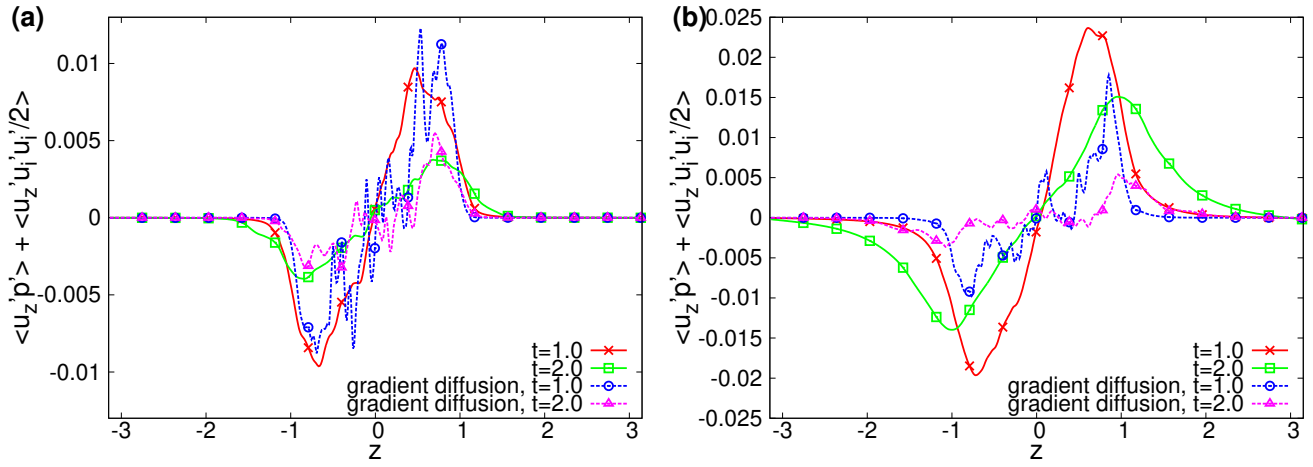

Figure 4.6: Comparison between the total energy flux due to turbulence, $\langle u_z' p' \rangle + \langle u_z' u_i' u_i'/2 \rangle$, and the gradient-diffusion approximation for runs (a) r0 and (b) r1 at $t = 1$ and 2.

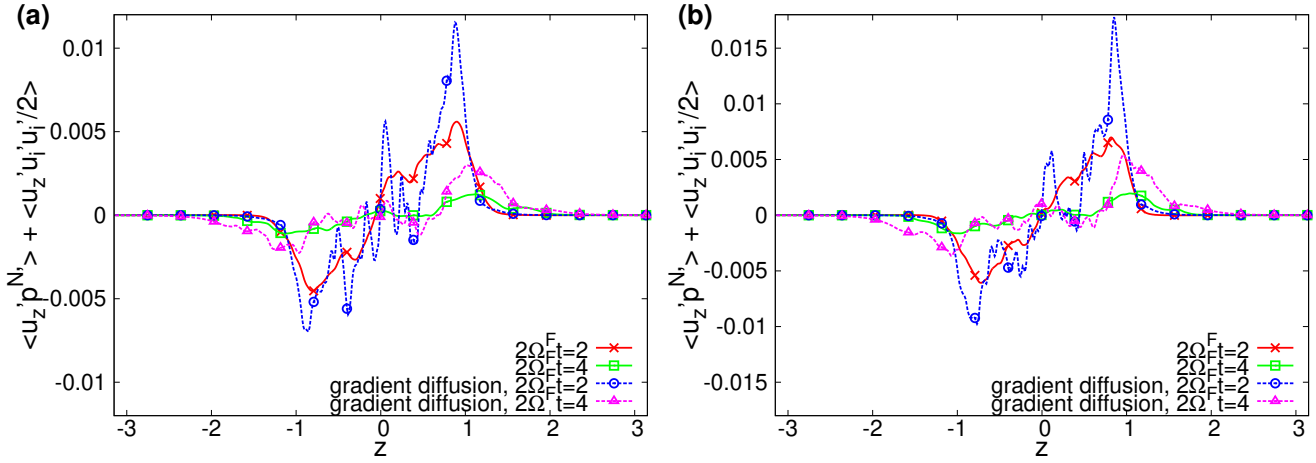

Figure 4.7: Comparison between the total energy flux due to the nonlinearity of turbulence, $\langle u_z' p^{\mathrm{N}\prime} \rangle + \langle u_z' u_i' u_i'/2 \rangle$, and the gradient-diffusion approximation for runs (a) r08 and (b) r1 at the time $2\Omega^{\mathrm{F}} t = 2$ and 4.

4.4 Assessment of the new model expressed by the turbulent helicity

For the model of the energy flux due to the rotational pressure, $\langle u_i' p^{\Omega\prime} \rangle$, the newly proposed model given by Eq. (4.2) is a good candidate. In the present simulation configuration, the new model is written as

$$\left\langle u_z' p^{\Omega\prime} \right\rangle = -C_{PDH} \frac{K^3}{\varepsilon^2} H 2\Omega^{\mathrm{F}}. \tag{4.12}$$

4.4.1 Time evolution of the turbulent helicity

In order to assess the validity of the model given by Eq. (4.12), the spatial distribution of the turbulent helicity should be investigated. Figures 4.8(a) and (b) respectively show the spatial distribution of the turbulent helicity H at each time for runs r0 and r1. As seen in Fig. 4.8(a), the turbulent helicity just decreases as the time goes by for run r0. For run r1 [Fig. 4.8(b)], however, the positive turbulent helicity is developed at $z < 0$, while the negative turbulent helicity is developed at $z > 0$. The same segregation of the turbulent helicity was shown in the previous studies [Godeferd & Lollini (1999); Ranjan & Davidson (2014)]. Ranjan & Davidson (2014) suggested that this segregation of the turbulent helicity is the result of the propagation of inertial wave; namely, the wave packets with negative helicity propagate upward in the direction of the rotation axis ($z > 0$), while the wave packets with positive helicity propagate downward ($z < 0$). As a result, the negative turbulent helicity is dominant at $z > 0$, while the positive turbulent helicity is dominant at $z < 0$. In the context of the RANS equation, this segregation of the turbulent helicity can be also explained as follows. In the present flow configuration, the transport equation for the turbulent helicity given by Eqs. (2.26) and (2.27a)–(2.27g) reads

$$\frac{\partial H}{\partial t} = 2\Omega^{\mathrm{F}} \frac{2}{3} \frac{\partial K}{\partial z} + \cdots, \tag{4.13}$$

where the turbulent energy related part of the Coriolis effect term Co^H [Eq. (2.27g)] is only written as a leading term. Considering the spatial distribution of the turbulent energy K shown in Figs. 4.2 and 4.3, $\partial K/\partial z > 0$ at $z < 0$, while $\partial K/\partial z < 0$ at $z > 0$. Since the rotation rate is positive $\Omega^{\mathrm{F}} > 0$, the positive turbulent helicity is generated at $z < 0$, while the negative turbulent helicity is generated at $z > 0$. Since the source of the turbulent helicity is dependent on the rotation rate Ω^{F}, the value of the turbulent heicity itself increases as the rotation rate increases as shown in Fig. 4.9.

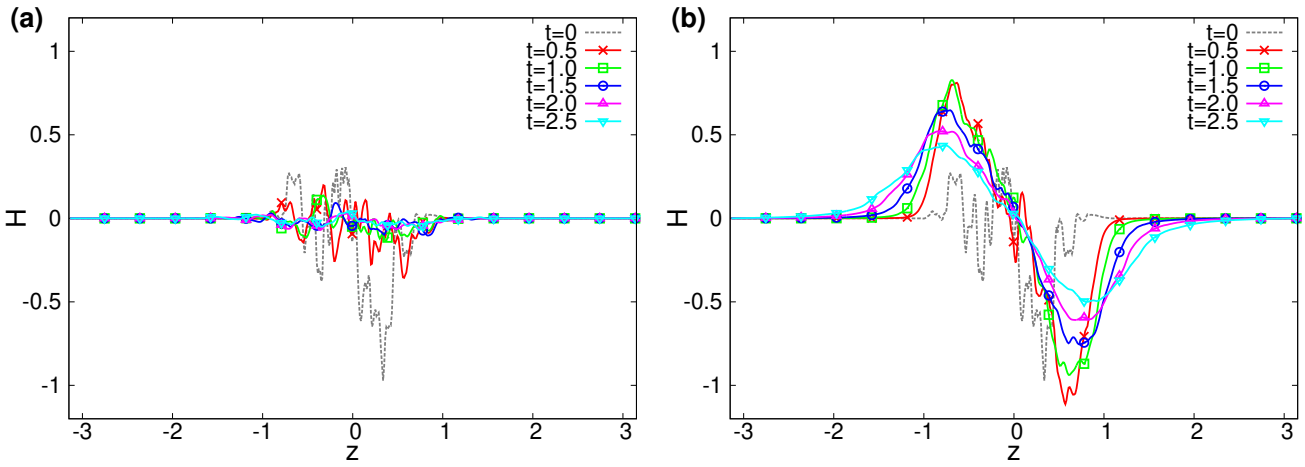

Figure 4.8: Spatial distribution of the turbulent helicity at each time for runs (a) r0 and (b) r1.

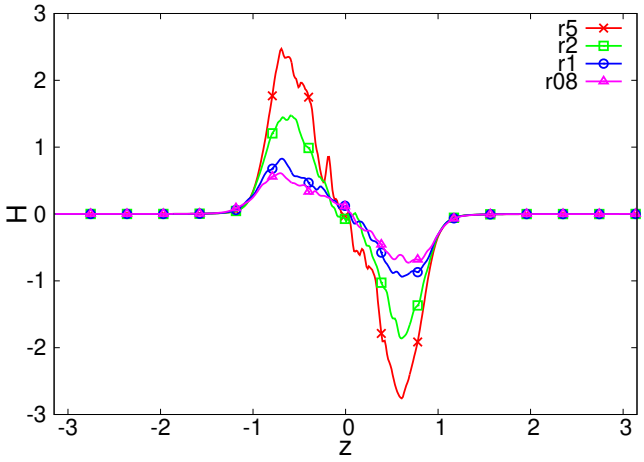

Figure 4.9: Spatial distribution of the turbulent helicity for each run at the time $2\Omega^{\rm F}t = 2$.

4.4.2 Assessment of the model for energy flux due to the rotational pressure

Figure 4.10 shows the spatial distribution for the energy flux due to the rotational pressure, $\langle u_z' p^{\Omega\prime}\rangle$, for run r1 at each time. Considering the spatial distribution of the turbulent helicity shown in Figs. 4.8 and 4.9, it is seen that the model given by Eq. (4.12) qualitatively accounts for the spatial distribution of the energy flux due to the rotational pressure; namely, the estimation that $\langle u_z' p^{\Omega\prime}\rangle \propto -H$ seems to be good. Figures 4.11(a) and (b) respectively show the comparison between the exact value of $\langle u_z' p^{\Omega\prime}\rangle$ and the prediction by the present model given by Eq. (4.12) for runs r08 and r1 at the time $2\Omega^{\rm F}t = 2$ and 4. Here, the model constant is set to $C_{PDH} = 0.03$ so that the model agrees with the exact value at

the time $2\Omega^{\rm F}t = 2$. The present model predicts the spatially broad distribution of the energy flux which cannot be predicted by the gradient-diffusion approximation [Fig. 4.6(b)]. In this sense, the present model successfully accounts for the energy flux due to the rotational pressure.

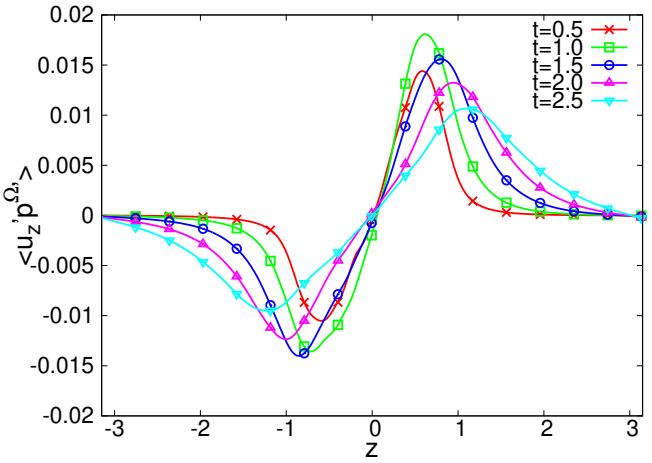

Figure 4.10: Spatial distribution of the energy flux due to the rotational pressure, $\langle u_z' p^{\Omega\prime} \rangle$, for run r1 at each time.

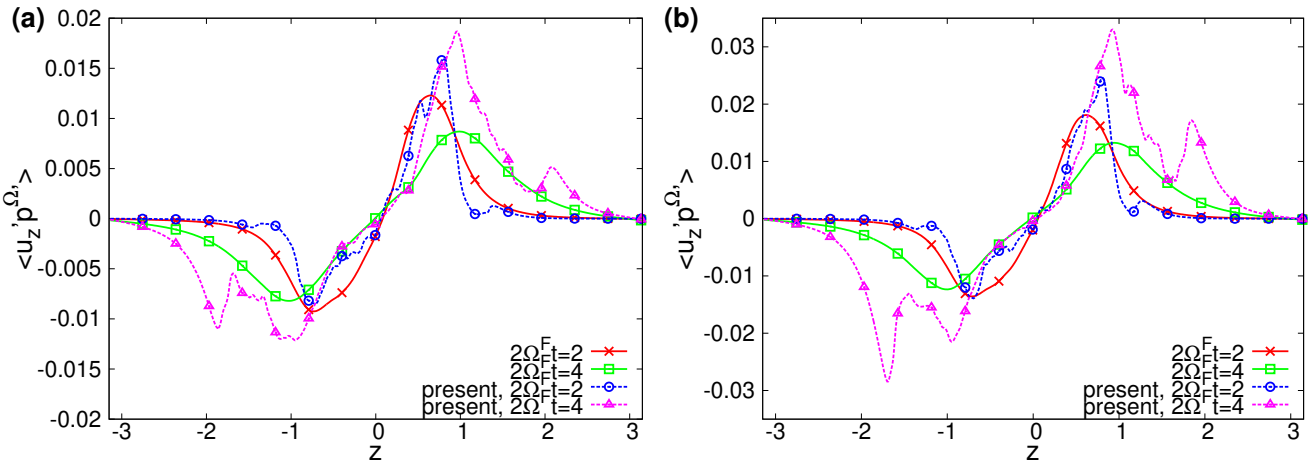

Figure 4.11: Comparison between the energy flux due to the rotational pressure, $\langle u_z' p^{\Omega\prime} \rangle$, and the present model given by Eq. (4.12) for runs (a) r08 and (b) r1 at the time $2\Omega^{\rm F}t = 2$ and 4.

4.4.3 Evaluation of the present model from analytical viewpoint

Although the present model given by Eq. (4.12) succeeded in predicting the spatially broad distribution of the energy flux due to the rotational pressure, its accuracy decreases at the later time at $2\Omega^{\mathrm{F}}t = 4$ especially at $1 < |z| < 2$, as seen in Fig. 4.11. We examine the causes of this inconsistency in detail. Here, we consider the Fourier transformation in the homogeneous directions:

$$q(\boldsymbol{x}) = \int \mathrm{d}\boldsymbol{k}_\perp \hat{q}(\boldsymbol{k}_\perp, z)\mathrm{e}^{i\boldsymbol{k}_\perp\cdot\boldsymbol{x}_\perp}, \tag{4.14}$$

$$\hat{q}(\boldsymbol{k}_\perp, z) = \frac{1}{(2\pi)^2}\int \mathrm{d}\boldsymbol{x}_\perp q(\boldsymbol{x})\mathrm{e}^{-i\boldsymbol{k}_\perp\cdot\boldsymbol{x}_\perp}, \tag{4.15}$$

where $\boldsymbol{x}_\perp = (x, y)$ and $\boldsymbol{k}_\perp = (k_x, k_y)$. Here and hereafter, the double integral is simply denoted as $\int \mathrm{d}\boldsymbol{k}_\perp (= \int_{-\infty}^{\infty}\mathrm{d}k_x \int_{-\infty}^{\infty}\mathrm{d}k_y)$. The energy spectrum in $k_\perp (= \sqrt{k_x^2 + k_y^2})$ space can be defined as

$$K = \int_0^\infty \mathrm{d}k_\perp E(k_\perp, z). \tag{4.16}$$

Figure 4.12 shows the energy spectrum in $k_\perp$ space for run r1 at the time $2\Omega^{\mathrm{F}}t = 4$. It is clearly seen that the energy spectrum at $|z| > 1$ is concentrated at the low-wavenumber region at $k_\perp < 8$. This result suggests that the low-wavenumber modes of energy are transferred faster than the high-wavenumber modes. Therefore, the turbulence at $|z| > 1$ is not fully developed in the $k_\perp$ space. In such a case, ε takes a smaller value than the fully-developed state of turbulence since ε itself is closely related to high-wavenumber modes. Since the model given by Eq. (4.12) involves ε in the denominator, the small value of ε gives the large value of $\langle u_z' p^{\Omega\prime}\rangle$. Hence, it is expected that the overestimation of the present model at $1 < |z| < 2$ seen in Fig. 4.11 comes from the small value of ε in the coefficient of the model given by Eq. (4.12) due to the immature state of turbulence in the $k_\perp$ space.

Using the Fourier transformation given by Eqs. (4.14) and (4.15), the Poisson equation for the rotational pressure is written as

$$\left(-k_\perp^2 + \frac{\partial^2}{\partial z^2}\right)\hat{p}^{\Omega}(\boldsymbol{k}_\perp, z) = \hat{\omega}_z(\boldsymbol{k}_\perp, z)2\Omega^{\mathrm{F}}. \tag{4.17}$$

In the present flow configuration, this equation can be analytically solved as

$$\hat{p}^{\Omega}(\boldsymbol{k}_\perp, z) = -\int_{-\infty}^{\infty}\mathrm{d}z'\frac{1}{2}k_\perp^{-1}\mathrm{e}^{-k_\perp|z-z'|}\hat{\omega}_z(\boldsymbol{k}_\perp, z')2\Omega^{\mathrm{F}}. \tag{4.18}$$

Then, the energy flux due to the rotational pressure is expressed as follows:

$$\begin{aligned}
\left\langle u_z' p^{\Omega\prime}\right\rangle &= \int \mathrm{d}\boldsymbol{k}_\perp \int \mathrm{d}\boldsymbol{k}_\perp' \left\langle \hat{u}_z(\boldsymbol{k}_\perp, z)\hat{p}^{\Omega\prime}(\boldsymbol{k}_\perp', z)\right\rangle \mathrm{e}^{i(\boldsymbol{k}_\perp + \boldsymbol{k}_\perp')\cdot\boldsymbol{x}_\perp} \\
&= \int \mathrm{d}\boldsymbol{k}_\perp \Re\left[\left\langle \hat{u}_z(\boldsymbol{k}_\perp, z)\hat{p}^{\Omega\prime *}(\boldsymbol{k}_\perp, z)\right\rangle\right] \\
&= -\int \mathrm{d}\boldsymbol{k}_\perp \int_{-\infty}^{\infty}\mathrm{d}z'\frac{1}{2}k_\perp^{-1}\mathrm{e}^{-k_\perp|z-z'|}\Re\left[\left\langle \hat{u}_z'(\boldsymbol{k}_\perp, z)\hat{\omega}_z'^{*}(\boldsymbol{k}_\perp, z')\right\rangle\right]2\Omega^{\mathrm{F}},
\end{aligned} \tag{4.19}$$

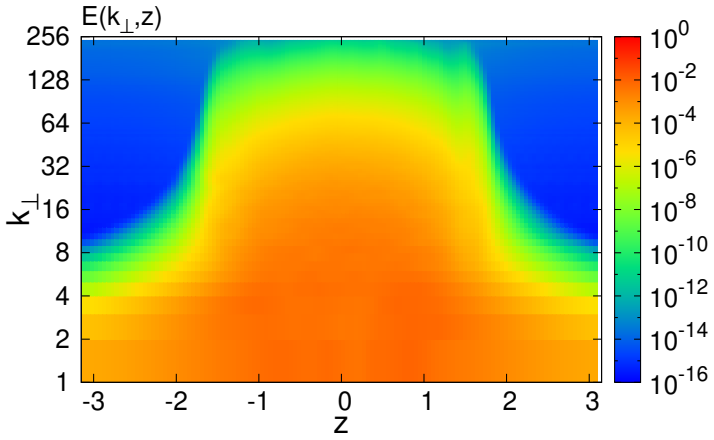

Figure 4.12: Energy spectrum in $k_\perp$ space for run r1 at the time $2\Omega^{\rm F}t = 4$.

where the homogeneity in the x and y directions is used. We rewrite this equation as

$$\left\langle u_z' p^{\Omega\prime} \right\rangle = -M^H H_{zz} 2\Omega^{\rm F}, \tag{4.20}$$

$$M^H = \frac{1}{H_{zz}} \int {\rm d}\boldsymbol{k}_\perp \int_{-\infty}^{\infty} {\rm d}z' \frac{1}{2} k_\perp^{-1} {\rm e}^{-k_\perp |z-z'|} \Re \left[\left\langle \hat{u}_z'(\boldsymbol{k}_\perp, z) \hat{\omega}_z'^*(\boldsymbol{k}_\perp, z') \right\rangle \right] 2\Omega^{\rm F}, \tag{4.21}$$

where $H_{zz} = \langle u_z' \omega_z' \rangle$. Here, M^H has the dimension of the square of length scale. M^H involves information on the integral length scale of H_{zz} in the $k_\perp$ space and the length of the correlation between $\hat{u}_z'(\boldsymbol{k}_\perp, z)$ and $\hat{\omega}_z'(\boldsymbol{k}_\perp, z')$ along the z direction.

For isotropic turbulence, we can evaluate $H_{zz} = H/3$. Figure 4.13 shows the ratio of H to H_{zz} at the time $2\Omega^{\rm F}t = 2$ and 4 for runs r08 and r1. It is seen that $H/H_{zz} \simeq 3$ at $|z| < 1$, meaning that the turbulence is nearly isotropic at $|z| < 1$. However, $H/H_{zz} \simeq 2$ at $|z| > 1$. This anisotropy can be explained from the viewpoint of the polarization of inertial wave. Ranjan (2017) showed that inertial wave solution gives

$$\tilde{u}_i(\boldsymbol{k}) \tilde{u}_i^*(\boldsymbol{k}) = 2 \frac{k^2}{k_\perp^2} \tilde{u}_z(\boldsymbol{k}) \tilde{u}_z^*(\boldsymbol{k}), \tag{4.22}$$

where $\tilde{\boldsymbol{u}}(\boldsymbol{k})$ denotes the coefficient for the three dimensional Fourier transformation of velocity. As discussed in Appendix D, $\boldsymbol{k} \simeq \boldsymbol{k}_\perp$ mode waves have fast group velocity. Using the solution for $\tilde{\boldsymbol{\omega}}(\boldsymbol{k})$ of inertial wave given by Eq. (D5), helicity for $\boldsymbol{k} \simeq \boldsymbol{k}_\perp$ mode waves reads

$$\tilde{u}_i(\boldsymbol{k}) \tilde{\omega}_i^*(\boldsymbol{k}) = 2 \frac{k^2}{k_\perp^2} \tilde{u}_z(\boldsymbol{k}) \tilde{\omega}_z^*(\boldsymbol{k}) \simeq 2 \tilde{u}_z(\boldsymbol{k}) \tilde{\omega}_z^*(\boldsymbol{k}). \tag{4.23}$$

We can interpret that $H \simeq 2H_{zz}$ from this relation although we cannot exactly derive $H/H_{zz} = 2$ from Eq. (4.23) due to the inhomogeneity in the z direction.

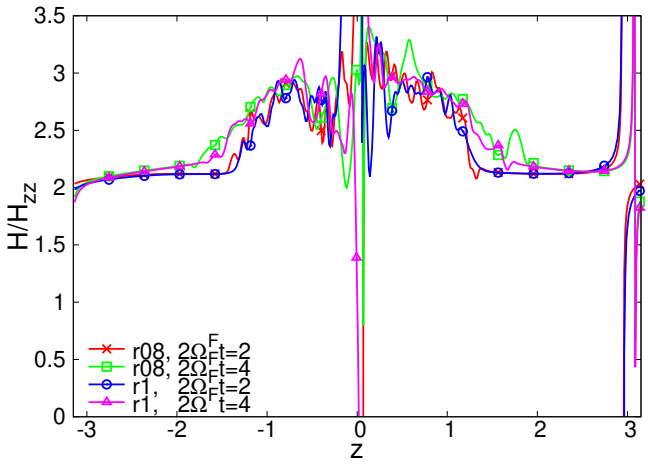

Figure 4.13: Ratio of H to H_{zz} at the time $2\Omega^{\rm F}t = 2$ and 4 for runs r08 and r1.

Next, we approximate M^H in terms of the length scale related to energy rather than helicity. In the case that two-point correlation between $\hat{u}'_z(\boldsymbol{k}_\perp, z)$ and $\hat{\omega}'_z(\boldsymbol{k}_\perp, z')$ along the z direction is nearly constant in the range $|z - z'| < 1/k_\perp$, $\int_{-\infty}^{\infty} {\rm d}z' \exp[-k_\perp|z - z'|]$ in Eq. (4.21) can be calculated separately. In such a case, we can approximate M^H as

$$M^H = \frac{1}{H_{zz}} \int {\rm d}\boldsymbol{k}_\perp k_\perp^{-2} \Re \left[\left\langle \hat{u}'_z(\boldsymbol{k}_\perp, z) \hat{\omega}'^*_z(\boldsymbol{k}_\perp, z) \right\rangle \right] 2\Omega^{\rm F}, \tag{4.24}$$

When the isotropic case is concerned and the integral length scale of helicity in the $k_\perp$ space can be expressed by the integral length scale of energy, we have $M^H \sim (L^K)^2$ where

$$L^K = \frac{1}{2K} \int {\rm d}\boldsymbol{k}_\perp k_\perp^{-1} \Re \left[\left\langle \hat{u}'_i(\boldsymbol{k}_\perp, z) \hat{u}'^*_i(\boldsymbol{k}_\perp, z) \right\rangle \right]. \tag{4.25}$$

Figure 4.14 shows the ratio of M^H to $(L^K)^2$ at the time $2\Omega^{\rm F}t = 2$ and 4 for runs r08 and r1. It is seen that $M^H/(L^K)^2$ depends on the space and time. However, $M^H \simeq 0.5(L^K)^2$ is a reasonable approximation at $|z| \sim 1$ in which the energy flux due to the rotational pressure is large [see, Figs. 4.10 and 4.11].

Since we focus on the model for turbulent flow rather than the flow described by inertial wave governed by the linearized equation, we adopt $H_{zz} = H/3$ and $M^H = 0.5(L^K)^2$ which are estimated at $|z| \simeq 1$. Then, Eq. (4.20) is reduced to

$$\left\langle u'_z p^{\Omega\prime} \right\rangle = -C_{PDHM} (L^K)^2 H 2\Omega^{\rm F}, \tag{4.26}$$

where $C_{PDHM} (= 0.5/3 = 0.17)$ is a constant. Figure 4.15 shows the comparison between exact value of $\langle u'_z p^{\Omega\prime} \rangle$ and Eq. (4.26) for runs r08, r1, and r2 at the time $2\Omega^{\rm F}t = 2$ and 4. It is seen that the overestimation of the model seen in Fig. 4.11 is decreased for Eq. (4.26). Equation (4.26) also gives a good prediction for run r2 where the rotation rate is larger or the Rossby number is smaller. For fully-developed turbulence,

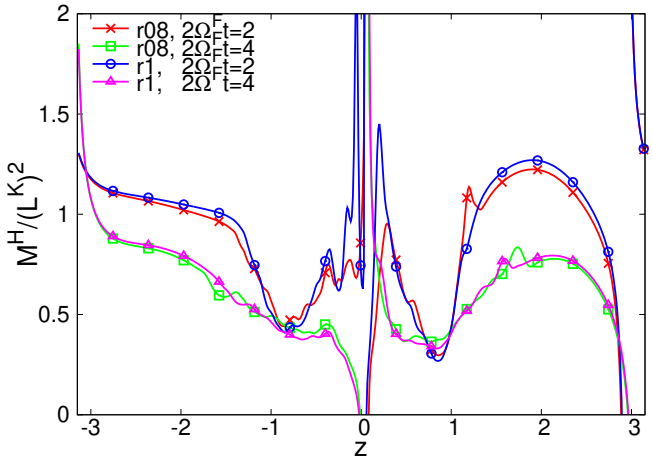

Figure 4.14: Ratio of M^H to $(L^K)^2$ at the time $2\Omega^{\rm F}t = 2$ and 4 for runs r08 and r1.

the integral scale of energy can be expressed as $L^K \sim K^{3/2}/\varepsilon$ according to the Taylor's dissipation law [Taylor (1935)]. In such a case, Eq. (4.26) is reduced to the model given by Eq. (4.12). In fact, Fig. 4.16 shows that the ratio of L^K to $K^{3/2}/\varepsilon$ is nearly constant at developed turbulence region at $|z| < 1$ and it is evaluated as $L^K/(K^{3/2}/\varepsilon) = 0.45$. Here, $L^K/(K^{3/2}/\varepsilon) = 0.45$ gives $C_{PDH}(= C_{PDHM} \times 0.45^2) = 0.034$, which is close to the value estimated at Fig. 4.11. Consequently, the newly proposed model given by Eq. (4.12) is applicable to fully-developed and nearly isotropic turbulence.

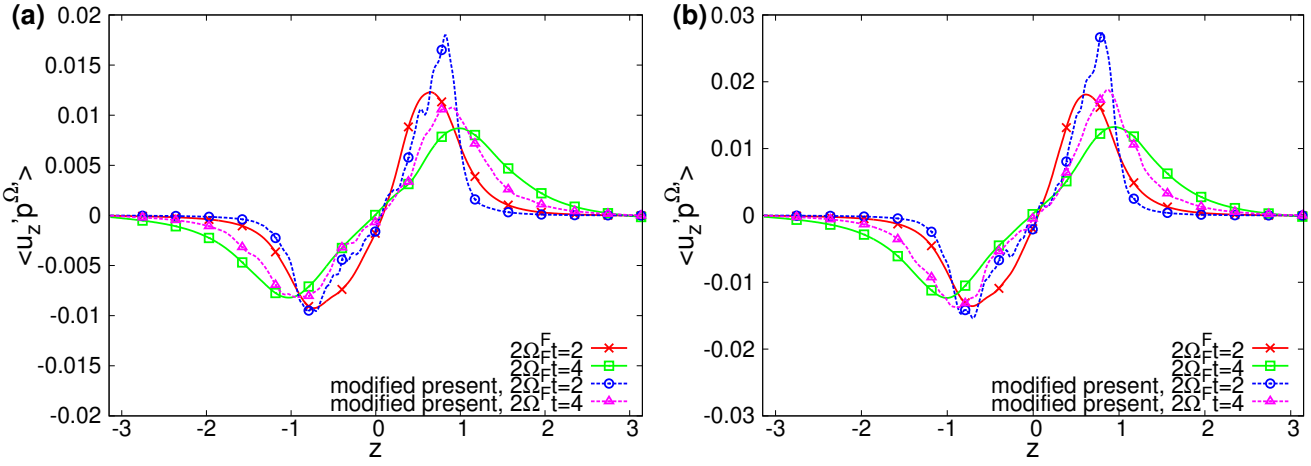

Figure 4.15: Comparison between the energy flux due to the rotational pressure, $\langle u_z' p^{\Omega\prime} \rangle$, and Eq. (4.26) for runs (a) r08, (b) r1 at the time $2\Omega^{\rm F}t = 2$ and 4.

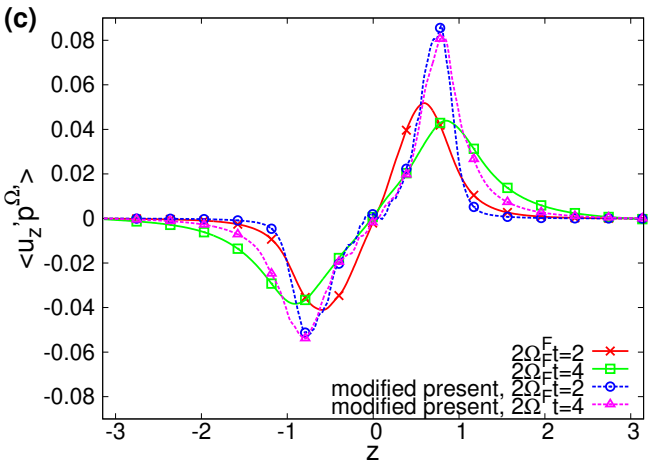

Figure 4.15: (continued) Comparison between the energy flux due to the rotational pressure, $\langle u_z' p^{\Omega\prime} \rangle$, and Eq. (4.26) for (c) r2 at the time $2\Omega^{\mathrm{F}} t = 2$ and 4.

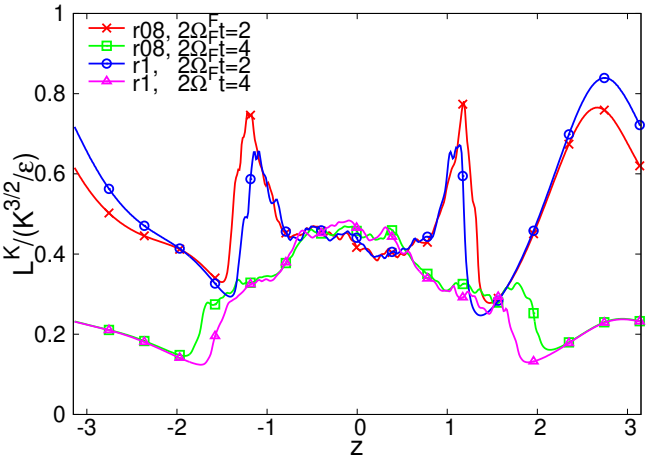

Figure 4.16: Ratio of L^K to $K^{3/2}/\varepsilon$ for runs r08 and r1 at the time $2\Omega^{\mathrm{F}} t = 2$ and 4.

4.5 Summary

In this chapter, we performed the numerical simulation of decaying inhomogeneous turbulence similar to the oscillating-grid turbulence. In the present simulation, the fast energy transport in the direction of the rotation axis was observed in rotating cases as shown in Figs. 4.2, 4.3, and 4.4. This result is consistent with the previous studies [Dickinson & Long (1983); Davidson *et al.* (2006); Kolvin *et al.* (2009); Ranjan & Davidson (2014)]. In the budget for the turbulent energy transport equation, the pressure diffusion associated with the rotation has significant contribution to the fast energy transport in the rotating system as shown in Fig. 4.5. It was shown that the gradient-diffusion approximation cannot predict the spatial distribution of the energy flux due to the rotational pressure which is a part of the pressure induced by the effect of the system rotation. The newly proposed model accompanied with the turbulent helicity given by Eq. (4.12) accounts for the spatially broad distribution of the energy flux due to the rotational pressure $\langle u_z' p^{\Omega\prime} \rangle$ as shown in Fig. 4.11. However, the model given by Eq. (4.12) overestimates the DNS value at the later time at $2\Omega^{\mathrm{F}} t = 4$ due to the immature state of turbulence in the $k_\perp$ space. This overestimation was reduced when we use the integral scale of energy in the $k_\perp$ space L^K for the coefficient [Eq. (4.26)] instead of K and ε [Eq. (4.12)].

We should note that Eq. (4.26) was obtained by means of two assumptions. One is the isotropy of the turbulent helicity $H_{zz} = H/3$. The other is that M^H is expressed in terms of the integral length scale of energy in the $k_\perp$ space L^K. When the turbulence is fully developed, we can assume $L^K \sim K^{3/2}/\varepsilon$. In such a case, Eq. (4.26) is reduced to Eq. (4.12). Hence, the model given by Eq. (4.12) is valid when the turbulence is fully developed and nearly isotropic. In this sense, the model given by Eq. (4.12) can be used in predicting the energy diffusion at the initial stage of the present simulation or the statistically steady state which can be established if we use the external forcing confined around $z = 0$. The latter is also useful to examine the validity of the present model in fully developed turbulence. In such a simulation, the energy diffusion by the rotation and turbulence given by the second to fourth terms on the right-hand side of Eq. (4.9) is balanced with the energy dissipation in the region where the turbulent energy is not injected. When the rotation is strong, it is expected that the turbulent energy reaches the edge of the box boundary without enough decaying. In such a case, the turbulence field is much affected by the box boundary. In order to avoid the effect of the boundary, large box length in the z direction is required. For anisotropic turbulence, some modification for the model given by Eq. (4.12) should be considered. Moreover, the model given by Eq. (4.12) should be modified in order to apply to the turbulence including the immature turbulence region. These points should be examined in the future work.

Chapter 5

Discussion

5.1 Comparison with the previous model

5.1.1 Extension of the helicity model to anisotropic turbulence

As discussed in Sec. 2.3.4 and Appendix B, the nonlinear eddy-viscosity model for the Reynolds stress can be proposed based on the Reynolds stress transport. Owing to the newly proposed model for the pressure diffusion and pressure–strain correlation terms given by Eqs. (3.31) and (3.32), we can propose more general algebraic model for the Reynolds stress accompanied with the turbulent helicity. Substituting Eq. (3.34) iteratively into B_{ij} on the right-hand side, we have

$$\begin{aligned} B_{ij} = & -2\nu^{\mathrm{T}} S_{ij} + \tau^{V} V_{ij} \\ & + \zeta_{SS} \left[S_{i\ell} S_{\ell j} \right]_{\mathrm{D}} - \zeta_{SW} \left(S_{i\ell} W_{\ell j} + S_{j\ell} W_{\ell i} \right) + \zeta_{DS} \left[\frac{\mathfrak{D} S_{ij}}{\mathfrak{D} t} \right]_{\mathrm{D}} \\ & - \zeta_{SV} \left[S_{i\ell} V_{\ell j} + S_{j\ell} V_{\ell i} \right]_{\mathrm{D}} - \zeta_{WV} \left(W_{i\ell} V_{\ell j} + W_{j\ell} V_{\ell i} \right) + \zeta_{DV} \left[\frac{\mathfrak{D} V_{ij}}{\mathfrak{D} t} \right]_{\mathrm{D}} + \cdots , \end{aligned} \tag{5.1}$$

where

$$V_{ij} = \left[\frac{\partial}{\partial x_j} \left(\frac{K^3}{\varepsilon^2} H \Omega_i^{\mathrm{A}} \right) + \frac{\partial}{\partial x_i} \left(\frac{K^3}{\varepsilon^2} H \Omega_j^{\mathrm{A}} \right) \right]_{\mathrm{D}} . \tag{5.2}$$

In Eq. (5.1), the terms on the third line denote the higher order effect of the turbulent helicity. In the present simulation shown in Chap. 3, the turbulence is almost isotropic as seen in Fig. 3.6. In such a case, the terms on the second or third lines of Eq. (5.1) have little contribution. In the turbulent shear flows, however, turbulence is generally anisotropic. For example, in the turbulent swirling flow in a straight pipe [Kitoh (1991); Steenbergen (1995)] or the turbulent flow in a straight pipe with wall rotation [Orlandi (1997)], the turbulence is both helical and anisotropic. For such anisotropic helical turbulent flows, the terms on the third line in Eq. (5.1) possibly play significant roles.

5.1.2 Evaluation of model constant

The conventional model constant for the eddy-viscosity model C_ν is estimated as $C_\nu = 0.09$, while the TSDIA predicts $C_\nu = 0.125$ by using Eqs. (C60) and (C74). In this sense, the estimation for model constants with the aid of the TSDIA is meaningful. In Sec. 4.4.1, we estimate the constant for the model for the energy flux due to the rotational pressure given by Eq. (4.2) as $C_{PDH} = 0.03$. The TSDIA gives C_{PDH} as Eq. (F10) by means of the inertial range helicity spectrum given by Eq. (C57) and the evaluation for the turbulent helicity dissipation rate given by Eq. (C69). For the constant for the inertial range helicity spectrum C_H, Borue & Orszag (1997) estimates $C_H = 1$ for the numerical simulation using the hyperviscosity, while André & Lesieur (1977) estimates $C_H = 2.23$ using the EDQNM closure model. For the constant for the turbulent helicity dissipation rate $C_{\varepsilon H}$, the simulation for the Ekman boundary layer performed by Deusebio & Lindborg (2014) suggests $1 < C_{\varepsilon H} < 2$ at the logarithmic region. Hence, the value of C_{PDH} predicted by the TSDIA gives

$$C_{PDH} = \begin{cases} 0.00039 & \text{for } C_H = C_{\varepsilon H} = 2, \\ 0.025 & \text{for } C_H = C_{\varepsilon H} = 1. \end{cases} \tag{5.3}$$

Due to the ambiguity of C_H and $C_{\varepsilon H}$, and the application of simplified inertial range helicity spectrum given by Eq. (C57), the accuracy of this estimation of C_{PDH} is ambiguous. However, the present estimation $C_{PDH} = 0.03$ is not so different from the estimation for the case $C_H = C_{\varepsilon H} = 1$ by the TSDIA. In the case that $C_H = C_{\varepsilon H} = 1$, the TSDIA gives $C_\eta = 0.0016$ through Eq. (C74) for the constant for the helicity model given by Eq. (2.76). This value is comparable to that used in Yokoi & Yoshizawa (1993), $C_\eta = 0.003$, adjusted to predict the sustainment of the dent axial mean velocity in the turbulent swirling flow in a straight pipe. Therefore, the present estimation of C_{PDH} is acceptable from the theoretical view point.

5.2 Physical interpretation of correlation between velocity and pressure fluctuations

5.2.1 Relationship between inertial wave and velocity–pressure fluctuations correlation

In Sec. 4.1, it was suggested that the property of the present model accompanied with the turbulent helicity given by Eq. (4.2) is closely similar to that of the group velocity of inertial waves. In order to see this point more clearly, we consider the homogeneous isotropic but non-mirror symmetric turbulent field. In such a case, the energy flux due to the pressure can be non-zero. Using the three-dimensional Fourier transformation, the correlation between the velocity and the rotational pressure fluctuations reads

$$\left\langle u_i' p^{\Omega\prime} \right\rangle = -\int \mathrm{d}\boldsymbol{k} \int \mathrm{d}\boldsymbol{k}' i\epsilon_{j\ell m} \frac{k_\ell'}{k'^2} 2\Omega_j^{\mathrm{F}} \left\langle \tilde{u}_i'(\boldsymbol{k}) \tilde{u}_m'(\boldsymbol{k}') \right\rangle = -\int \mathrm{d}\boldsymbol{k}\ \frac{1}{2k} \frac{E^H(k)}{4\pi k^2} \frac{1}{k} M_{ij}(\boldsymbol{k}) 2\Omega_j^{\mathrm{F}}, \tag{5.4}$$

where $M_{ij}(\boldsymbol{k})$ is defined in Eq. (2.38) and use is made of Eqs. (2.40) and (2.41). Note that Eq. (4.19) in which the turbulence is inhomogeneous in the z direction corresponds to this equation for homogeneous

turbulence. Equation (5.4) suggests that the turbulent helicity invokes the energy flux due to the rotational pressure. When the rotation rate is so high that the nonlinear term is neglected, Eq. (D6) is satisfied. Note that Eq. (D6) is satisfied regardless of the presence of the kinematic viscosity [Ranjan (2017)]. Statistical average of Eq. (D6) reads

$$E^H(k) = \mp 2kE(k). \tag{5.5}$$

Substituting Eq. (5.5) and the group velocity of inertial waves C_i^{g} given by Eq. (D4) into Eq. (5.4), we have

$$\left\langle u_i' p^{\Omega\prime} \right\rangle = \int \mathrm{d}\boldsymbol{k}\ \frac{E(k)}{4\pi k^2} C_i^{\mathrm{g}}. \tag{5.6}$$

Equation (5.6) can be interpreted as the energy flux due to the group velocity of inertial waves. Therefore, the energy flux due to the rotational pressure is tightly connected to the group velocity of inertial waves. It should be noted that Eq. (5.6) is only valid for the linearized equation (D1). However, Eq. (5.4) is valid for the case of fully nonlinear turbulence as long as homogeneity and isotropy are guaranteed. In this sense, the usage of the turbulent helicity for the model for $\langle u_i' p^{\Omega\prime} \rangle$ is more general expression than inertial wave propagation.

5.2.2 Statistical interpretation of relationship between velocity–pressure fluctuations correlation and the turbulent helicity

In a statistical sense, the physical mechanism of the relationship between the velocity–rotational pressure fluctuations correlation and the turbulent helicity can be understood as follows. Here, we set the rotation axis in the z direction. Since the rotational pressure obeys Eq. (4.6), we have

$$\nabla^2 p^{\Omega\prime} = 2\omega_z' \Omega^{\mathrm{F}}. \tag{5.7}$$

Here, we consider the case in which $\Omega^{\mathrm{F}} > 0$. Equation (5.7) suggests that the local minimum of $p^{\Omega\prime}$ is likely to be associated with $\omega_z' > 0$, while the local maximum of $p^{\Omega\prime}$ is associated with $\omega_z' < 0$. This correspondence can be interpreted by the effect of the Coriolis force; namely, the positive ω_z' invokes the radially outward velocity fluctuation $\delta u_r > 0$ due to the Coriolis force. Considering the continuity equation for $\delta\boldsymbol{u}$, $\boldsymbol{\nabla} \cdot \delta\boldsymbol{u} = 0$, the radially outward velocity fluctuation $\delta u_r > 0$ is accompanied with the axially inward velocity fluctuation δu_z. Since the effect of rotation on u_z is solely caused by the rotational pressure p^{Ω}, the generation of the axially inward velocity fluctuation δu_z indicates the decrease of the pressure inside the vortex, $\delta p < 0$. On the other hand, the negative ω_z' invokes the radially inward velocity fluctuation $\delta u_r < 0$. It is accompanied with the axially outward velocity fluctuation δu_z, which indicates the increase of the pressure inside the vortex, $\delta p > 0$. When we consider the positive velocity fluctuation in the z direction $u_z' > 0$, the positive vorticity fluctuation in the z direction $\omega_z' > 0$ gives the positive helicity $u_z'\omega_z' > 0$ and $u_z'\delta p < 0$, while the negative vorticity fluctuation $\omega_z' < 0$ gives the negative helicity $u_z'\omega_z' < 0$ and $u_z'\delta p > 0$. Entirely similarly, when we consider the negative velocity fluctuation in the z direction $u_z' < 0$, the positive vorticity fluctuation $\omega_z' > 0$ gives the negative helicity

$u'_z\omega'_z < 0$ and $u'_z\delta p > 0$, while the negative vorticity fluctuation $\omega'_z < 0$ gives the positive helicity $u'_z\omega'_z > 0$ and $u'_z\delta p < 0$. As a result, $u'_z\delta p$ is always positive when the helicity is negative $u'_z\omega'_z < 0$, while $u'_z\delta p$ is always negative when the helicity is positive $u'_z\omega'_z > 0$. This mechanism is schematically described in Fig. 5.1. Consequently, the negative turbulent helicity is always associated with $\langle u'_z p^{\Omega\prime}\rangle > 0$, while the positive turbulent helicity is always associated with $\langle u'_z p^{\Omega\prime}\rangle < 0$. Strictly speaking, $\langle u'_z p^{\Omega\prime}\rangle$ is not directly associated with the turbulent helicity $H(= \langle u'_i\omega'_i\rangle)$ but the z component of the turbulent helicity $H_{zz}(= \langle u'_z\omega'_z\rangle)$. However, the presence of the turbulent helicity H indicates the presence of H_{zz}. For isotropic turbulence, we can evaluate $H = 3H_{zz}$ and the usage of H is justified as discussed in Sec. 4.4.3. In this sense, the model for $\langle u'_i p^{\Omega\prime}\rangle$ using H is a primitive one. For strongly anisotropic turbulence, some modification of the model given by Eq. (4.2) should be considered.

Note that the presence of δu_r does not necessarily cause the increase or decrease of u_z inside the vortex which leads to the mean velocity generation. For example, we consider the case where $H > 0$ and $\omega'_z > 0$ which corresponds to the top-right case in Fig. 5.1. In this case, u_z inside the vortex is decreased due to the convection by the radially outward velocity fluctuation δu_r. However, u_z should be increased due to the convection by the axially inward velocity fluctuation δu_z at the same time. Hence, the total amount of u_z is not necessarily changed due to the convection by $\delta\boldsymbol{u}$. In order to examine the mean velocity generation, we have to consider the generation of the Reynolds stress as discussed in the next subsection.

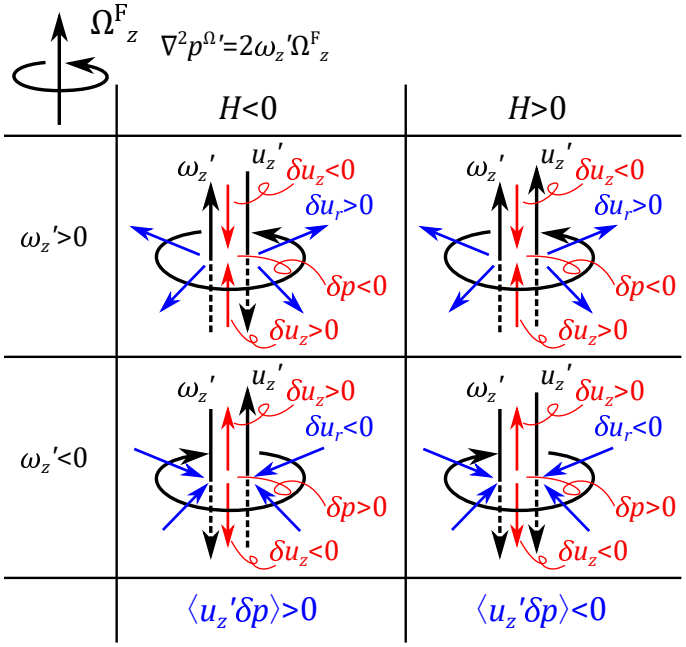

Figure 5.1: Schematic diagram for the relationship between the velocity–rotational pressure fluctuations correlation and the turbulent helicity.

5.2.3 Correlation between velocity and pressure fluctuations as a flux of the Reynolds stress

In the Reynolds stress transport equation, the correlation between velocity and pressure fluctuations appears as

$$\frac{\partial R_{ij}}{\partial t} = -\frac{\partial}{\partial x_j}\left\langle u_i' p' \right\rangle - \frac{\partial}{\partial x_i}\left\langle u_j' p' \right\rangle + \cdots . \tag{5.8}$$

In this equation, $\langle u_i' p' \rangle$ can be interpreted as a flux of the Reynolds stress in the j-th direction, while $\langle u_j' p' \rangle$ as a flux of the Reynolds stress in the i-th direction. Here, we consider the case that the rotation axis is set in the x direction and the turbulence field is inhomogeneous in the y direction as is the case of the simulation shown in Chap. 3. In the simulation shown in Chap. 3, the positive turbulent helicity is injected around $y = 0$, so that $\langle u_x' p^{\Omega\prime} \rangle < 0$ there. This correlation between the velocity and the rotational pressure fluctuations invokes the negative flux of R_{xy} in the y direction where its absolute value takes maximum at $y = 0$. Even if the Reynolds stress is initially zero and does not have any other source terms, the flux due to the rotational pressure is able to transport R_{xy} from $y > 0$ to $y < 0$. Since R_{xy} can take both positive and negative value, $R_{xy} > 0$ is established at $y < 0$, while $R_{xy} < 0$ is established at $y > 0$, in an anti-symmetric form. This process is schematically shown in Fig. 5.2. This anti-symmetric distribution of R_{xy} generates the axial mean velocity from the zero-mean-velocity condition.

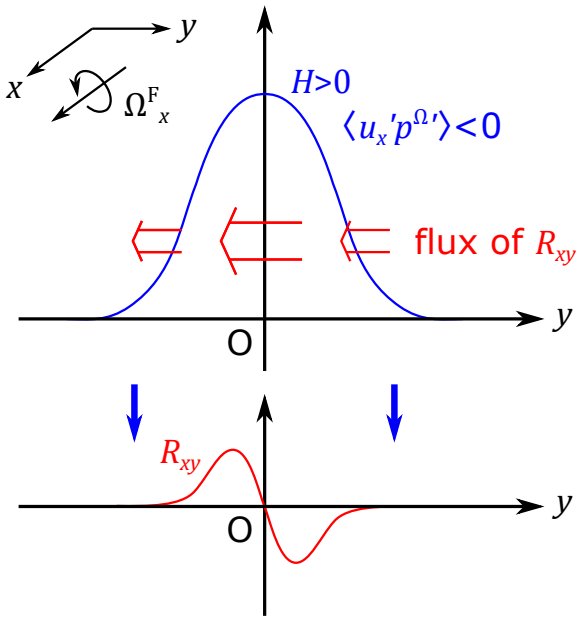

Figure 5.2: Schematic diagram for the Reynolds stress flux in the simulation shown in Chap. 3.

5.3 Proposition of new non-dimensional parameter associated with helicity

According to the model given by Eq. (4.2), it is expected that the energy flux due to the rotational pressure $\langle u_i' p^{\Omega\prime} \rangle$ plays a significant role when not only the system rotation but also the turbulent helicity exists in the turbulent flow. In the conventional rotating turbulence, the Rossby number Ro[$= U/(L\Omega^{\mathrm{F}})$] is used for representing the intensity of rotation in the turbulent flow where U and L denote the characteristic velocity and length scale, respectively. For inhomogeneous turbulence, however, the significance of the energy flux due to the rotational pressure discussed in this study cannot be expressed in terms of the conventional Rossby number; namely, the energy flux due to the rotational pressure can be zero when the turbulent helicity is zero even if the Rossby number is small. Hence, a new non-dimensional parameter associated with the turbulent helicity is needed for judging the significance of the energy flux due to the rotational pressure for general turbulent flows. Yokoi & Brandenburg (2016) discussed the importance of the ratio of the helicity term to the eddy-viscosity term in the model given by Eq. (2.76) expressed by

$$\frac{|\eta^{\mathrm{T}} 2\Omega^{\mathrm{F}} \boldsymbol{\nabla} H|}{|\nu^{\mathrm{T}} \boldsymbol{\nabla} \boldsymbol{U}|}. \tag{5.9}$$

This value must be useful for judging the effect of the turbulent helicity on the mean velocity or the Reynolds stress. This ratio can be also interpreted as the ratio of the pressure diffusion associated with the rotation to the production term in the Reynolds stress transport equation,

$$\frac{|\eta^{\mathrm{T}} 2\Omega^{\mathrm{F}} \boldsymbol{\nabla} H|}{|\nu^{\mathrm{T}} \boldsymbol{\nabla} \boldsymbol{U}|} \sim \frac{|\Pi_{ij}^{\Omega}|}{|K S_{ij}|}, \tag{5.10}$$

where

$$\Pi_{ij}^{\Omega} = -\frac{\partial}{\partial x_j} \left\langle u_i' p^{\Omega\prime} \right\rangle - \frac{\partial}{\partial x_i} \left\langle u_j' p^{\Omega\prime} \right\rangle. \tag{5.11}$$

In the context of energy flux, $\langle u_i' p^{\Omega\prime} \rangle$ should be compared with the energy flux due to the nonlinearity of turbulence given by $\langle u_i' p^{\mathrm{N}\prime} \rangle + \langle u_i' u_j' u_j'/2 \rangle$. Namely, the ratio given by

$$\frac{|\langle u_i' p^{\mathrm{N}\prime} \rangle + \langle u_i' u_j' u_j'/2 \rangle|}{|\langle u_i' p^{\Omega\prime} \rangle|} \tag{5.12}$$

can be used to judge the significance of the energy flux due to the rotational pressure. Here, we put the rotation dependent value $\langle u_i' p^{\Omega\prime} \rangle$ to the denominator similar to the conventional Rossby number. As discussed in Sec. 4.3.3, the gradient-diffusion approximation gives a good prediction for the energy flux due to the nonlinearity of turbulence. On the other hand, the energy flux due to the rotational pressure is modeled by Eq. (4.12). Thus, we define the helical Rossby number as follows:

$$\mathrm{Ro}^{H} = \left| \frac{(K^2/\varepsilon) \nabla_{\parallel} K}{(K^3/\varepsilon^2) H \Omega^{\mathrm{A}}} \right| = \left| \frac{\varepsilon \nabla_{\parallel} K}{K H \Omega^{\mathrm{A}}} \right|, \tag{5.13}$$

where $\nabla_{\parallel}$ denotes the spatial derivative in the direction of the absolute vorticity and $\Omega^{\rm A}$ denotes the absolute value of the absolute vorticity. In contrast to the conventional Rossby number, the helical Rossby number can be infinity when the turbulent helicity vanishes even if the rotation rate is high. This property is appropriate for judging the significance of the energy flux due to the rotational pressure which is associated with the turbulent helicity. Figure 5.3 shows the spatial distribution of the helical Rossby number given by Eq. (5.13) for each run at $2\Omega^{\rm F}t = 2$ in the simulation shown in Chap. 4. It can be seen that the value of Ro^H decreases as the rotation rate increases at $|z| \simeq 1$ in which the energy flux due to the rotational pressure is maximum (see Figs. 4.10 or 4.11). For the model constants, $C_\nu/\sigma_K = 0.22$ is appropriate for the gradient-diffusion approximation given by Eq. (4.11), while $C_{PDH} = 0.03$ for the newly proposed model. In this sense, $(0.22/0.03)\mathrm{Ro}^H \simeq 1$, that is $\mathrm{Ro}^H \simeq 0.03/0.22 (\simeq 0.14)$ can be a criterion of the energy flux due to the rotation and the turbulent helicity exceeds the flux expressed by the gradient-diffusion approximation. In fact, Ro^H is comparable to 0.14 at $|z| \simeq 1$ for runs r08 and r1, while it is smaller than 0.14 for runs r2 and r5 in which the time evolution of the width of the turbulence region is very close to the linear inviscid solution [see Fig. 4.4(b)].

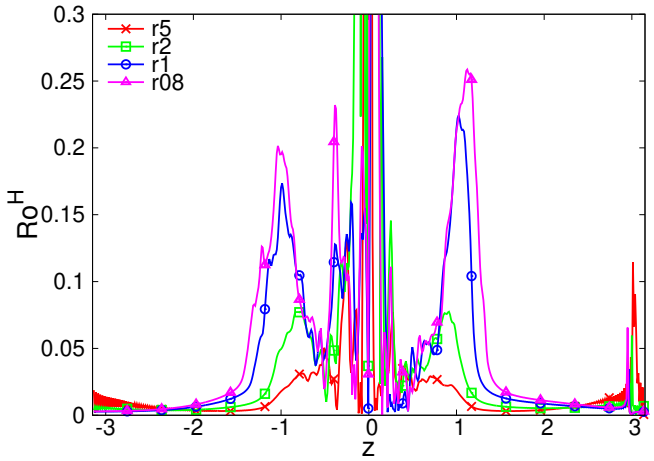

Figure 5.3: Spatial distribution of the helical Rossby number given by Eq. (5.13) for each run at $2\Omega^{\rm F}t = 2$ in the simulation shown in Chap. 4.

Although the physical meaning of the helical Rossby number given by Eq. (5.13) is clear, it is somewhat complex since it involves the spatial derivative. Here, we define the simplified helical Rossby number as

$$\mathrm{Ro}_{\rm s}^H = \left| \frac{\varepsilon^2}{K^{3/2} H \Omega^{\rm A}} \right|. \tag{5.14}$$

Figure 5.4 shows the spatial distribution of the simplified helical Rossby number given by Eq. (5.14) for each run at $2\Omega^{\rm F}t = 2$ in the simulation shown in Chap. 4. It is seen that $\mathrm{Ro}_{\rm s}^H$ also decreases as the rotation rate increases at $|z| \simeq 1$ similar to Ro^H shown in Fig. 5.3. Therefore, the simplified Rossby number is also expected to be useful for judging the significance of the energy flux due to the rotational pressure which is associated with the turbulent helicity.

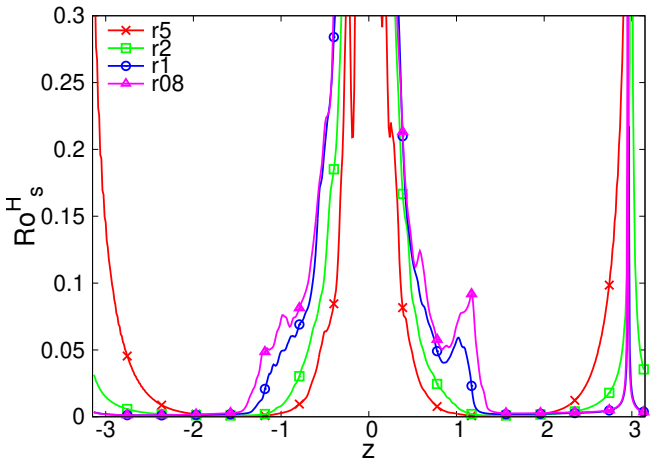

Figure 5.4: Spatial distribution of the simplified helical Rossby number given by Eq. (5.14) for each run at $2\Omega^{\mathrm{F}}t = 2$ in the simulation shown in Chap. 4.

5.4 Application of the model involving the turbulent helicity

In this paper, the mechanism that the turbulent helicity affects the Reynolds stress transport was clarified. This result suggests the significance to consider the effect of the turbulent helicity on the Reynolds stress and the turbulent energy transport in applying the RANS model to the turbulent flows accompanied with rotation or swirling motion. Especially, the effect of the turbulent helicity on the turbulent energy transport discussed in Chap. 4 is not considered in the previous studies. By using the model for the Reynolds stress given by Eqs. (2.76) or (3.35) and for the turbulent energy diffusion given by Eq. (4.1) in which they involve the turbulent helicity, the accuracy of the RANS model in predicting the turbulent flows accompanied with rotation or swirling motion is expected to be improved. Namely, it enables us to predict high-Reynolds-number turbulent flows accompanied with swirling motion such as the wake vortices behind an aircraft [Spalart (1998)] or supercell in meteorological flow [Lilly (1986); Noda & Niino (2010)] with much smaller numerical cost than using the DNS. However, we should remark the following points in applying the RANS model involving the turbulent helicity.

In the application of the RANS model involving the turbulent helicity, we have to determine the value of the turbulent helicity in the subject flow. One of the useful way of evaluating the value of the turbulent helicity is to solve its transport equation given by Eqs. (2.26) and (2.27a)–(2.27g). However, we have to develop the closed model for ε^H [Eq. (2.27b)], Π^H [Eq. (2.27c)], and T^H [Eq. (2.27d)] in order to numerically solve the transport equation for the turbulent helicity. Yokoi & Yoshizawa (1993) proposed the model for the transport equation for the turbulent helicity and they applied its model to the turbulent swirling flow in a straight pipe. In their modeling, the flux of the turbulent helicity is modeled by using the gradient diffusion approximation. However, it is expected that the effect of rotation appears through $\langle \omega_j' p' \rangle$ in Π^H as the effect of rotation on the turbulent energy transport appears through $\langle u_j' p' \rangle$. Namely, further discussion for modeling the transport equation for the turbulent helicity is needed. Moreover,

the effect of the turbulent helicity and the rotation on the turbulent energy dissipation rate ε should be examined in detail. The effect of anisotropy discussed in Sec. 5.1.1 should be also discussed.

When we consider a high speed turbulent flow such as the wake vortices behind an aircraft [Spalart (1998)], the effect of compressibility of fluid becomes significant. For compressible fluid, the effect of the dilatation $\boldsymbol{\nabla} \cdot \boldsymbol{u}$ or the spatiotemporal change of the mass density are added to the Poisson equation for the pressure given by Eq. (2.17). In such a case, however, the effect of rotation does not change its form. Namely, the modeling proposed in this study given by Eqs. (3.31), (3.32), (3.31), and (4.1) will hold although other effects associated with the compressibility will be added to the terms related to the pressure fluctuation.

Chapter 6

Summary and conclusions

In this study, we revealed the mechanism that the turbulent helicity affects the Reynolds stress. In the previous studies, it has been discussed the relationship between helicity and the vortex dynamo effect, which describes the large-scale local velocity generation. However, the mechanism that helicity affects the mean velocity is not clarified. The numerical simulation of rotating turbulence in which the turbulent helicity is injected locally in space was performed. In this simulation, the mean velocity in the direction of the rotation axis was generated only when the rotation rate is non-zero and the turbulent helicity is injected. The budget for the transport equation for the Reynolds stress was investigated to clarify the source of the mean velocity. As a result, the pressure diffusion term, which is the spatial derivative of the correlation between the velocity and the pressure fluctuations, has a significant contribution to the phenomenon of the axial mean velocity generation. It was revealed that the pressure diffusion term can be expressed in terms of the turbulent helicity. The general model for the pressure diffusion term accompanied with the turbulent helicity was proposed by means of the statistical turbulence closure theory, the TSDIA. By considering the effect of the pressure diffusion, we obtained the model for the Reynolds stress accompanied with the turbulent helicity, which had been proposed by the previous study. The model for the Reynolds stress accompanied with the turbulent helicity can account for the axial mean velocity generation phenomenon without contradiction to the simulation results. In the conventional turbulence modeling, the pressure diffusion term had been neglected. However, it had a leading contribution in the present simulation. In this sense, the present study pointed out the critical shortfalls of the conventional turbulence models for rotating turbulence accompanied with the turbulent helicity.

In rotating turbulence, it was known that the turbulent energy is transferred faster in the direction of the rotation axis than in the non-rotating case. The conventional turbulence model for energy flux described by the gradient-diffusion approximation cannot predict this fast energy transport in the direction of the rotation axis. The newly proposed model for the pressure diffusion term accompanied with the turbulent helicity is expected to account for this fast energy transport phenomenon in rotating turbulence. We performed the numerical simulation of decaying inhomogeneous turbulence in a rotating system. As a result, it was shown that the pressure diffusion term associated with the system rotation had a significant contribution to the fast energy transport in rotating turbulence. The newly proposed model in this study

succeeded in predicting the energy flux due to the pressure associated with the rotation, which is referred to as the rotational pressure. Although the model had a tendency to overestimate the value due to the immature state of turbulence in the scale space, the consistency of the present model for fully developed turbulence was suggested.

We extend the previous turbulence modeling based on the Reynolds stress transport to the model accompanied with the turbulent helicity. Then, we propose a more general algebraic model for the Reynolds stress accompanied with the turbulent helicity. This model is expected to play significant roles for anisotropic and helical turbulent flows. The value of the model constant for the newly proposed term associated with the turbulent helicity estimated in the present study was confirmed to be acceptable from the theoretical viewpoint. The physical mechanism of the correlation between the velocity and the rotational pressure fluctuations was discussed. It was shown that the correlation between the velocity and the rotational pressure fluctuations is tightly connected to the group velocity of inertial waves governed by the linearized equation. The relationship between the velocity–rotational-pressure correlation and the turbulent helicity was discussed in a statistical viewpoint. It was discussed that the correlation between the velocity and the rotational pressure fluctuations can be interpreted as a flux of the Reynolds stress, leading to the mean velocity generation phenomenon. Finally, we define the helical Rossby number as an index for judging the significance of the energy flux due to the rotational pressure in general turbulent flows. In contrast to the conventional Rossby number, the helical Rossby number involves the turbulent helicity. Owing to this property, the helical Rossby number can be infinite when the turbulent helicity is zero even if the rotation rate is high. Using the helical Rossby number, we can judge the significance of the energy flux due to the rotational pressure for general turbulent flows.

Acknowledgment

The author acknowledges to Prof. Fujihiro Hamba for generous supports and encouragements. The author also acknowledges to Dr. Nobumitsu Yokoi for valuable comments and discussion. The author is grateful to the members of the Hamba group for many supports during my graduate school days.

Appendix

A Derivation of the Navier–Stokes equation in a rotating system

Let us consider a rotating system with a constant angular velocity $\{\boldsymbol{x}^\dagger\}$ relative to a static system $\{\boldsymbol{x}\}$. We can set the axis of the angular velocity in the z direction without loss of generality. Hence, the transformation rule between the systems $\{\boldsymbol{x}^\dagger\}$ and $\{\boldsymbol{x}\}$ is written as

$$\boldsymbol{x}^\dagger = \mathbf{Q}\boldsymbol{x} = \begin{bmatrix} \cos(\Omega^{\mathrm{F}} t) & \sin(\Omega^{\mathrm{F}} t) & 0 \\ -\sin(\Omega^{\mathrm{F}} t) & \cos(\Omega^{\mathrm{F}} t) & 0 \\ 0 & 0 & 1 \end{bmatrix} \boldsymbol{x}, \tag{A1}$$

where Ω^{F} denotes the absolute value of the angular velocity of the system rotation. Schematic diagram for the transformation between the systems $\{\boldsymbol{x}^\dagger\}$ and $\{\boldsymbol{x}\}$ is shown in Fig. A1. Since we consider the transformation between the two Cartesian coordinates, the effect of curvature of the coordinate is not included.

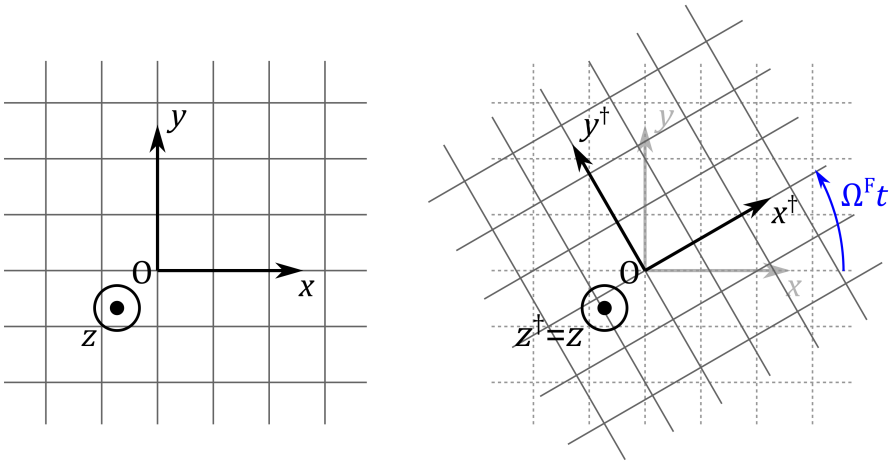

Figure A1: Schematic diagram for the transformation between the systems $\{\boldsymbol{x}^\dagger\}$ and $\{\boldsymbol{x}\}$.

The Eulerian velocity in the $\{\boldsymbol{x}\}$ system $\boldsymbol{u}(\boldsymbol{x})$ is expressed as

$$\boldsymbol{u}(\boldsymbol{x}) \equiv \lim_{\Delta t \to 0} \frac{\Delta \boldsymbol{x}}{\Delta t}, \tag{A2}$$

while the Eulerian velocity in the $\{\boldsymbol{x}^\dagger\}$ system $\boldsymbol{u}^\dagger(\boldsymbol{x}^\dagger)$ is written as

$$\boldsymbol{u}^\dagger(\boldsymbol{x}^\dagger) \equiv \lim_{\Delta t \to 0} \frac{\Delta \boldsymbol{x}^\dagger}{\Delta t} = \lim_{\Delta t \to 0} \frac{\Delta (\mathsf{Q}\boldsymbol{x})}{\Delta t} = \lim_{\Delta t \to 0} \frac{\Delta \mathsf{Q}}{\Delta t}\boldsymbol{x} + \mathsf{Q} \lim_{\Delta t \to 0} \frac{\Delta \boldsymbol{x}}{\Delta t}. \tag{A3}$$

Here we have

$$\lim_{\Delta t \to 0} \frac{\Delta \mathsf{Q}}{\Delta t} = \Omega^{\mathrm{F}} \begin{bmatrix} -\sin(\Omega^{\mathrm{F}} t) & \cos(\Omega^{\mathrm{F}} t) & 0 \\ -\cos(\Omega^{\mathrm{F}} t) & -\sin(\Omega^{\mathrm{F}} t) & 0 \\ 0 & 0 & 0 \end{bmatrix} = \Omega^{\mathrm{F}} \begin{bmatrix} 0 & 1 & 0 \\ -1 & 0 & 0 \\ 0 & 0 & 0 \end{bmatrix} \mathsf{Q}. \tag{A4}$$

Alternatively, we can write $\lim_{\Delta t \to 0} \Delta Q_{ij}/\Delta t = \epsilon_{i\ell 3} \Omega^{\mathrm{F}} Q_{\ell j}$. Hence, Eq. (A3) reads

$$\begin{aligned} & u_i^\dagger(\boldsymbol{x}^\dagger) = \epsilon_{ij3} \Omega^{\mathrm{F}} Q_{j\ell} x_\ell + Q_{ij} u_j(\boldsymbol{x}) \\ & \Leftrightarrow Q_{ij} u_j(\boldsymbol{x}) = u_i^\dagger(\boldsymbol{x}^\dagger) - \epsilon_{ij3} \Omega^{\mathrm{F}} x_j^\dagger. \end{aligned} \tag{A5}$$

Equation (A5) can be generalized as

$$\mathsf{Q}\boldsymbol{u}(\boldsymbol{x}) = \boldsymbol{u}^\dagger(\boldsymbol{x}^\dagger) - \boldsymbol{x}^\dagger \times \boldsymbol{\Omega}^{\mathrm{F}}. \tag{A6}$$

Equation (A6) denotes the transformation rule for the velocity between the $\{\boldsymbol{x}\}$ and $\{\boldsymbol{x}^\dagger\}$ systems. The Lagrangian derivative d/dt of the velocity in a static system can be written as

$$\frac{d\boldsymbol{u}}{dt}(\boldsymbol{x}) \equiv \lim_{\Delta t \to 0} \frac{\Delta \boldsymbol{u}(\boldsymbol{x})}{\Delta t} = \frac{\partial \boldsymbol{u}}{\partial t}(\boldsymbol{x}) + [\boldsymbol{u}(\boldsymbol{x}) \cdot \boldsymbol{\nabla}]\, \boldsymbol{u}(\boldsymbol{x}). \tag{A7}$$

The Lagrangian derivative of the velocity in a rotating system reads

$$\begin{aligned} \frac{d\boldsymbol{u}^\dagger}{dt}(\boldsymbol{x}^\dagger) \equiv \lim_{\Delta t \to 0} \frac{\Delta \boldsymbol{u}^\dagger(\boldsymbol{x}^\dagger)}{\Delta t} &= \frac{\partial \boldsymbol{u}^\dagger}{\partial t}(\boldsymbol{x}^\dagger) + \left[\boldsymbol{u}^\dagger(\boldsymbol{x}^\dagger) \cdot \boldsymbol{\nabla}^\dagger\right] \boldsymbol{u}^\dagger(\boldsymbol{x}^\dagger) \\ &= \lim_{\Delta t \to 0} \frac{\Delta \mathsf{Q}}{\Delta t} \boldsymbol{u}(\boldsymbol{x}) + \mathsf{Q} \lim_{\Delta t \to 0} \frac{\Delta \boldsymbol{u}}{\Delta t}(\boldsymbol{x}) + \lim_{\Delta t \to 0} \frac{\Delta \boldsymbol{x}^\dagger}{\Delta t} \times \boldsymbol{\Omega}^{\mathrm{F}} \\ &= [\mathsf{Q}\boldsymbol{u}(\boldsymbol{x})] \times \boldsymbol{\Omega}^{\mathrm{F}} + \mathsf{Q} \frac{d\boldsymbol{u}}{dt}(\boldsymbol{x}) + \boldsymbol{u}^\dagger(\boldsymbol{x}^\dagger) \times \boldsymbol{\Omega}^{\mathrm{F}} \\ &= 2\boldsymbol{u}^\dagger(\boldsymbol{x}^\dagger) \times \boldsymbol{\Omega}^{\mathrm{F}} - \left(\boldsymbol{x}^\dagger \times \boldsymbol{\Omega}^{\mathrm{F}}\right) \times \boldsymbol{\Omega}^{\mathbf{F}} + \mathsf{Q} \frac{d\boldsymbol{u}}{dt}(\boldsymbol{x}). \end{aligned} \tag{A8}$$

Hence, the transformation rule for the Lagrangian derivative of the velocity between the $\{\boldsymbol{x}\}$ and $\{\boldsymbol{x}^\dagger\}$ systems is written as

$$\mathsf{Q} \frac{d\boldsymbol{u}}{dt}(\boldsymbol{x}) = \frac{d\boldsymbol{u}^\dagger}{dt}(\boldsymbol{x}^\dagger) - 2\boldsymbol{u}^\dagger(\boldsymbol{x}^\dagger) \times \boldsymbol{\Omega}^{\mathrm{F}} + \left(\boldsymbol{x}^\dagger \times \boldsymbol{\Omega}^{\mathrm{F}}\right) \times \boldsymbol{\Omega}^{\mathrm{F}}. \tag{A9}$$

Under the transformation rule given by Eq. (A1), the pressure and the viscous terms in the Navier–Stokes equation are transformed as

$$\frac{\partial p}{\partial x_i^\dagger}(\boldsymbol{x}^\dagger) = Q_{ji}^{-1}\frac{\partial}{\partial x_j}p(\boldsymbol{x}) = Q_{ij}\frac{\partial p}{\partial x_j}(\boldsymbol{x}), \tag{A10}$$

$$\nu\nabla^{\dagger 2}u_i^\dagger(\boldsymbol{x}^\dagger) = \nu Q_{\ell a}^{-1}Q_{ma}^{-1}\frac{\partial^2}{\partial x_\ell \partial x_m}\left[Q_{ij}u_j(\boldsymbol{x})\right] + \nu\nabla^{\dagger 2}\left(\epsilon_{ijn}x_j^\dagger\Omega_n^{\mathrm{F}}\right) = Q_{ij}\nu\nabla^2 u_j(\boldsymbol{x}), \tag{A11}$$

where use is made of $Q_{ji} = Q_{ij}^{-1}$, $Q_{i\ell}Q_{\ell j}^{-1} = \delta_{ij}$, and $p(\boldsymbol{x}) = p^\dagger(\boldsymbol{x}^\dagger) = p(\boldsymbol{x}^\dagger)$. Thus, under the transformation rule given by Eq. (A1), the Navier–Stokes equation is transformed as

$$\begin{aligned}&\mathsf{Q}\left[\frac{d\boldsymbol{u}}{dt}(\boldsymbol{x}) + \boldsymbol{\nabla}p(\boldsymbol{x}) - \nu\nabla^2\boldsymbol{u}(\boldsymbol{x})\right]\\ &= \frac{d\boldsymbol{u}^\dagger}{dt}(\boldsymbol{x}^\dagger) - 2\boldsymbol{u}^\dagger(\boldsymbol{x}^\dagger)\times\boldsymbol{\Omega}^{\mathrm{F}} + \left(\boldsymbol{x}^\dagger\times\boldsymbol{\Omega}^{\mathrm{F}}\right)\times\boldsymbol{\Omega}^{\mathrm{F}} + \boldsymbol{\nabla}^\dagger p(\boldsymbol{x}^\dagger) - \nu\nabla^{\dagger 2}\boldsymbol{u}^\dagger(\boldsymbol{x}^\dagger) = 0.\end{aligned} \tag{A12}$$

Note that third term on the right-hand side of Eq. (A12) can be rewritten as follows [Yoshizawa (1998)]:

$$\left(\boldsymbol{x}^\dagger\times\boldsymbol{\Omega}^{\mathrm{F}}\right)\times\boldsymbol{\Omega}^{\mathrm{F}} = \left(\boldsymbol{\Omega}^{\mathrm{F}}\cdot\boldsymbol{x}^\dagger\right)\boldsymbol{\Omega}^{\mathrm{F}} - \left(\Omega^{\mathrm{F}}\right)^2\boldsymbol{x} = \frac{1}{2}\boldsymbol{\nabla}\left[\left(\boldsymbol{\Omega}^{\mathrm{F}}\cdot\boldsymbol{x}^\dagger\right)^2 - \left(\Omega^{\mathrm{F}}\right)^2 x^{\dagger 2}\right] = -\frac{1}{2}\boldsymbol{\nabla}\left(\boldsymbol{\Omega}^{\mathrm{F}}\times\boldsymbol{x}^\dagger\right)^2. \tag{A13}$$

Finally, the Navier–Stokes equation in a rotating system is written as

$$\frac{\partial u_i}{\partial t} + u_j\frac{\partial u_i}{\partial x_j} = \frac{\partial u_i}{\partial t} + \frac{\partial}{\partial x_j}(u_iu_j) = -\frac{\partial p^{\mathrm{tot}}}{\partial x_i} + \nu\nabla^2 u_i + 2\epsilon_{ij\ell}u_j\Omega_\ell^{\mathrm{F}}, \tag{A14}$$

where † is omitted, the incompressible condition $\boldsymbol{\nabla}\cdot\boldsymbol{u} = 0$ is used, and $p^{\mathrm{tot}} = p - (\boldsymbol{\Omega}^{\mathrm{F}}\times\boldsymbol{x})^2/2$.

B Covariance for the transport equation and the algebraic model for the Reynolds stress

The straightforward extension of the nonlinear eddy-viscosity model given by Eq. (2.58) to the rotating system is written as

$$\begin{aligned}R_{ij} = {}&\frac{2}{3}K\delta_{ij} - 2\nu^{\mathrm{T}}S_{ij} + \zeta_{SS}\left[S_{i\ell}S_{\ell j}\right]_{\mathrm{D}} + \zeta_{SW}\left(S_{i\ell}W_{\ell j} + S_{j\ell}W_{\ell i}\right)\\ &+ \zeta_{SSW}\left(S_{i\ell}S_{\ell m}W_{mj} + S_{j\ell}S_{\ell m}W_{mi}\right) + \cdots,\end{aligned} \tag{B1}$$

However, the extension of the modeling proposed by Pope (1975) to the rotating system gives the different model; namely, W_{ij}^{N} in Eq. (2.58) is replaced by $W_{ij}^{\times} = W_{ij}^{\mathrm{N}} - C\epsilon_{ij\ell}\Omega_\ell^{\mathrm{F}}$ where $C \neq 1$ [Gatski & Speziale (1993); Wallin & Johanson (2000)]. This result is inconsistent with the Euclidean invariance, which is the invariance under the transformation by the system rotation [Weis & Hutter (2003); Hamba (2006)], or the

covariance of the Reynolds stress [Ariki (2015)]. This inconsistency comes from the fact that the weak-equilibrium assumption, $D(R_{ij}/K)/Dt = 0$, violates the Euclidean invariance [Weis & Hutter (2003); Hamba (2006)]. Since the covariance of physical quantities is tightly connected to their objectivity, it is significant to consider the covariance of the model for the Reynolds stress itself or its transport equation. Ariki (2015) discussed more general class of invariance of the fluid system involving the Reynolds stress and its transport. Here, we adopt the upper convected derivative which is generally covariant time derivative under the coordinate transformation [see, e.g., Speziale (1987); Ariki (2015)]. The mean upper convected derivative of the second rank tensor A_{ij}, $\mathfrak{D}A_{ij}/\mathfrak{D}t$, is defined in the Cartesian coordinates as

$$\frac{\mathfrak{D}A_{ij}}{\mathfrak{D}t} = \frac{\partial A_{ij}}{\partial t} + U_\ell \frac{\partial A_{ij}}{\partial x_\ell} - \frac{\partial U_i}{\partial x_\ell} A_{\ell j} - \frac{\partial U_j}{\partial x_\ell} A_{i\ell}. \tag{B2}$$

Hence, the modeled transport equation for the deviatoric part of the Reynolds stress given by Eq. (2.54) is rewritten as follows:

$$\begin{aligned}\left[\frac{\mathfrak{D}B_{ij}}{\mathfrak{D}t}\right]_{\mathrm{D}} &= -C_{S1}\frac{\varepsilon}{K}B_{ij} - \left(\frac{4}{3} - C_{R1}\right) K S_{ij} - (2 - C_{R2})\left[S_{i\ell}B_{\ell j} + S_{j\ell}B_{\ell i}\right]_{\mathrm{D}} \\ &\quad - (2 - C_{R3})\left(W_{i\ell}B_{\ell j} + W_{j\ell}B_{\ell i}\right) \\ &\quad + \frac{\partial}{\partial x_\ell}\left[C_D \frac{K}{\varepsilon}\left(R_{im}\frac{\partial R_{j\ell}}{\partial x_m} + R_{jm}\frac{\partial R_{i\ell}}{\partial x_m} + R_{\ell m}\frac{\partial R_{ij}}{\partial x_m}\right)\right]_{\mathrm{D}} + \nu\nabla^2 B_{ij} + \left[F_{ij}\right]_{\mathrm{D}}. \end{aligned} \tag{B3}$$

Here, each term in Eq. (B3) is written in a covariant form. When the quasi-homogeneity condition is assumed and the external work is assumed to be neglected, Eq. (B3) is reduced to

$$\begin{aligned} B_{ij} = &-\frac{4 - 3C_{R1}}{3C_{S1}}\frac{K^2}{\varepsilon}S_{ij} \\ &- \frac{2 - C_{R2}}{C_{S1}}\frac{K}{\varepsilon}\left[S_{i\ell}B_{\ell j} + S_{j\ell}B_{\ell i}\right]_{\mathrm{D}} - \frac{2 - C_{R3}}{C_{S1}}\frac{K}{\varepsilon}\left(W_{i\ell}B_{\ell j} + W_{j\ell}B_{\ell i}\right) - \frac{1}{C_{S1}}\frac{K}{\varepsilon}\left[\frac{\mathfrak{D}B_{ij}}{\mathfrak{D}t}\right]_{\mathrm{D}}. \end{aligned} \tag{B4}$$

Note that the weak-equilibrium assumption is not adopted. Substituting this expression iteratively into B_{ij} on the right-hand side, we can obtain the algebraic Reynolds stress model satisfying the covariance:

$$\begin{aligned} B_{ij} = &-2\nu^{\mathrm{T}}S_{ij} + \zeta_{SS}\left[S_{i\ell}S_{\ell j}\right]_{\mathrm{D}} - \zeta_{SW}\left(S_{i\ell}W_{\ell j} + S_{j\ell}W_{\ell i}\right) \\ &+ \zeta_{SSW}\left(S_{i\ell}S_{\ell m}W_{mj} + S_{j\ell}S_{\ell m}W_{mi}\right) + \zeta_{DS}\left[\frac{\mathfrak{D}S_{ij}}{\mathfrak{D}t}\right]_{\mathrm{D}} + \cdots. \end{aligned} \tag{B5}$$

The last term in Eq. (B4) denotes the history effect of the mean strain on the Reynolds stress which was discussed in the context of the nonequilibrium effect [Hamilington & Dahm (2008)] and theoretically obtained [Ariki (2014, 2018)].

C Details for calculations of the TSDIA

C.1 Each order equation in the TSDIA

Under the two-scale expansion given by Eqs. (2.60) and (2.61), the incompressible condition for the mean velocity and the velocity fluctuation are rewritten as

$$\frac{\partial U_i}{\partial X_i} = 0, \quad \frac{\partial u_i'}{\partial \xi_i} + \delta \frac{\partial u_i'}{\partial X_i} = 0. \tag{C1}$$

The momentum equation for the velocity fluctuation given by (2.20) is similarly rewritten as follows:

$$\begin{aligned} &\frac{\partial u_i'}{\partial \tau} + U_j \frac{\partial u_i'}{\partial \xi_j} + \frac{\partial}{\partial \xi_j}(u_i' u_j') + \frac{\partial p'}{\partial \xi_i} - \nu \frac{\partial^2 u_i'}{\partial \xi_j \partial \xi_j} - 2\epsilon_{ij\ell} u_j' \Omega_\ell^{\mathrm{F}} \\ &= \delta \left[-u_j' \frac{\partial U_i}{\partial X_j} - \frac{D u_i'}{DT} - \frac{\partial p'}{\partial X_i} - \frac{\partial}{\partial X_j}(u_i' u_j' - R_{ij}) + \nu \frac{\partial^2 u_i'}{\partial \xi_j \partial X_j} \right] + \delta^2 \nu \frac{\partial^2 u_i'}{\partial X_j \partial X_j}, \end{aligned} \tag{C2}$$

where

$$\frac{D}{DT} = \frac{\partial}{\partial T} + U_j \frac{\partial}{\partial X_j}, \tag{C3}$$

and the external forcing is neglected for simplicity of theoretical treatment. Substituting the parameter expansion given by Eq. (2.62) and the Fourier transformation given by Eqs. (2.63) and (2.64) into Eqs. (C1) and (C2), $O(\delta^0 |\Omega^{\mathrm{F}}|^0)$ field equations read

$$k_i \tilde{u}_i^{(00)}(\boldsymbol{k}; \tau) = 0, \tag{C4}$$

$$\frac{\partial \tilde{u}_i^{(00)}}{\partial t}(\boldsymbol{k}; \tau) = -ik_j \int \mathrm{d}\boldsymbol{p} \int \mathrm{d}\boldsymbol{q}\ \delta(\boldsymbol{k} - \boldsymbol{p} - \boldsymbol{q}) \tilde{u}_i^{(00)}(\boldsymbol{p}; \tau) \tilde{u}_j^{(00)}(\boldsymbol{q}; \tau) - ik_i \tilde{p}^{(00)}(\boldsymbol{k}; \tau) - \nu k^2 \tilde{u}_i^{(00)}(\boldsymbol{k}; \tau). \tag{C5}$$

Here and hereafter, the dependence on slow variables $(\boldsymbol{X}; T)$ are omitted. Equations (C4) and (C5) correspond to the original continuity equation and the Navier–Stokes equation in the Fourier space given by Eqs. (2.34) and (2.35) with $\boldsymbol{\Omega}^{\mathrm{F}} = 0$, except for the dependence on the slow variables $(\boldsymbol{X}; T)$. The pressure $\tilde{p}^{(00)}(\boldsymbol{k}; \tau)$ can be calculated from Eqs. (C4) and (C5) as

$$\tilde{p}^{(00)}(\boldsymbol{k}; \tau) = -\frac{k_i k_j}{k^2} \int \mathrm{d}\boldsymbol{p} \int \mathrm{d}\boldsymbol{q}\ \delta(\boldsymbol{k} - \boldsymbol{p} - \boldsymbol{q}) \tilde{u}_i^{(00)}(\boldsymbol{p}; \tau) \tilde{u}_j^{(00)}(\boldsymbol{q}; \tau) \tag{C6}$$

Then, Eq. (C5) is rewritten as

$$\frac{\partial \tilde{u}_i^{(00)}}{\partial \tau}(\boldsymbol{k}; \tau) = -iM_{ij\ell}(\boldsymbol{k}) \int \mathrm{d}\boldsymbol{p} \int \mathrm{d}\boldsymbol{q}\ \delta(\boldsymbol{k} - \boldsymbol{p} - \boldsymbol{q}) \tilde{u}_j^{(00)}(\boldsymbol{p}; \tau) \tilde{u}_\ell^{(00)}(\boldsymbol{q}; \tau) - \nu k^2 \tilde{u}_i^{(00)}(\boldsymbol{k}; \tau), \tag{C7}$$

where $M_{ij\ell}(\boldsymbol{k})$ is already defined in Eq. (2.38). For $O(\delta^n|\Omega^{\rm F}|^m)$ fields with $n > 0$, the incompressible condition is not written as $k_i\tilde{u}_i^{(nm)} = 0$ but

$$ik_i\tilde{u}_i^{(nm)}(\boldsymbol{k};\tau) + \frac{\partial\tilde{u}_i^{(n-1,m)}}{\partial X_i^{\rm I}}(\boldsymbol{k};\tau) = 0, \tag{C8}$$

where

$$\frac{\partial}{\partial X_i^{\rm I}} = {\rm e}^{i\boldsymbol{k}\cdot\boldsymbol{U}\tau}\frac{\partial}{\partial X_i}{\rm e}^{-i\boldsymbol{k}\cdot\boldsymbol{U}\tau}. \tag{C9}$$

Hence, $\tilde{\boldsymbol{u}}^{(nm)}(\boldsymbol{k};\tau)$ does not satisfy the solenoidal condition in $\boldsymbol{k}$ space. This shortfall can be resolved by introducing the following velocity $\tilde{\boldsymbol{u}}^{{\rm S}(nm)}(\boldsymbol{k};\tau)$ [Hamba (1987)]:

$$\tilde{u}_i^{{\rm S}(nm)}(\boldsymbol{k};\tau) = \tilde{u}_i^{(nm)}(\boldsymbol{k};\tau) - i\frac{k_i}{k^2}\frac{\partial\tilde{u}_j^{(n-1,m)}}{\partial X_j^{\rm I}}(\boldsymbol{k};\tau), \tag{C10}$$

where this velocity satisfies $k_i\tilde{u}_i^{{\rm S}(nm)}(\boldsymbol{k};\tau) = 0$. Equations for $O(\delta^0|\Omega^{\rm F}|)$, $O(\delta|\Omega^{\rm F}|^0)$, and $O(\delta|\Omega^{\rm F}|)$ are written as follows:

$$\begin{aligned}
&\frac{\partial\tilde{u}_i^{(01)}}{\partial t}(\boldsymbol{k};\tau) + 2iM_{ij\ell}(\boldsymbol{k})\int{\rm d}\boldsymbol{p}\int{\rm d}\boldsymbol{q}\;\delta(\boldsymbol{k}-\boldsymbol{p}-\boldsymbol{q})\tilde{u}_j^{(00)}(\boldsymbol{p};\tau)\tilde{u}_\ell^{(01)}(\boldsymbol{q};\tau) + \nu k^2\tilde{u}_i^{(01)}(\boldsymbol{k};\tau) \\
&\qquad = 2M_{in}(\boldsymbol{k})\epsilon_{nj\ell}\tilde{u}_j^{(00)}(\boldsymbol{k};\tau)e_\ell^\Omega, \qquad\qquad (\text{C11}) \\
&\tilde{p}^{(01)}(\boldsymbol{k};\tau) = -\frac{2k_ik_j}{k^2}\int{\rm d}\boldsymbol{p}\int{\rm d}\boldsymbol{q}\;\delta(\boldsymbol{k}-\boldsymbol{p}-\boldsymbol{q})\tilde{u}_i^{(00)}(\boldsymbol{p};\tau)\tilde{u}_j^{(01)}(\boldsymbol{q};\tau) - 2i\epsilon_{ij\ell}\frac{k_i}{k^2}\tilde{u}_j^{(00)}(\boldsymbol{k};\tau)e_\ell^\Omega, \qquad\qquad (\text{C12}) \\
&\frac{\partial\tilde{u}_i^{{\rm S}(10)}}{\partial\tau}(\boldsymbol{k};\tau) + 2iM_{ij\ell}(\boldsymbol{k})\int{\rm d}\boldsymbol{p}\int{\rm d}\boldsymbol{q}\;\delta(\boldsymbol{k}-\boldsymbol{p}-\boldsymbol{q})\tilde{u}_j^{(00)}(\boldsymbol{p};\tau)\tilde{u}_\ell^{{\rm S}(10)}(\boldsymbol{q};\tau) + \nu k^2\tilde{u}_i^{{\rm S}(10)}(\boldsymbol{k};\tau) \\
&\qquad = -M_{ij}(\boldsymbol{k})\tilde{u}_\ell^{(00)}(\boldsymbol{k};\tau)\frac{\partial U_j}{\partial X_\ell} - \frac{D\tilde{u}_i^{(00)}}{DT^{\rm I}}(\boldsymbol{k};\tau) \\
&\qquad\quad - M_{in}(\boldsymbol{k})M_{nj\ell m}(\boldsymbol{k})\frac{\partial}{\partial X_j^{\rm I}}\left[\int{\rm d}\boldsymbol{p}\int{\rm d}\boldsymbol{q}\;\delta(\boldsymbol{k}-\boldsymbol{p}-\boldsymbol{q})\tilde{u}_\ell^{(00)}(\boldsymbol{p};\tau)\tilde{u}_m^{(00)}(\boldsymbol{q};\tau)\right] \\
&\qquad\quad + 2M_{ij\ell}(\boldsymbol{k})\int{\rm d}\boldsymbol{p}\int{\rm d}\boldsymbol{q}\;\delta(\boldsymbol{k}-\boldsymbol{p}-\boldsymbol{q})\tilde{u}_j^{(00)}(\boldsymbol{p};\tau)\frac{q_\ell}{q^2}\frac{\partial\tilde{u}_m^{(00)}}{\partial X_m^{\rm I}}(\boldsymbol{q};\tau) \\
&\qquad\quad - \delta(\boldsymbol{k})\frac{\partial}{\partial X_j}\left\langle u_i^{(00)}u_j^{(00)}\right\rangle + i\nu k_j\frac{\partial\tilde{u}_i^{(00)}}{\partial X_j^{\rm I}}(\boldsymbol{k};\tau), \qquad\qquad (\text{C13}) \\
&\tilde{p}^{(10)}(\boldsymbol{k};\tau) = -\frac{2k_ik_j}{k^2}\int{\rm d}\boldsymbol{p}\int{\rm d}\boldsymbol{q}\;\delta(\boldsymbol{k}-\boldsymbol{p}-\boldsymbol{q})\tilde{u}_i^{(00)}(\boldsymbol{p};\tau)\tilde{u}_j^{(10)}(\boldsymbol{q};\tau) + 2i\frac{k_i}{k^2}\tilde{u}_j^{(00)}(\boldsymbol{k};\tau)\frac{\partial U_i}{\partial X_j} \\
&\qquad\quad + 2i\frac{1}{k^2}M_{ij\ell}(\boldsymbol{k})\frac{\partial}{\partial X_i^{\rm I}}\left[\int{\rm d}\boldsymbol{p}\int{\rm d}\boldsymbol{q}\;\delta(\boldsymbol{k}-\boldsymbol{p}-\boldsymbol{q})\tilde{u}_j^{(00)}(\boldsymbol{p};\tau)\tilde{u}_\ell^{(00)}(\boldsymbol{q};\tau)\right], \qquad\qquad (\text{C14})
\end{aligned}$$

$$\frac{\partial \tilde{u}_i^{\mathrm{S}(11)}}{\partial \tau}(\boldsymbol{k};\tau) + 2iM_{ij\ell}(\boldsymbol{k}) \int \mathrm{d}\boldsymbol{p} \int \mathrm{d}\boldsymbol{q}\ \delta(\boldsymbol{k}-\boldsymbol{p}-\boldsymbol{q}) \tilde{u}_j^{(00)}(\boldsymbol{p};\tau) \tilde{u}_\ell^{\mathrm{S}(11)}(\boldsymbol{q};\tau) + \nu k^2 \tilde{u}_i^{\mathrm{S}(11)}(\boldsymbol{k};\tau)$$
$$= 2i\epsilon_{i\ell m} \frac{k_\ell}{k^2} \frac{\partial \tilde{u}_n^{(00)}}{\partial X_n^{\mathrm{I}}}(\boldsymbol{k};\tau) e_m^\Omega + 2iM_{in}(\boldsymbol{k}) \epsilon_{j\ell m} \frac{k_j}{k^2} \frac{\partial \tilde{u}_\ell^{(00)}}{\partial X_n^{\mathrm{I}}}(\boldsymbol{k};\tau) e_m^\Omega$$
$$- M_{ij}(\boldsymbol{k}) \tilde{u}_\ell^{(01)}(\boldsymbol{k};\tau) \frac{\partial U_j}{\partial X_\ell} - \frac{D\tilde{u}_i^{(01)}}{DT^{\mathrm{I}}}(\boldsymbol{k};\tau)$$
$$- 2iM_{ij\ell}(\boldsymbol{k}) \int \mathrm{d}\boldsymbol{p} \int \mathrm{d}\boldsymbol{q}\ \delta(\boldsymbol{k}-\boldsymbol{p}-\boldsymbol{q}) \tilde{u}_j^{(10)}(\boldsymbol{p};\tau) \tilde{u}_\ell^{(01)}(\boldsymbol{q};\tau)$$
$$- 2M_{in}(\boldsymbol{k}) M_{nj\ell m}(\boldsymbol{k}) \frac{\partial}{\partial X_j^{\mathrm{I}}} \left[\int \mathrm{d}\boldsymbol{p} \int \mathrm{d}\boldsymbol{q}\ \delta(\boldsymbol{k}-\boldsymbol{p}-\boldsymbol{q}) \tilde{u}_\ell^{(00)}(\boldsymbol{p};\tau) \tilde{u}_m^{(01)}(\boldsymbol{q};\tau) \right]$$
$$+ 2M_{ij\ell}(\boldsymbol{k}) \int \mathrm{d}\boldsymbol{p} \int \mathrm{d}\boldsymbol{q}\ \delta(\boldsymbol{k}-\boldsymbol{p}-\boldsymbol{q}) \tilde{u}_j^{(00)}(\boldsymbol{p};\tau) \frac{q_\ell}{q^2} \frac{\partial \tilde{u}_m^{(01)}}{\partial X_m^{\mathrm{I}}}(\boldsymbol{q};\tau)$$
$$- \delta(\boldsymbol{k}) \frac{\partial}{\partial X_j} \left\langle u_i^{(00)} u_j^{(01)} + u_i^{(10)} u_j^{(00)} \right\rangle + i\nu k_j \frac{\partial \tilde{u}_i^{(01)}}{\partial X_j^{\mathrm{I}}}(\boldsymbol{k};\tau), \tag{C15}$$

$$\tilde{p}^{(11)}(\boldsymbol{k};\tau) = -\frac{2k_i k_j}{k^2} \int \mathrm{d}\boldsymbol{p} \int \mathrm{d}\boldsymbol{q}\ \delta(\boldsymbol{k}-\boldsymbol{p}-\boldsymbol{q}) \left[\tilde{u}_i^{(00)}(\boldsymbol{p};\tau) \tilde{u}_j^{(11)}(\boldsymbol{q};\tau) + \tilde{u}_i^{(10)}(\boldsymbol{p};\tau) \tilde{u}_j^{(01)}(\boldsymbol{q};\tau) \right]$$
$$+ 2i \frac{k_i}{k^2} \tilde{u}_j^{(01)}(\boldsymbol{k};\tau) \frac{\partial U_i}{\partial X_j} + 4i \frac{1}{k^2} M_{ij\ell}(\boldsymbol{k}) \frac{\partial}{\partial X_i^{\mathrm{I}}} \left[\int \mathrm{d}\boldsymbol{p} \int \mathrm{d}\boldsymbol{q}\ \delta(\boldsymbol{k}-\boldsymbol{p}-\boldsymbol{q}) \tilde{u}_j^{(00)}(\boldsymbol{p};\tau) \tilde{u}_\ell^{(01)}(\boldsymbol{q};\tau) \right]$$
$$- 2i\epsilon_{i\ell m} \frac{k_i}{k^2} \tilde{u}_\ell^{\mathrm{S}10} e_m^\Omega - 2\epsilon_{n\ell m} \frac{1}{k^2} \left(\delta_{jn} - \frac{2k_j k_n}{k^2} \right) \frac{\partial \tilde{u}_\ell^{(00)}}{\partial X_j^{\mathrm{I}}}(\boldsymbol{k};\tau) e_m^\Omega, \tag{C16}$$

where $\boldsymbol{e}^\Omega (= \boldsymbol{\Omega}^{\mathrm{F}}/\Omega^{\mathrm{F}})$ denotes the unit vector in the direction of the rotation axis,

$$\frac{D}{DT^{\mathrm{I}}} = \mathrm{e}^{i\boldsymbol{k}\cdot\boldsymbol{U}\tau} \frac{D}{DT} \mathrm{e}^{-i\boldsymbol{k}\cdot\boldsymbol{U}\tau}, \tag{C17}$$

and

$$M_{ij\ell m}(\boldsymbol{k}) = \frac{1}{2}\delta_{i\ell}\delta_{jm} + \frac{1}{2}\delta_{im}\delta_{j\ell} - \delta_{ij}\frac{k_\ell k_m}{k^2}. \tag{C18}$$

C.2 Introduction of the response function

The remarkable feature of the DIA is to introduce the response function for the Navier–Stokes equation. The same technique is adopted to the basic $O(\delta^0|\Omega^{\mathrm{F}}|^0)$ field in the TSDIA. When an infinitesimal disturbance $\Delta\tilde{\boldsymbol{f}}$ is added to the basic field equation given by Eq. (C7), the equation for the linearized disturbed velocity $\Delta\tilde{\boldsymbol{u}}$ reads

$$\frac{\partial \Delta\tilde{u}_i}{\partial \tau}(\boldsymbol{k};\tau) + 2iM_{ij\ell}(\boldsymbol{k}) \int \mathrm{d}\boldsymbol{p} \int \mathrm{d}\boldsymbol{q}\ \delta(\boldsymbol{k}-\boldsymbol{p}-\boldsymbol{q}) \tilde{u}_j^{(00)}(\boldsymbol{p};\tau) \Delta\tilde{u}_\ell(\boldsymbol{q};\tau) + \nu k^2 \Delta\tilde{u}_i(\boldsymbol{k};\tau) = M_{ij}(\boldsymbol{k}) \Delta\tilde{f}_j(\boldsymbol{k};\tau), \tag{C19}$$

where $M_{ij}(\boldsymbol{k})$ is inserted for $\Delta\tilde{\boldsymbol{f}}(\boldsymbol{k};\tau)$ to satisfy the solenoidal condition for any disturbances. The response function can be defined by the functional derivative as

$$\tilde{G}_{ij}(\boldsymbol{k},\boldsymbol{k}';\tau,\tau') \equiv \lim_{\Delta\tilde{\boldsymbol{f}}\to 0} \frac{\Delta\tilde{u}_i(\boldsymbol{k};\tau)}{\Delta\tilde{f}_j(\boldsymbol{k}';\tau')}, \tag{C20}$$

and this obeys the following equation:

$$\begin{aligned}&\frac{\partial\tilde{G}_{ij}}{\partial\tau}(\boldsymbol{k},\boldsymbol{k}';\tau,\tau') + 2iM_{i\ell m}(\boldsymbol{k})\int \mathrm{d}\boldsymbol{p}\int \mathrm{d}\boldsymbol{q}\ \delta(\boldsymbol{k}-\boldsymbol{p}-\boldsymbol{q})\tilde{u}_\ell^{(00)}(\boldsymbol{p};\tau)\tilde{G}_{mj}(\boldsymbol{q},\boldsymbol{k}';\tau,\tau') + \nu k^2\tilde{G}_{ij}(\boldsymbol{k},\boldsymbol{k}';\tau,\tau')\\ &= M_{ij}(\boldsymbol{k})\delta(\boldsymbol{k}-\boldsymbol{k}')\delta(\tau-\tau').\end{aligned} \tag{C21}$$

Note that $k_i\tilde{G}_{ij}(\boldsymbol{k},\boldsymbol{k}';\tau,\tau') = 0$ due to the incompressible condition. Hence, the disturbed velocity is formally solved as

$$\Delta\tilde{u}_i(\boldsymbol{k};\tau) = \int_{-\infty}^{\tau}\mathrm{d}\tau'\int \mathrm{d}\boldsymbol{k}'\tilde{G}_{ij}(\boldsymbol{k},\boldsymbol{k}';\tau,\tau')\Delta f_j(\boldsymbol{k}';\tau'). \tag{C22}$$

Here, we define

$$\tilde{G}_{ij}(\boldsymbol{k},\boldsymbol{k}';\tau,\tau) = \frac{1}{2}M_{ij}(\boldsymbol{k})\delta(\boldsymbol{k}-\boldsymbol{k}'),\quad \int_{-\infty}^{\tau}\mathrm{d}\tau'\ \delta(\tau-\tau')q(\tau') = \frac{1}{2}q(\tau). \tag{C23}$$

With the aid of this response function, we can formally solve the higher order velocity equations given by Eqs. (C11), (C13), and (C15). Namely, we have

$$\tilde{u}_i^{(01)}(\boldsymbol{k};\tau) = \int_{-\infty}^{\tau}\mathrm{d}\tau'\int \mathrm{d}\boldsymbol{k}'\tilde{G}_{ia}(\boldsymbol{k},\boldsymbol{k}';\tau,\tau')M_{an}(\boldsymbol{k}')\epsilon_{nj\ell}\tilde{u}_j^{(00)}(\boldsymbol{k}';\tau')2e_\ell^\Omega, \tag{C24}$$

$$\begin{aligned}\tilde{u}_i^{\mathrm{S}(10)}(\boldsymbol{k};\tau) =& -\int_{-\infty}^{\tau}\mathrm{d}\tau'\int \mathrm{d}\boldsymbol{k}'\tilde{G}_{ia}(\boldsymbol{k},\boldsymbol{k}';\tau,\tau')M_{aj}(\boldsymbol{k}')\tilde{u}_\ell^{(00)}(\boldsymbol{k}';\tau')\frac{\partial U_j}{\partial X_\ell}\\ &-\int_{-\infty}^{\tau}\mathrm{d}\tau'\int \mathrm{d}\boldsymbol{k}'\tilde{G}_{ia}(\boldsymbol{k},\boldsymbol{k};\tau,\tau')\frac{D\tilde{u}_a^{(00)}}{DT^{\mathrm{I}}}(\boldsymbol{k}';\tau') + O(|\tilde{u}^{(00)}|^2) + \cdots,\end{aligned} \tag{C25}$$

$$\begin{aligned}\tilde{u}_i^{\mathrm{S}(11)}(\boldsymbol{k};\tau) =& \int_{-\infty}^{\tau}\mathrm{d}\tau'\int \mathrm{d}\boldsymbol{k}'\tilde{G}_{ia}(\boldsymbol{k},\boldsymbol{k}';\tau,\tau')i\epsilon_{a\ell m}\frac{k'_\ell}{k'^2}\frac{\partial\tilde{u}_n^{(00)}}{\partial X_n^{\mathrm{I}}}(\boldsymbol{k}';\tau')2e_m^\Omega\\ &+\int_{-\infty}^{\tau}\mathrm{d}\tau'\int \mathrm{d}\boldsymbol{k}'\tilde{G}_{ia}(\boldsymbol{k},\boldsymbol{k}';\tau,\tau')iM_{an}(\boldsymbol{k}')\epsilon_{j\ell m}\frac{k'_j}{k'^2}\frac{\partial\tilde{u}_\ell^{(00)}}{\partial X_n^{\mathrm{I}}}(\boldsymbol{k};\tau')2e_m^\Omega\\ &-\int_{-\infty}^{\tau}\mathrm{d}\tau'\int \mathrm{d}\boldsymbol{k}'\tilde{G}_{ia}(\boldsymbol{k},\boldsymbol{k}';\tau,\tau')M_{aj}(\boldsymbol{k}')\tilde{u}_\ell^{(01)}(\boldsymbol{k}';\tau')\frac{\partial U_j}{\partial X_\ell}\\ &-\int_{-\infty}^{\tau}\mathrm{d}\tau'\int \mathrm{d}\boldsymbol{k}'\tilde{G}_{ia}(\boldsymbol{k},\boldsymbol{k}';\tau,\tau')\frac{D\tilde{u}_a^{(01)}}{DT^{\mathrm{I}}}(\boldsymbol{k}';\tau') + O(|\tilde{u}^{(00)}|^2) + \cdots,\end{aligned} \tag{C26}$$

where only the leading terms are written.

C.3 Renormalized approximation for homogeneous isotropic field

In order to calculate the velocity correlations, some assumptions for the velocity field and the response function are required. The equations of the DIA can be derived by using other approximation method such as the diagram theory [Wyld (1961)] or the renormalized approximation [Kraichnan (1977)]. For the brief reviews of the approximation methods, please refer Kaneda (2007). Here, the renormalized approximation method [Kraichnan (1977); Kaneda (1981)] is adopted. We introduce a parameter $\lambda(=1)$ to the inter-scale interaction term in the basic field equation (C7) and the response function equation (C21) for convenience; namely, we have

$$\frac{\partial \tilde{u}_i^{(00)}}{\partial \tau}(\boldsymbol{k};\tau) + \nu k^2 \tilde{u}_i^{(00)}(\boldsymbol{k};\tau) = -\lambda i M_{ij\ell}(\boldsymbol{k}) \int \mathrm{d}\boldsymbol{p} \int \mathrm{d}\boldsymbol{q}\ \delta(\boldsymbol{k}-\boldsymbol{p}-\boldsymbol{q}) \tilde{u}_j^{(00)}(\boldsymbol{p};\tau) \tilde{u}_\ell^{(00)}(\boldsymbol{q};\tau), \tag{C27}$$

$$\frac{\partial \tilde{G}_{ij}}{\partial \tau}(\boldsymbol{k},\boldsymbol{k}';\tau,\tau') + \nu k^2 \tilde{G}_{ij}(\boldsymbol{k},\boldsymbol{k}';\tau,\tau') = -2\lambda i M_{i\ell m}(\boldsymbol{k}) \int \mathrm{d}\boldsymbol{p} \int \mathrm{d}\boldsymbol{q}\ \delta(\boldsymbol{k}-\boldsymbol{p}-\boldsymbol{q}) \tilde{u}_\ell^{(00)}(\boldsymbol{p};\tau) \tilde{G}_{mj}(\boldsymbol{q},\boldsymbol{k}';\tau,\tau') + M_{ij}(\boldsymbol{k})\delta(\boldsymbol{k}-\boldsymbol{k}')\delta(\tau-\tau'). \tag{C28}$$

We expand the basic field velocity $\tilde{\boldsymbol{u}}^{(00)}(\boldsymbol{k};\tau)$ and the response function $\tilde{G}_{ij}(\boldsymbol{k};\tau,\tau')$ in powers of λ as

$$\tilde{u}_i^{(00)}(\boldsymbol{k};\tau) = \sum_{\lambda=0}^{\infty} \tilde{u}_i^{(\lambda|00)}(\boldsymbol{k};\tau), \tag{C29}$$

$$\tilde{G}_{ij}(\boldsymbol{k}.\boldsymbol{k}';\tau,\tau') = \sum_{\lambda=0}^{\infty} \tilde{G}_{ij}^{(\lambda)}(\boldsymbol{k},\boldsymbol{k}';\tau,\tau'). \tag{C30}$$

Hence, $O(\lambda^0)$ velocity field reads

$$\begin{aligned} &\frac{\partial \tilde{u}_i^{(0|00)}}{\partial \tau}(\boldsymbol{k};\tau) + \nu k^2 \tilde{u}_i^{(0|00)}(\boldsymbol{k};\tau) = 0 \\ \Leftrightarrow\ &\tilde{u}_i^{(0|00)}(\boldsymbol{k},\boldsymbol{X};\tau,T) = \tilde{v}_i(\boldsymbol{k},\boldsymbol{X};T)\mathrm{e}^{-\nu k^2 \tau}. \end{aligned} \tag{C31}$$

Similarly, $O(\lambda^0)$ response function reads

$$\begin{aligned} &\frac{\partial \tilde{G}_{ij}^{(0)}}{\partial \tau}(\boldsymbol{k},\boldsymbol{k}';\tau,\tau') + \nu k^2 \tilde{G}_{ij}^{(0)}(\boldsymbol{k},\boldsymbol{k}';\tau,\tau') = M_{ij}(\boldsymbol{k})\delta(\boldsymbol{k}-\boldsymbol{k}')\delta(\tau-\tau') \\ \Leftrightarrow\ &\tilde{G}_{ij}^{(0)}(\boldsymbol{k},\boldsymbol{k}',\boldsymbol{X};\tau,\tau',T) = M_{ij}(\boldsymbol{k}) g(\boldsymbol{k},\boldsymbol{X};T)\mathrm{e}^{-\nu k^2(\tau-\tau')}\delta(\boldsymbol{k}-\boldsymbol{k}')\Theta(\tau-\tau'), \end{aligned} \tag{C32}$$

where $\Theta(\tau-\tau')$ is the step function defined as

$$\Theta(x) = \begin{cases} 1 & (x>0), \\ \dfrac{1}{2} & (x=0), \\ 0 & (x<0). \end{cases} \tag{C33}$$

Note that $g(\boldsymbol{k},\boldsymbol{X};T)=1$ when $\tilde{G}^{(0)}(\boldsymbol{k},\boldsymbol{k}',\boldsymbol{X};\tau,\tau',T)$ satisfies $\tilde{G}^{(0)}(\boldsymbol{k},\boldsymbol{k}',\boldsymbol{X};\tau,\tau,T)=\tilde{G}(\boldsymbol{k},\boldsymbol{k}',\boldsymbol{X};\tau,\tau,T)$ and Eq. (C23). The equation for $O(\lambda)$ velocity reads

$$\frac{\partial\tilde{u}_i^{(1|00)}}{\partial\tau}(\boldsymbol{k};\tau)+\nu k^2\tilde{u}_i^{(1|00)}(\boldsymbol{k};\tau)=-2iM_{ij\ell}(\boldsymbol{k})\int\mathrm{d}\boldsymbol{p}\int\mathrm{d}\boldsymbol{q}\;\delta(\boldsymbol{k}-\boldsymbol{p}-\boldsymbol{q})\tilde{u}_j^{(0|00)}(\boldsymbol{p};\tau)\tilde{u}_\ell^{(0|00)}(\boldsymbol{q};\tau). \tag{C34}$$

This equation can be solved by using $\tilde{G}_{ij}^{(0)}(\boldsymbol{k},\boldsymbol{k}',\tau,\tau')$ as

$$\tilde{u}_i^{(1|00)}(\boldsymbol{k};\tau)=-\mathrm{d}\tau'\int\mathrm{d}\boldsymbol{k}'\tilde{G}_{ia}^{(0)}(\boldsymbol{k},\boldsymbol{k}';\tau,\tau')2iM_{aj\ell}(\boldsymbol{k}')\int\mathrm{d}\boldsymbol{p}\int\mathrm{d}\boldsymbol{q}\;\delta(\boldsymbol{k}'-\boldsymbol{p}-\boldsymbol{q})\int_{-\infty}^{\tau}\tilde{u}_j^{(0|00)}(\boldsymbol{p};\tau')\tilde{u}_\ell^{(0|00)}(\boldsymbol{q};\tau'). \tag{C35}$$

We assume that $O(\lambda^0)$ field velocities are statistically independent of each other and $O(\lambda^0)$ velocity and $O(\lambda^0)$ response function are also statistically independent. Under this condition, triple correlation of the basic field velocities can be calculated as follows:

$$\begin{aligned}
\left\langle\tilde{u}_i^{(00)}(\boldsymbol{k};\tau)\tilde{u}_j^{(00)}(\boldsymbol{p};\tau)\tilde{u}_\ell^{(00)}(\boldsymbol{q};\tau)\right\rangle &= \left\langle\tilde{u}_i^{(0|00)}(\boldsymbol{k};\tau)\tilde{u}_j^{(0|00)}(\boldsymbol{p};\tau)\tilde{u}_\ell^{(0|00)}(\boldsymbol{q};\tau)\right\rangle \\
&\quad+\lambda\left\langle\tilde{u}_i^{(1|00)}(\boldsymbol{k};\tau)\tilde{u}_j^{(0|00)}(\boldsymbol{p};\tau)\tilde{u}_\ell^{(0|00)}(\boldsymbol{q};\tau)\right\rangle \\
&\quad+\lambda(\text{two permuted terms})+O(\lambda^2) \\
&=-\lambda\int_{-\infty}^{\tau}\mathrm{d}\tau'\int\mathrm{d}\boldsymbol{k}'\int\mathrm{d}\boldsymbol{p}'\int\mathrm{d}\boldsymbol{q}'\;\delta(\boldsymbol{k}'-\boldsymbol{p}'-\boldsymbol{q}')2iM_{abc}(\boldsymbol{k}') \\
&\quad\times\left\langle\tilde{G}_{ia}^{(0)}(\boldsymbol{k},\boldsymbol{k}';\tau,\tau')\tilde{u}_b^{(0|00)}(\boldsymbol{p}';\tau')\tilde{u}_c^{(0|00)}(\boldsymbol{q}';\tau')\tilde{u}_j^{(0|00)}(\boldsymbol{p};\tau)\tilde{u}_\ell^{(0|00)}(\boldsymbol{q};\tau)\right\rangle \\
&\quad+\lambda(\text{two permuted terms})+O(\lambda^2) \\
&=-\lambda\int_{-\infty}^{\tau}\mathrm{d}\tau'\int\mathrm{d}\boldsymbol{k}'\tilde{G}_{ia}^{(0)}(\boldsymbol{k},\boldsymbol{k}';\tau,\tau')\int\mathrm{d}\boldsymbol{p}'\int\mathrm{d}\boldsymbol{q}'\;\delta(\boldsymbol{k}'-\boldsymbol{p}'-\boldsymbol{q}') \\
&\quad\times 2iM_{abc}(\boldsymbol{k}')\Big[\tilde{Q}_{jb}^{(0|00)}(\boldsymbol{p};\tau,\tau')\delta(\boldsymbol{p}+\boldsymbol{p}')\tilde{Q}_{\ell c}^{(0|00)}(\boldsymbol{q};\tau,\tau')\delta(\boldsymbol{q}+\boldsymbol{q}') \\
&\qquad\qquad+\tilde{Q}_{jc}^{(0|00)}(\boldsymbol{p};\tau,\tau')\delta(\boldsymbol{p}+\boldsymbol{q}')\tilde{Q}_{\ell b}^{(0|00)}(\boldsymbol{q};\tau,\tau')\delta(\boldsymbol{q}+\boldsymbol{p}')\Big] \\
&\quad+\lambda(\text{two permuted terms})+O(\lambda^2) \\
&=-\lambda\int_{-\infty}^{\tau}\mathrm{d}\tau'\int\mathrm{d}\boldsymbol{k}'\tilde{G}_{ia}^{(0)}(\boldsymbol{k},\boldsymbol{k}';\tau,\tau')\delta(\boldsymbol{k}'+\boldsymbol{p}+\boldsymbol{q}')2iM_{abc}(\boldsymbol{k}') \\
&\quad\times\left[\tilde{Q}_{jb}^{(0|00)}(\boldsymbol{p};\tau,\tau')\tilde{Q}_{\ell c}^{(0|00)}(\boldsymbol{q};\tau,\tau')+\tilde{Q}_{jc}^{(0|00)}(\boldsymbol{p};\tau,\tau')\tilde{Q}_{\ell b}^{(0|00)}(\boldsymbol{q};\tau,\tau')\right] \\
&\quad+\lambda(\text{two permuted terms})+O(\lambda^2),
\end{aligned} \tag{C36}$$

where

$$\left\langle\tilde{u}_i^{(0|00)}(\boldsymbol{k};\tau)\tilde{u}_j^{(0|00)}(\boldsymbol{k}';\tau')\right\rangle=\tilde{Q}_{ij}^{(0|00)}(\boldsymbol{k};\tau,\tau')\delta(\boldsymbol{k}+\boldsymbol{k}'). \tag{C37}$$

Note that $\tilde{G}_{ij}^{(0)}(\boldsymbol{k},\boldsymbol{k}';\tau,\tau')$ itself is the statistical value as seen in Eq (C32), and Eq. (C37) corresponds to Eq. (2.40) for homogeneous isotropic turbulence. After the correlation is expressed by $\tilde{Q}_{ij}^{(0|00)}(\boldsymbol{k};\tau,\tau')$ and $\tilde{G}_{ij}^{(0)}(\boldsymbol{k},\boldsymbol{k}';\tau,\tau')$, we invert the λ expansion as

$$\tilde{Q}_{ij}^{(0|00)}(\boldsymbol{k};\tau,\tau') = \tilde{Q}_{ij}^{(00)}(\boldsymbol{k};\tau,\tau') - \lambda^2\tilde{Q}_{ij}^{(2|00)}(\boldsymbol{k};\tau,\tau') + \cdots, \tag{C38}$$

$$\left\langle \tilde{G}_{ij}^{(0)}(\boldsymbol{k},\boldsymbol{k}';\tau,\tau')\right\rangle = \left\langle \tilde{G}_{ij}(\boldsymbol{k},\boldsymbol{k}';\tau,\tau')\right\rangle - \lambda\left\langle \tilde{G}_{ij}^{(1)}(\boldsymbol{k},\boldsymbol{k}';\tau,\tau')\right\rangle + \cdots, \tag{C39}$$

where $\tilde{Q}_{ij}^{(00)}(\boldsymbol{k};\tau,\tau')$ is defined in Eq. (2.65). Here, $O(\lambda)$ term in the expansion of $\tilde{Q}_{ij}^{(00)}(\boldsymbol{k};\tau,\tau')$ vanishes. Substituting Eqs. (C38) and (C39) into the correlations and truncating at $O(\lambda)$, any correlations are expressed by $\tilde{Q}_{ij}^{(00)}(\boldsymbol{k};\tau,\tau')$ and $\left\langle \tilde{G}_{ij}(\boldsymbol{k},\boldsymbol{k}';\tau,\tau')\right\rangle$. Since $\left\langle \tilde{G}_{ij}(\boldsymbol{k},\boldsymbol{k}';\tau,\tau')\right\rangle$ is the statistical value for homogeneous isotropic field, it is written as

$$\left\langle \tilde{G}_{ij}(\boldsymbol{k},\boldsymbol{k}';\tau,\tau')\right\rangle = M_{ij}(\boldsymbol{k})\tilde{G}(k;\tau,\tau')\delta(\boldsymbol{k}-\boldsymbol{k}'), \tag{C40}$$

where $\tilde{G}(k;\tau,\tau')$ is the statistical value. This truncation is referred to as the renormalized approximation [Kraichnan (1977); Kaneda (1981)]. With the aid of the renormalized approximation, Eq. (C36) reads

$$\begin{aligned}\left\langle \tilde{u}_i^{(00)}(\boldsymbol{k};\tau)\tilde{u}_j^{(00)}(\boldsymbol{p};\tau)\tilde{u}_\ell^{(00)}(\boldsymbol{q};\tau)\right\rangle = -2iM_{ibc}(\boldsymbol{k})\delta(\boldsymbol{k}+\boldsymbol{p}+\boldsymbol{q})\int_{-\infty}^{\tau}\mathrm{d}\tau'\tilde{G}(k;\tau,\tau')\\ \times\left[\tilde{Q}_{jb}^{(00)}(\boldsymbol{p};\tau,\tau')\tilde{Q}_{\ell c}^{(00)}(\boldsymbol{q};\tau,\tau') + \tilde{Q}_{jc}^{(00)}(\boldsymbol{p};\tau,\tau')\tilde{Q}_{\ell b}^{(00)}(\boldsymbol{q};\tau,\tau')\right]\\ + (\text{two permuted terms}).\end{aligned} \tag{C41}$$

C.4 Calculation of the Reynolds stress

Up to $O(\delta|\Omega^{\mathrm{F}}|)$, the Reynolds stress is expressed as

$$\begin{aligned}R_{ij} = \left\langle u_i^{(00)}u_j^{(00)}\right\rangle + |\Omega^{\mathrm{F}}|\left[\left\langle u_i^{(01)}u_j^{(00)}\right\rangle + \left\langle u_i^{(00)}u_j^{(01)}\right\rangle\right] + \delta\left[\left\langle u_i^{(10)}u_j^{(00)}\right\rangle + \left\langle u_i^{(00)}u_j^{(10)}\right\rangle\right]\\ + \delta|\Omega^{\mathrm{F}}|\left[\left\langle u_i^{(11)}u_j^{(00)}\right\rangle + \left\langle u_i^{(10)}u_j^{(01)}\right\rangle + \left\langle u_i^{(01)}u_j^{(10)}\right\rangle + \left\langle u_i^{(00)}u_j^{(11)}\right\rangle\right]\end{aligned} \tag{C42}$$

In the TSDIA, the separation of variables between $\boldsymbol{k}$ and $(\boldsymbol{X};T)$ for $\tilde{\boldsymbol{v}}(\boldsymbol{k},\boldsymbol{X};T)$ in Eq. (C31) is assumed; namely,

$$\tilde{v}_i(\boldsymbol{k},\boldsymbol{X};T) = \tilde{v}_i(\boldsymbol{k})Z(\boldsymbol{X};T). \tag{C43}$$

For simplicity, we pick up linear terms in $\partial U_i/\partial X_j$ or $\boldsymbol{e}^{\Omega}$. For example, $\langle u_i^{(10)} u_j^{(00)} \rangle$ is calculated as follows:

$$
\begin{aligned}
\left\langle u_i^{(10)} u_j^{(00)} \right\rangle &= \int \mathrm{d}\boldsymbol{k} \int \mathrm{d}\boldsymbol{k}' \left\langle \tilde{u}_i^{(10)}(\boldsymbol{k};\tau) \tilde{u}_j^{(00)}(\boldsymbol{k};\tau) \right\rangle \mathrm{e}^{i(\boldsymbol{k}+\boldsymbol{k}')\cdot(\boldsymbol{\xi}-\boldsymbol{U}\tau)} \\
&= -\int \mathrm{d}\boldsymbol{k} \int \mathrm{d}\boldsymbol{k}' \int_{-\infty}^{\tau} \mathrm{d}\tau' \int \mathrm{d}\boldsymbol{k}'' M_{a\ell}(\boldsymbol{k}'') \left\langle \tilde{G}_{ia}(\boldsymbol{k},\boldsymbol{k}'';\tau,\tau') \tilde{u}_m^{(00)}(\boldsymbol{k}'';\tau') \tilde{u}_j^{(00)}(\boldsymbol{k}';\tau) \right\rangle \\
&\qquad \times \mathrm{e}^{i(\boldsymbol{k}+\boldsymbol{k}')\cdot(\boldsymbol{\xi}-\boldsymbol{U}\tau)} \frac{\partial U_\ell}{\partial X_m} + \cdots \\
&= -\int \mathrm{d}\boldsymbol{k} \int \mathrm{d}\boldsymbol{k}' \int_{-\infty}^{\tau} \mathrm{d}\tau' \int \mathrm{d}\boldsymbol{k}'' \tilde{G}_{ia}^{(0)}(\boldsymbol{k},\boldsymbol{k}'';\tau,\tau') M_{a\ell}(\boldsymbol{k}'') \tilde{Q}_{jm}^{(0|00)}(\boldsymbol{k}';\tau,\tau') \delta(\boldsymbol{k}'+\boldsymbol{k}'') \\
&\qquad \times \mathrm{e}^{i(\boldsymbol{k}+\boldsymbol{k}')\cdot(\boldsymbol{\xi}-\boldsymbol{U}\tau)} \frac{\partial U_\ell}{\partial X_m} + O(\lambda) + \cdots \\
&= -\int \mathrm{d}\boldsymbol{k}\ M_{i\ell}(\boldsymbol{k}) \int_{-\infty}^{\tau} \mathrm{d}\tau' \tilde{G}(k;\tau,\tau') \tilde{Q}_{jm}^{(00)}(-\boldsymbol{k};\tau,\tau') \frac{\partial U_\ell}{\partial X_m} + \cdots \\
&= -\int \mathrm{d}\boldsymbol{k}\ M_{i\ell}(\boldsymbol{k}) \int_{-\infty}^{\tau} \mathrm{d}\tau' \tilde{G}(k;\tau,\tau') \\
&\qquad \times \left[M_{jm}(-\boldsymbol{k}) \frac{E^{\mathrm{B}}(k;\tau,\tau')}{4\pi k^2} + \frac{i}{2} \epsilon_{jmn} \frac{k_n}{k^2} \frac{E^{H\mathrm{B}}(k;\tau,\tau')}{4\pi k^2} \right] \frac{\partial U_\ell}{\partial X_m} + \cdots \\
&= -\int \mathrm{d}\boldsymbol{k}\ M_{i\ell}(\boldsymbol{k}) M_{jm}(\boldsymbol{k}) \int_{-\infty}^{\tau} \mathrm{d}\tau' \tilde{G}(k;\tau,\tau') \frac{E^{\mathrm{B}}(k;\tau,\tau')}{4\pi k^2} \frac{\partial U_\ell}{\partial X_m} + \cdots \\
&= -\int_0^{\infty} \mathrm{d}k \int_{-\infty}^{\tau} \mathrm{d}\tau' \tilde{G}(k;\tau,\tau') E^{\mathrm{B}}(k;\tau,\tau') \left(\frac{2}{5} \frac{\partial U_i}{\partial X_j} + \frac{1}{15} \frac{\partial U_j}{\partial X_i} \right) + \cdots .
\end{aligned}
\tag{C44}
$$

Here, use is made of $\partial U_i/\partial X_i = 0$, Eq. (2.65) and

$$
\begin{aligned}
\int \mathrm{d}\boldsymbol{k}\ \frac{k_i k_j}{k^2} f(k) &= \frac{1}{3} \delta_{ij} \int \mathrm{d}\boldsymbol{k}\ f(k), \quad \int \mathrm{d}\boldsymbol{k}\ k_i f(k) = 0, \\
\int \mathrm{d}\boldsymbol{k}\ \frac{k_i k_j k_\ell k_m}{k^2} f(k) &= \frac{1}{15} \left(\delta_{ij}\delta_{\ell m} + \delta_{i\ell}\delta_{jm} + \delta_{im}\delta_{j\ell} \right) \int \mathrm{d}\boldsymbol{k}\ f(k),
\end{aligned}
\tag{C45}
$$

where $f(k)$ denotes an arbitrary function of k. Similarly, other terms on the right-hand side of Eq. (C42) read

$$
\left\langle u_i^{(01)} u_j^{(00)} \right\rangle = \frac{1}{3} \epsilon_{ij\ell} \int_0^{\infty} \mathrm{d}k \int_{-\infty}^{\tau} \mathrm{d}\tau' \tilde{G}(k;\tau,\tau') E^{\mathrm{B}}(k;\tau,\tau') e_\ell^{\Omega} + \cdots , \tag{C46}
$$

$$
\begin{aligned}
\left\langle u_i^{(11)} u_j^{(00)} \right\rangle &= \left(-\frac{1}{20} \delta_{i\ell}\delta_{jm} + \frac{1}{30} \delta_{im}\delta_{j\ell} + \frac{7}{60} \delta_{ij}\delta_{\ell m} \right) \\
&\qquad \times \frac{\partial}{\partial X_m} \left[\int_0^{\infty} \mathrm{d}k\ k^{-2} \int_{-\infty}^{\tau} \mathrm{d}\tau' \tilde{G}(k;\tau,\tau') E^{H\mathrm{B}}(k,\boldsymbol{X};\tau,\tau',T) \right] 2 e_\ell^{\Omega} + \cdots ,
\end{aligned}
\tag{C47}
$$

$$
\left\langle u_i^{(10)} u_j^{(01)} \right\rangle = \left(\frac{1}{15} \delta_{i\ell}\delta_{jm} - \frac{1}{60} \delta_{im}\delta_{j\ell} - \frac{1}{60} \delta_{ij}\delta_{\ell m} \right)
$$

$$\times \frac{\partial}{\partial X_m}\left[\int_0^\infty \mathrm{d}k\; k^{-2}\int_{-\infty}^{\tau}\mathrm{d}\tau'\tilde{G}(k;\tau,\tau')E^{HB}(k,\boldsymbol{X};\tau,\tau',T)\right]2e_\ell^\Omega+\cdots. \tag{C48}$$

In this calculation, we use

$$\begin{aligned}\left\langle \tilde{u}_i^{(00)}(\boldsymbol{k},\boldsymbol{X};\tau,T)\frac{\partial}{\partial X_\ell}\tilde{u}_j^{(00)}(\boldsymbol{k}',\boldsymbol{X};\tau',T)\right\rangle &= \left\langle \tilde{v}_i(\boldsymbol{k})Z(\boldsymbol{X};T)\frac{\partial}{\partial X_\ell}\left[\tilde{v}_j(\boldsymbol{k}')Z(\boldsymbol{X};T)\right]\right\rangle \mathrm{e}^{-\nu k^2(\tau+\tau')}+O(\lambda)\\ &= \frac{1}{2}\frac{\partial}{\partial X_\ell}\left[\left\langle\tilde{v}_i(\boldsymbol{k})\tilde{v}_j(\boldsymbol{k}')\right\rangle Z(\boldsymbol{X};T)^2\mathrm{e}^{-\nu k^2(\tau+\tau')}\right]+O(\lambda)\\ &= \frac{1}{2}\frac{\partial}{\partial X_\ell}\tilde{Q}_{ij}^{(0|00)}(\boldsymbol{k},\boldsymbol{X};\tau,\tau',T)\delta(\boldsymbol{k}+\boldsymbol{k}')+O(\lambda)\\ &= \frac{1}{2}\frac{\partial}{\partial X_\ell}\tilde{Q}_{ij}^{(00)}(\boldsymbol{k},\boldsymbol{X};\tau,\tau',T)\delta(\boldsymbol{k}+\boldsymbol{k}').\end{aligned} \tag{C49}$$

Then, Eq. (C42) reads

$$R_{ij}=\left(\frac{2}{3}K^{\mathrm{B}}+\frac{2}{9}\delta|\Omega^{\mathrm{F}}|I_\ell\{2,E^{HB}(k,\boldsymbol{X};\tau,\tau',T)\}2e_\ell^\Omega\right)\delta_{ij}-\nu^{\mathrm{T}}\delta\left(\frac{\partial U_i}{\partial X_j}+\frac{\partial U_j}{\partial X_i}\right)+\delta|\Omega^{\mathrm{F}}|\Gamma_{ij}+\cdots, \tag{C50}$$

where K^{B} is given by Eq. (2.66),

$$\nu^{\mathrm{T}}=\frac{7}{15}\int_0^\infty \mathrm{d}k\int_{-\infty}^{\tau}\mathrm{d}\tau'\tilde{G}(k;\tau,\tau')E^{\mathrm{B}}(k;\tau,\tau'), \tag{C51}$$

$$\Gamma_{ij}=\frac{1}{30}\left[I_j\{2,E^{HB}(k,\boldsymbol{X};\tau,\tau',T)\}2e_i^\Omega+I_i\{2,E^{HB}(k,\boldsymbol{X};\tau,\tau',T)\}e_j^\Omega\right]_{\mathrm{D}}, \tag{C52}$$

$[A_{ij}]_{\mathrm{D}}$ is already defined in connection to Eqs. (2.51), and

$$I_i\{n,Q\}=\frac{\partial}{\partial X_i}\left[\int_0^\infty \mathrm{d}k\; k^{-n}\int_{-\infty}^{\tau}\mathrm{d}\tau'\tilde{G}(k;\tau,\tau')Q(k,\boldsymbol{X};\tau,\tau',T)\right]. \tag{C53}$$

The turbulent energy and the turbulent helicity are calculated as follows:

$$K=K^{\mathrm{B}}+\frac{1}{3}\delta|\Omega^{\mathrm{F}}|I_i\{2,E^{HB}(k,\boldsymbol{X};\tau,\tau',T)\}2e_i^\Omega+\cdots, \tag{C54}$$

$$H=H^{\mathrm{B}}+\frac{4}{3}\delta|\Omega^{\mathrm{F}}|I_i\{0,E^{\mathrm{B}}(k,\boldsymbol{X};\tau,\tau',T)\}2e_i^\Omega+\cdots, \tag{C55}$$

C.5 Simplification for the spectra and response function

In order to model the turbulence correlations in terms of K and ε, we adopt the simple function form in the inertial range suggested by Kolmogorov (1941) to $E^{\mathrm{B}}(k,\boldsymbol{X};\tau,\tau',T)$, $E^{HB}(k,\boldsymbol{X};\tau,\tau',T)$, and $\tilde{G}(k,\boldsymbol{X};\tau,\tau',T)$; namely they are expressed by using the dissipation rate ε, the wavenumber, and the

time difference $\tau - \tau'$ as [Shimomura (1998); Yokoi (2016)]

$$E^{\rm B}(k,\boldsymbol{X};\tau,\tau',T) = E^{\rm B}(k,\boldsymbol{X};\tau,\tau,T)\exp\left[-C_\omega[\varepsilon(\boldsymbol{X};T)]^{1/3}k^{2/3}|\tau-\tau'|\right],$$

$$E^{\rm B}(k,\boldsymbol{X};\tau,\tau,T) = C_K[\varepsilon(\boldsymbol{X};T)]^{2/3}k^{-5/3}\Theta(k-k^{\rm C}), \tag{C56}$$

$$E^{H\rm B}(k,\boldsymbol{X};\tau,\tau',T) = E^{H\rm B}(k,\boldsymbol{X};\tau,\tau,T)\exp\left[-C_\omega[\varepsilon(\boldsymbol{X};T)]^{1/3}k^{2/3}|\tau-\tau'|\right],$$

$$E^{H\rm B}(k,\boldsymbol{X};\tau,\tau,T) = C_H[\varepsilon(\boldsymbol{X};T)]^{-1/3}\varepsilon^H(\boldsymbol{X};T)k^{-5/3}\Theta(k-k^{H\rm C}), \tag{C57}$$

$$\tilde{G}(k,\boldsymbol{X};\tau,\tau',T) = \exp\left[-C_\omega[\varepsilon(\boldsymbol{X};T)]^{1/3}k^{2/3}(\tau-\tau')\right]\Theta(\tau-\tau'), \tag{C58}$$

where C_K, C_H, and C_ω are constants and $k^{\rm C}$ and $k^{H\rm C}$ denote the containing scale of the turbulent energy and helicity, respectively. The inertial range spectrum for helicity given by Eq. (C57) was first suggested by Brissaud *et al.* (1973) in the case that both helicity and energy exhibit the inter-scale energy transfer. This spectrum had been confirmed in many works [André & Lesieur (1977); Borue & Orszag (1997); Koprov *et al.* (2005); Baerenzung *et al.* (2008); Deusebio & Lindborg (2014)]. Note that the energy spectrum proportional to $k^{-5/3}$ was not reproduced by the DIA [Kraichnan (1959)]. Moreover, the response function equation in a steady state with the inertial range spectrum exhibits the infrared divergence [Leslie (1971); Yoshizawa (1998)]. These shortfalls were overcome by introducing the Lagrangian picture [Kraichnan (1965); Kaneda (1981)]. Recently, the closure theory for inhomogeneous turbulence combining the two-scale method and the Lagrangian picture was developed [Ariki (2014, 2018)]. In the Eulerian framework, the inertial range spectrum can be justified with the aid of the modified DIA with the low-wavenumber cutoff [Yoshizawa (1978)]. In this method, the constraint for the constants is given as follows:

$$\frac{C_\omega}{[C_K/(4\pi)]^2} = 30.1, \quad \frac{C_\omega^2}{C_K/(4\pi)} = 1.49, \tag{C59}$$

which lead to

$$C_\omega = 0.420, \quad C_K = 1.48. \tag{C60}$$

The value of C_K is reasonable in comparison to the estimation by Sreenivasan (1995), which gave $C_K = 1.62 \pm 0.17$, or the high-resolution DNS, which gave $C_K = 1.8 \pm 0.1$ [Ishihara *et al.* (2016)]. For C_H, Borue & Orszag (1997) estimates $C_H = 1$ for the numerical simulation using the hyperviscosity, while André & Lesieur (1977) estimates $C_H = 2.23$ using the EDQNM closure model. Hence, the basic field turbulent energy and helicity are calculated as follows:

$$K^{\rm B} = \int_0^\infty {\rm d}k\ E^{\rm B}(k,\boldsymbol{X};\tau,\tau,T) = \frac{3}{2}C_K\varepsilon^{2/3}(k^{\rm C})^{-2/3}, \tag{C61}$$

$$H^{\rm B} = \int_0^\infty {\rm d}k\ E^{H\rm B}(k,\boldsymbol{X};\tau,\tau,T) = \frac{3}{2}C_H\varepsilon^{-1/3}\varepsilon^H(k^{H\rm C})^{-2/3}. \tag{C62}$$

The eddy viscosity ν^{T} given by Eq. (C51) is calculated as follows:

$$\begin{aligned}
\nu^{\mathrm{T}} &= \frac{7}{15}\int_0^\infty \mathrm{d}k \int_{-\infty}^{\tau} \mathrm{d}\tau' \exp\left[-2C_\omega \varepsilon^{1/3}k^{2/3}(\tau-\tau')\right]\Theta(\tau-\tau')C_K\varepsilon^{2/3}k^{-5/3}\Theta(k-k^{\mathrm{C}}) \\
&= \frac{7}{15}\int_0^\infty \mathrm{d}k \frac{1}{2C_\omega}\varepsilon^{-1/3}k^{-2/3}C_K\varepsilon^{2/3}k^{-5/3}\Theta(k-k^{\mathrm{C}}) \\
&= \frac{7}{30C_\omega}\varepsilon^{-1/3}\int_0^\infty \mathrm{d}k\ C_K\varepsilon^{2/3}k^{-7/3}\Theta(k-k^{\mathrm{C}}) \\
&= \frac{7}{30C_\omega}\varepsilon^{-1/3}\frac{3}{4}C_K\varepsilon^{2/3}(k^{\mathrm{C}})^{-4/3} \\
&= \frac{7}{60C_\omega}\varepsilon^{-1/3}(k^{\mathrm{C}})^{-2/3}K^{\mathrm{B}}
\end{aligned} \tag{C63}$$

$I_i\{2, E^{H\mathrm{B}}(k,\boldsymbol{X};\tau,\tau',T)\}$ is calculated as

$$\begin{aligned}
&I_i\{2, E^{H\mathrm{B}}(k,\boldsymbol{X};\tau,\tau',T)\} \\
&= \frac{\partial}{\partial X_i}\left[\int_0^\infty \mathrm{d}k\ k^{-2}\int_{-\infty}^{\tau}\mathrm{d}\tau' \exp\left[-2C_\omega\varepsilon^{1/3}k^{2/3}(\tau-\tau')\right]\Theta(\tau-\tau')C_H\varepsilon^{-1/3}\varepsilon^H k^{-11/3}\Theta(k-k^{H\mathrm{C}})\right]2e_i^\Omega \\
&= \frac{\partial}{\partial X_i}\left[\int_0^\infty \mathrm{d}k\ k^{-2}\frac{1}{2C_\omega}\varepsilon^{-1/3}k^{-2/3}C_H\varepsilon^{-1/3}\varepsilon^H k^{-5/3}\Theta(k-k^{H\mathrm{C}})\right]2e_i^\Omega \\
&= \frac{\partial}{\partial X_i}\left[\frac{1}{2C_\omega}\varepsilon^{-1/3}\int_0^\infty \mathrm{d}k\ C_H\varepsilon^{-1/3}\varepsilon^H k^{-13/3}\Theta(k-k^{H\mathrm{C}})\right]2e_i^\Omega \\
&= \frac{\partial}{\partial X_i}\left[\frac{1}{2C_\omega}\varepsilon^{-1/3}\frac{3}{10}C_H\varepsilon^{-1/3}\varepsilon^H(k^{H\mathrm{C}})^{-10/3}\right]2e_i^\Omega \\
&= \frac{1}{10C_\omega}\varepsilon^{-1/3}(k^{H\mathrm{C}})^{-8/3}\frac{\partial H^{\mathrm{B}}}{\partial X_i}2e_i^\Omega.
\end{aligned} \tag{C64}$$

Here, we neglect $\boldsymbol{X}$ derivatives of ε and $k^{H\mathrm{C}}$ for simplicity. Thus, Γ_{ij} given by Eq. (C52) reads

$$\Gamma_{ij} = \frac{1}{300C_\omega}\varepsilon^{-1/3}(k^{H\mathrm{C}})^{-8/3}\left[\frac{\partial H^{\mathrm{B}}}{\partial X_j}2e_i^\Omega + \frac{\partial H^{\mathrm{B}}}{\partial X_i}2e_j^\Omega\right]_{\mathrm{D}}. \tag{C65}$$

Similarly, the second term on the right-hand side of Eq. (C55) reads

$$\frac{\partial}{\partial X_i}\left[\int_0^\infty \mathrm{d}k\int_{-\infty}^{\tau}\mathrm{d}\tau'\tilde{G}(k,\boldsymbol{X};\tau,\tau',T)E^{\mathrm{B}}(k,\boldsymbol{X};\tau,\tau',T)\right]2e_i^\Omega = \frac{1}{4C_\omega}\varepsilon^{-1/3}(k^{\mathrm{C}})^{-2/3}\frac{\partial K^{\mathrm{B}}}{\partial X_i}2e_i^\Omega. \tag{C66}$$

We express K^{B} and H^{B} in Eqs. (C54) and (C55) in terms of K and H as follows:

$$K^{\mathrm{B}} = K - \frac{1}{3}\delta|\Omega^{\mathrm{F}}|\frac{1}{10C_\omega}\varepsilon^{-1/3}(k^{H\mathrm{C}})^{-8/3}\frac{\partial H^{\mathrm{B}}}{\partial X_i}2e_i^\Omega + \cdots, \tag{C67}$$

$$H^{\mathrm{B}} = H - \frac{4}{3}\delta|\Omega^{\mathrm{F}}|\frac{1}{4C_\omega}\varepsilon^{-1/3}(k^{\mathrm{C}})^{-2/3}\frac{\partial K^{\mathrm{B}}}{\partial X_i}2e_i^\Omega + \cdots. \tag{C68}$$

Here, we give an evaluation for the dissipation rate of the turbulent helicity ε^H using K, ε, and H as [Yokoi & Yoshizawa (1993)]

$$\varepsilon^H = C_{\varepsilon H}\frac{\varepsilon}{K}H. \tag{C69}$$

The estimation of Eq. (C69) was confirmed to be reasonable at the logarithmic region in a turbulent Ekman boundary layer [Deusebio & Lindborg (2014)]. Substituting Eqs. (C61), (C62), and (C69) into (C67) and (C68), we have

$$(k^{\mathrm{C}})^{-2/3} = \frac{2}{3C_K}\varepsilon^{-2/3}K - O(\delta|\Omega^{\mathrm{F}}|) + \cdots, \tag{C70}$$

$$(k^{H\mathrm{C}})^{-2/3} = \frac{2}{3C_H C_{\varepsilon H}}\varepsilon^{-2/3}K - O(\delta|\Omega^{\mathrm{F}}|) + \cdots. \tag{C71}$$

Substituting Eqs. (C63), (C65), (C67), (C68), (C70), and (C71) into Eq. (C50), the Reynolds stress reads

$$\begin{aligned} R_{ij} = {} & \frac{2}{3}K\delta_{ij} - \frac{7}{90C_\omega C_K}\frac{K^2}{\varepsilon}\delta\left(\frac{\partial U_i}{\partial X_j} + \frac{\partial U_j}{\partial X_i}\right) + \frac{4}{6075C_\omega C_H^4 C_{\varepsilon H}^4}\frac{K^4}{\varepsilon^3}\delta|\Omega^{\mathrm{F}}|\left[\frac{\partial H}{\partial X_j}2e_i^\Omega + \frac{\partial H}{\partial X_i}2e_j^\Omega\right]_{\mathrm{D}} \\ & + O(\delta^2|\Omega^{\mathrm{F}}|) + O(\delta^2|\Omega^{\mathrm{F}}|^2) + \cdots. \end{aligned} \tag{C72}$$

This manipulation corresponds to the renormalized approximation discussed in the Sec. C.3. When we take the replacement of $\boldsymbol{X} \mapsto \delta\boldsymbol{x}$ and $|\Omega^{\mathrm{F}}|2\boldsymbol{e}^\Omega \mapsto \boldsymbol{\Omega}^{\mathrm{A}}(= \boldsymbol{\Omega} + 2\boldsymbol{\Omega}^{\mathrm{F}})$, the Reynolds stress up to $O(\delta|\Omega^{\mathrm{F}}|)$ results in

$$R_{ij} = \frac{2}{3}K\delta_{ij} - 2\nu^{\mathrm{T}}S_{ij} + \eta^{\mathrm{T}}\left[\frac{\partial H}{\partial x_j}\Omega_i^{\mathrm{A}} + \frac{\partial H}{\partial x_i}\Omega_j^{\mathrm{A}}\right]_{\mathrm{D}}, \tag{C73}$$

where

$$\nu^{\mathrm{T}} = \frac{7}{90C_\omega C_K}\frac{K^2}{\varepsilon}, \quad \eta^{\mathrm{T}} = \frac{4}{6075C_\omega C_H^4 C_{\varepsilon H}^4}\frac{K^4}{\varepsilon^3}. \tag{C74}$$

D Properties of inertial wave

Inertial wave is governed by the linearized Navier–Stokes equation in a rotating system:

$$\frac{\partial u_i}{\partial t} = -\frac{\partial p}{\partial x_i} + 2\epsilon_{ij\ell}u_j\Omega_\ell^{\mathrm{F}}. \tag{D1}$$

Here, the incompressible condition is also satisfied, $\partial u_i/\partial x_i = 0$, and the viscous and forcing terms are neglected. Taking the curl of each term in Eq. (D1), the equation for the vorticity reads

$$\frac{\partial \omega_i}{\partial t} = 2\Omega_j^{\mathrm{F}}\frac{\partial u_i}{\partial x_j}. \tag{D2}$$

Taking the curl again and time derivative of each term in Eq. (D2), we have [Davidson (2004)]

$$\frac{\partial^2}{\partial t^2}\nabla^2 u_i = \left(2\Omega_j^{\rm F}\frac{\partial}{\partial x_j}\right)^2 u_i. \tag{D3}$$

This is the wave equation for the inertial wave. Here, we consider the wave solution $\boldsymbol{u} = \tilde{\boldsymbol{u}}\mathrm{e}^{i(\boldsymbol{k}\cdot\boldsymbol{x}-\varpi t)}$ and substitute this into Eq. (D3). Then, the frequency ϖ and the group velocity $\boldsymbol{C}^{\rm g}$ are derived as

$$\varpi = \pm\frac{2\Omega_i^{\rm F}k_i}{k}, \quad C_i^{\rm g} = \pm\frac{1}{k}M_{ij}(\boldsymbol{k})2\Omega_j^{\rm F}, \tag{D4}$$

where $M_{ij}(\boldsymbol{k})$ is already defined in Eq. (2.38). Substituting the wave solution and the frequency ϖ into Eq. (D2), we have

$$\tilde{\omega}_i = \mp k\tilde{u}_i. \tag{D5}$$

Hence, the vorticity and the velocity are always aligned for the inertial waves [Moffatt (1970)]. In other words, inertial wave has helical structure where the helicity is given by

$$\tilde{u}_i\tilde{\omega}_i^* = \mp k|\tilde{u}_i|^2. \tag{D6}$$

This result indicates that the progressive wave $\varpi > 0$ has negative helicity, while the backward wave has positive helicity, where we assume $\Omega_i^{\rm F}k_i > 0$. Schematic diagram for a progressive wave with negative helicity is shown in Fig. D1.

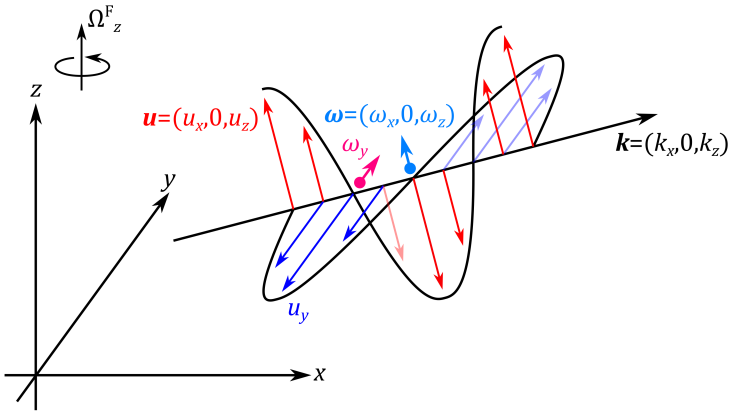

Figure D1: Schematic diagram for inertial wave propagation. Here, the rotation axis is set in the z direction, the wavenumber is given as $\boldsymbol{k} = (k_x, 0, k_z)$, and $k_x, k_z, \varpi > 0$ is assumed.

When the wavenumber is almost parallel to the rotation axis, $\boldsymbol{k} \simeq \boldsymbol{k}_\parallel$, the group velocity reads

$$C_i^{\rm g} \simeq \pm\frac{2}{k_\parallel}\left(\Omega_i^{\rm F} - \Omega^{\rm F}\frac{k_{\parallel i}}{k_\parallel}\right) \simeq 0. \tag{D7}$$

On the other hand, when the wavenumber is almost perpendicular to the rotation axis, $\boldsymbol{k} \simeq \boldsymbol{k}_\perp$, the group velocity reads

$$C_i^{\mathrm{g}} \simeq \pm \frac{2}{k_\perp} \Omega_i^{\mathrm{F}}. \tag{D8}$$

Hence, $\boldsymbol{k} \simeq \boldsymbol{k}_\perp$ mode waves have faster the group velocity than $\boldsymbol{k} \simeq \boldsymbol{k}_\parallel$ modes. Moreover, the direction of the fast group velocity given by Eq. (D8) is parallel to the rotation axis. Note that the sign of the group velocity of inertial waves is also related to the sign of helicity. Namely, the wave packets with negative helicity propagate upward in the direction of the rotation axis, while the wave packets with positive helicity propagate downward.

E Concept of large eddy simulation

In the large eddy simulation (LES), filter average is applied to governing equations. Eddies larger than the filter scale (grid scale, GS) are directly solved, while eddies smaller than the filter scale (subgrid scale, SGS) are modeled. Filtered quantity $\overline{q}$ is defined by using the filter function $G(\boldsymbol{x}, \boldsymbol{x}')$ as

$$\overline{q}(\boldsymbol{x}) = \int \mathrm{d}\boldsymbol{x}' \; G(\boldsymbol{x}, \boldsymbol{x}') q(\boldsymbol{x}'). \tag{E1}$$

The filter function is decomposed into each direction as $G(\boldsymbol{x}, \boldsymbol{x}') = G(x, x')G(y, y')G(z, z')$. Here, the top-hat filter,

$$G(x_i, x_i') = \begin{cases} \dfrac{1}{\overline{\Delta}_i} & \text{for } -\dfrac{\overline{\Delta}_i}{2} \le x_i - x_i' \le \dfrac{\overline{\Delta}_i}{2}, \\ 0 & \text{for } x_i - x_i' \le -\dfrac{\overline{\Delta}_i}{2}, \quad x_i - x_i' \ge \dfrac{\overline{\Delta}_i}{2}, \end{cases} \tag{E2}$$

or the Gaussian filter,

$$G(x_i, x_i') = \left(\frac{6}{\pi \overline{\Delta}_i} \right)^{1/2} \exp\left[-\frac{(x_i - x_i')^2}{\overline{\Delta}_i^2 / 6} \right], \tag{E3}$$

is often used where $\overline{\Delta}_i$ denotes the filter width for i-th direction. In the above filters, the filter function can be written as $G(\boldsymbol{x}, \boldsymbol{x}') = G(\boldsymbol{x} - \boldsymbol{x}')$. When $\overline{\Delta}_i$ is constant in space, filtering operation and spatial derivative are commutative; namely,

$$\overline{\frac{\partial q}{\partial x_i}} = \int \mathrm{d}\boldsymbol{x}' G(\boldsymbol{x} - \boldsymbol{x}') \frac{\partial q(\boldsymbol{x}')}{\partial x_i'} = -\int \mathrm{d}\boldsymbol{x}' \frac{\partial G(\boldsymbol{x} - \boldsymbol{x}')}{\partial x_i'} q(\boldsymbol{x}') = \int \mathrm{d}\boldsymbol{x}' \frac{\partial G(\boldsymbol{x} - \boldsymbol{x}')}{\partial x_i} q(\boldsymbol{x}') = \frac{\partial \overline{q}}{\partial x_i}. \tag{E4}$$

Hence, the filtered governing equation reads

$$\frac{\partial \overline{u}_i}{\partial x_i} = 0, \tag{E5}$$

$$\frac{\partial \overline{u}_i}{\partial t} = -\frac{\partial}{\partial x_j}(\overline{u}_i \overline{u}_j + \tau_{ij}^{\mathrm{sgs}}) - \frac{\partial \overline{p}}{\partial x_i} + \frac{\partial}{\partial x_j}(2\nu \overline{s}_{ij}) + 2\epsilon_{ij\ell} \overline{u}_j \Omega_\ell^{\mathrm{F}} + \overline{f}_i, \tag{E6}$$

where $\tau_{ij}^{\rm sgs}(=\overline{u_iu_j}-\overline{u}_i\overline{u}_j)$ denotes the SGS stress.

A standard model for the SGS stress is the eddy-viscosity model:

$$\tau_{ij}^{\rm sgs}=\frac{2}{3}k^{\rm sgs}\delta_{ij}-2\nu^{\rm sgs}\overline{s}_{ij}, \tag{E7}$$

where $k^{\rm sgs}[=(\overline{u_iu_i}-\overline{u}_i\overline{u}_i)/2]$ denotes the SGS energy and $\nu^{\rm sgs}$ denotes the SGS viscosity. The transport equations for the GS energy $\overline{u}_i\overline{u}_i/2$ and the SGS energy $k^{\rm sgs}$ are written as

$$\frac{\partial}{\partial t}\left(\frac{1}{2}\overline{u}_i\overline{u}_i\right)=-2\nu^{\rm sgs}\overline{s}_{ij}\overline{s}_{ij}+\cdots \tag{E8}$$

$$\frac{\partial k^{\rm sgs}}{\partial t}=2\nu^{\rm sgs}\overline{s}_{ij}\overline{s}_{ij}-2\nu\left(\overline{s_{ij}s_{ij}}-\overline{s}_{ij}\overline{s}_{ij}\right)+\cdots, \tag{E9}$$

where only the leading terms are written. Hence, $2\nu^{\rm sgs}\overline{s}_{ij}\overline{s}_{ij}$ represents the energy cascade rate from the GS to the SGS across the filter scale. Note that $k^{\rm sgs}$ is incorporated into $\overline{p}$ in Eq. (E6) and $\overline{p}+2k^{\rm sgs}/3$ is often treated as the GS pressure.

For the model for the SGS viscosity $\nu^{\rm sgs}$, the Smagorinsky model [Smagorinsky (1963)] given by Eq. (3.3) is the most popular and frequently used. The Smagorinsky model is derived as follows. When the filter wavenumber $1/\overline{\Delta}$ is set in the inertial range, the energy cascade rate across this wavenumber can be assumed to be equal to the energy dissipation there, so that the first and second terms on the right-hand side of Eq. (E9) are balanced as

$$2\nu^{\rm sgs}\overline{s}_{ij}\overline{s}_{ij}=2\nu\left(\overline{s_{ij}s_{ij}}-\overline{s}_{ij}\overline{s}_{ij}\right)=\varepsilon^{\rm sgs}. \tag{E10}$$

This process is schematically shown in Fig. E1. Note that $\varepsilon^{\rm sgs}$ is different from the statistically averaged SGS dissipation rate $\varepsilon^{\rm SGS}(=2\langle\nu^{\rm sgs}\overline{s}_{ij}\overline{s}_{ij}\rangle)$; namely, $\varepsilon^{\rm sgs}\neq\varepsilon^{\rm SGS}$. According to Kolmogorov (1941), $\nu^{\rm sgs}$ can be described in terms of the filter width $\overline{\Delta}$ and the dissipation rate $\varepsilon^{\rm sgs}$ when the filter wavenumber $1/\overline{\Delta}$ is set in the inertial range. Hence, we have

$$\nu^{\rm sgs}=(C_S\overline{\Delta})^{4/3}(\varepsilon^{\rm sgs})^{1/3}, \tag{E11}$$

where C_S is the Smagorinsky constant. Substituting Eq. (E11) into Eq. (E10), we have

$$\begin{aligned}&2\nu^{\rm sgs}\overline{s}_{ij}\overline{s}_{ij}=(\nu^{\rm sgs})^3(C_S\overline{\Delta})^{-4}\\ \Leftrightarrow\ &\nu^{\rm sgs}=(C_S\overline{\Delta})^2\sqrt{2\overline{s}_{ij}\overline{s}_{ij}}.\end{aligned} \tag{E12}$$

This is nothing but the Smagorinsky model given by Eq. (3.3). For the value of the Smagorinsky constant C_S, it is not universal but the following value is adopted for typical turbulent flows [Yoshizawa (1998); Kida & Yanase (1999)]:

$$C_S\simeq\begin{cases}0.2 & \text{for homogeneous isotropic turbulence,}\\ 0.15 & \text{for turbulence mixing-layer,}\\ 0.1 & \text{for turbulence channel flow.}\end{cases} \tag{E13}$$

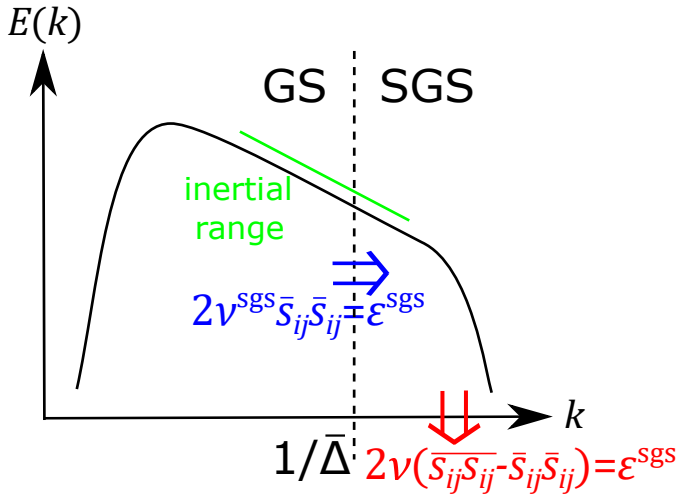

Figure E1: Schematic diagram for the energy cascade from the GS to the SGS across the filter scale. Here, $E(k)$ denotes the energy spectrum and k denotes the wavenumber.

F Calculation for the pressure diffusion and pressure–strain correlation by means of the TSDIA

In the TSDIA given in Appendix C in detail, each order pressure and velocity fluctuations are given in Eqs. (C6), (C12), (C14), (C16), and (C23)–(C26). The pressure diffusion and pressure–strain correlation terms in the Reynolds stress transport equation are expanded up to $O(\delta|\Omega^{\mathrm{F}}|)$ as

$$\Pi_{ij} = \delta\left\{\frac{\partial}{\partial X_j}\left[\left\langle u_i^{(00)}p^{(00)}\right\rangle + |\Omega^{\mathrm{F}}|\left(\left\langle u_i^{(01)}p^{(00)}\right\rangle + \left\langle u_i^{(00)}p^{(01)}\right\rangle\right)\right]\right\} + (i \leftrightarrow j), \tag{F1}$$

$$\begin{aligned}\Phi_{ij} = {} & 2\left\langle p^{(00)}s_{ij}^{\xi(00)}\right\rangle + 2\delta\left[\left\langle p^{(10)}s_{ij}^{\xi(00)}\right\rangle + \left\langle p^{(00)}s_{ij}^{\xi(10)}\right\rangle + \left\langle p^{(00)}s_{ij}^{X(00)}\right\rangle\right] \\ & + 2|\Omega^{\mathrm{F}}|\left[\left\langle p^{(01)}s_{ij}^{\xi(00)}\right\rangle + \left\langle p^{(01)}s_{ij}^{\xi(01)}\right\rangle\right] \\ & + 2\delta|\Omega^{\mathrm{F}}|\left[\left\langle p^{(11)}s_{ij}^{\xi(00)}\right\rangle + \left\langle p^{(10)}s_{ij}^{\xi(01)}\right\rangle + \left\langle p^{(01)}s_{ij}^{\xi(10)}\right\rangle\right. \\ & \qquad \left. + \left\langle p^{(01)}s_{ij}^{X(00)}\right\rangle + \left\langle p^{(00)}s_{ij}^{\xi(11)}\right\rangle + \left\langle p^{(00)}s_{ij}^{X(01)}\right\rangle\right],\end{aligned} \tag{F2}$$

where

$$s_{ij}^{\xi(nm)} = \frac{1}{2}\left(\frac{\partial u_i^{(nm)}}{\partial \xi_j} + \frac{\partial u_j^{(nm)}}{\partial \xi_i}\right), \quad s_{ij}^{X(nm)} = \frac{1}{2}\left(\frac{\partial u_i^{(nm)}}{\partial X_j} + \frac{\partial u_j^{(nm)}}{\partial X_i}\right). \tag{F3}$$

For simplicity, we pick up linear terms in $\partial U_i/\partial X_j$ or $\boldsymbol{e}^{\Omega}$, and $O(|u^{(00)}|^3)$ terms are neglected. Then, the right-hand side of Eqs. (F1) and (F2) are calculated as

$$\Pi_{ij} = \frac{1}{3}\delta|\Omega^{\mathrm{F}}|\left[\frac{\partial}{\partial X_j}\left(\int_0^\infty \mathrm{d}k\ k^{-2}E^{H\mathrm{B}}(k,\boldsymbol{X};\tau,\tau,T)2e_i^{\Omega}\right)+(i\leftrightarrow j)\right]+O(|u^{(00)}|^3)+\cdots, \tag{F4}$$

$$\Phi_{ij} = \frac{2}{5}K^{\mathrm{B}}\delta\left(\frac{\partial U_i}{\partial X_j}+\frac{\partial U_j}{\partial X_i}\right)-\frac{3}{10}\delta|\Omega^{\mathrm{F}}|\left[\frac{\partial}{\partial X_j}\left(\int_0^\infty \mathrm{d}k\ k^{-2}E^{H\mathrm{B}}(k,\boldsymbol{X};\tau,\tau,T)2e_i^{\Omega}\right)+(i\leftrightarrow j)\right]_{\mathrm{D}} + O(|u^{(00)}|^3)+\cdots. \tag{F5}$$

It should be noted that the coefficient of helicity related term in the pressure diffusion given by Eq. (F4) is slightly larger than that in the pressure–strain correlation given by Eq. (F5); namely $1/3 > 3/10$. With the aid of the simplification of the helicity spectrum for the basic field given by Eq. (C57), we have

$$\int_0^\infty \mathrm{d}k\ k^{-2}E^{H\mathrm{B}}(k,\boldsymbol{X};\tau,\tau,T) = \frac{3}{8}C_H\varepsilon^{-1/3}\varepsilon^H(k^{H\mathrm{C}})^{-8/3}. \tag{F6}$$

Substituting Eqs. (C69) and (C71) into Eq. (F6), we have

$$\int_0^\infty \mathrm{d}k\ k^{-2}E^{H\mathrm{B}}(k,\boldsymbol{X};\tau,\tau,T) = \frac{1}{4}\left(\frac{2}{3C_HC_{\varepsilon H}}\right)^3\frac{K^3}{\varepsilon^2}H - O(\delta|\Omega^{\mathrm{F}}|). \tag{F7}$$

Substituting Eqs. (C67) and (F7) into Eqs. (F4) and (F5), and taking the replacement of $\boldsymbol{X}\mapsto\delta\boldsymbol{x}$ and $|\Omega^{\mathrm{F}}|2\boldsymbol{e}^{\Omega}\mapsto\boldsymbol{\Omega}^{\mathrm{A}}$, the model expression for the pressure diffusion and pressure–strain correlation up to $O(\delta|\Omega^{\mathrm{F}}|)$ and $O(|u^{(00)}|^2)$ read

$$\Pi_{ij} = C_{PDH}\left[\frac{\partial}{\partial x_j}\left(\frac{K^3}{\varepsilon^2}\Omega_i^{\mathrm{A}}\right)+\frac{\partial}{\partial x_i}\left(\frac{K^3}{\varepsilon^2}\Omega_j^{\mathrm{A}}\right)\right] \tag{F8}$$

$$\Phi_{ij} = C_{R1}KS_{ij} - C_{PSH}\left[\frac{\partial}{\partial x_j}\left(\frac{K^3}{\varepsilon^2}\Omega_i^{\mathrm{A}}\right)+\frac{\partial}{\partial x_i}\left(\frac{K^3}{\varepsilon^2}\Omega_j^{\mathrm{A}}\right)\right]_{\mathrm{D}}, \tag{F9}$$

where $C_{R1} = 4/5$ and

$$C_{PDH} = \frac{1}{12}\left(\frac{2}{3C_HC_{\varepsilon H}}\right)^3,\quad C_{PSH} = \frac{3}{40}\left(\frac{2}{3C_HC_{\varepsilon H}}\right)^3. \tag{F10}$$

The first term on the right-hand side of Eq. (F9) corresponds to the second term on the right-hand side of Eq. (2.51) which is proposed by Launder *et al.* (1975). Note that the calculation result of the TSDIA predicts $C_{PDH} > C_{PSH}$, as previously noted in connection to Eqs. (F4) and (F5).

G Details for homogeneous isotropic turbulence used in the initial condition

In order to make the initial condition for the simulation of decaying inhomogeneous turbulence shown in Chap. 4, we perform a pre-computation of decaying homogeneous isotropic turbulence. The external

forcing is not used in this simulation. The box size is $L_x \times L_y \times L_z = 2\pi \times 2\pi \times 2\pi$ and the number of the grid point is $N_x \times N_y \times N_z = 512 \times 512 \times 512$. For the space discretization, the pseudo-spectral method is used and the aliasing error is eliminated by using the phase shift method [Orszag (1969); Kida & Yanase (1999)]. For time integration, the third-order Runge–Kutta scheme is adopted for nonlinear and viscous terms. The time step is set to $\Delta t = 10^{-3}$. The initial velocity field is generated by random variable. The initial energy spectrum is given by $E(k) \propto k^4 \exp[-2(k/k^{\mathrm{p}})^2]$ where $k^{\mathrm{p}} = 6$, while the helicity spectrum is not given. The initial value of the turbulent energy is set to $K = 2$. The kinematic viscosity is set to $\nu = 10^{-3}$.

Figure G1 shows the time evolution of the turbulent energy K and its dissipation rate ε. Here and hereafter, the volume average is adopted for the statistical average. The turbulent energy just decays as the time goes by, while the dissipation rate first increases and starts decaying at $t = 0.8$. Note that $k_{\max}\eta \geq 1$ at any time in this simulation where $k_{\max} = \sqrt{2} \times 512/3$ and $\eta[= (\nu^3/\varepsilon)^{1/4}]$ denotes the Kolmogorov length scale which characterizes the smallest scale of turbulence; namely, the resolution of this simulation is sufficient in predicting low-order moments [Watanabe & Gotoh (2007)]. We use the velocity field at $t = 1.12$ for making the initial condition for the simulation of decaying inhomogeneous turbulence, which is denoted as $\boldsymbol{u}^{\mathrm{hit}}$ in Sec. 4.2.1. The integral length scale L^{int} at that time is $L^{\mathrm{int}} = 0.516$ where

$$L^{\mathrm{int}} = \frac{3\pi}{4K} \int_0^\infty \mathrm{d}k \; k^{-1} E(k). \tag{G1}$$

The Reynolds number based on the Taylor microscale $\mathrm{Re}_\lambda (= u^{\mathrm{rms}}\lambda/\nu)$ is $\mathrm{Re}_\lambda = 49.7$ where $u^{\mathrm{rms}} = 2K/3$ and $\lambda = \sqrt{15\nu u^{\mathrm{rms}}/\varepsilon}$. Figure G2(a) shows the time evolution of the energy spectrum. It is confirmed that the energy spectrum starts self-similarly decaying at $t = 1.12$. This fact indicates that the turbulence is fully developed at this time. Figure G2(b) shows the comparison of the energy spectrum between the present simulation and the result performed by Hamba (2015). Here, the wavenumber and the spectrum are normalized by the Kolmogorov scale η and the dissipation rate ε. The spectra are similar to each other. At $k\eta = 0.5$, the energy spectrum given by the present simulation has slightly larger value than the result of Hamba (2015). This difference is considered to be caused by the difference of the value of k^{p}; namely, $k^{\mathrm{p}} = 6$ in the present simulation, while $k^{\mathrm{p}} = 3.5$ in Hamba (2015).

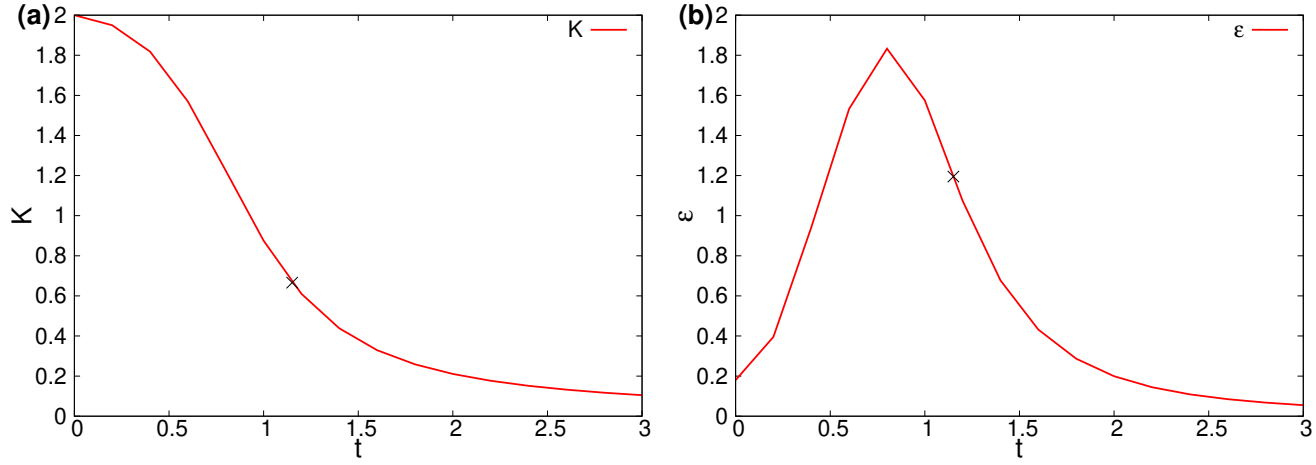

Figure G1: Time evolution of (a) the turbulent energy and (b) the turbulent energy dissipation rate. The cross symbol denotes the point which is used for making the initial condition for the simulation of decaying inhomogeneous turbulence.

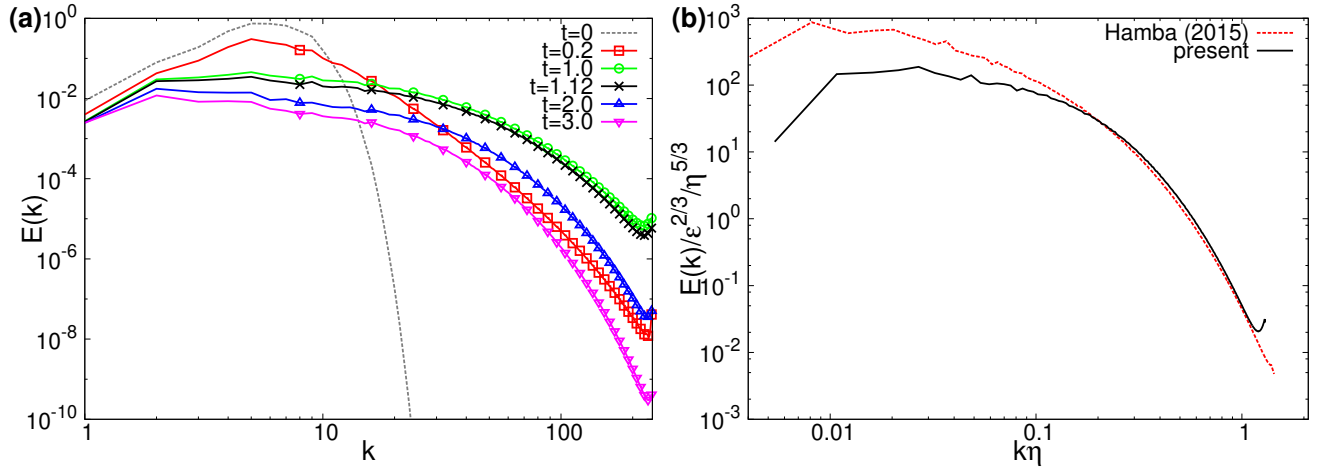

Figure G2: (a) Energy spectrum at each time. (b) Comparison of the energy spectrum between the present simulation and the result performed by Hamba (2015).

Bibliography

André, J.C. & Lesieur, M. 1977 Influence of helicity on the evolution of isotropic turbulence at high Reynolds number. *J. Fluid Mech.* **81**, 187.

Ariki, T. 2014 Mean-Lagrangian renormalization theory of inhomogeneous turbulent flow. PhD thesis, The University of Tokyo.

Ariki, T. 2015 Covariance of fluid-turbulence theory. *Phys. Rev. E* **91**, 053001.

Ariki, T. 2018 Constitutive theory of inhomogeneous turbulent flow based on two-scale Lagrangian formalism. *arXiv:1801.10435* .

Baerenzung, J., Politano, H., Ponty, Y. & Pouquet, A. 2008 Spectral modeling of turbulent flows and the role of helicity. *Phys. Rev. E* **77**, 046303.

Bardina, J., Ferziger, J. H. & Rogallo, R. S. 1985 Effect of rotation on isotropic turbulence: computation and modelling. *J. Fluid Mech.* **154**, 321.

Biferale, L., Musacchio, S. & Toschi, F. 2012 Inverse energy cascade in three-dimensional isotropic turbulence. *Phys. Rev. Lett.* **108**, 164501.

Biferale, L., Musacchio, S. & Toschi, F. 2013 Split energy–helicity cascades in three-dimensional homogeneous and isotropic turbulence. *J. Fluid Mech.* **730**, 309.

Borue, V. & Orszag, S. A. 1997 Spectra in helical three-dimensional homogeneous isotropic turbulence. *Phys. Rev. E* **55**, 7005.

Brandenburg, A. & Subramanian, K. 2005 Astrophysical magnetic fields and nonlinear dynamo theory. *Phys. Reports* **417**, 1.

Brissaud, A., Frisch, U., Leorat, J., Lesieur, M. & Mazure, A. 1973 Helicity cascades in fully developed isotropic turbulence. *Phys. Fluids* **16**, 1366.

Cambon, C. & Jacquin, L. 1989 Spectral approach to non-isotropic turbulence subjected to rotation. *J. Fluid Mech.* **202**, 295.

Cambon, C., Mansour, N. N. & Godeferd, F. S. 1997 Energy transfer in rotating turbulence. *J. Fluid Mech.* **337**, 303.

Chen, Q., Chen, S. & Eyink, G. L. 2003 The joint cascade of energy and helicity in three-dimensional turbulence. *Phys. Fluids* **15**, 361.

Craft, T. J., Launder, B. E. & Suga, K. 1996 Development and application of a cubic eddy-viscosity model of turbulence. *Int. J. Heat Fluid flow* **17**, 108.

Davidson, P. A. 2004 *Turbulence: An Introduction for Scientists and Engineers*. Oxford: Oxford University Press.

Davidson, P. A., Staplehurst, P. J. & Dalziel, S. B. 2006 On the evolution of eddies in a rapidly rotating system. *J. Fluid Mech.* **557**, 135.

Deusebio, E. & Lindborg, E. 2014 Helicity in the Ekman boundary layer. *J. Fluid Mech.* **755**, 654.

Dickinson, S. C. & Long, R. R. 1978 Laboratory study of the growth of a turbulent layer of fluid. *Phys. Fluids* **21**, 1698.

Dickinson, S. C. & Long, R. R. 1983 Oscillating-grid turbulence including effects of rotation. *J. Fluid Mech.* **126**, 315.

Eswaran, V. & Pope, S. B. 1988 An examination of forcing in direct numerical simulations of turbulence. *Comput. Fluids* **16**, 257.

Frisch, U., She, Z. S. & Sulem, P. L. 1987 Large-scale flow driven by the anisotropic kinetic alpha effect. *Physica D* **28**, 382.

Fukagata, K. & Kasagi, N. 2002 Highly energy-conservative finite difference method for the cylindrical coordinate system. *J. Comput. Phys.* **181**, 478.

Gatski, T. B. & Speziale, C. G. 1993 On explicit algebraic stress models for complex turbulent flows. *J. Fluid Mech.* **254**, 59.

Gillespie, D. T. 1996 The mathematics of Brownian motion and Johnson noise. *Am. J. Phys.* **64**, 225.

Godeferd, F. S. & Lollini, L. 1999 Direct numerical simulations of turbulence with confinement and rotation. *J. Fluid Mech.* **393**, 257.

Gvaramadze, V. V., Khomenko, G. A. & Tur, A. V. 1989 Large-scale vortices in helical turbulence of incompressible fluid. *Geophys. Astrophys. Fluid Dyn.* **46**, 53.

Hamba, F. 1987 Statistical analysis of chemically reacting passive scalars in turbulent shear flows. *J. Phys. Soc. Jpn.* **56**, 79.

Hamba, F. 2006 Euclidean invariance and weak-equilibrium condition for the algebraic Reynolds stress model. *J. Fluid Mech* **569**, 399.

Hamba, F. 2015 Turbulent energy density and its transport equation in scale space. *Phys. Fluids* **27**, 085108.

Hamba, F. 2017 History effect on the Reynolds stress in turbulent swirling flow. *Phys. Fluids* **29**, 025103.

Hamilington, P. E. & Dahm, W. J. A. 2008 Reynolds stress closure for nonequilibrium effects in turbulent flows. *Phys. Fluids* **20**, 115101.

Hanjalić, K. & Launder, B. 2011 *Modelling Turbulence in Engineering and the Environment: Second-Moment Routes to Closure*. Cambridge University Press.

Herring, J. R. 1974 Approach of axisymmetric turbulence to isotropy. *Phys. Fluids* **17**, 859.

Hopfinger, E. J. & Toly, J.-A. 1976 Spatially decaying turbulence and its relation to mixing across density interfaces. *J. Fluid Mech.* **78**, 155.

Inagaki, K. & Hamba, F. 2018 Energy transport due to pressure diffusion enhanced by helicity and system rotation in inhomogeneous turbulence. *Phys. Rev. Fluids* **3**, 124601.

Inagaki, K., Yokoi, N. & Hamba, F. 2017 Mechanism of mean flow generation in rotating turbulence through inhomogeneous helicity. *Phys. Rev. Fluids* **2**, 114605.

Ishihara, T., Morishita, K., Yokokawa, M., Uno, A. & Kaneda, Y. 2016 Energy spectrum in high-resolution direct numerical simulations of turbulence. *Phys. Rev. Fluids* **1**, 082403.

Jakirlić, S., Hanjalić, K. & Tropea, C. 2000 Second-moment closure analysis of rotating and swirling confined flows. In *European Congress on Computational Methods in Applied Sciences and Engineering, Barcelona*, pp. 11–14.

Kaneda, Y. 1981 Renormalized expansions in the theory of turbulence with the use of the Lagrangian position function. *J. Fluid Mech.* **107**, 131.

Kaneda, Y. 2007 Lagrangian renormalized approximation of turbulence. *Fluid Dyn. Res.* **39**, 526.

Kessar, M., Plunian, F., Stepanov, R. & Balarac, G. 2015 Non-Kolmogorov cascade of helicity-driven turbulence. *Phys. Rev. E* **92**, 031004.

Kida, S. & Yanase, S. 1999 *Turbulence dynamics*. Tokyo: Asakura (in Japanese).

Kitoh, O. 1991 Experimental study of turbulent swirling flow in a straight pipe. *J. Fluid Mech.* **225**, 445.

Kobayashi, T. & Yoda, M. 1987 Modified k–ε model for turbulent swirling flow in a straight pipe. *JSME Int. J.* **30**, 66.

Kolmogorov, A. N. 1941 The local structure of turbulence in incompressible viscous fluid for very large Reynolds numbers. *Dokl. Akad. Nauk. SSSR* **30**, 299.

Kolvin, I., Cohen, K., Vardi, Y. & Sharon, E. 2009 Energy transfer by inertial waves during the buildup of turbulence in a rotating system. *Phys. Rev. Lett.* **102**, 014503.

Koprov, B. M., Koprov, V. M., Ponomarev, V. M. & Chkhetiani, O. G. 2005 Experimental studies of turbulent helicity and its spectrum in the atmospheric boundary layer. *Dokl. Phys.* **50**, 419.

Kraichnan, R. H. 1959 The structure of isotropic turbulence at very high Reynolds numbers. *J. Fluid Mech.* **5**, 497.

Kraichnan, R. H. 1965 Lagrangian-history closure approximation for turbulence. *Phys. Fluids* **8**, 575.

Kraichnan, R. H. 1967 Inertial ranges in two-dimensional turbulence. *Phys. Fluids* **10**, 1417.

Kraichnan, R. H. 1973 Helical turbulence and absolute equilibrium. *J. Fluid Mech.* **59**, 745.

Kraichnan, R. H. 1977 Eulerian and Lagrangian renormalization in turbulence theory. *J. Fluid Mech.* **83**, 349.

Krause, F. & Rädler, K.-H. 1980 *Mean-field Magnetohydrodynamics and Dynamo Theory*. Oxford: Pergamon Press.

Launder, B. E., Reece, G. J. & Rodi, W. 1975 Progress in the development of a Reynolds-stress turbulence closure. *J. Fluid Mech.* **68**, 537.

Leslie, D. C. 1971 *Developments in the Theory of Turbulence*. Oxford: Clarendon Press.

Li, Y., Meneveau, C., Chen, S. & Eyink, G. L. 2006 Subgrid-scale modeling of helicity and energy dissipation in helical turbulence. *Phys. Rev. E* **74**, 026310.

Lilly, D. K. 1986 The structure, energetics and propagation of rotating convective storms. Part II: Helicity and storm stabilization. *J. Atmos. Sci.* **43**, 126.

Linkmann, M. 2018 Effects of helicity on dissipation in homogeneous box turbulence. *J. Fluid Mech.* **856**, 79.

Matsunaga, N., Sugihara, Y., Komatsu, T. & Masuda, A. 1999 Quantitative properties of oscillating-grid turbulence in a homogeneous fluid. *Fluid Dyn. Res.* **25**, 147.

Moffatt, H. K. 1969 The degree of knottedness of tangled vortex lines. *J. Fluid Mech.* **35**, 117.

Moffatt, H. K. 1970 Dynamo action associated with random inertial waves in a rotating conducting fluid. *J. Fluid Mech.* **44**, 705.

Moffatt, K. H. 1978 *Field Generation in Electrically Conducting Fluids*. Cambridge: Cambridge University Press.

Morinishi, Y., Nakabayashi, K. & Ren, Q. 2001*a* Dynamics of anisotropy on decaying homogeneous turbulence subjected to system rotation. *Phys. Fluids* **13**, 2912.

Morinishi, Y., Nakabayashi, K. & Ren, Q. 2001*b* A new DNS algorithm for rotating homogeneous decaying turbulence. *Int. J. Heat Fluid Flow* **22**, 30.

Morinishi, Y., Nakabayashi, K. & Ren, S. 2001*c* Effects of helicity and system rotation on decaying homogeneous turbulence. *JSME Int. J., Ser. B* **44**, 410.

Noda, A. T. & Niino, H. 2010 A numerical investigation of a supercell tornado: Genesis and vorticity budget. *J. Meteorol. Soc. Jpn.* **88**, 135.

Okamoto, M. 1994 Theoretical investigation of an eddy-viscosity-type representation of the Reynolds stress. *J. Phys. Soc. Jpn.* **63**, 2102.

Okamoto, M. 1995 Theoretical turbulence modelling of homogeneous decaying flow in a rotating frame. *J. Phys. Soc. Jpn.* **64**, 2854.

Orlandi, P. 1997 Helicity fluctuations and turbulent energy production in rotating and non-rotating pipes. *Phys. Fluids* **9**, 2045.

Orszag, S. A. 1969 Numerical methods for the simulation of turbulence. *Phys. Fluids* **12**, II–250.

Piomelli, U. 1999 Large-eddy simulation: achievements and challenges. *Prog. Aerosp. Sci.* **35**, 335.

Pope, S. B. 1975 A more general effective-viscosity hypothesis. *J. Fluid Mech.* **72**, 331.

Pope, S. B. 2000 *Turbulent flows*. Cambridge: Cambridge University Press.

Ranjan, A. 2017 Segregation of helicity in inertial wave packets. *Phys. Rev. Fluids* **2**, 033801.

Ranjan, A. & Davidson, P. A. 2014 Evolution of a turbulent cloud under rotation. *J. Fluid Mech.* **756**, 488.

Reynolds, O. 1883 An experimental investigation of the circumstances which determine whether the motion of water shall he direct or sinuous, and of the law of resistance in parallel channels. *Phil. Trans. R. Soc. Lond.* **174**, 935.

Rogers, M. M. & Moin, P. 1987 Helicity fluctuations in incompressible turbulent flows. *Phys. Fluids* **30**, 2662.

Schumann, U. 1977 Realizability of Reynolds-stress turbulence models. *Phys. Fluids* **20**, 721.

Shih, T.-H., Zhu, J. & Lumley, J. L. 1993 A realizable Reynolds stress algebraic equation model. *NASA TM 105993* .

Shih, T.-H., Zhu, J. & Lumley, J. L. 1995 A new Reynolds stress algebraic equation model. *Comput. Methos Appl. Mech. Engrg.* **125**, 287.

Shimomura, Y. 1998 A theoretical study of the turbulent diffusion in incompressible shear flows and in passive scalars. *Phys. Fluids* **10**, 2636.

Shimomura, Y. & Yoshizawa, A. 1986 Statistical analysis of anisotropic turbulent viscosity in a rotating system. *J. Phys. Soc. Jpn.* **55**, 1904.

Smagorinsky, J. 1963 General circulation experiments with the primitive equations. I. The basic experiment. *Mon. Weather Rev.* **91**, 99.

Spalart, P. R. 1998 Airplane trailing vortices. *Annu. Rev. Fluid Mech.* **30**, 107.

Speziale, C. G. 1987 On nonlinear K–l and K–ϵ models of turbulence. *J. Fluid Mech.* **178**, 459.

Speziale, C. G., Sarkar, S. & Gatski, T. B. 1991 Modelling the pressure–strain correlation of turbulence: an invariant dynamical systems approach. *J. Fluid Mech.* **227**, 245.

Speziale, C. G., Younis, B. A. & Berger, S. A. 2000 Analysis and modelling of turbulent flow in an axially rotating pipe. *J. Fluid Mech.* **407**, 1.

Sreenivasan, K. R. 1995 On the universality of the Kolmogorov constant. *Phys. Fluids* **7**, 2778.

Steenbergen, W. W. 1995 Turbulent pipe flow with swirl. PhD thesis, Technische Universiteit Eindhoven.

Stepanov, R., Frick, P., Dulin, V. & Markovich, D. 2018 Analysis of mean and fluctuating helicity measured by To-moPIV in swirling jet. *EPJ Web Conf.* **180**, 02097.

Stepanov, R., Golbraikh, E., Frick, P. & Shestakov, A. 2015 Hindered energy cascade in highly helical isotropic turbulence. *Phys. Rev. Lett.* **115**, 234501.

Taulbee, D. B. 1992 An improved algebraic Reynolds stress model and corresponding nonlinear stress model. *Phys. Fluids A* **4**, 2555.

Taylor, G. I. 1935 Statistical theory of turbulence. *Proc. R. Soc. A* **151**, 421.

Wallace, J. M., Balint, J.-L. & Ong, L. 1992 An experimental study of helicity density in turbulent flows. *Phys. Fluids A* **4**, 2013.

Wallin, S. & Johanson, A. V. 2000 An explicit algebraic Reynolds stress model for incompressible and compressible turbulent flows. *J. Fluid Mech.* **403**, 89.

Watanabe, T. & Gotoh, T. 2007 Inertial-range intermittency and accuracy of direct numerical simulation for turbulence and passive scalar turbulence. *J. Fluid Mech.* **590**, 117.

Weis, J. & Hutter, K. 2003 On Euclidean invariance of algebraic Reynolds stress models in turbulence. *J. Fluid Mech.* **476**, 63.

Wyld, H. W. 1961 Formulation of the theory of turbulence in an incompressible fluid. *Ann. Phys.* **14**, 143.

Yokoi, N. 2016 Modeling helicity dissipation-rate equation. In *Progress in Turbulence VI, Springer Proceedings in Physics 165* (ed. J. Peinke *et al.*), pp. 93–96. Heidelberg: Springer.

Yokoi, N. & Brandenburg, A. 2016 Large-scale flow generation by inhomogeneous helicity. *Phys. Rev. E* **93**, 033125.

Yokoi, N. & Yoshizawa, A. 1993 Statistical analysis of the effects of helicity in inhomogeneous turbulence. *Phys. Fluids A* **5**, 464.

Yoshimatsu, K., Midorikawa, M. & Kaneda, Y. 2011 Columnar eddy formation in freely decaying homogeneous rotating turbulence. *J. Fluid Mech.* **677**, 154.

Yoshizawa, A 1978 A governing equation for the small-scale turbulence. II. Modified DIA approach and Kolmogorov's -5/3 power low. *J. Phys. Soc. Jpn.* **45**, 1734.

Yoshizawa, A. 1984 Statistical analysis of the derivation of the Reynolds stress from its eddy-viscosity representation. *Phys. Fluids* **27**, 1377.

Yoshizawa, A. 1998 *Hydrodynamic and Magnetohydrodynamic Turbulent Flows: Modelling and Statistical Theory*. Dordrecht: Kluwer.

Yoshizawa, A. 2002 Statistical analysis of mean-flow effects on the pressure–velocity correlation. *Phys. Fluids* **14**, 1736.